UNIVERSITY OF SOUTHAMPTON

FACULTY OF ENGINEERING, SCIENCE & MATHEMATICS

School of Physics and Astronomy

Chameleon Metals - Investigating the Response to Light of Sub-Wavelength Metallic Meshes

by

Steven Coyle

Thesis for the degree of Doctor of Philosophy

April 2004

UNIVERSITY OF SOUTHAMPTON

ABSTRACT

FACULTY OF ENGINEERING, SCIENCE AND MATHEMATICS
PHYSICS AND ASTRONOMY

Doctor of Philosophy

CHAMELEON METALS – INVESTIGATING THE RESPONSE TO LIGHT OF SUB-WAVELENGTH METALLIC MESHES

By Steven Coyle

This thesis describes experimental investigations into the optical response of novel metallic films structured in the size regime 300nm-10μm in the visible region. The films are deposited electrochemically through a template composed of self-assembled latex colloids. The metal grows up through the interstitial voids, creating an inter-linked macroporous film. The film thickness can be carefully controlled by varying the depth of and the charge passed through the aqueous, metallic ion complex solution. After deposition the colloids are removed through dissolution to leave a free-standing metallic film.

Films made from gold and platinum have been shown to have interesting optical responses, most notably dramatic colour changes with variation in thickness. The description of such behaviour is complicated by the strongly diffractive nature of the original template and the contribution of localised features of self-assembled colloidal arrangements. Further intricacy is provided by the morphology of the pore mouth of individual cavities within the mesh as the film is grown above one radius thickness of the colloids.

Currently, no model satisfactorily describes the reflectivity of these films. Instead, five different approaches are investigated; interference based on reflections off the flat top surface and from within the voids themselves, a confined plasmon model based on studies of metallic voids, diffraction off a two dimensional grating, a surface plasmon model based on a two dimensional plasmonic band gap materials and finally, a finite element analysis of the voids.

The results generated with these models are compared against systematic white light experiments of the reflectivity of gold and platinum films deposited through well-ordered templates composed of a monolayer spheres of diameter 700nm, graded in thickness from 0nm - 700nm. Normal incidence reflectivity show several noticeable features; thin films below one quarter sphere height, the spectra exhibit behaviour consistent with reflections off a grating; thicker films several reflectivity dips are observed which move towards longer wavelength with increasing film thickness.

Reflectivity studying the polarisation show a distinct difference between the gold and platinum films; gold shows reflectivity minima consistent with scattering of surface plasmons off the voids. Platinum, on the other hand, is incapable of supporting surface plasmon modes and so its response to polarised light is almost identical to that of normal incidence unpolarised light.

My family and other animals

Table of Contents

Acknowledgements

I would like to thank my supervisor, Professor Jeremy Baumberg, for giving me the opportunity to pursue this research and for his constant hard work on my behalf, as well as his enthusiasm and encouragement over the last three (and a bit) years,

Secondly, I would like to thank my collaborators in the School of Chemistry Professor Phil Bartlett, Dr. Mamdouh Abdelsalam and Dr. Mohamed Ghanem for their hard work in producing the samples tested in this thesis. Without their input this project would not have been possible and without their determination to improve the quality of the films much of the understanding we now have would not have happened.

Thirdly, I would like to thank the members, past and present, of the Ultrafast Group who have have always been happy to help, explain and encourage. I would most like to thank Dr. Caterina Netti for her input at the beginning of this project in imparting some of her considerable scientific expertise and experience. Furthermore, I would like to thank Dr. Pavlos Lagoudakis for his help and insight in discussions and help in the lab. I would also like to express thanks to Dr. David Smith for his support and also Tim Kelf for his work on this project as he takes over from me.

Fourthly, I would like to thank the various people who I have worked with during this project especially Dr. David Whittaker, for his work on the first theoretical models of our structures, and the Holey Fibre Group from the Optoelectronics Research Centre and the Quantum Optoelectronics Group members whose various inputs and suggestions were especially helpful at difficult moments.

I would like to thank my family for their unstinting support and love throughout my studies. Finally, I would like to thank Claire for all her help, love and support and for always being there.

Southampton, UK
April, 2004

Steven Coyle

Selected Publications

- Spherical MicroMirrors from Templated Self-Assembly: Polarization Rotation on the Micron Scale
  S. Coyle, G. V. Prakash, and J. J. Baumberg, M. Abdelsalam and P. N. Bartlett Appl. Phys. Lett. 83, 767 (2003)

- Confined Plasmons in Metallic Nanocavities
  S. Coyle, M. C. Netti, J. J. Baumberg, M. A. Ghanem, P. R. Birkin P. N. Bartlett, D. M. Whittaker Phys. Rev. Lett. **87**, 176081-1 (2001)

- Confined Surface Plasmons in Gold Photonic Nanocavities
  M. C. Netti, S. Coyle, J. J. Baumberg, M. A. Ghanem, P. R. Birkin P. N. Bartlett, D. M. Whittaker, Adv. Mat. **13**, 1368 (2001)

- Optical Properties of Nanostructured Films
  P. N. Bartlett, J. J. Baumberg, S. Coyle, M. A. Abdelsalam Faraday Discussion **125**, 19 (2003)

- Preparation of Arrays of Isolated Spherical Cavities by Self-Assembly of Polystyrene Spheres on Self-Assembled Pre-patterned Macroporous Films,
  M. A. Abdelsalam, S. Coyle, P. N. Bartlett, J. J. Baumberg, Adv. Mat. **16**, 90 (2004)

- UV Generation in pure silica holey fibre
  J. H. V. Price, T. M. Monro, K. Furusawa, W. Belardi, J. C. Baggett, S. Coyle, J. J. Baumberg, R. Paschotta, D. J. Richardson, Appl. Phys. B, **77**, 291 (2003)

Chapter 1

Introduction

In recent years nanoscience has emerged as a hugely promising avenue of science, encompassing conventionally divergent areas in the study of systems and processes in the size regime between $\sim$ 0.1nm to 100's nm. Across this vast scale lies some of the most studied phenomena in science; the sub-nanometre scale encompasses quantum phenomena observed in semiconductors and metals as well as the complexity of the double helix structure of DNA. At the opposite end of the spectrum lies the complexity of interactions of light with structures on the same size scale as its wavelength as well as biological molecules.

Unlike many new research areas, it is difficult to define the beginning of this field; it has not been preceded by one single ground-breaking discovery; instead it has evolved from the realisation that different areas of science are able to make significant contributions to seemingly unrelated topics due to the convergence in interest of the same size regime. Richard Feynman's seminal talk to the American Physical Science in 1959 entitled *"There's Plenty of Room at the Bottom - An invitation to a new field of Physics"* [1] was one of the first to suggest that controlling matter on the nanoscale had the potential to impact on areas from data storage to biology. On these length scales matter acts very differently from both its bulk behaviour and its individual constituent atoms. Material properties and interactions could therefore be radically altered by merely arranging it on nanoscale lengths.

This thesis studies the optical response of structures at the sub-micron end of the nanoscience spectrum, where properties are determined by the structure being of the same order of magnitude as the wavelengths of incident electromagnetic radiation.

Progress achieved in moulding the electronic properties of materials using electron wavelength-scale structures, such as semiconductors, has encouraged much enterprise to be focused on repeating this success for light. Progress in the field of controlling light, known as photonics, has been rapid. The resulting intricate photonic properties arise from a complex blend of reflections and scatterings determined by the wavelength-, polarisation- and angle of incidence-dependent responses of the material from sub-micron structures, both individually and as part of a periodic array. The results can, at first sight, seem counterintuitive; for example, a transparent dielectric can be made into a perfect reflector, a so-called photonic band gap material, by removing material in a wavelength scale periodic array of cylinders, Fig. 1.1(a) [2, 3]. In contrast, drilling periodic holes through optically thick metals produces a transmission many orders of magnitude greater than would be expected from standard aperture theory, Fig. 1.1(b) [4]. Intriguingly, the study of photonic systems has also uncovered the exploitation of highly scattering structures in nature; the irridescent displays of some species of butterfly Fig. 1.1(c) [5], [6], and the sea mouse, Fig. 1.1(d) [7], have been found to have great similarities with recent technological advances. In the case of butterflies observations suggest that the response to polarised light of the wings is actually used as a mating signal [8].

One of the key challenges impeding progress in manufacturing sub-micron architectures is that traditional top-down methods have so far struggled to produce cost-effective, high-quality samples. The realisation that evolution has been able to produce strong photonic effects suggests that artificial architectures could be built from a combination of forces inherent to a system, known as self-assembly. At present, self-assembly of complex systems still poses substantial challenges, although a measure of success has been achieved with very simple constituents, such as sub-micron spheres.

This thesis will discuss the photonic properties of macroporous metals structured from self-assembled casts of sub-micron spheres. The interest in the work stems from attempts to exploit the inherent simplicity of self-assembled structures with the strong interaction of light with well-ordered sub-micron structures. The research has been conducted collaboratively between the School of Physics and Astronomy and the

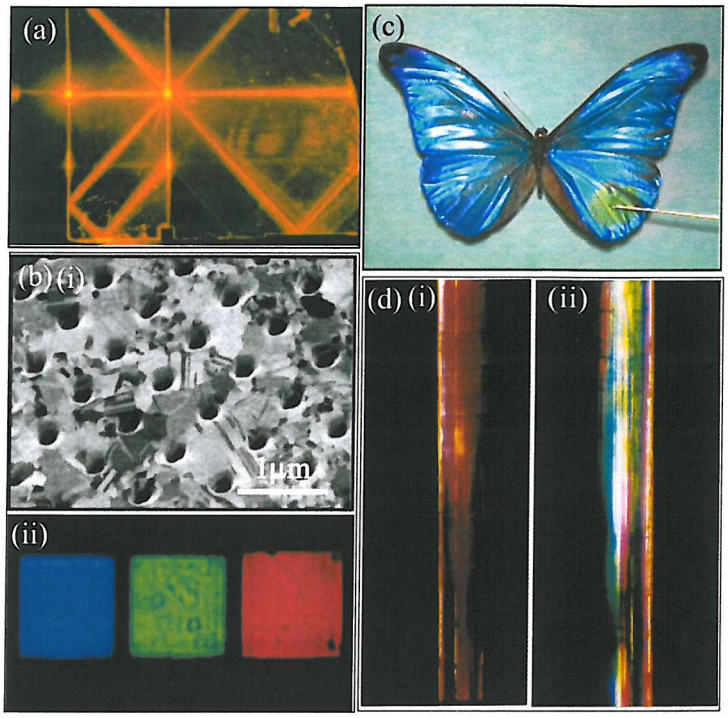

Figure 1.1: Images of photonic properties from nanoscale photonic systems (a) six-way diffraction from a photonic crystal [15]; (b)(i) Focused ion Beam image of 150nm diameter holes with a period of 900nm in a polycrystalline silver film [4]; (ii) Transmission images of free-standing, optically thick silver films: the blue, green and red arrays had hole periods of 300, 450, 550nm and hole diameters 155, 180, 225nm respectively (see chapter 3 for discussion) [10]; (c) Morpho rhetenor butterfly, whose wings are an irridescent blue, the green section of the wing has had its colour changed by adding a solvent to it which changes the path length of the interference condition [11]; (d) The photonic properties of the spine of the sea mouse (i) Light Incident perpendicular to the axis of the sea mouse's spine is red (ii) Off-axis incidence light shows blues and greens[12] (http://www.physics.usyd.edu.au/ nicolae/seamouse.html)

School of Chemistry in Southampton. The resulting structures have a high degree of complexity in regard to their physical topology and their response to light. Their most striking feature is their reflectivity which shows dramatic colour changes depending on the metal, its thickness and the template periodicity, hence the title "Chameleon Metals" Fig. 1.2(a, b). The samples are strongly diffracting, implying the films are well-ordered and uniform, Fig. 1.2(c, d). When viewed with scanning electron microscopy (SEM) the films show regularly spaced open cavity structures, Fig. 1.2(e, f). Atomic force microscopy also reveals the topological structure of these surfaces and shows the interconnections between the spheres, Fig. 1.2(i). The latex sphere template can be arranged into large area crystals which can be easily viewed with a CCD camera and a zoom lens Fig. 1.2(h). The electrochemical growth methods are capable of producing a smooth spherical surface inside the cavities, as shown by high magnification optical micrographs of reflections from cavities larger than a micron Fig. 1.2(i). As well as possesing interesting optical properties, macroporous films also show different physical properties in comparison with planar samples, such as super-hydrophobicity, Fig. 1.2(j).

The thesis is presented as follows.

Chapter 2 discusses the background to this work such as recent advances in photonic systems and describes self-assembled structures and the factors which influences their final state.

Chapter 3 describes the optical properties of the metals used to make the structures studied in this thesis; gold, platinum and silver. Their properties as bulk materials are discussed as well as their properties at the nanoscale, such as nanoparticles and gratings. Their responses are explained in terms of modifying the surface plasmon response of a metal through its structure.

Chapter 4 describes the preparation methods used to assemble latex sphere templates, the electrochemical plating conditions and discusses the surface morphology of the samples.

Chapter 5 describes the experimental techniques used to probe the optical properties of the films in the visible range using coherent and incoherent broadband sources.

Chapter 6 describes the various approaches needed to model the films' responses

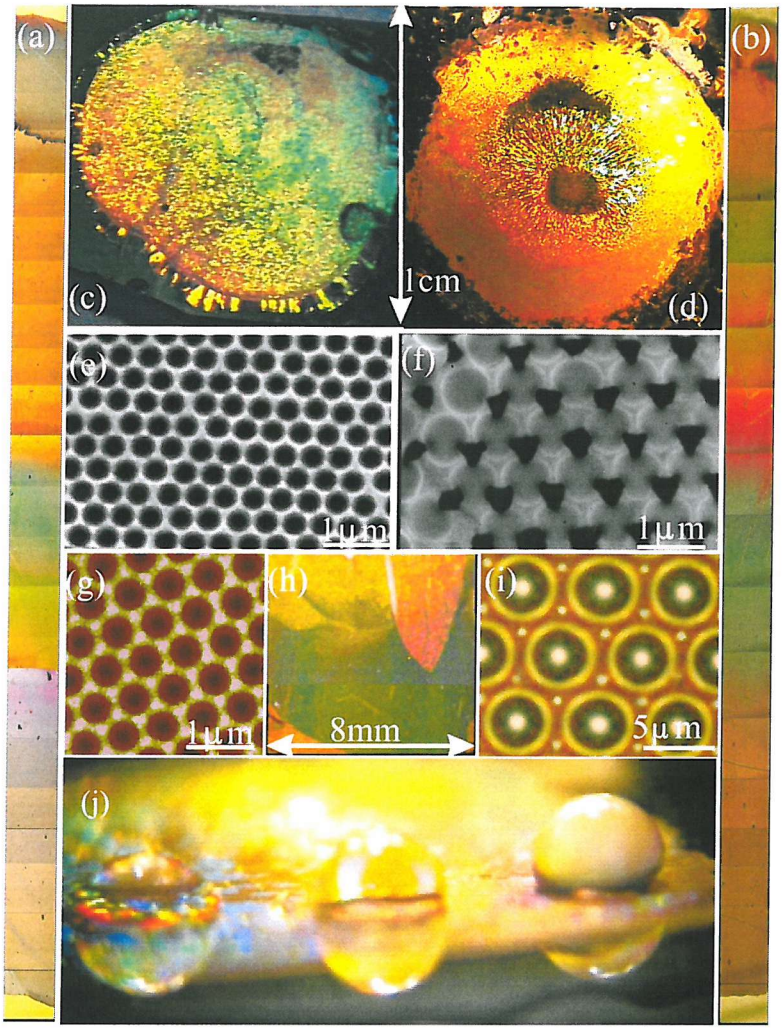

Figure 1.2: Chameleon Metals: Microscope images of macroporous films of (a) platinum and (b) gold templated through arrays of 500nm diameter latex spheres, step graded in thickness from 0 to 500nm thick. Optical images of diffracted light from metal films deposited through a 700nm diameter sphere template of (c) Pt and (d) Au.(e) Scanning Electron Micrographs of films cast from (e) a sphere monolayer template and (f) from a multiple layer template. (g) Atomic Force Microscopy scan of a metallic film cast from 900nm diameter spheres which show how the voids interconnect. (h) Image of diffraction from a latex sphere template showing two highly ordered regions. (i) Reflection of Au micron-sized cavities at high magnification. (j) Contact angle of water on a graded macroporous film.

to light; including a ray optic model, Mie scattering of light by small particles and voids and photonic/plasmonic band gap calculations. Further developments of these ideas are discussed using models of finite difference time domain calculations.

Chapter 7 outlines the initial experimental results of the response to visible light at normal and acute angles of incidence of both metals made from sub-micron and micron sphere templates.

Chapter 8 discusses more detailed results on the reflectivity of metals at both normal and near normal angles of incidence and discusses the success of each of the models described in chapter 6 in modelling the observed spectral features.

Chapter 9 describes possible future directions and concludes the thesis.

Chapter 2

Complex Photonic Systems and Simple Self-Assembly

Before discussing the metallic structures studied in later chapters, a brief overview of the two areas which provided the initial motivation is outlined; photonics and self-assembly. The title of this chapter might at first appear to be a little confused in describing both complex and simple systems. This problem arises from the usage of "photonic" and "self-assembly" in a variety of different contexts. In general, photonic systems could be used as a description of many interactions involving light, whereas self-assembly refers to anything which coheres or aggregates due to forces inherent to the system, including extremely complicated things such as living organisms. With this in mind the title refers to systems which exhibit interactions that cannot be calculated analytically and involve the aggregation of sub-micron geometrical shapes such as spheres.

Although this thesis is not about photonic crystals as such, the intention in mentioning them briefly is to illustrate the uses and potential benefits of controlling light with sub-wavelength structures, as well as the challenges which have yet to be overcome.

2.1 Photonic Band Gap Structures

2.1.1 Maxwell's Equations

Before discussing specific examples, Maxwell's equations, which govern light/matter interactions, are introduced (in S. I. Units)[9]. An electromagnetic field in space is represented by two vectors **E** and **B**, the electric vector and the magnetic induction respectively. To describe the effect of the field on a material a second set of vectors are used; the electric current density, **j**, the electric displacement, **D**, and the magnetic vector, **H**. The vectors are related by two equations

$$\nabla \times \mathbf{H} - \frac{\delta \mathbf{D}}{\delta t} = \mathbf{j} \tag{2.1}$$

$$\nabla \times \mathbf{E} + \frac{\delta \mathbf{B}}{\delta t} = 0 \tag{2.2}$$

Furthermore, two scalar relations are used.

$$\nabla \cdot \mathbf{B} = 0 \tag{2.3}$$

$$\nabla \cdot \mathbf{D} = \rho \tag{2.4}$$

In the case of the response of homogeneous dielectric material there are no sources of light and no free charges or currents. Therefore, we can write $\rho = \mathbf{j} = 0$. Also, in relating the electric displacement, **D**, to the electric vector, **E**, and the magnetic induction, **B** to the magnetic vector **H** the material is assumed to have linear relationships; i.e. $\mathbf{D} = \epsilon(r)\mathbf{E}(\mathbf{r})$ and $\mathbf{B} = \mu_o \mathbf{H}$ ($\mathbf{r}$ is a spatial vector and because the magnetic permeability is very nearly one, the magnetic induction and vector are taken to be exactly equal). Further manipulation of these equations in this form is beyond the scope of this thesis, except to note that in writing the magnetic and electric fields as temporally harmonic it is possible to derive the equation used to model these materials, known as the master equation.

$$\nabla \times \left[\frac{(1}{\epsilon}(\mathbf{r}) \times \mathbf{H}(\mathbf{r})\right] = \left[\frac{\omega}{c}\right]^2 \mathbf{H}(\mathbf{r}) \tag{2.5}$$

The nature of this equation is complex and it cannot be solved analytically. However, a good idea of why band gaps form in materials can be gained from an intuitive approach.

2.1.2 Background

Although it is generally claimed that Purcell was the first to discuss the modification of the radiation properties of a dipole by the presence of a mirror [13], interest in this area was aroused by two papers published in 1987 [2, 3]. These discussed emulating the success of controlling electrons within semiconductor materials with materials engineered to mould and control the flow of light. The electronic properties of semiconductors have been extensively studied and successfully exploited in many devices such as laser diodes and electronic switches. The root cause of such success is the range of electronic properties exploited through the strong interaction of the periodic structure of semiconductors with electrons. Periodic structures produce standing waves through satisfying the Bragg condition in the first Brillouin zone [14], which in one dimension is given by:

$$k = \pm\frac{1}{2}G = \pm n\frac{\pi}{a} \tag{2.6}$$

where k=wavevector, G= reciprocal lattice vectors, n= integer and a=lattice constant.

This system produces energy gaps at $k = \pm n\pi/a$ where two different standing waves exist with different potential energies and distribute electrons in different configurations in the lattice Fig. 2.1(a). Yablonovitch's insight [2] was to consider whether Bragg reflections in more than one dimension could be attempted with light rather than electrons [16] (Fig. 2.1(b)). In keeping with solid state physics terminology, the gap in energy created by this energy difference is known as a "photonic band gap" (PBG). In the same way that the atomic lattice in materials like silicon confines electrons in three dimensions, a three dimensional photonic crystal would confine electromagnetic fields of a certain bandwidth in three dimensions. Such a crystal would depend on multiple scattering effects to produce a lossless reflection if

the bulk dielectric material is inherently transparent to light. The consequences of this effect are profound: a photonic crystal made with a defect state could effectively localise/trap a photon of the appropriate wavelength. PBG materials surrounding an excited atom with a band gap tuned around the emission wavelength would extend the lifetime of the state by spontaneous emission control [18].

In describing the properties of photonic crystals, the dimensionality of the system is extremely important. Photonic band gaps engineered in 1, 2 or 3 dimensions are shown in Fig. 2.2. A band gap in 2 dimensions could be produced through the periodic arrangement of vertical pillars whereas a three dimensional gap would require a complex 3 dimensional periodic refractive index contrast. However, even then the right refractive indices and lattice type have to be chosen carefully to get photonic gaps for all directions and polarisations. When the electric fields are confined in less than three dimensions, leaky modes exist, i.e modes not inhibited by the band gap due to having a momentum component out of the plane of confinement.

2.1.3 Progress and Problems

To assess how to advance the field of photonics it is useful to discuss why controlling electrons is very much more advanced than controlling light. Photons in the visible part of the spectrum have much longer wavelengths ($\sim 400-800$nm) than electrons ($\sim$ 0.1nm), consequently researchers in the two fields have concentrated their research on vastly different length scales. In the case of electrons, nature has already constructed the necessary length scales from atoms in crystalline materials such as Si, Ga, As and C. However, the periodicity required for light is more problematic; we must look for structures engineered on sub-wavelength scales [17], which are less abundant in nature. As mentioned in the introduction, nature has not been totally unhelpful in providing answers to this problem, with examples such as butterfly wings [5], but these are far more complex to understand and construct. Furthermore, photons are bosons, and so fundamentally different in nature from electrons (fermions). In some instances this advantageous - light beams do not interact with each other, but in terms of finding a photonic analog of charge density, or a gateable potential barrier these differences are a hindrance.

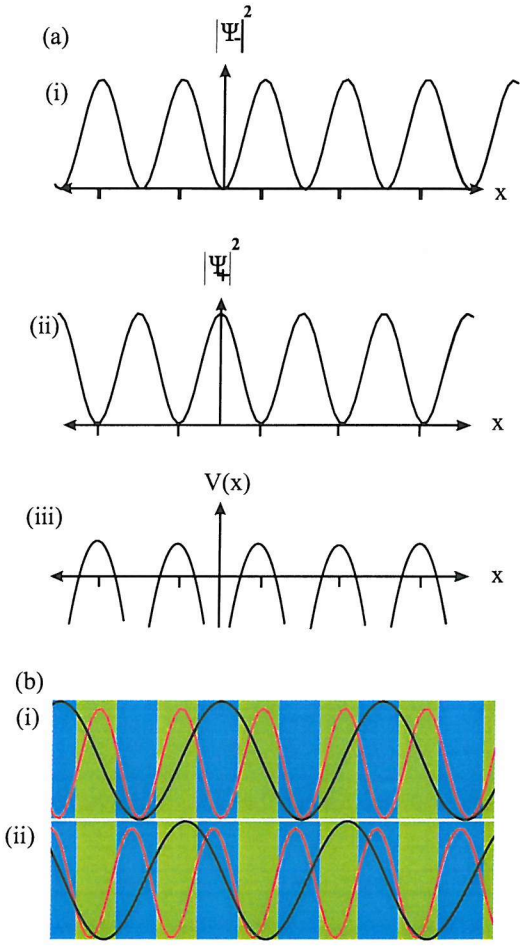

Figure 2.1: The similarity between (a) electrons in a periodic potential field and (b) light in a Bragg reflector. (a) In a periodic field there are two stationary wave solutions which can be combined as either (i) ψ_- or (ii)ψ_+ in the presence of the potential (iii) V(x) which localises on or between the ion cores. (b) The electric field distribution in a $\lambda/4$ stack of alternating electric fields (black curves)can either have its anti-nodes in the (i) higher refractive index material (blue) or (ii) the lower refractive index material (green) which localise the electric field power (red curves) in one material or the other, again creating an energy difference.

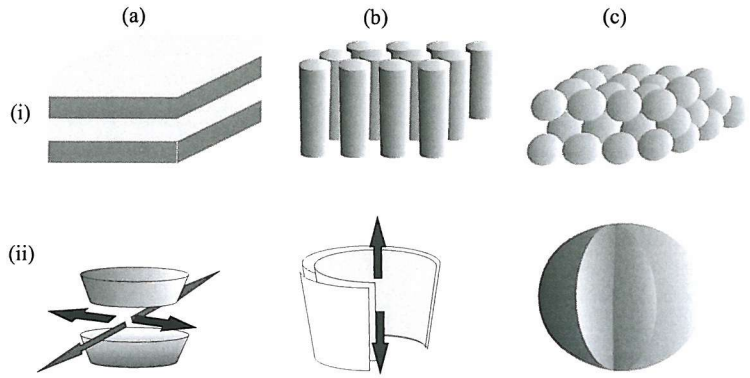

Figure 2.2: Photonic crystals of various dimensions (a) 1D , (b) 2D (c) 3D (i) Schematics showing structure geometries required to confine, (ii) Dimensions in which radiation is confined, arrows show in which direction leaky modes can exist.

One very interesting feature of photonic crystals which arises from the master equation, eqn. 2.5, that sets it apart from Schröedinger's equation is that it has no fundamental length scale. In other words, the concept of localising electromagnetic fields is independent of their wavelength, provided the response of the material does not change with wavelength. This effect was exploited with the first experimental verification of a band gap, discovered in the microwave region, which showed a stop band from 13-15GHz [19] (Fig. 2.3(a)).

Much theoretical and experimental effort has been devoted to discovering which periodic arrangements are capable of producing a photonic band gap. By the very nature of the required periodicity needed to produce band gaps in both the technologically crucial " telecoms window" (1.5μm), and the visible regime, fabrication strategies are complicated. Therefore, as a first step towards producing photonic crystals, the reduced dimensional route has proved the most successful in demonstrating practical devices; such as polarisation splitting [20], guiding and bending with a radius smaller than one wavelength [21] and so called superprism effects [22] (large changes in propagation angle for small deviations in incident beam angle). Theoretical studies of 2 dimensional structures have indicated that a number of possible periodic structures have photonic band gaps including triangular [23] and graphite. The triangular has proved to be less promising because it produces a narrow gap with dimensions small enough to provide significant problems in fabrication [24]. A further intriguing

discovery, both theoretically [25] and experimentally [26, 27] has been PBG's in 2D quasiperiodic structures (Fig. 2.3(b)). The comparatively higher levels of symmetry of theses crystals eliminates waveguiding modes coincident with the photonic crystal and their reduced orientational order produces a more isotropic scattering process.

Despite success in producing 2D crystals the ultimate aim of many researchers is still practical 3D band gap fabrication routes. Many schemes have attempted to produce a 3D band gap including; stacking layers of parallel dielectric rods with each layer rotated by 90^o relative to the one below [28, 29] (Fig. 2.3 (c)), tetragonal lattices of slanted pores [30] and an alternating stack structure made from 2 2D photonic crystal lattices (Fig. 2.3(d)) as well as using rods in air and air cylinders in dielectric [31] (Fig. 2.3(e)).

All the examples given above have been proved to show the much fêted band gap. However, all share a common failing of having expensive and complex manufacturing processes. In some cases these are so complex as to render the finished product fragile enough as to be unlikely ever to be made. Given the complexity of the calculations there is a real need for experimental data in order to gain a better understanding of the interaction of light in such architectures. All these fabrication strategies are are adapted from the silicon microelectronics industry [13], which, while offering many years of expertise and development in the ability to grow thin, well-ordered layers, does not offer satisfactory solutions to the problem of removing large numbers of regular sub-micron holes or cylinders needed to produce the required index contrast. In many cases electron-beam drilling has to be used to drill the structures, as standard photolithography methods are too coarse. The lack of a cost-effective reliable fabrication route has proved to be one of the main stumbling blocks in progressing the technology. Rather than improve these techniques further, many researchers have suggested that an alternative route lies with exploiting the inherent periodicity of self-organising systems.

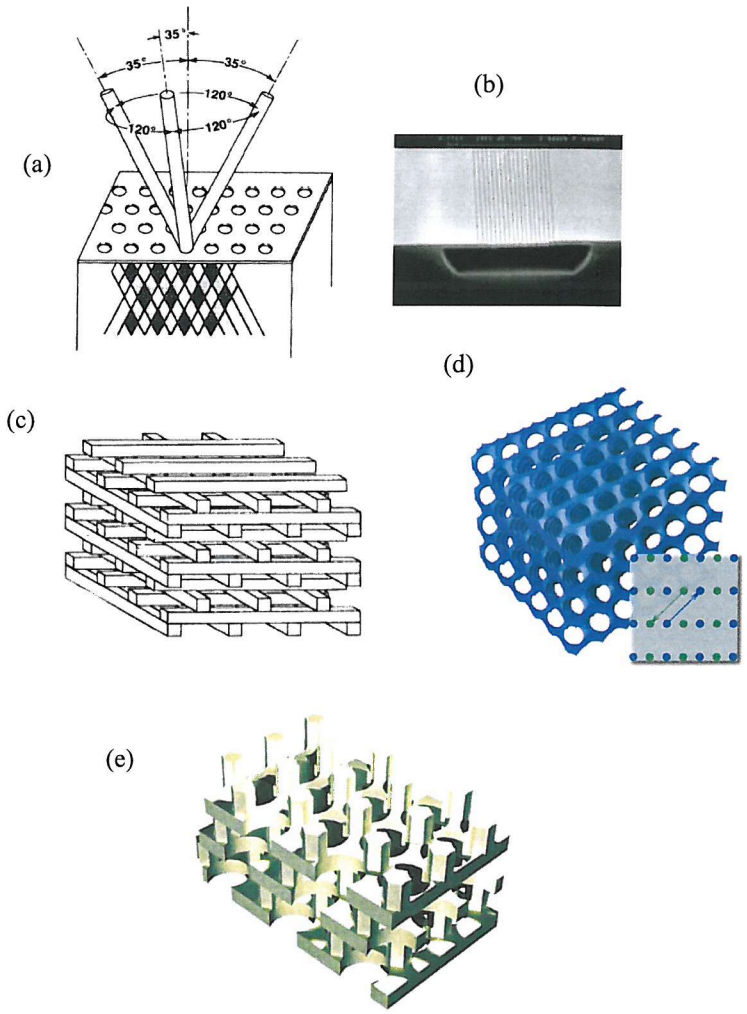

Figure 2.3: Schmeatic images of Some Photonic Band Gap Crystals (a) Yablonovite: the world's first experimental demonstration of band gaps [19]. (b)A Scanning electron micrograph of world's first visible wavelength photonic crystal from [15]. (c) Schematic of stacking layers "woodpile" arrangement [29]. (d) Tetragonal crystal, inset shows top view of the pores where the arrows indicate the directions for the two sets of pores which are produced through two separate drilling processes [30]. (e) A 3D crystal made from 2 2D crystals which shows one vertical period and three horizontal periods [31]

2.2 Self-Organisation and Self-Assembly

The field of self-assembly is tremendously broad, but here we restrict our attention to the assembly of spheres. This is a sensible move considering the immense practical and theoretical challenges associated with dissecting the optical response of such intricate architectures. The idea of microfabrication using well-ordered self-assembled systems predates that of PBGs, with the use of spherical colloidal particles as a large area lithographic mask, so called "natural lithography" [32]. Theoretical studies on self-organised systems based on latex (n= 1.3) and TiO_2 (n= 2.8) spheres have shown that colloidal systems do not possess a photonic band gap. However, the inverse structure, filling the interstitial spaces between the spheres and removing the spheres, does have a complete 3D band gap because it has a higher proportion of void space, producing a larger difference in the energy distribution of consecutive modes [34, 33]. The inverse opal structure is also of interest as it provides a technique of producing nano-structured materials cheaply and efficiently and even producing monodisperse colloids of materials which cannot be formed using chemical methods [35]. These observations raise two important questions; can self-assembled structures have a high enough degree of order to realise this potential, and how can the proposed infilling be achieved? This section is divided in two; the first discusses colloidal structures and the methods used to produce ordered arrays, and the second describes different methods used to achieve an inverse architecture. In reviewing progress in this field the two most studied materials, silica and polymer latex [36], will be considered, although the samples reported later on in this thesis were made solely of latex spheres due to the ease with which they can be removed from the final structure.

2.2.1 Colloidal Particles

Colloid Production

Colloidal particles are commercially available as monodisperse solutions (variation in diameters typically $\sim$ 1%), with size ranging from 1nm to 50μm. The size range is set by the translational diffusion of the particles due to Brownian motion of the dispersing medium's particles. Latex spheres are made chemically through emulsion

polymerisation, with monodispersity achieved through controlling the reaction rate with temperature, and having a high flux of free radical initiators which imbed in the forming spheres and continue the polymerisation process. Silica spheres are made through the Stober method which involves the reaction of complex inorganic solutions to produce Si_2O which then aggregates with other molecules. Why this process leads to monodisperse products is still subject to much speculation but one theory suggests that a repulsive force exists between micelle aggregates which increases with sphere size so smaller spheres are more likely to coalesce. Repulsion between spheres is vital if a solution rather than a precipitous mass is to be produced, so spheres of both materials have polar groups terminating their surfaces. Charging the dispersing medium with the opposite polarity also helps suspend the spheres in solution.

Crystallisation

Allowing a solution of colloidal spheres to evaporate on a glass substrate produces a 2D or 3D crystal structure. Intriguingly, much debate still centres on why spheres with the same charge are attracted to each other [37, 38]. A colloidal solution is balanced between the van der Waal's attractions from charge fluctuations within each particle, random motion due to thermal energy and electrostatic interactions between colloids and surrounding ions. Why pairs of particles repel, but large groups cohere on a confining surface is thought to be due to the rearrangement of the surrounding ions to produce long range attraction.

Aside from this point is the problem of determining in which packing arrangement the spheres will settle, as well as the extent that defects intrinsic to the system appear. In the interests of simplicity, the colloids are modelled as hard spheres and do not suffer deformation on coalescence in close packed arrangements. Although close packed arrangements are generally produced using saturated solutions with large crystal formation favoured over smaller ones, it is of interest to note that experiments and theory also show that crystal nucleation with saturation experiences a maximum due to an increase in the free energy of the solid/liquid interface [39]. This process is very dependent upon the dispersity in sizes of the spheres and in the case of monodispersity the effect is probably not important.

The stacking entropy of two dimensional hard-sphere close packed crystals show a difference in entropy between hexagonal close packing (hcp) and face centred cubic (fcc) packing of only $10^{-3}k_B$ per sphere [40]. Entropy is highest for fcc packing and so is favoured over hcp as the free energy difference is only determined by entropy considerations. The stacking probability in such systems is usually denoted by α where $\alpha = 0$ represents a hcp structure of stacking sequence ABABABA, and $\alpha = 1$ for a fcc stacking structure ABCABC. Early studies on natural opals revealed that the most common type of structure belonged to random hexagonally close packed samples (rhcp)$\alpha = 0.5$. Samples of self-assembled synthetic opals for photonic band gaps have been shown to have a value of α of $0.8 - 0.9$ [41]. Experiments conducted in microgravity conditions on crystallisation of colloidal systems have revealed the importance of gravity on forming fcc crystals [42]. These crystals also only exhibit random hexagonal packing and have dendritic instabilities, which are also not seen in gravity conditions. It is also noted that experiments on polystyrene spheres below 150nm in diameter at low concentrations have revealed a phase transition to a body centred cubic (bcc) lattice [43], suggesting repulsion between spheres is strongly dependent upon sphere diameter and solution charges. This thesis concentrates on colloidal solutions larger than 150nm and so it is highly unlikely that the bcc construction will be encountered.

The small difference in entropy of close packed arrangements explains the large concentration of defects in self-assembled systems. The most common, and therefore the most unavoidable defects, are plane stacking faults concentrated in the plane perpendicular to the direction of growth [41]. Clearly these features of colloidal systems represent an important obstacle in producing samples which can compete with those made from top-down methods. As well as inhibiting progress in self-assembled photonic bandgap materials, these features also cause problems with other areas of research utilising these structures, with time spent on accounting for defects rather than investigating the properties of the fabricated structure. Producing ordered single domain crystals with as few defects as possible has been the goal of many groups and various strategies have been proposed to overcome the problems above.

Well Ordered Templates

From a technological point of view, the size of crystal domains will be very important n deciding whether self-assembly can rival the "top-down" methods discussed previously, However, this condition cannot be understood entirely in isolation, other factors such as electric field penetration and scattering will also have an important technological impact. The dispersion in sphere size is also important in obtaining well-ordered templates, especially in comparison with templates obtained from solutions of much greater size dispersity. Currently, the increase in crystal size in well-ordered templates continues with areas greater than $100\mu m^2$ of sub-micron spheres now possible.

The simplest method of template preparation is to allow the solution to evaporate on a glass slide held in place with a small ring [44]. Observation of this set-up reveals that two sets of forces play an important role in determining the ordering. First, the presence of a meniscus across the sample varies the volume of fluid across the cell, and therefore the number of packing layers; with the shallowest part, and so the least number of stacking layers, found at the centre of the ring. Secondly, evaporation in the cell creates a flux of water particles and latex spheres towards the evaporation site. Importantly, the ordering of layers starts when the thickness of the solution becomes equal to the diameter of the spheres. Therefore, within the ring the crystal will aggregate from the centre outwards, with the number of packing layers increasing radially. The main factors governing the formation in this setup are revealed to be the attractive capillary forces and the convective flux towards the evaporation site. Studies on the capillary force between two particles which are either floating or partially submerged reveal that particles are attracted to one another when the product of the sine of the contact angles of the two spheres is greater than 0, and repulsive when they are less than 0 [45, 46, 47], Fig. 2.4. The strength of the forces in the partially submerged case derives from the particles' wettability; in the case of floating particles the interaction is derived from the particles' weight and is consequently weaker. Also of importance is the effect of the film periphery on particles. In the case of partially submerged films, the particles are attracted to the edge of the film, but are pushed away from it in the case of floating particles. In

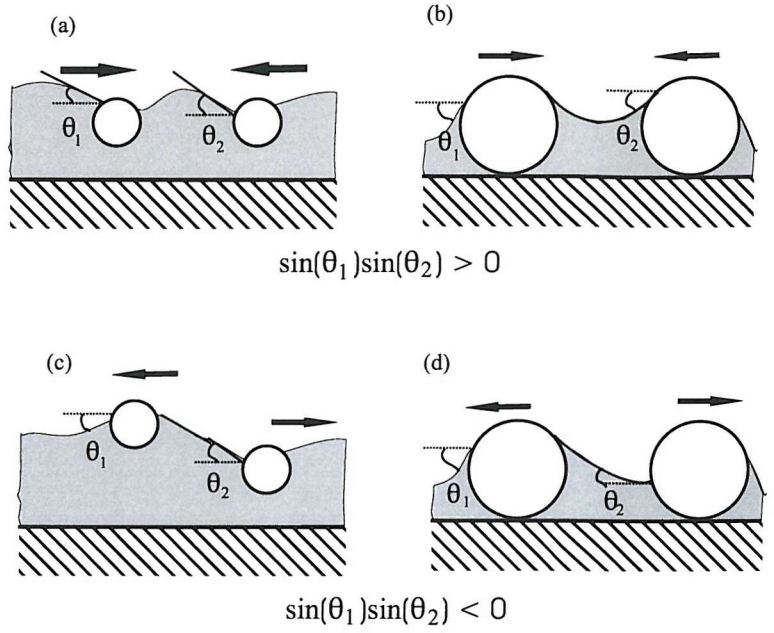

Figure 2.4: Comparison of forces between floating particles (a) and (c) whose forces are driven by gravity and partially submerged particles (b) and (d) whose forces are driven by wetting. θ_1 and θ_2 represent the meniscus slope angles. Note the sign of θ is by convention only e.g $\theta > 0$ for convex meniscus

the sedimentation process particles at the thinnest part of the film will be expelled, producing many crystallites due to the large number of nucleating sites (deposited particles). With this in mind, and the complications associated with the presence of the meniscus, it is evident that although simple to execute, the sedimentation process is not a productive way to proceed.

The strength of capillary forces on particles has led many to investigate ways to exploit it in ordering colloids. One method suggests dipping a wettable plate into a solution [48]. This is conceptually similar to the well-known Langmuir-Blodgett technique for particle array formation which transfers monolayers floating on a solution onto a solid substrate. Particle arrays spontaneously form at the plate/suspension/air contact. Withdrawing the plate at the same rate as the array formation it is possible to form large area arrays of monolayers (Fig. 2.5(a)). Following this work it was possible to control the number of layers of spheres by altering the sphere concentration, the sphere diameter and the meniscus height [49]. Fabricating thicker layers requires successive dip coating cycles. An improved technique used a capillary cell

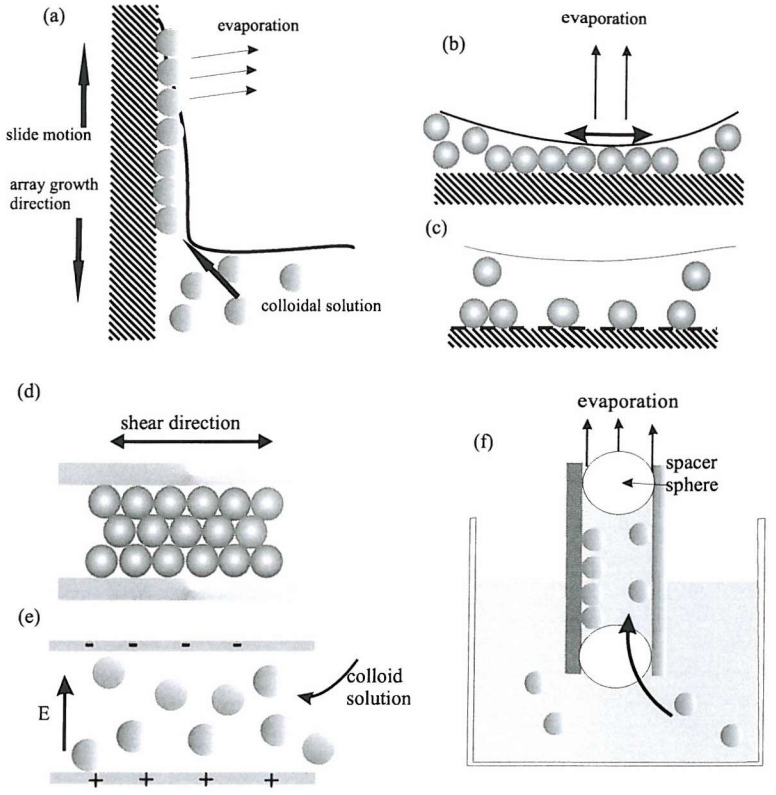

Figure 2.5: Procedures to produce close packed sphere arrangements.(a) Growing monolayer arrays using the capillary force effect at the interface between the substrate/solution interface with the substrate motion in the opposite direction to the template; the flux of particles is drawn towards the substrate due to the capillary force also.(b) Sedimentation in an evaporating solution held in place by a ring; the meniscus plays an important role in determining the ordering and the number of packing levels. (c) Using a lithographically defined surface to deposit spheres. (d) shear alignment. (e) electrophoresis. (f) capillary action between two glass slides.

of two parallel substrates held apart by large sphere spacers [50], with the bottom of the cell placed in a colloid solution which fills due to capillary action. By controlling the concentration (approximately 1%) at a controlled temperature, single domains of over 100μm of 300nm diameter spheres were produced (Fig. 2.5(f)).

One complication with the above plans was that they were thought to be restricted to sphere sizes under 0.4μm due to larger particles having a faster sedimentation rate than the solvent evaporation (with higher temperatures known to produce more disordered films) [51]. This was overcome by one research group with a sweeping meniscus method much like [49] by applying a convection current from the bottom of the solution to the top so supplying a continuous flow of particles towards the

meniscus region [52].

As well as capillary forces, a host of other ideas have also been shown to produce large areas ($> 100\mu$m across) of ordered spheres. Spheres can be aligned between two plates through shear motion in one direction, although samples have been shown to suffer cracking when one of the plates is removed [53] (Fig. 2.5(d)). While this method may raise issues about the mechanical stability on such small length scales, a way to avoid this problem could be to use the electrostatic charge on the colloids by organising particles between electrodes [54] (Fig. 2.5(e)). Particles of diameters between 16nm to 2μm have been shown to be moved by both dc and ac fields. The use of ac fields suggest that the particle-induced flow is due to the presence of current gradients. Such an approach could, in future, prove a useful method to produce templates on an industrial scale, although it suffers from the need to control the charge on the surface of the particles, the temperature and the concentration of both spheres and free electrolytes [55].

All the methods mentioned above have deposited spheres on a flat substrate without attempting to influence colloidal flows using sub micron patterning (Fig. 2.5(c)). Although traditional photolithography has only limited use in three dimensional sub-micron geometries, it has been used to make channels in which spheres are made to flow into using a flow of nitrogen [56]. This method has also been used to inject different size spheres into parts of the same cell to change the diffractive properties in steps across the sample [57]. Substrates have also been patterned with electrostatic charges using microcontact printing [58, 59]. This technique can be used to pattern areas 1 cm^2 with spheres arranged in small section arrangements rather than as a continuous crystal.

2.2.2 Obtaining the Inverse Structure

Filling self-assembled sphere templates with a second material poses several problems. First, the sphere template suffers from structural weakness and secondly, it needs to be removed once the structure is filled. One solution has been to sinter the structure, to slightly melt the spheres so they form necks between one another [60]. This creates a stable interconnected network topology with a route for etching material to penetrate

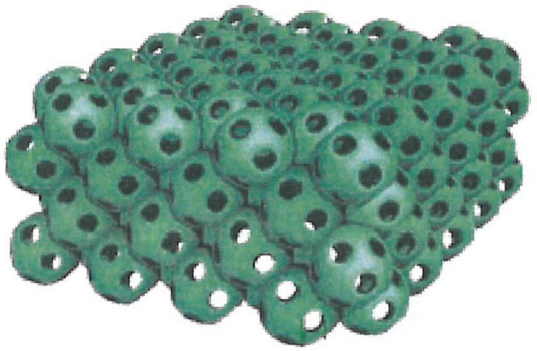

Figure 2.6: Structural model of a surface template inverse opal from [61]. The holes in the sphere surfaces represent the position of the necks from sintering.

(Fig. 2.6). However, it has to be used precisely; heating for too long increases the necks , blocking the path of the second material [61]. Infilling the sphere structure poses a number of challenges especially in attempting to avoid only partial filling which beset many early attempts. After infiltration the template is removed; silica spheres are removed using HF [52] or a fluorine based etching procedure [60] whereas latex colloids are removed with an organic solvent, such as toluene [62], or calcination (heating) [63, 64].

The optimum filling of the space for photonic band gaps according to theoretical studies is $\sim$ 80% air [33]. From the point of view of structural stability, it is preferable that as much of the interstitial space is filled as possible. Several infiltration strategies have emerged of which one, electrochemical deposition, has been used exclusively to make the samples studied in this thesis. As an introduction, the alternative methods are mentioned by way of explanation as to why electrochemistry was chosen.

The requirement of high refractive index and low absorption to produce photonic band gaps, made semiconductors a natural choice for many researchers. The tendency was therefore to use conventional techniques of semiconductor growth to attempt filling potential photonic constructions such as chemical vapour deposition (CVD). Initial trials were hindered by problems associated with insufficient infilling although some more recent reports suggest success has been achieved in making silicon inverse structures [65]. However, it appears that early difficulties dissuaded research on this technique.

One of the most widely used methods for infilling is to use nanocrystals with sizes at least 10 times smaller than the smallest channel of the opal [65]. This technique involves filling the interstitial holes with nanoparticles from solution using much the same idea as to make the initial template. Templates made from a wide variety of materials from metals, such as gold [66] to semiconductors such as CdSe [67] have been fabricated using this method. One of the many pitfalls of this system is that the resulting skeleton is very weak and prone to cracking [66]. Furthermore, even sintering the template before removal leads to significant shrinkage (up to 30% of the final material [63]. The magnitude of deformation has been shown to be reduced with better packing of the nanocrystals, for example by using electrophoresis which reduced shrinkage to $\sim$ 3% [64].

Electrochemical deposition offers many advantages over other methods; it produces a high density of deposited material in the interstitial holes producing volume templating as opposed to coating the surface of the spheres. Therefore, the cast does not suffer shrinkage when the template is removed. With no shrinkage the resulting cast is free-standing, robust and accurately reflects the ordering size and morphology of the initial sphere template. A wide range of materials can be used to fill the voids such as polymers [69], metals [70] and semiconductors [71]. Fine control over the film thickness is also possible through the control of the current passed to deposit the film. It is also ideal for use in growing thin layers as the deposited film can be made uniform. Experimental details of the deposition process is described in Chapter 4.

2.2.3 Metal Structures

The malleable robust nature of the electrochemically deposited metals described above also suggests that they are an attractive proposition for building nanoscale structures. Furthermore, electrochemical self-assembly is a relatively inexpensive route to access this size scale, especially in comparison to many of the complex fabrication strategies outlined in this chapter. However, the optical properties of metals, and specifically their opacity to visible and infra-red wavelengths, has led to them being generally considered unsuitable photonic devices in these wavelength regimes. Investigations in the microwave region on 3D copper wire mesh diamond structure

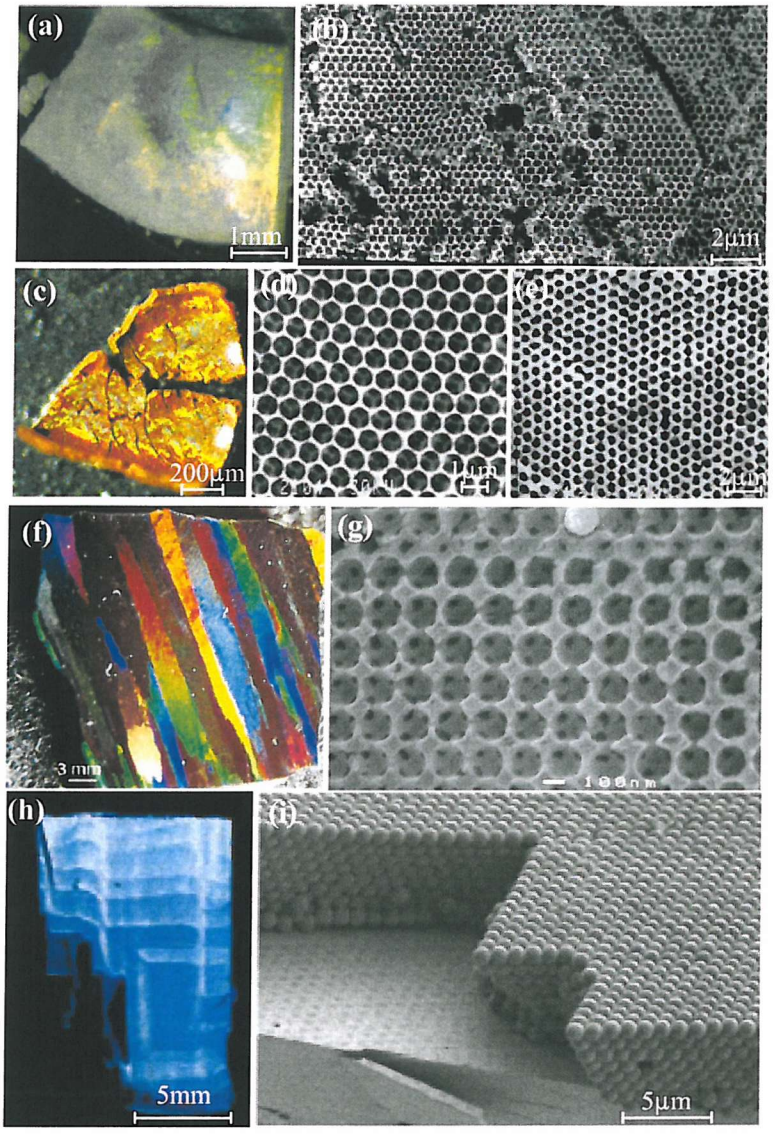

Figure 2.7: Images of inverse templating. (a) Photograph of TiO_2 inverse opals with the different colours showing the different planes and (b)SEM of the crystal substrate, which shows a large degree of irregularity and many defects [63]. (c) Inverse Au sample made from nanocrystal sintering, the structure has many visible cracks; two different methods of removing the template were attempted (d) dissolution and (e) calcination which are both SEM images [66] (e) Photograph of inverse opal of graphite showing a polycrystalline structure, (f) an SEM of the structure shows the ordering and also a SiO_2 sphere at the top of the image which has not been removed by the etching process. (g) Image of a Si wafer, with the horizontal lines showing monolayer steps and (h) a large scale cross-sectional SEM of the structure [52].

have shown, as in the dielectric case, the presence of forbidden bands at a frequency, f, corresponding to the lattice spacing [72]. However, a new forbidden band which starts at 0 and continues to $\frac{1}{2}$f, is also found which is described as a type of plasma cutoff frequency caused by the presence of conduction electrons in the copper wire. Therefore, even in the relatively simple case of microwave frequencies, where metals are less lossy than at optical frequencies, their response is more complex. To date, research into metal photonic band gaps in the infra-red or optical regimes have been somewhat limited, and restricted to the infra-red region, using tungsten photonic crystals [68, 73]. Once again, the fabrication strategy, relying on a photonic band gap crystal composed of stacked silicon rods as a template [74] and using CVD methods to cover the structure with tungsten, is time-consuming and complex. The distinguishing feature with this research in comparison with almost all other photonic band gap research is that as it is made of a tungsten it could be made into an incandescent bulb with improved black body emission characteristics [73]. This strongly suggests that although metal structures are unlikely candidates for applications envisaged for the more conventional photonic band gap devices, they may well find uses due to their high conductivity and strength.

Chapter 3

Metals

The physical properties of metals have been studied extensively over many thousands of years. Their structural strength, ductility, maleability, conductivity of thermal and electrical energy have been pivotal in the development of mankind. In recent years the cutting edge of science has focussed on the response of materials to light. Although known for centuries as being highly reflective, the optical properties of metals have a richness and variety of responses unmatched and, in comparison with other materials, relatively unexplored in the emerging field of photonics. This chapter first introduces some of their elementary properties and discuss how their behaviour changes with surface morphology and periodicity. This work mainly concerns itself with gold, a metal both valued for its chemical stability and lustre but also known to have a curious nature which has been exploited since medieval times with gold colloids used in stained glass windows to produce red colouring. This mix of stability, durability and sensitive optical response make it an ideal metal to use. Also, the properties of both silver and platinum will also be described, as these metals have also been studied in later chapters.

3.1 Properties of Metals

3.1.1 Optical Constants

First a return to Maxwell's equations, introduced in the previous chapter, to describe the optical response of metals, which now have to account for the presence of freely flowing conduction electrons.

$$\nabla \times \mathbf{H} - \frac{\delta \mathbf{E}}{\delta t} = \sigma \mathbf{E} \tag{3.1}$$

$$\nabla \times \mathbf{E} + \mu \frac{\delta \mathbf{H}}{\delta t} = 0 \tag{3.2}$$

where $\mathbf{j} = \sigma \mathbf{E}$

$$\nabla \cdot \mathbf{E} = \frac{\rho}{\epsilon \epsilon_0} \tag{3.3}$$

$$\nabla \cdot \mathbf{H} = 0 \tag{3.4}$$

Through manipulation of the above equations the response to electric fields can be revealed. For example, by taking the divergence of 3.1 and substituting the result from 3.3 and also differentiating 3.3 and then combining the two resulting equations it is possible to obtain an expression for the electrical charge density response with time.

$$\rho = \rho_0 e^{\frac{-t}{\tau}} \tag{3.5}$$

where

$$\tau = \frac{\epsilon_0 \epsilon}{\sigma} \tag{3.6}$$

The fluctuations of charge density decay exponentially with time and with a relaxation time inversely proportional to the conductivity. In metals this will be an extremely small time scale. The timescale of the relaxation is fast enough that at optical frequencies it is sensible to suggest that equation 3.5 be set equal to zero.

Further manipulation of Maxwell's equations also reveal the velocity of light through a medium

$$v = \frac{c}{\sqrt{\epsilon\mu}} \tag{3.7}$$

where c is the speed of light in a vacuum. Introducing the concept of a complex refractive index, N, which is equated to the equation above obtaining expressions for the complex dielectric function, ϵ.

$$N = n + i\kappa \tag{3.8}$$

$$\epsilon = \epsilon_1 + \epsilon_2 \tag{3.9}$$

$$\epsilon_1 = n^2 - \kappa^2 \tag{3.10}$$

$$\epsilon_2 = 2n\kappa \tag{3.11}$$

$$n = \sqrt{\frac{\sqrt{\epsilon_1^2 + \epsilon_2^2} + \epsilon_1}{2}} \tag{3.12}$$

$$\kappa = \sqrt{\frac{\sqrt{\epsilon_1^2 + \epsilon_2^2} - \epsilon_1}{2}} \tag{3.13}$$

A plane wave solution of Maxwell's equations in free space in one dimension has the form

$$\mathbf{E} = \mathbf{E}_0 \exp(i\mathbf{k} \cdot \mathbf{x} - i\omega t), \tag{3.14}$$

$$\mathbf{H} = \mathbf{H}_0 \exp(i\mathbf{k} \cdot \mathbf{x} - i\omega t) \tag{3.15}$$

where $\mathbf{k} = \frac{2\pi}{\lambda}$ and λ is the free space wavelength of the radiation. In taking account of the refractive index on the propagation of the wave, the imaginary part determines the propagation distance of the wave:

$$\mathbf{E} = \mathbf{E}_0 \exp(\frac{-2\pi\kappa x}{\lambda}) \exp(i\frac{i2\pi n x}{\lambda} - i\omega t) \tag{3.16}$$

This equation therefore immediately gives the penetration depth into a material, defined as the length over which the strength of the field will reduce by $1/e$:

$$\delta(\lambda) = \frac{\lambda}{\pi\kappa(\lambda)} \tag{3.17}$$

Reflection at a Plane Boundary

The reflection and transmission at a plane boundary can be used to deduce expressions relating these quantities to the microscopic properties of the material. The reflectivity is given by:

$$R = |\tilde{r}|^2 = \frac{(n-1)^2 + \kappa^2}{(n+1)^2 + \kappa^2} \tag{3.18}$$

where $\tilde{r}$ is known as the amplitude reflection coefficient. The reflection coefficient can also be written in such a way as to emphasize the properties of the light influenced by the material:

$$\tilde{r} = re^{i\phi} \tag{3.19}$$

The angle ϕ is the phase angle, and r the amplitude of the wave. The reflectivity can therefore be high with either a large value of n or κ. For the purposes of this discussion, metals are considered as crystals of ionic cores surrounded by delocalised electrons. The electric field of electromagnetic radiation induces an equal and opposite field inside the metal as the delocalised electrons respond to expel the electrical field. Consequently, since the electrons respond in antiphase to incident light, reflected rays will suffer a phase change. In a perfect loss-free, zero time response model this change in phase would be exactly π radians. However, in a real metal this is not the case and the exact change in phase is calculated using experimentally determined refractive indices.

Electric fields behave very differently in metals in comparison with dielectrics. At a boundary between the two the polarisation of the light will have a significant bearing on the outcome. There are two mutually independent, orthogonal polarisation states of interest, Transverse Electric (TE) and Transverse Magnetic (TM). TE polarisation has the electric field component perpendicular to the plane of incidence, whereas TM has its magnetic field component perpendicular to the plane. Therefore, in considering the phase change in reflection the polarisation of the light will also have to be taken into account. Using the Fresnel formulae for refraction and reflection at a boundary

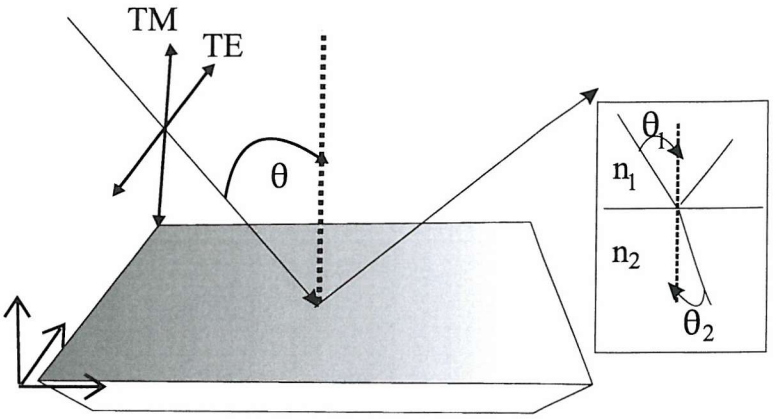

Figure 3.1: Reflection off a surface with incident polarisations TE and TM and angle of incidence θ. Inset: angles θ_1 and θ_2 used in the Fresnel equations.

[9] for TE polarisation:

$$R_{TE} = r_{12}e^{i\phi_{12}} = \frac{n_1\cos(\theta_1) - n_2\cos(\theta_2)}{n_1\cos(\theta_1) + n_2\cos(\theta_2)} \tag{3.20}$$

With the above, and replacing $n_2\cos(\theta_2)$ by the expression $u_2 + iv_2$ with n_2, complex, written in the form $n_2 + i\kappa_2$, the phase change can then be extracted.

$$\tan(\phi_{TE}) = \frac{2v_2n_1\cos(\theta_1)}{u_2^2 + v_2^2 - n_1^2cos^2(\theta_1)} \tag{3.21}$$

The expression for TM is predictably more complicated because of the penetration of the electric field into the metal surface itself.

$$\tan(\phi_{TM}) = 2n_1n_2\cos(\theta_1)\frac{2\kappa_2u_2 - (1 - \frac{\kappa^2}{n_2^2})v_2}{n_2^4(1+\kappa_2^2)cos^2(\theta_1) - n_1^2(u_2^2 + v_2^2)} \tag{3.22}$$

3.1.2 Theories of Optical Response

It is common practice in describing the optical response of metals to reach for the Drude theory. However, the metals studied in this thesis are not simple metals because their optical response is not governed exclusively by their delocalised electrons. Instead, d-band electrons in their outer shell also contribute to the response, due to their closeness energetically to visible light. Therefore, both the Drude model and the Lorentz model, usually reserved for dielectrics, are used to account for the contribution of bound states.

The Lorentz Model

The Lorentz model treats the response of a medium to an electric field as a set of damped harmonic oscillators with mass, m, charge, **e**, and a linear restoring force, **Kx**, with **K**, the force constant and **x**, the displacement. The damping is provided by the term $b\dot{\mathbf{x}}$ where b is the damping constant. The driving force is produced by a local electrical field, E_{local}, and the atoms are assumed not to radiate. The equation of motion is given by:

$$m\ddot{x} + b\dot{x} + \mathbf{Kx} = \mathbf{e}E_{local} \tag{3.23}$$

The solution to this equation has terms expressing the oscillatory nature and transients to describe the damping. The oscillatory part is written as.

$$\mathbf{x} = \frac{(e/m)E}{\omega_0^2 - \omega^2 - i\gamma\omega} \tag{3.24}$$

$\omega_0^2 = K/m$ is known as the natural frequency of the system, while $\gamma = b/m$ represents the damping. Expressing the displacement in the form $Ae^{i\theta}(eE/m)$, with A, the amplitude and θ, the phase angle, the oscillator behaviour can be parameterised.

$$A = \frac{1}{[(\omega_0^2 - \omega^2)^2 + \gamma^2\omega^2]^{1/2}} \tag{3.25}$$

$$\theta = \tan^{-1}\left(\frac{\gamma\omega}{\omega_0^2 - \omega^2}\right) \tag{3.26}$$

Using the constitutive relation linking polarisation and applied electric field:

$$P = \chi\epsilon_0\mathbf{E} \tag{3.27}$$

the dielectric function of this system can then be derived using 3.24 and the above.

$$\epsilon = 1 + \chi = 1 + \frac{\omega_P^2}{\omega_0^2 - \omega^2 - i\gamma\omega} \tag{3.28}$$

The quantity ω_P is known as the plasma frequency and is defined as

$$\omega_P^2 = \frac{ne^2}{m\epsilon_0} \tag{3.29}$$

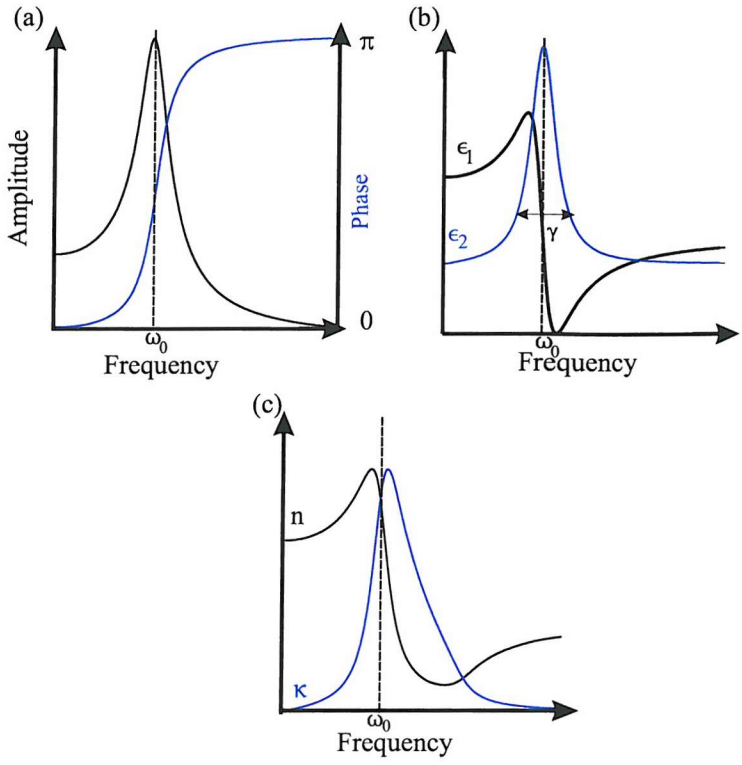

Figure 3.2: The optical response and parameters of a Lorentz material with increasing frequency. (a) Phase and oscillator displacement. (b) The real and imaginary parts of the dielectric function. (c) The real and imaginary parts of the refractive index.

where n is the number of oscillators per unit volume. The real and imaginary parts of the dielectric functions can also be represented and the complex refractive indices can then be worked using the relations 3.12, 3.13.

$$\epsilon_1 = 1 + \frac{\omega_P^2(\omega_0^2 - \omega^2)}{(\omega_0^2 - \omega^2)^2 + \gamma^2\omega^2} \tag{3.30}$$

$$\epsilon_2 = \frac{\omega_P^2\gamma\omega}{(\omega_0^2 - \omega^2)^2 + \gamma^2\omega^2} \tag{3.31}$$

The response of a material described by these equations is shown in Fig. 3.2. In particular, the amplitude of the oscillations is a maximum at ω_0. The material shows normal dispersion except in the region around round ω_0 where the real part of the dielectric function decreases with increasing frequency.

The Drude Model

The Drude model is used to describe the optical response of metals, whose behaviour in general is determined by their delocalised electrons. Once again the system can be described as a set of oscillators with the difference being that the spring constant is set to zero which sets the natural frequency ω_0 to zero also. The dielectric constant is therefore given by

$$\epsilon = 1 - \frac{\omega_P^2}{\omega^2 + i\gamma\omega} \tag{3.32}$$

For completeness the real and imaginary parts are also shown.

$$\epsilon_1 = 1 - \frac{\omega_P^2}{\omega^2 + \gamma^2} \tag{3.33}$$

$$\epsilon_2 = \frac{\omega_P^2 \gamma}{\omega(\omega^2 + \gamma^2)} \tag{3.34}$$

The Drude model emphasizes the effect of the plasma energy in contrast to the Lorentz model. If excited at the plasma frequency, the system has an ϵ value of 0 then from Maxwell's equations the electric field is no longer at right angles to the propagation direction. The plasma frequency therefore represents a longitudinal oscillation of electrons and in keeping with quantum mechanical terminology, is known as a plasmon, a quantized charge density fluctuation.

3.1.3 D-Band Metal Reflectivity

The three metals that are now concentrated on, Au, Pt and Ag, have an optical response that is noticeably different from that predicted by the Drude model. All three have optical properties heavily influenced by the proximity of the d-band shell to the Fermi energy and its much flatter dispersion than the s band (see later, Fig. 3.7). Therefore, as well as behaviour due to delocalised electron response the metals will also exhibit interband (between energy bands) transitions [75]. This anomalous behaviour was most readily observed in the noble metals, notably silver , [76]. The reflection spectrum for silver exhibits a sharp dip in reflectivity near 3.8eV, with the rest of the behaviour showing some similarities with that expected from the Drude

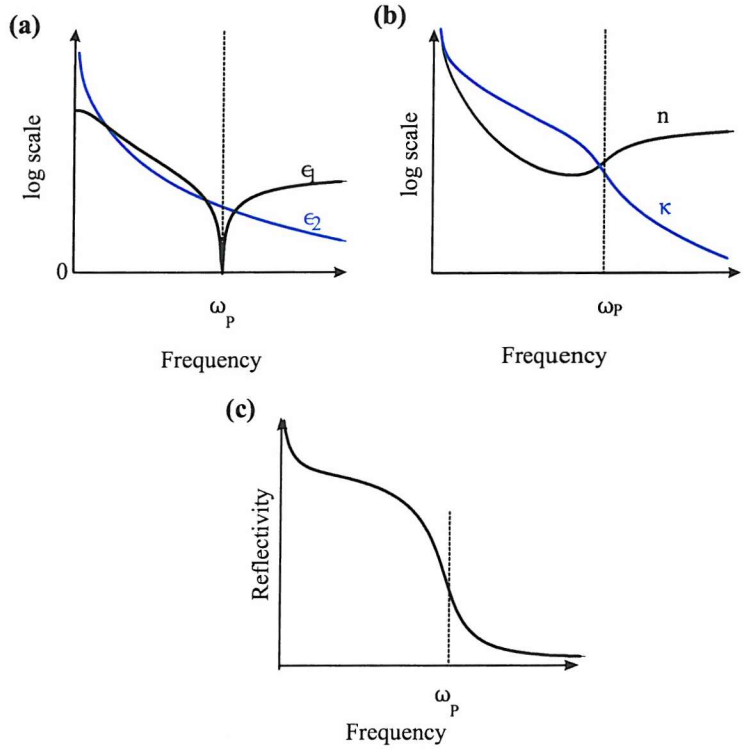

Figure 3.3: Optical response and parameters of a Drude material with increasing frequency (a)ϵ_1 and ϵ_2 note:the absolute value of ϵ_1 is shown, it is negative below ω_P. (b) complex refractive index, n and κ, and (c) the reflectivity.

formula [77]. If the plasmon energy for Ag is niavely calculated from 3.29 it is found to be 9.2eV. To account for this discrepancy, the complex dielectric of these metals is expressed as a summation of two separate effects; the intraband (free electron) part and the interband (bound-electron) part [78].

$$\epsilon = \epsilon^f(\omega) + \epsilon^b(\omega) \tag{3.35}$$

The intraband contribution is described by the Drude model and the interband part is described by a semiquantum mechanical approach based upon the Lorentz model described above:

$$\epsilon = 1 - \frac{\Omega_P^2}{\omega(\omega - i\gamma_0)} \tag{3.36}$$

where $\Omega_P = \sqrt{\mathbf{f}_0\omega_P}$, is the plasma frequency of intraband transitions and oscillator strength γ_0.

$$\epsilon^b(\omega) = \sum_{j=1}^{k} \frac{\mathbf{f}_j\omega_P^2}{(\omega_j^2 - \omega^2) + i\omega\gamma_j} \tag{3.37}$$

where ω_P is the plasmon frequency, k the number of oscillators with frequency ω_j, strength $\mathbf{f}_j$ and lifetime $1/\gamma_j$.

Rather than attempt the Herculean tack of calculating the different constants from band structure calculations, [78] parametrises the optical constants from data collected from a number of authors and experiments, minimising the risk of spurious results from ill-prepared samples. Various measurement techniques were used including polarimetry, electron energy loss spectroscopy, ellispometry, transmittance through thin samples and conductivity which again should minimise errors. For completeness a second model was also used by the authors, the Brendel-Bormann which is used to model the linewidth broadening as a Gaussian distribution rather than a Lorentzian, in order to fit the experimental data better at high energies.

The properties of the three metals of interest in the visible region are shown in Figs. 3.4, 3.5, 3.6. It is important to state that the effect the presence of d-band electrons have on the optical properties of the metals. In the case of Au and Ag, sharp dips in the reflectivity are observed corresponding to plasmon interactions similar to those

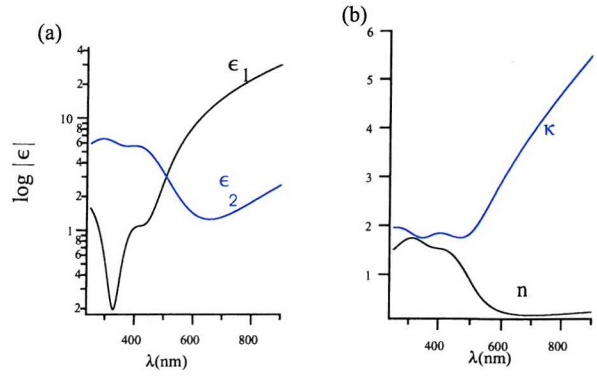

Figure 3.4: (a) Absolute values of real and imaginary parts of ϵ for Au. (b) Corresponding values of real and imaginary parts of the refractive index.

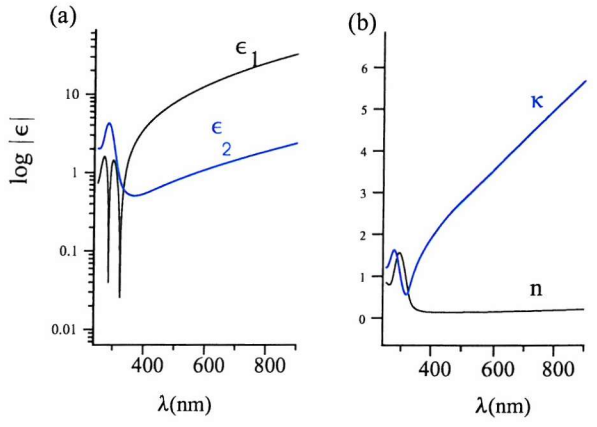

Figure 3.5: (a) Absolute values of real and imaginary parts of ϵ for Ag. (b) Corresponding values of real and imaginary parts of the refractive index.

predicted by the Drude model. Platinum shows only an increase in reflectivity with longer wavelengths, much like a Drude metal below the plasmon energy. The reason for these differences are found in their outer electron band structures. In the case of Ag and Au, the general outer electron configuration is: $Xd^{10}, (X+1)s^1$, whereas Pt has the configuration $Xd^9, (X+1)s^1$. Ag and Au have one conduction electron per atom to contribute to the delocalised plasma, and a d-band close to the Fermi surface capable of making an interband transition.

The complexity of the task of understanding the influence of the d band on the response to light can be shown by comparing the Drude model calculation of Au and Ag and the experimentally determined dielectric constant. This gives the energy

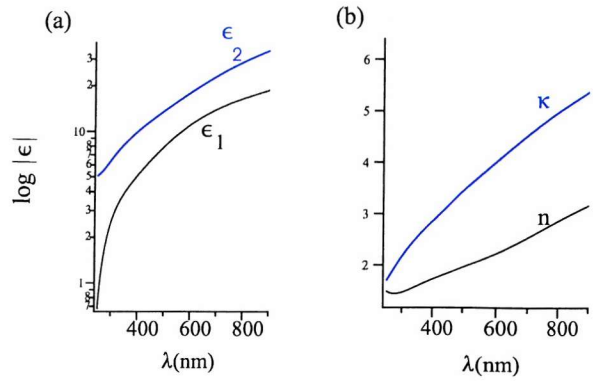

Figure 3.6: (a) Absolute values of real and imaginary parts of ϵ for Pt. (b) Corresponding values of real and imaginary parts of the refractive index.

at which interband transitions begin to influence the dielectric response to light, which for gold is 1.8eV (690nm) and for silver, 2eV (620nm)[76]. It is at these wavelengths that non-radiative damping processes are observed in the time dynamics of the response of metal nanoparticles [79]. The reflectivities of silver and gold also show significant falls in strength at 3.5eV (354nm) [80] and 2.4eV (516nm) [81], respectively. This rather puzzling feature of having a step-like change at one energy, and an exponential tail extending to lower energies was subject to some debate; the explanation was eventually found in the splitting of the interband absorption edge [82].

Taking the band structure of gold as an example, the effect of Van Hove singularities, where the Fermi surface is tangent is to the Brillouin zone, in the density of states in a region with a high number of states, dominates the optical response at energies near the Fermi level Fig. 3.7(a) [81]. Along the different zone directions, the proximity of the d-band to to the intersection of the Fermi surface and the sp-conduction band varies, Fig. 3.7(b), accounting for the difference between the energy at which the d-band influences the optical response, and the onset of a step-change. Note, that electrons in the 6s and 6p band do not have distinct symmetries but instead have a mixed character and as such are referred to as the sp-band [83].

The presence of Van Hove singularities along the L direction produces a high density of states leading to a high probability of excitation, whereas the lower density of states along the X direction has only a low density accounting for the presence of

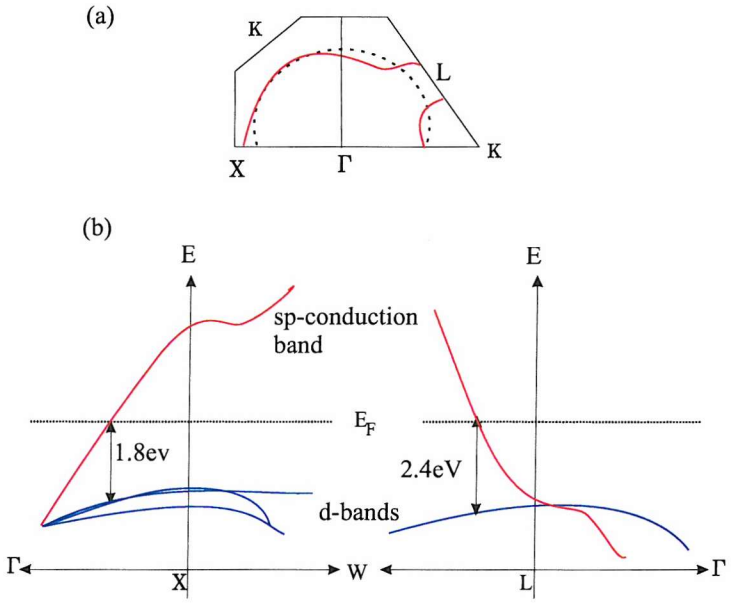

Figure 3.7: (a) Simplified diagram of the dispersion relation for the 5d and 6sp conduction bands in Au [81, 85] showing the region of the band structure close to the Fermi surface. The high density of states in the region account for the interband absorption and emission processes in the visible spectrum. (b) A map of the Fermi surface between the high symmetry points of the first Brillouin zone of gold, with the deformation in the spherical free electron surface due to Van Hove singularities in the density of states.

a strong transition at 2.4eV and only a weak one at 1.8eV. Photons with less energy than 1.8eV incident on a gold surface experience a free-electron like response driven by the single electron contribution per gold atom to the conduction electron gas, Fig. 3.4. The resulting reflectivities of both silver and gold are therefore wavelength dependent, Fig .3.8(a). Silver shows a much sharper reflectivity change than gold, indicating that its density of states is very low, except at its principle transition energy, 3.5eV.

Platinum's response to visible wavelength light is less dramatic than either gold or silver and, consequently, far less studied than either, Fig. 3.6. Nevertheless it shows significant deviation from the behaviour described by the Drude model, Fig. 3.3. Although its reflectivity is less dramatic than the other two metals, platinum's electronic structure is more complex, as shown by the presence of holes in both the d- and sp-conduction band, revealing that they cross in energy [84]. However, it is reasonably straightforward to understand Pt's response to light by considering it reflectivity spectrum in relation to that of Au and Ag, Fig. 3.8. The shallow increase in reflectivity reveal the influence of d-band electrons, notably the presence of weak interband transitions.

As well as calculating the reflectivity from the dielectric values of the metals, it is also possible to calculate the penetration depth using eqn. 3.17, Fig. 3.8. Once again, the effects of interband transitions in gold and silver are obvious, with large increases in the penetration at wavelengths corresponding to the transition energy. Platinum's penetration depth is smaller than the other two metals in the visible region.

3.2 Properties of Metallic Structures

3.2.1 Colloids and Metallic Shells

As well as influencing the bulk properties, the features discussed above also heavily influence the behaviour of these metals when placed in restricted volumes and shapes. The most prominent example is that of gold colloids, whose red colouring was investigated by both Faraday and Mie [86], and shown to be due to prominent sharp

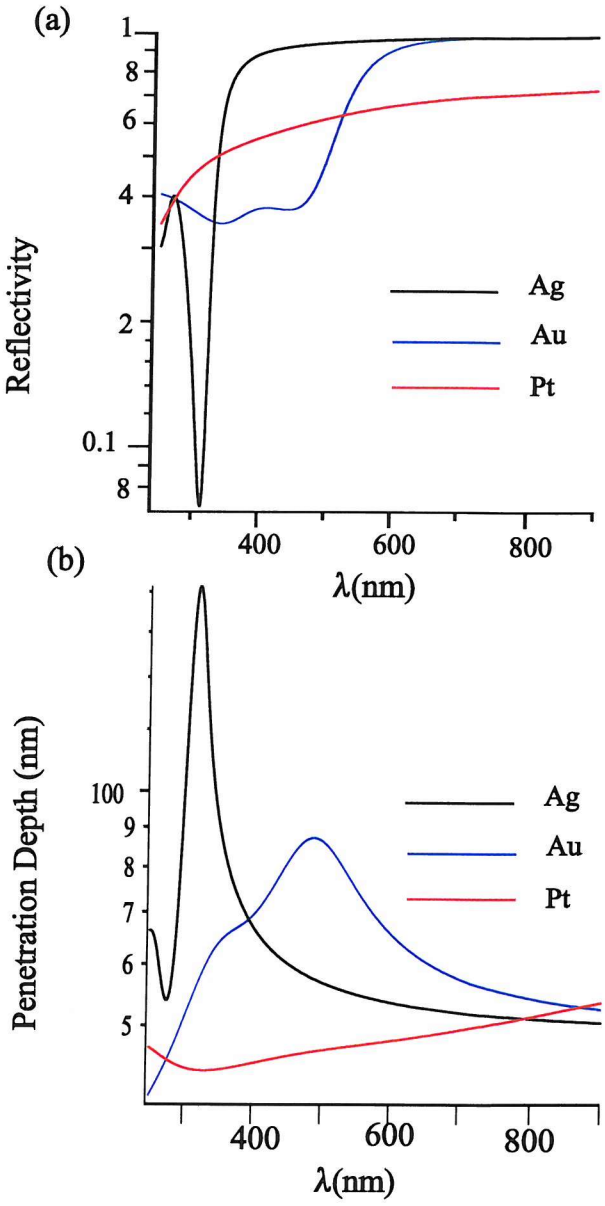

Figure 3.8: (a) Reflectivity of Silver, Gold and Platinum. (b)Penetration depth of electric fields for the three metals.

absorption by plasmons [80]. Furthermore, silver colloids also show sharp absorption whereas Platinum shows a broad absorption continuum [87].

Introduction

The purpose of this section is to illustrate that colour change in small particles is a function of the size, shape and surroundings of particles. The different colouring of gold colloids prompted Mie to construct his theory on the scattering of light by a sphere. The solution is somewhat cumbersome with the need to express incoming plane waves in spherical harmonics. A detailed discussion of this theory is not given and the resultant expressions from Bohren & Huffman [80] are merely stated. Another important development in the research of metals has been the use of dielectric cores covered with a uniform thickness of metal known as a nanoshell. These areas are of technological interest for their potential use as waveguides [88] or for targeted drug delivery, using a gold nanoshell to cover a thermally responsive polymer which collapses upon absorption of light [89]. The main optical response of both types of nanoparticle will be briefly described.

Colloids

Beginning with spheres much smaller than the wavelength, the electrostatic equations can be used in place of the full set of Maxwell's equations [90]. We consider a sphere, radius R, dielectric constant $\epsilon(\omega)$:

$$\nabla \cdot \mathbf{D} = 0 \tag{3.38}$$

$$\nabla \times \mathbf{E} = 0 \tag{3.39}$$

If the constitutive relation, 3.27, is used also, then the equations can be written in terms of polarisation.

$$\frac{\epsilon(\omega)}{\epsilon(\omega) - 1} \nabla \cdot \mathbf{P} = 0 \tag{3.40}$$

$$\frac{1}{[\epsilon(\omega)-1]}\nabla\times\mathbf{P}=0 \tag{3.41}$$

There are three solutions to these equations, two of which give longitudinal or transverse bulk modes dependent on $\epsilon(\omega)$ being 0 or ∞ at a finite ω which is not the case here. Instead, we are concerned with the surface mode solution: $\nabla\cdot\mathbf{P}=0,\nabla\times\mathbf{P}=0$. Representing both the field inside and outside the sphere in terms of spherical harmonics and equating them at the surface of the sphere obtains the surface mode frequencies [90].

$$\epsilon(\omega_\ell)=-\epsilon_m\left(\frac{\ell+1}{\ell}\right),\ell=1,2,3,.. \tag{3.42}$$

where ϵ_m is the dielectric constant of the surrounding medium. The polarisation of this mode decays away from the surface of the sphere with a $r^{\ell-1}$ dependence so the $\ell=1$ mode has a constant amplitude and is called the *Frölich* frequency ω_F. The *Frölich* frequency is calculated by

$$\epsilon(\omega_F)=-2\epsilon_m \tag{3.43}$$

Using the Drude model of a simple metal the *Frölich* frequency can be determined as a function of ω_P. When the nanoparticle is in air this is given by.

$$\omega_F=\frac{\omega_P}{\sqrt{3}} \tag{3.44}$$

This result above is extremely useful in explaining the dramatic colour change in comparison with bulk materials in the small sphere limit.

As well as providing an accurate model of the response of spherical colloids to light, this approach can also explain the response of spheroidal colloids. Under deformation the surface plasmon resonance splits in two, resulting in resonances excited by light polarised parallel to the short and long axes respectively [91]. The response of spheroidal particles can be worked out using the same approach as spherical particles and applying the appropriate geometrical scale factors [92]. Therefore, in the electrostatic regime, particle shape controls the overall surface plasmon properties, underlining the importance of the interface in this phenomena.

Studying the dynamics of gold colloids have also revealed the effect of interband transitions on the properties of surface plasmons [93]. Surface plasmon damping

has been shown to increase more by optical pumping at the interband transition energy than at the surface plasmon energy, suggesting that SP's relax through several routes including scattering off phonons and electron-electron scattering. Interband excitation is therefore a useful way of controlling the optical repsonse of noble metal colloids.

The exact equation for any size sphere is given by way of completeness. It involves solving Maxwell's equations and looking for transverse solutions for

$$\nabla \cdot \mathbf{E} = 0 \tag{3.45}$$

This result is not derived but merely stated, and is solved using the Helmholtz equation for both the electric and magnetic components [90].

$$\nabla^2 \mathbf{E} + k^2 \mathbf{E} = 0 \tag{3.46}$$

$$\nabla^2 \mathbf{H} + k^2 \mathbf{H} = 0 \tag{3.47}$$

Both equations are solved using spherical Bessel functions,and conditions of continuity at the sphere surface give an equation for TM surface plasmon polaritons [90]

.

$$\epsilon_m h_\ell(k_o R)[k_i R j_{ell}(k_i R)]' - \epsilon(\omega) j_\ell(k_i R)[k_o R h_\ell(k_o R)]' = 0 \tag{3.48}$$

The equation for TE modes is given by :

$$j_\ell(k_i R)[k_o R h_\ell(k_o R)]' - h_\ell(k_o R)[k_i R j_\ell(k_i R)]' = 0 \tag{3.49}$$

R is the radius of the sphere; the subscripts i and o denote whether the field is inside or outside the sphere; j is a spherical Bessel function a and h is a spherical Hankel function.

There are no solutions for TE modes in the frequency range in which $\epsilon(\omega)$ is negative, and so TE surface modes do not exist. For TM modes, solutions do exist, so TM polarisation couples to modes on a sphere.

The above approach presents theoretical challenges which are usually avoidable when the size of the colloids are sufficiently small to use the electrostatic approximation. Research into colloids now extends across chemistry and physics with different

fabrication routes, with the easily observable surface plasmon resonance is proving very interesting for detection techniques such as Surface Enhanced Raman Spectroscopy (SERS) [94]. Several groups have also found that light can be transported along size scales below the diffraction limit using arrays of closely spaced nanoparticles using their near field interactions [95] [96]. Both research areas are made possible by the electric field enhancement between the particles, creating a hybrid mode with a squeezed electric field [97].

Nanoshells

The optical response of a nanoparticle can be further manipulated using a dielectric core surrounded by a metal shell. Experiments on Au coated cores of Au_2S have shown an ability to shift the plasmon resonance from $650 - 900$nm [98]. The shell thickness determines the peak absorption wavelength, with thicker shells producing lower energy resonances. As in the case of colloids, the optical response of these particles can be derived from a electrostatic considerations. Taking into account the radius of the core (r_1), and of the particle (r_2), with dielectric constants $\epsilon_1, \epsilon_2, \epsilon_3$ as denoted in Fig. 3.9, it is assumed that the dielectrics do not have imaginary components, allowing a simple equation describing the plasmon resonance to be derived [99].

$$\frac{r_1}{r_2} = \left[1 + \frac{3}{2}\frac{\epsilon_2'(\lambda)(\epsilon_1 + 2\epsilon_3)}{[\epsilon_2'(\lambda)]^2 - \epsilon_2'(\lambda)(\epsilon_1 + \epsilon_3) + (\epsilon_1\epsilon_3 - (\epsilon_2''(\lambda)^2)}\right]^{1/3} \tag{3.50}$$

where ϵ_1, ϵ_2 and ϵ_3 are the dielectric constants for the shell environment, the shell itself and the particle core respectively.

Applying this formula to a core of Au_2S ($\epsilon_3 = 5.442$) the authors show that for certain ratios of shell thicknesses the peak plasmon resonance shifts to lower energies with thicker Au coverings, Fig. 3.9(b) [99]. Also shown are the plasmon shifts for a nanoshell in air, rather than in solution, and also a hollow Gold shell in air. In each case, the only change in the shell's response to these different environments is to shift the resonances to higher energies for a fixed shell/core thickness ratio. Nanoshells offer a convenient method of controlling the optical response of a metallic system, which, in contrast to other sub-micron structures, have the advantage of a relatively

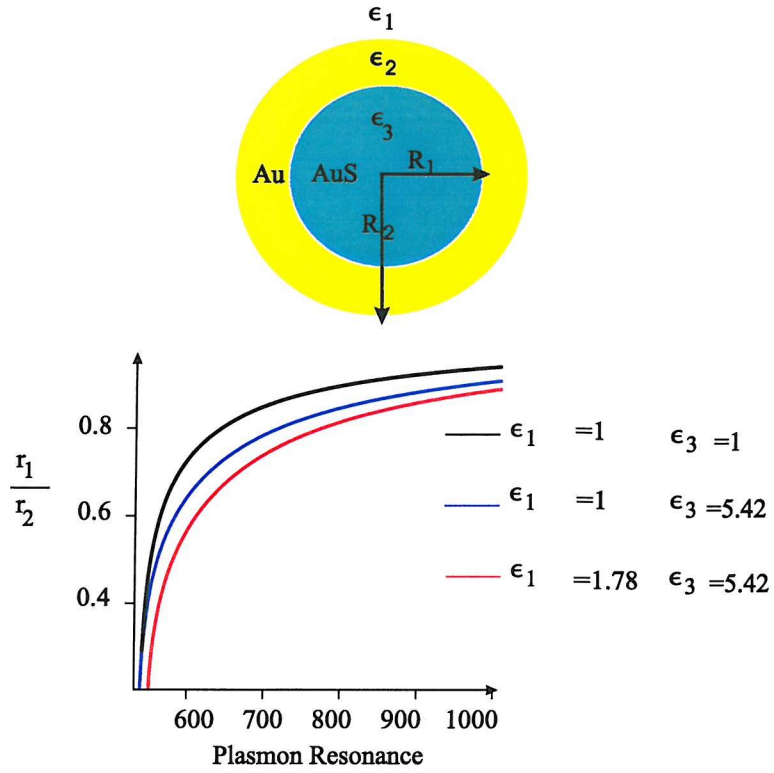

Figure 3.9: (a)A au nanoshell with core radius r_1 and outer radius r_2.(b) Calculations based on [99] with different dielectric materials inside and outside the Au shell, showing how the plasmon resonance changes with increases in the ratio r_1/r_2.

simple fabrication strategy of "wet chemistry". Although it is claimed that by altering the ratio of the core diameter to the shell thickness the plasmon resonance can be shifted far into the infra-red, it is unclear whether the shell growth can be controlled to the degree necessitated by the calculations [100]. Longer wavelengths also require that the dielectric constants to be independent of thickness, which is only correct above a critical thickness; for gold this is about 25nm [76]. Furthermore, the plasmon resonance begins to flatten and broaden towards longer wavelengths, weakening the response. In purely practical terms, one of the main pitfalls of nanoshells will be coagulation which will inhibit their usefulness.

3.2.2 Gratings and Surface Plasmons

Introduction

The interaction of light with gratings has intrigued researchers since the discovery by Wood [101, 102, 103] of sudden changes in the reflective efficiency of a grating while observing a white light spectrum. The change in efficiency was found to be most pronounced in the case of TM radiation. The first attempt at an explanation of this behaviour was by Rayleigh in 1907 [104] who suggested the changes were due to a diffracted order "passing off" over the grating horizon. The position of the changes were due to orders of the grating having an angle of diffraction greater than that between the incoming light and the surface of the grating. The diffraction grating equation is [103]:

$$d(\sin(\theta) + \sin(\alpha)) = m\lambda \tag{3.51}$$

where d =periodicity of the grating, λ is the incident wavelength, m is the diffracted order and θ and α are as shown in Fig. 3.10. Also shown is the azimuthal angle ϕ, the angle the incident light makes in the plane of the grating with the grating vector, k_g.

Rayleigh anomalies would therefore be expected when $\alpha = 90$ so the wavelengths at these conditions can be calculated:

$$\lambda = \frac{d(\sin(\theta) + 1)}{m} \tag{3.52}$$

In this description of grating behaviour, the polarisation dependence of the anomalies is explained by the inability of the grating to sustain a TE field propagating parallel to the surface. Therefore, less energy is available to be redistributed when the other order passes off, hence the anomalies are less pronounced for TE polarisation [103]. Further work by Fano[105, 106] suggested that in fact there were two types of anomaly; (a) a sharp anomaly of change in reflectivity with positions determined by the Rayleigh criteria and, (b) an anomaly which did not fit the above explanation. The discovery by Ritchie of surface plasmons (SP) [107] explained this second observation.

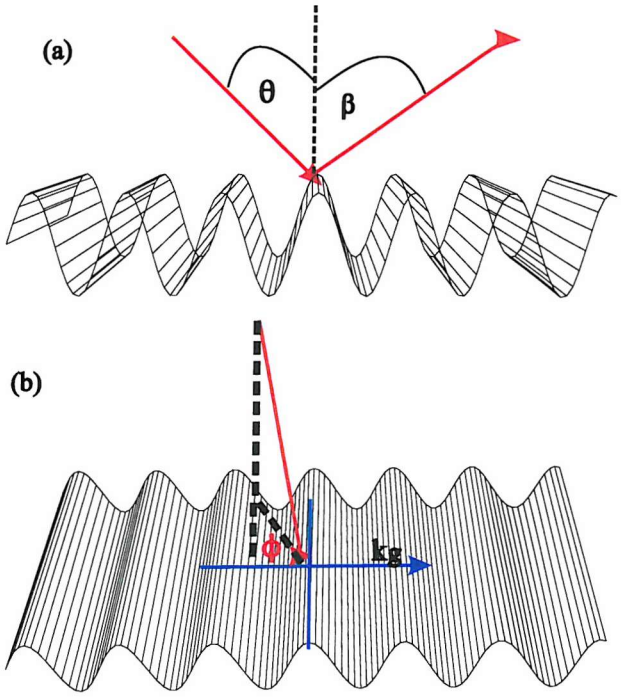

Figure 3.10: (a)A sinusoidal grating with an angle of incidence (or polar angle) θ, incident wavelength λ and with a diffraction angle α. (b) Azimuthal angle ϕ with respect to the grating vector k_g.

Surface Plasmons

A surface plasmon, or more strictly, a surface plasmon polariton, is characterised by a coherent longitudinal oscillation of conduction electrons on a metal boundary accompanied by a transverse electromagnetic field with and its maximum at the surface, which penetrates both the metal and the dielectric with its maximum at the surface [108]. If the interface between the two boundaries is parallel to the x-axis, perpendicular to the z axis, and situated at $z = 0$ with the dielectric at $z \geq 0$ and the metal at $z \leq 0$, the electric field can be described by the following.

$$E = E_0 \exp\{+i(k_x x \pm k_z z - \omega t\} \tag{3.53}$$

where $+$ is for $z \geq 0$ and $-$ for $z \leq 0$ to ensure exponential decay, $k_x = 2\pi/\lambda_p$ where λ_p is the wavelength of the plasma oscillation (Fig. 3.11).

The wave vector k_x can be expressed, using Maxwell's equations as a function of the dielectric functions of the metal(ϵ_a), which is complex, and the assumed to be

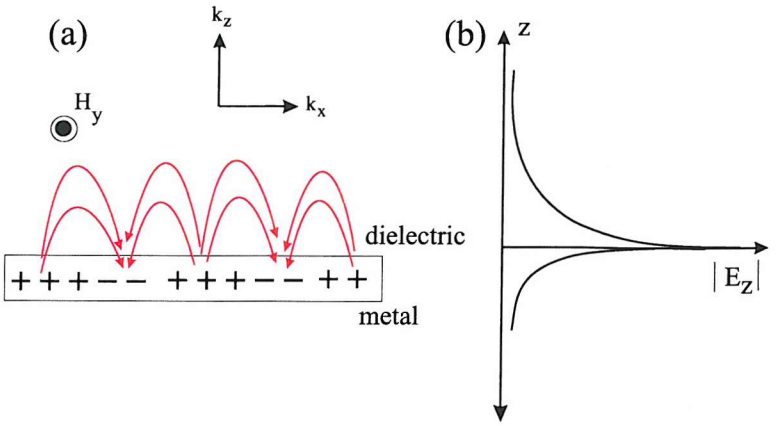

Figure 3.11: (a) A propagating surface plasmon and the charges in the x direction, also showing the magnetic field. (b) Exponential decay of the electric field from the surface; the field decays far more quickly in the metal compared to the dielectric.

real dielectric (ϵ_b).

$$k_x = \frac{\omega}{c}\left(\frac{\epsilon_a \epsilon_b}{\epsilon_a + \epsilon_b}\right)^{1/2} \tag{3.54}$$

where ω/c is the free space wave vector. The surface plasmon wave vector is complex and has real (k_{x1}) and imaginary (k_{x2}) parts:

$$k_{x1} = \frac{\omega}{c}\left(\frac{\epsilon_{a1} \epsilon_b}{\epsilon_{a1} + \epsilon_b}\right)^{1/2} \tag{3.55}$$

$$k_{x2} = \frac{\omega}{c}\left(\frac{\epsilon_{a1} \epsilon_b}{\epsilon_{a1} + \epsilon_b}\right)^{3/2} \frac{\epsilon_{a2}}{2(\epsilon_{a1})^2} \tag{3.56}$$

Surface plasmons are further characterised by a set of length scales which describe their behaviour and interaction with a metal surface. These include the propagation length, δ_{SP}, surface plasmon wavelength, λ_{SP}, penetration depth in the metal, δ_m and in the dielectric, δ_d. The surface plasmon wavelength, λ_{SP} is defined through its wave vector, eqn. 3.54. The propagation length, δ_{SP}, determines how far along the surface a SP can propagate, which for some free-electron like metals, such as silver can be as long as 1mm at infra-red wavelengths [109] and is estimated as :

$$\frac{\delta_{SP}}{\lambda} = \frac{(\epsilon_{a1})^2}{2\pi\epsilon_{a2}} \tag{3.57}$$

The penetration depth in both the metal and the dielectric determines the spatial

extent of the surface plasmon which are determined by the following [108]:

$$\delta_m = \frac{\lambda}{2\pi}\left(\frac{\epsilon_{a1}+\epsilon_b}{\epsilon_b^2}\right)^{1/2}, \delta_d = \frac{\lambda}{2\pi}\left(\frac{\epsilon_{a1}+\epsilon_b}{\epsilon_{a1}^2}\right)^{1/2} \tag{3.58}$$

The surface plasmon dispersion for a flat surface Drude metal with no losses can be calculated using its dielectric constants, Fig. 3.12(a). The dispersion relation has two distinct branches. The upper branch, for frequencies above the bulk plasma energy, is usually discounted in discussions about the response to light as for most metals these frequencies are in the UV. At these energies the reflectivity of the metal falls rapidly as the conduction electrons cannot oscillate above the plasma frequency, and so are unable to screen out the incident field. The upper branch is therefore absorptive and does not support bound interface states. The lower branch is the observed dispersion relation for the metal. It asymptotically reaches the cut-off value of $\omega_p/\sqrt{2}$, the frequency where ϵ_1 reaches 1. At low wavevector the relationship is almost linear and the surface plasmon has photon-like behaviour. At higher momenta the group velocity of the plasmon ($\delta\omega/\delta k$) approaches 0. Here, the surface plasmon is a true hybrid state of transverse and longitudinal electric fields.

The graph of the dispersion relation for surface plasmons on real metals, Fig. 3.12(b), shows that the behaviour is quite different from that of an ideal metal. Silver shows the most similarity with the ideal case, suggesting that it will be better at supporting surface plasmons than gold and platinum. Gold also shows a deviation from the light line, indicating an ability to also support surface plasmon propagation. In the same way, the dispersion for platinum remains identical to the light line, showing that it is not able to support surface modes.

From equation 3.54 the surface plasmon wave-vector is always greater than the free-space wave vector or, on a dispersion curve, always is to the right of the light cone. This so-called momentum mismatch explains why on a flat metal surface these effects are not seen. Although, various ideas have been pursued in order to couple to surface plasmons, the only method discussed here is that of a grating.

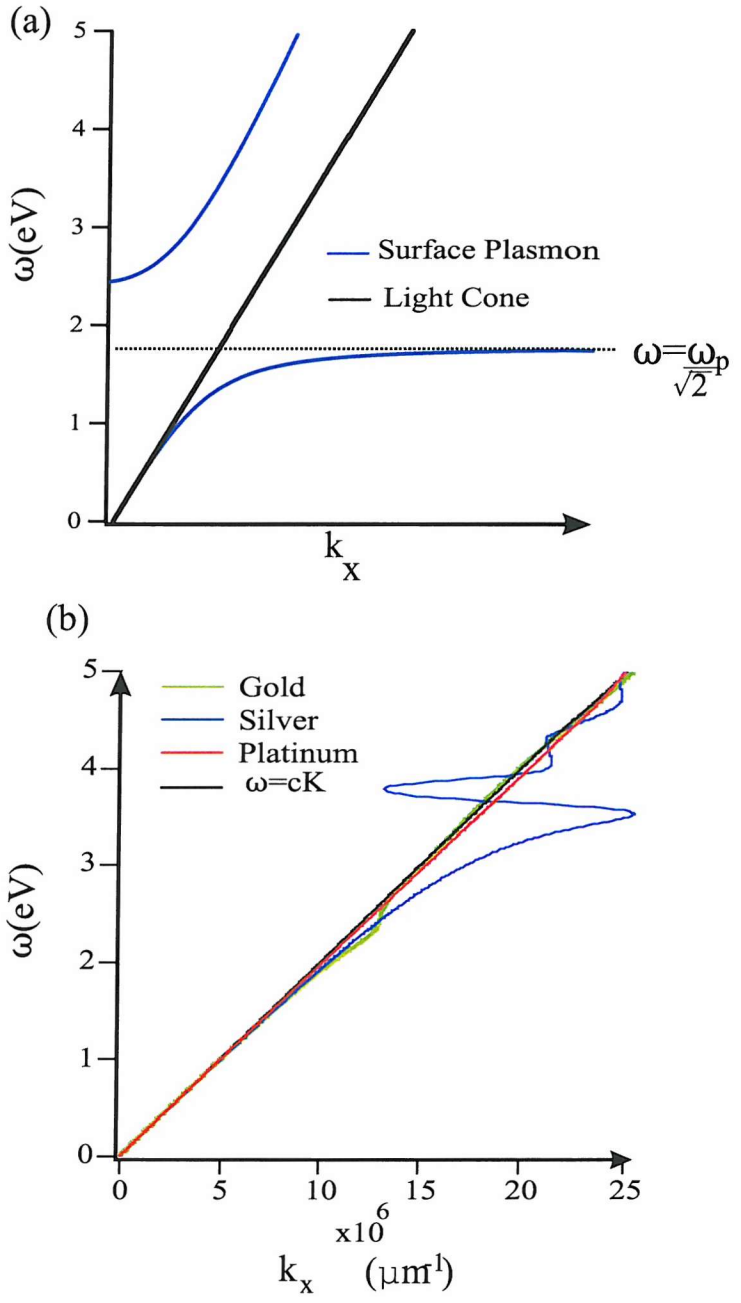

Figure 3.12: (a)Dispersion relation for a perfect metal with a bulk plasma oscillation at 2.5eV with the light cone marked on. (b) Calcualted surface plasmon dispersion relations for Au, Ag, Pt using actual dielectric constants.

Coupling to Surface Plasmons with Gratings

Gratings support surface plasmons through the addition of extra in-plane momentum to incident light due its periodicity; a grating with a period, L has momentum $k_g = 2\pi/L$. For example, if light has an angle of incidence θ:

$$k_x = \frac{\omega}{c}\sin(\theta) \pm mk_g = \frac{\omega}{c}\left(\frac{\epsilon_a}{\epsilon_a + 1}\right)^{1/2} \tag{3.59}$$

It is assumed that in the first instance of shallow gratings that the grating does not affect the properties of the plasmon itself; it merely allows incident photons to couple to the surface [108]. The equation above has to be further modified to account for the direction of the plasmon with respect to the grating grooves. The azimuthal angle, ϕ is defined to be 90^o when the plasmon travels parallel to the grating periodicity. A photon hitting the grating at some arbitrary angle ϕ will experience a reduced momentum as the grating spacing is increased by a factor of $1/\sin(\phi)$.

$$k_x = \frac{\omega}{c}\sin(\theta) \pm mk_g \sin(\phi) = \frac{\omega}{c}\left(\frac{\epsilon_a}{\epsilon_a + 1}\right)^{1/2} \tag{3.60}$$

Surface Plasmon Interactions: Band Gaps

An interesting feature of SP's is their interaction with one another, first observed by Steward (Fig. 3.13)[110]. Stewart observed two plasmon resonances as the angle of incidence was varied with the expectation that the two would coincide. Rather than merge, they showed anti-crossing, indicating that the two plasmons had the same energy, but propagated in opposite directions and therefore produced standing waves [103]. This behaviour has some notable similarities with that of photonic crystals. In direct comparison with the dielectric stack discussed in section 2.1.2, two counter-propagating SP's have the same periodicity but different energies, caused by the different electric field distributions with respect to the grating features [111]. Although a band gap does exist in the dispersion relation of a purely sinusodial grating, the momentum is too great to be coupled to. The SP will only be noticeably perturbed by the surface modulation when equal to very near half the Bragg wave vector (Fig. 3.14(a)). Further modification of the surface is needed to support a photonic, or more correctly plasmonic, band gap. One suggested method to produce

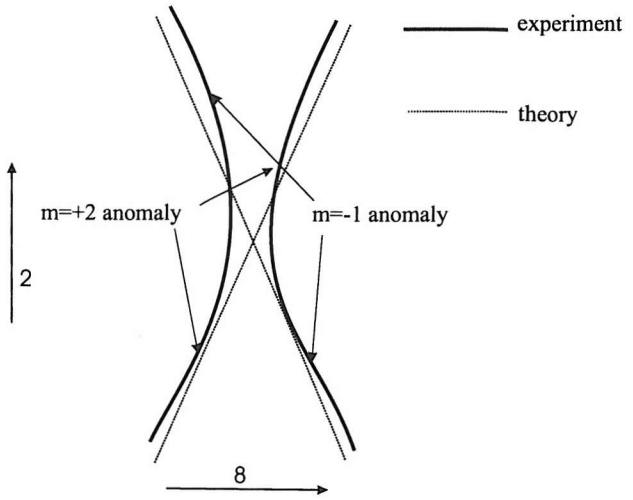

Figure 3.13: Repulsion of surface plasmons [110]

such a perturbation is to distort the grating profile with a first-harmonic component twice the period of the grating [111, 112] (Fig. 3.14(b)). A physical insight into what effect the band gap has is formed from considering the charge distributions of the states at the band gap (Fig. 3.14(c)). Using the analogy of the dielectric stack, but with the energy of the two states determined by how much the electric field lines are distorted by the structure, the origin of the energy gap between the two states becomes apparent. Numerical simulations on double period gratings show much stronger absorption features than traditional grating structures [113]

Another feature of gratings is their ability to convert the polarisation of incident light. Polarisation conversion is related to symmetry breaking, for example where the grating vector is not parallel to incident wavelengths which is known as off-axis or conical diffraction [114]. Experiments on blazed gratings have shown conversion from s (TE) to p (TM) conversion when the azimuthal incident angle, ϕ, is 90^o [112]. The physical mechanism behind this is again due to the opening up of a plasmonic band gap due to the interaction of a first harmonic component coupling two propagating surface plasmons together. However, rather than the one dimensional counter-propagation discussed beforehand, the plasmons due to the ± 1 diffraction order have a component of motion in opposite direction which produces a standing wave along one axis and a propagating one in the other.

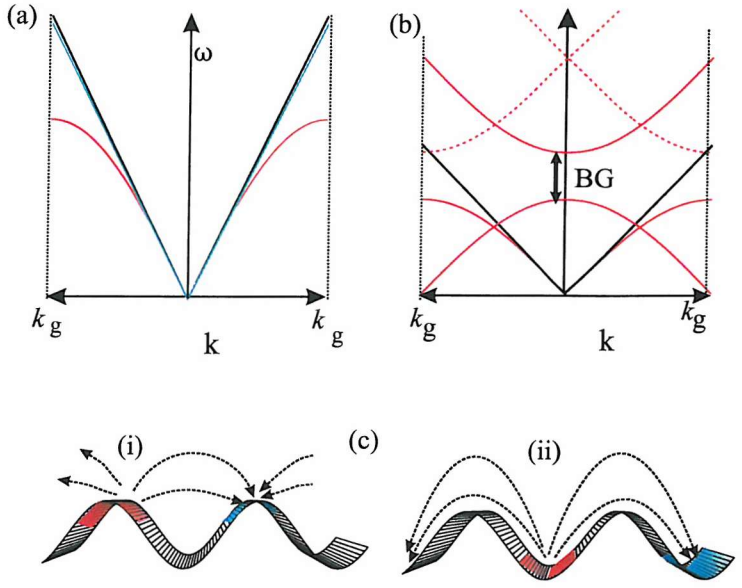

Figure 3.14: Surface Plasmon Band Gap constructions. (a) Dispersion of surface plasmon on a flat substrate (blue line) calculated using the figures for silver at $\lambda = 633nm$ [112] and on a grating of period k_g (red line); the black line is the light cone. (b) The effect of adding a second component of corrugation [111]. This added component produces a band gap (BG) of SP states inside the light cone. (c) Electric field charge distribution, red denotes negative and blue denotes positive (i) lower branch distribution (ii) upper branch field distribution, whose field lines are more distorted by the structure.

Effect of Deep Grating and High Aspect Ratio Grooves

So far only the grating periodicity and shape have been discussed as influencing the reflection properties. One of the main features of the experiments described in later chapters is the study of metallic structures as a function of film thickness, and so one area of interest is to ask what effect varying the depth of the grating has on its optical response. As described above, incident wavelengths are described by two angles θ and ϕ. In order not to confuse matters, the case of normal incidence ($\theta = 0^o$) and electric vector perpendicular to the grooves ($\phi = 0^o$) will be considered only. The effect of changing the grating height and the grating symmetry is discussed.

If the symmetry of the grating is preserved, with the grating groove smaller than twice the propagation length of the SP in the dielectric, and the depth increased, then the fields on either side of the grating interact. At certain grating depths this interaction becomes a coupled mode in which the plasmon either side of the groove strongly interacts with itself creating stationary surface plasmons, rather than travelling solutions [115]. These are sometimes termed self-coupled surface plasmon (polaritons) (SCSP(P)) [116]. Keeping the wavelength fixed while varying the groove depth elicits a series of local reflectivity minima, corresponding to standing wave orders. Trapping plasmons in narrow metallic crevices has been shown theoretically to dominate the Surface Enhanced Raman Scattering (SERS) response [117], suggesting a potential application for deep gratings.

Considering the band structure of gratings such as the above, shows they exhibit flat-dispersion bands, indicating a strong modulation of the photonic density of states [118]. The root cause of this behaviour is standing wave SP's. Very much like the tight binding model for energy bands, the interaction of many isolated energy level systems (atoms or, in this case, grooves) produce a band structure. The interaction of these bands with light shows strong anti-crossing effects and can be excited at normal incidence. In considering the reflectivity at normal incidence for symmetric gratings with a 700nm pitch and a groove depth from $0 - 700$nm for a wavelength range $700 - 1800$nm; a series of reflectivity ridges are observed which move towards longer wavelengths with increasing depth [119]. Wavelengths below 700nm were not

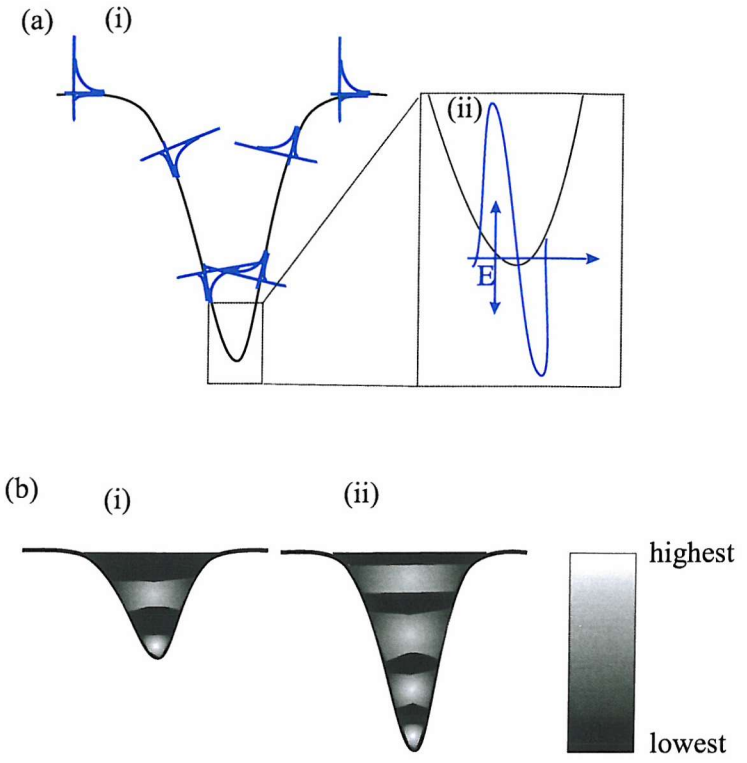

Figure 3.15: Surface Plasmons in deep gratings (a)(i) A traveling plasmon in a grating does not interact with itself when the width of the grating is greater than the penetration depth of the electric field in air. When the grating width is smaller than this the electric field on either side of the grating as in (ii) which produces a strong dipole across the grating. (b) Standing waves in deep gratings, shown are a representation of the spatial distribution of the magnetic field arrangements for resonances with (i) two and (ii) four nodes [115].

considered in this study because the grating would not be zero-order, complicating the calculations. The physical interpretation of these ridges are that they correspond to successive stationary surface plasmon field distributions.

The gratings discussed above were symmetric. As in the case of polarisation conversion, another way to generate interesting optical effects is through symmetry breaking, in this case by changing the shape of the grating. By breaking this directional symmetry it is possible to couple TE polarised light to stationary plasmons [116] and in so doing it is possible to access a second type of resonance, with odd magnetic field distribution within the grooves [119] (unlike the first which were even). This second type of resonance cannot couple to normally incident light on symmetric gratings. A second method used to break the symmetry of a deep grating is to alter

the angle ϕ to 90°[121]. At different polar angles (θ) a grating can couple to TM or TE polarised light due to a phase change between the top and the bottom of the grating. Two standing solutions are possible where the TE and TM excited modes have maxima at different parts of the grating.

Surface Shape Resonances in Gratings

Just as changing the depth on a sinusoidal grating can have a dramatic effect on the grating, deep rectangular gratings also have anomalous responses to incident light [122]. In particular, their ability to couple to TE polarised light is an interesting feature. However, these guided modes are usually not observed because they are shown to excite evanescent waves in the space between the grooves which have a magnitude similar to a mirror. Recent progress has shown deep grooves with TM polarised resonances, called surface shape resonances (SSR's) [123]. As the depth of a rectangular grating is altered the modes are initially SP in nature, i.e. dependent on period and material only. With increased thickness the modes move asymptotically towards lower energies. Furthermore some modes appear more waveguide-like than others, with a dependence on height shown at less deep grooves than others. Theses modes appear to show a hybrid character of both waveguide mode and surface plasmon. A slightly more complex arrangement also studied theoretically is that of a grating composed of bottle-shaped cavities [124], [125]. SSR's are reported to be independent of polarisation, and period of the grating. Instead, they manifest themselves in the grooves of the grating rather than along its surface, and so do not have the same boundary conditions usually associated with surface phenomena. These gratings also show depth dependent resonances, surface plasmon behaviour and hybridised modes. These studies indicate a way to evaluate the behaviour of a complex array of wavelength structures is to discriminate between TE and TM polarisation to identify the surface plasmon resonances and to consider height dependence resonances from SSR's. However, this method is not entirely useful in view of the hybrid nature of the resonances and the effects of stationary plasmons that has also been shown to occur in complex structures.

Two Dimensional Gratings

A drawback of sinusoidal gratings is that they are unable to exhibit a unidirectional two dimensional surface plasmon band gap. Taking inspiration from photonic band gap research, one technique to produce a band gap is to use a two dimensional array of hexagonally positioned periodic structures. Such a system has been verified experimentally with a holographically defined template of dots of radius $\sim$ 100nm covered with silver [126]. Different metals (Au, Ag, Al) modelled as an array of hexagonally defined scatters as described above have been shown theoretically to exhibit 2 dimensional band gaps with wavelength dependent band gaps [127]. The band gap width is further dependent on an individual metal's wavelength dependent response especially in relation to ohmic losses, with the widest band gap for each metal located at very different energies from one another. There are obvious advantages to producing energy gaps for surface states rather than bulk states; the challenge now is to produce samples which display these characteristics.

Problems with Gratings

In all the reviewed systems it appears that the spectral features observed experimentally are not as sharp as predicted by theoretical studies. The main reason for this and the hindrance to progress in grating technology, as in photonic crystals, is the manufacturing process. Typically, gratings are made through a process of interferographic exposure of two laser beams, usually in the blue or UV regions, on a photoresist [120]. The exposed photoresist is more soluble than unexposed regions and therefore easier to remove in the development process. The resulting product is typically not robust, and this is usually countered by ion etching the profile into a glass substrate. The three main drawbacks to this whole process have been identified as the nonlinear response of the photoresist to exposure, the inability of the solubility profile to be reproduced in development, especially in relation to removing unexposed ridges but not dissolving exposed deep troughs, and finally the surface of a sinusoidal profile is etched at different rates as the ion (or atom) etching rate is angle dependent [120]. In

a spectroscopic grating these drawbacks may not cause too much concern, but in gratings where the shape is critical, such as those described above, these three problems heavily influence the experimental realisation. These difficulties probably explain why experimental results have, in general, followed rather than preceded theoretical work.

3.2.3 Transmission Through Patterned Metal Surfaces

The discovery that a periodic array of sub-wavelength holes in a slab of metal several skin depths thick showed a much greater than expected transmission efficiency was an intriguing development in surface plasmon research [4]. A typical spectrum from [4] is shown in Fig. 3.16 for a Ag film with period, $a_0 = 900$nm, hole diameter, $d = 150$nm and thickness 200nm. The surprise finding in this result was that at wavelengths 10 times larger than the hole diameter, and with an effective skin depth $1/10th$ of the film thickness, it was possible to have a transmission of around 4%. Furthermore, if the transmission was calculated by dividing the fraction of light transmitted by the fractional area occupied by the holes it was found to be greater by a factor of two at an intensity maxima. In other words, light that hit the area surrounding the holes also transmitted light. Equally as surprising, was the fact that the holes didn't appear to diffract light either. This result was observed with other metals but with a non-metallic sample, germanium, the transmission was extremely small [128].

Work by Bethe on the diffraction properties of sub-wavelength holes [129] assumed the hole to be small enough compared to the wavelength of the radiation that the electric and magnetic components were constant across it. The discussion of this theory is too detailed for use here, instead we use as an approximate solution that both electric and magnetic fields for holes of the same order of magnitude as the hole will have a correction factor of $(ka)^2$ where $k = 2\pi/\lambda$ and a is the hole radius [128]. Therefore the correction for the intensity will be of order $(ka)^4$ or $(a/\lambda)^4$. In the case of the experiment outlined above, based on this formulation it would suggest that the transmission should only be of the order 10^{-3}. However, it should be noted that the author does not attempt to solve the problem of light through a cylinder as is the case above so this result should only serve as a guide. Nevertheless, it appears that

as a first approximation almost 1000 times more light is transmitted than would be expected.

The clue to the mechanism behind enhanced transmission lies with the periodicity of the array [128]. The minima in Fig. 3.16(a) are attributed to Wood's anomalies, section 3.2.2. These are given by

$$k = n\omega/c = 2\pi n/\lambda \tag{3.61}$$

where n is the refractive index of the dielectric medium.

The presence of surface plasmons are responsible for the transmission maxima; these effects are confirmed by altering the angle of incidence for both TE and TM polarisations which show a complex mode crossing dispersion curve for TM and no dependence for TE. The coupling of radiation to the array is given by

$$k_{sp} = k_x \pm iG_x \pm jG_y \tag{3.62}$$

with k_{sp} the surface plasmon wave vector, k_x component of the incident wave vector on the plane of the sample, i,j are integers and G_x and G_y reciprocal lattice vectors; $|G_x|, |G_y| = 2\pi/a_0$. The surface plasmon vector is associated with the dispersion relation for a smooth film, and the hole array is treated as a perturbation. At normal incidence:

$$(i^2 + j^2)^{1/2}\lambda = a_0\left(\frac{\epsilon_1\epsilon_2}{\epsilon_1 + \epsilon_2}\right)^{1/2} \tag{3.63}$$

where ϵ_1 is the dielectric it the metal and ϵ_2 is the dielectric of the interface medium. In the case of a film deposited on a substrate, as is the case in Fig. 3.16, then two sets of maxima are superimposed on one another in the resulting transmission spectrum. The transmission of the metal can be increased by a factor of ~ 10 by matching these two separate resonance conditions through altering the dielectric constant using index matching fluids [130]. Proof of this approach was provided using a free standing Ni film and measuring the transmittance before and after adding a layer of Ag to one side of the and then the other [131]. Although adding layers of Ag to the Ni substrate invariably thickened the film and decreased the hole diameters, the overall effect was to increase the transmittance. The increase was due to the different responses of the

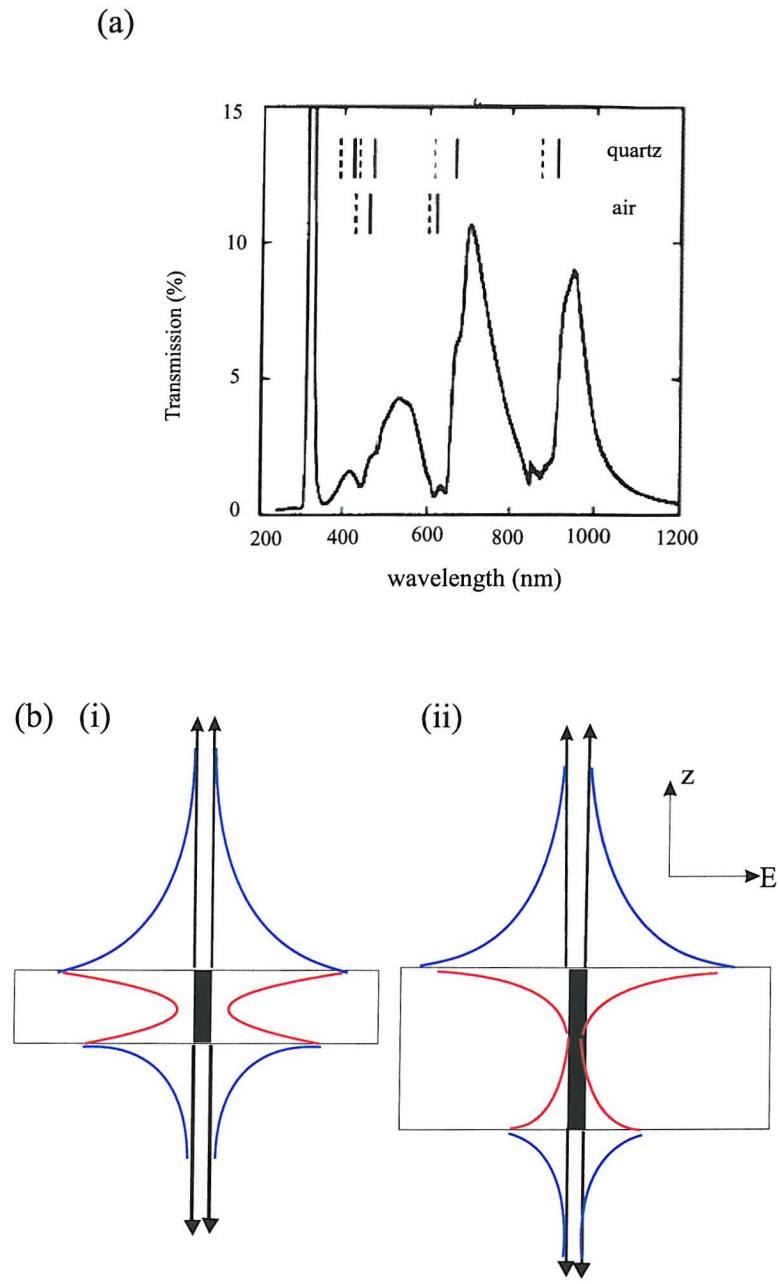

Figure 3.16: (a) Transmission spectra of light through an array of sub wavelength holes in a silver film on quartz. The full lines indicate the positions of the surface plasmon energies on the air and quartz sides corresponding to transmission maxima; the dotted lines indicate the positions of the Wood's anomalies and correspond to the transmission minima. (b) The two separate film thickness dependent regimes for surface plasmon interaction on a periodic surface, (i) with sufficiently thin films the SP's either side of the film interact to form a SP "molecule" (ii) Thicker films produce separate SPs on each side.

two metals at optical frequencies. Silver's dielectric constant has a real component significantly larger than its imaginary component while nickel's real and imaginary components are of similar sizes at visible wavelengths. Consequently, silver acts more like an ideal metal and is capable of sustaining plasmon resonances better than Ni.

This discovery was not without controversy. In an attempt to model the system, some researchers used a grating composed of narrow slits rather than holes [132, 133] and discovered that this system, as well as having surface plasmon resonances, also showed the appearance of effects from coupling to waveguide resonances within the slits. However, these studies have been subsequently proved to be unrelated to the experimental conditions, although experiments using slits in thick metal plates have now showed waveguiding effects in the microwave region [134]. Further theoretical endeavour was able to model a system with holes, providing the necessary explanation of the experimental observations [135]. The transmission at normal incidence, with the dielectric constant either side of the film and in the air holes themselves set to 1 can be expressed in the following way.

$$t_{00} = \frac{\tau_{01}^{12} e^{-|k_{z1}|h} \tau_{10}^{23}}{1 - \rho^2 e^{-2|q_{z1}|h}} \tag{3.64}$$

τ_{ij} is the probability amplitude to transmit an incident wave to an outgoing wave; $\tau_{01}^{12} = 2S_0/(G_2 + G_1)$, $\tau_{10}^{23} = 2G_2/(G_2 + G_1)$, $\rho = (G_2 - G_1)(G_2 + G_1)$. G_1 and G_2 are the conductances of region 1 and 2 where region 1 is air and 2 is the metal substrate, k_{z1} is the wave vector along z for a waveguide mode, z is taken to be perpendicular to the interfaces. ρ denotes the amplitude for reflection. The possible incoming wave vectors are denoted by $\mathbf{k}_{xi}$ where i denotes an integer. In the case here only the first order diffraction is accounted for so $\mathbf{k}_{x0} = 0$ or $\mathbf{k}_{x\pm1} = \pm\frac{2\pi}{L}$ where L is the lattice constant. Further simplification occurs if a perfect metal is assumed and taking $g = \omega/c$, $\mathbf{k}_{z1} = \sqrt{g^2 - \mathbf{k}_{x1}^2}$. Also, $G_2 = k_{z1}/g$, $G_1 = S_0^2 + 2S_1^2 g/\mathbf{k}_{z1}$ where $S_0 = d/L$, $S_1 = S_0 \sin(\mathbf{k}_{x1}d/2)/(\mathbf{k}_{x1}d/2)$.

At first sight this rather cumbersome expression would seem to prevent the possibility of large transmissions with $e^{-|k_{z1}|h}$ always $\ll 1$. However, the condition on ρ is also changed because only evanescent waves are considered and therefore the value of $|\rho|$ is not confined to 1 or under. Transmission peaks are observed when the graphs of

ρ and $e^{-|k_{z1}|h}$ versus wavelength intersect, proving that the observed transmission is due to resonance. In elucidating this, the authors [135] also uncover two film thickness regimes of the surface plasmon. For thin films the two surface plasmons on either side of the metal film couple together to form a "surface plasmon molecule", whereas for thicker films light is transferred from surface plasmon to surface plasmon before the molecule can form. When the molecule is formed the photon is assumed to behave very much like resonant electron tunneling. The condition for these two regimes is determined by the radiative time, t_{rad} for an isolated surface plasmon is given by approximately $(c\mathbf{k}_{z1})^{-1}$, and the time to form the molecule is $t_{res} = t_{rad}(d^3 e^{k_{|z1|}h}/L^3)$. With the increase in film thickness only t_{res} changes, and when the two become equal, the molecule is assumed to no longer exist. Although thicker films still show transmission enhancement due to the large surface field build-up, they are less efficient than thinner films. The above predictions have been experimentally verified experimentally, with thinner films showing higher, broader transmission peaks [136].

One question which these studies don't answer is what role the holes in the metal play in comparison with the effect of periodicity. It has been shown that a film with just periodicity is capable of enhanced transmission through large field enhancements from surface plasmons on both sides of a film[141]. There are two advantages of using holes; they provide a higher refractive index contrast to allow plasmon excitation, and also as low attenuation channels through which the evanescent field can channel energy to the other side of the film.

Using the idea of periodic structures as antennae for plasmons, and holes as low attenuation pathways, another suggested route is to use one sub-wavelength single hole surrounded by concentric rings with the matching periodicity for the desired surface plasmon coupling, to act as single sub-wavelength emitter [10]. There are two important features of such a structure. First, the grating on the input side appears to act as a collection antenna for the hole in the centre which could be of technological importance in creating sub-wavelength photonic devices. Secondly, in adding an exact copy of the grating on the output side the reciprocal situation on the input side is produced in that a highly diffracting source is made directional by the presence of the grating [109]. Numerical simulations also suggest that light is emitted from a small

region around the aperture.

3.3 Conclusion

Controlling light using structured metal surfaces is a promising field with many avenues currently being investigated. Presently, there appears to be a significant difference between the approach followed in studying colloids and that followed in planar structures. Whereas colloidal research is driven by the ability to make nanoparticles very simply using chemical means, grating technology relies on the more traditional techniques of photolithography and ion beam drilling. The reason for these different approaches is due to the fundamental differences in surface plasmon resonances in nanoparticles and planar grating surfaces. In nanoparticles the resonance is a result of the small dimensions and the resulting strongly scattering effects. Making strongly coupling particles therefore relies only on producing a small volume of metal. To couple light to flat surfaces is more problematic, relying on the momentum mismatch between incident light and surface states to be bridged by grating momenta. Furthermore, these states are very sensitive to local morphology and therefore making a device capable of interacting with light demands close careful control.

Chapter 4

Metal Self-Assembled Structures

This chapter describes the different methods used to self-assemble latex spheres on a conducting substrate and the subsequent electrochemical deposition of metal to make a free-standing three-dimensional "inverse" structure. A brief description of the sample preparation is given followed by a discussion about the surface morphology and ordering. Two techniques were used to study these structural characteristics; Scanning Electon Microscopy (SEMs) and Atomic Force Microscopy (AFM). Although SEMs are extremely useful for working out long and short range ordering, as well as giving a reasonable estimation of the film thickness, they do not reveal the structure inside individual cavities which sometimes can only be satisfactorily studied with AFM.

4.1 Sample Preparation.

4.1.1 Sphere Template Assembly

Two different methods were used to assemble latex spheres with the second drawing on much of the research described in section 2.2.1, as the need for well-ordered templates became necessary. A range of different sphere sizes were tried, from 200nm to 10μm, but for this discussion sphere sizes from $500 - 800$nm are concentrated on as these lengths scales were the main focus of investigation. Monodisperse polystyrene spheres were obtained commercially with a size variation of 1.3%, with the suspension homogenised with gentle inversions followed by sonication for 30 seconds. The first method relied purely on sedimentation to deposit spheres over a restricted area

using a 1cm diameter ring. As discussed in section 2.2.1, this technique has a number of drawbacks, especially the lack of control over the number of layers, and the inability to create long range ordering. A close packed arrangement of spheres was produced by virtue of using a high concentration of spheres. Visually, the sample has bright crystallites surrounded by a smooth metallic region indicating a close-packed short-range ordered centre with an amorphous centre towards the edges of the sample (Fig. 4.1). A lower concentration solution produced a completely amorphous sample which showed no diffractive properties.

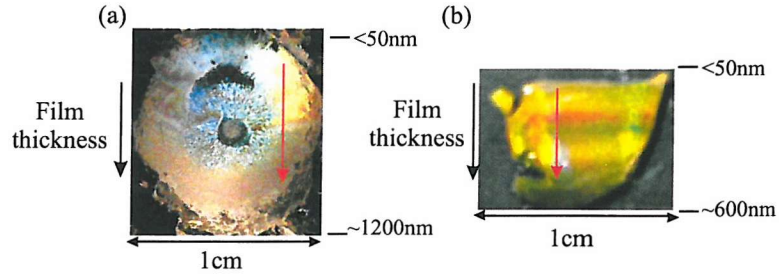

Figure 4.1: (a) Gold sample made from 750nm latex sphere template using a sedimentation technique and with a continuous increase in film thickness down the sample. The centre shows diffracted beams from centrally positioned crystallites while towards the edges the sample is amorphous. (b) A well-ordered step graded gold sample of a monolayered 700nm sphere template. The red arrows indicate the places along which spectra were taken for the two samples.

In an attempt to exert more control over the crystallisation stage, the idea of using capillary forces to pull particles together as discussed in section 2.2.1, was implemented using some of the ideas shown in Fig. 2.5(a). As well as close-packing, monolayer coverings of spheres were desirable in order to remove the effect of second layers on the optical response of the film. Capillary forces on the particles were increased through reduction of the contact angle of the sphere solution using self-assembly of cysteamine through immersion at room temperature over several days. The treated slide was held parallel to another slide, separated by $100\mu m$ using parafilm. An aqueous $1wt.\%$ suspension of latex spheres was added with a slight argon stream to remove trapped air bubbles. The filled cell was held vertically in an incubator to control the evaporation rate in a temperature controlled environment. No evidence of re-suspension of the spheres was observed when placed in electroplating solutions.

4.1.2 Electrochemical Deposition

Electrochemistry

A typical electrochemical cell consists of a three electrode arrangement; a working electrode onto which the desired product is deposited, a counter electrode to complete the circuit and a reference electrode to monitor the charge passed (Fig. 4.2(a)). The voltage passed between the counter electrode and the working electrode was used to reduce complex metal ions in solution to form a metal. The working electrode consisted of a $1cm^2$ flat film, made of evaporated layers of chromium followed by gold or indium tin oxide (ITO) which were chosen for their conductivity, flat geometry and unreactive response to the reactants or products. The counter electrode is designed to supply current without limiting the electrochemical cell's performance; the electrode used here was a platinum gauze to maximise the surface area over which gas could evolve. The reference electrode was made of saturated calomel, whose electrochemical potential is well-known and so is readily accounted for [137].

An understanding of the reaction process and the potential at which the reactants form products is found from cyclic voltammetry, which typically plots the voltage/current characteristics of an electrochemical cell as the voltage across the cell is varied. As an example, the cyclic voltammogram for the deposition of gold from Hexachloroplatinic acid (H_2PtCl_6) is shown (Fig. 4.2(b)). This shows the measured current at a particular voltage as the voltage is swept first to a negative potential and then back again. At small negative potentials, little current flows until the activation energy, point (i), is reached, whereupon the reaction starts. Here on in, the current increases with voltage as metal is deposited and so sources electrons. This continues until the current and the flow of material to the deposition site balance, point (ii), and the reaction rate is a maximum. Further increases in voltage from this point decreases the reaction rate as the ions cannot reach the electrode quickly enough. If the voltage is now swept towards positive voltages material is stripped off the electrode. The process does not follow the same path because the surface has been changed by the electrodeposition process.

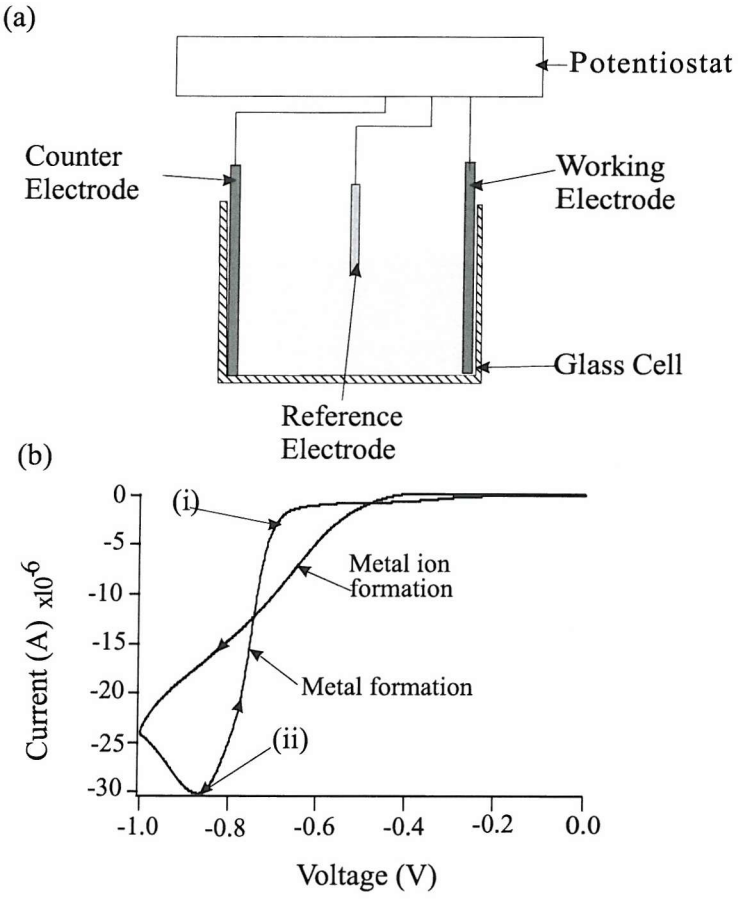

Figure 4.2: (a) Schematic representation of the experimental set-up used for electrochemical deposition (b) A typical voltammogram showing deposition of Au onto an electrode; (i) Indicates the energy of the potential barrier of this reaction, (ii) Potentiostatic point

Depositing through a template

The plating solution for Gold was a cyanide-free commercially available product from Technic Inc (Cranston, RI , USA). Platinum was deposited from Hexachloroplatinic acid (H_2PtCl_6), and silver from a low cyanide bath consisting of $K_4P_2O_4$, KCN and AgCN. Pt and Au were deposited on the templated electrode under potentiostatic conditions at 0.05V and -0.95V respectively. Silver was deposited using pulse plating because of the instability and poor adhesion of the resulting film associated with potentiostatic conditions. A first pulse of current density 20mA cm^{-2} for 100ms, which ensured good adhesion to the electrode, proceeded by a pulse train of 5mA cm^{-2} for 50μs with a rest time (zero current) of 1s.

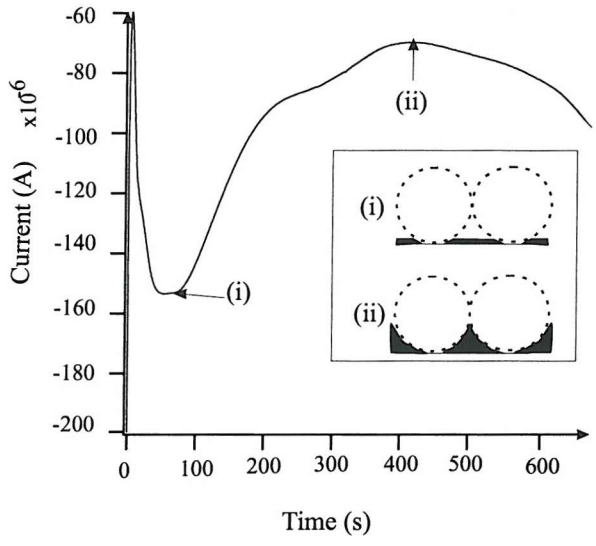

Figure 4.3: Graph of current versus time for an electrochemical deposition through a latex sphere template; (i) end of film nucleation and beginning of film deposition, (ii) film thickness reaches thickness of radius of sphere template.

Film thickness was controlled by accurate measurement of the total charge passed through the cell. As the film was deposited through an intricate template its rate was controlled by the surface area available. A plot of current passed through the cell against time reveals the deposition has several different stages (Fig. 4.3). Before point(i) is reached the current increases with time as the deposited metal begins to nucleate on the electrode's surface. At point(i) the film formed smoothly covers the electrode surface and the current then begins to decrease as the available surface

area decreases due to the geometry of the template. Point(ii) corresponds to the film thickness reaching half sphere height, which has the smallest possible surface area; the current though the cell increases after this point. The lack of symmetry about point (ii) suggests that the film deposition process around the latex spheres is also dependent on whether metal is deposited underneath or over the spheres.

As well as growing samples to a specific thickness, some were also grown with a graded film thickness in order to simplify analysis. Earlier samples were held vertically in the plating bath and the solution allowed to drain slowly creating a smooth thickness gradient as with the sample shown in Fig. 4.1(a). Templates of sphere monolayers were graded in steps by withdrawing the substrate from solution in a series of 500μm steps using a microstage Fig. 4.1(b). Grading the sample in a series of steps rather than a continuous increase in height allowed an easier correlation of optical and SEM observations.

After metal deposition the latex spheres were removed from the film by dissolution, made possible because the structure has an open pore, interconnected structure very much like that shown in Fig. 2.6. Initially, the spheres were dissolved with toluene, but later samples were washed in THF as it was discovered that Raman spectroscopy of samples in the former case showed the presence of residual latex.

4.2 SEM Sample Characterisation

4.2.1 Film Thickness

The main method used to characterise the surface morphology of these samples was electron microscopy. This allowed measurement of the pore mouth, r_{pore}, which, with the original sphere radius, r, allowed the film thickness, t, to be calculated with simple trigonometry:

$$t = r \pm (r^2 - r_{pore}^2)^{1/2} \tag{4.1}$$

The choice for sign for the $\pm$ term depends on whether the film is thicker or thinner than the radius of the sphere template. This technique had some obvious drawbacks, notably in attempting to judge the exact position when the template has grown beyond radius height; this of course distorted the thickness calculations considerably due

to the presence of squared terms. The process was also hindered by the inability to judge gentle gradients on the surface from a SEM image. Evidence from AFM measurements (see later) indicated that the spherical cavity lips are rounded rather than sharp which might be expected due to the coupled processes of diffusion and reaction involved in electrochemical deposition. The presence of rounded lips complicated precise measurement of the pore mouth diameter and was especially problematic at around radius height, due to the pore mouth changing slowly with film thickness. However, despite these drawbacks SEM measurements are at present the best method of determining film thickness; cross-sectioning the film obviously damages the sample and AFM measurements are complicated by the problem of increasing pore mouth obstruction after radius height.

4.2.2 Macroporous Film Appearance

The surface morphology of the samples was observed using SEM, and allowed measurement of the sphere centre to centre distance which showed that shrinkage of the sphere template to be minimal. A typical SEM image of a 140nm thick Platinum film formed from a 700nm diameter sphere template is shown in Fig. 4.4. Spherical voids with uniform pore mouths are left in the film after the removal of the latex spheres which, in this case here, are arranged in a close-packed array. The inside of the voids were not visible through SEM inspection and so it is not possible to determine their smoothness and shape. The visible parts of the film are the surfaces which are highly reflecting, whereas the darker regions show where electron reflection is less, or areas which reflect electrons away from the detector.

Disordered Films

To illustrate how the initial sphere template affects the resulting metallic sample, we detail the surface of the two sample shown in Fig. 4.1. The first sample, Fig. 4.1(a), was constructed with sphere of diameter 750nm using a simple sedimentation technique. The SEMs were taken along the red arrow, in the "amorphous region" which had short range order, about 10 sphere diameters (Fig. 4.5). When the film was very thin, the top surface was uneven (i), but in subsequent images, at thicker

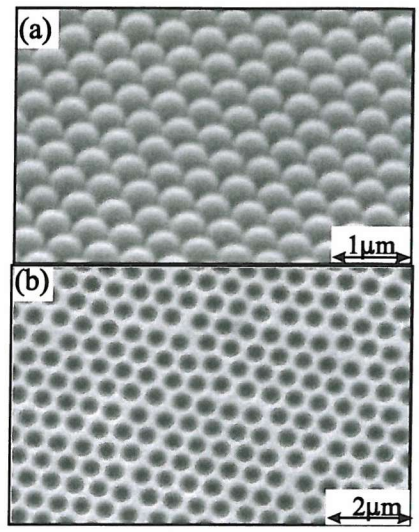

Figure 4.4: (a) Angled SEM image of a polystryene sphere template of diameter 500nm. (b) A 140nm thick platinum template from a 700nm diameter sphere template.

parts of the film, they appeared uniform. At first, the gold formed hemispherical cavities (i-iv), but the nature of the deposition is such that it was hindered by the presence of the second layer of spheres. The cavities were prevented from closing, and first the circular openings became hexagonal, followed by the formation of a three-fold symmetric pattern of interlinked holes (v-x) that connected the second layer hemisphere to the first. The interconnections show up in the SEMs as a series of dark circles at the corners of distorted hexagons (x). Also visible are dark areas directly above the centre of the lower sphere which indicates that the presence of the polystrene layer hindered growth.

SEM images taken of large areas of the sample show how the apparent well-ordered samples in Fig. 4.5 are actually domains of a disordered template, Fig. 4.6(a). Clearly, such a radical change in shape of the void apertures and the inherent long range disorder poses a very difficult challenge when attempting to understand how the different features influence the optical response. A side view of the sample shows the extent of the disorder in the sample, with well-defined ridges showing the edges of the voids (Fig. 4.6(b)). By way of comparison, two side views of samples made recently using the capillary force method are also shown (Fig. 4.6(c),(d)). These two

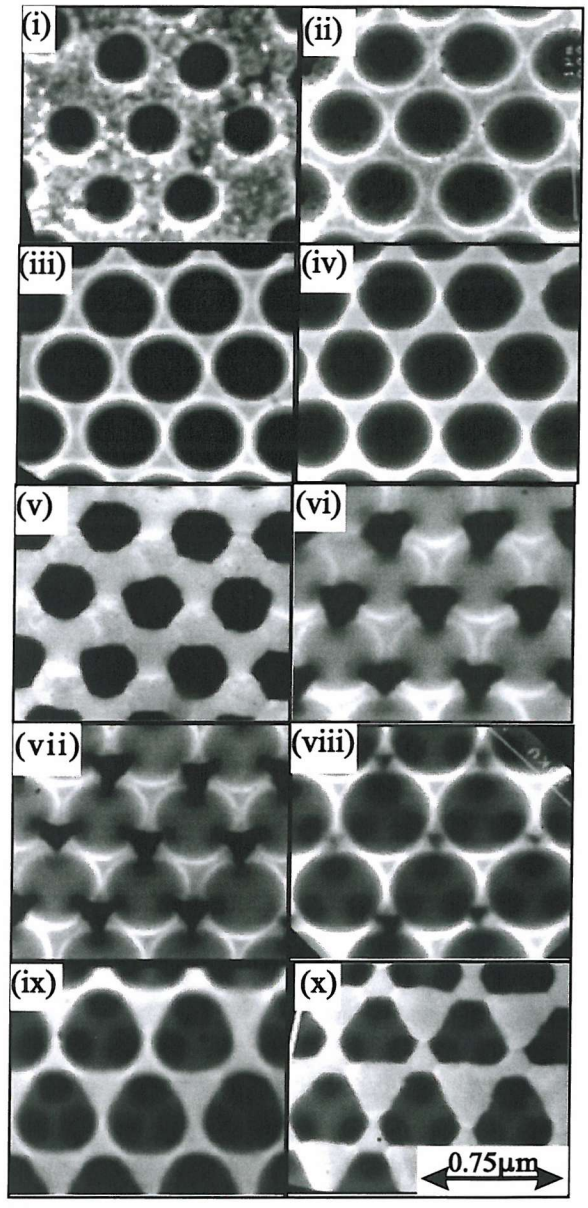

Figure 4.5: Scanning electron micrograph images of a 750nm template with continuously varying thickness down the sample(i) 50nm, (iv) 375nm, (x)1100nm . The lower area appears black and the second layer appears grey

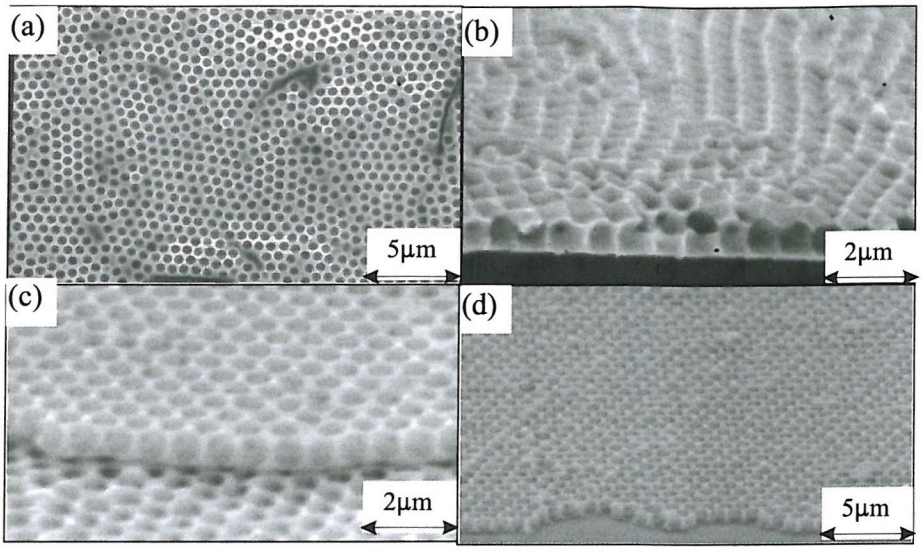

Figure 4.6: (a) SEM of large area of sample showing the disorder present in the original template. (b) A side view of this sample shows a significant degree of disorder. Two side views of well-ordered samples with (c) two well-ordered layers and (d) a well-ordered monolayer sample.

images show the vast improvement made in sample production since the beginning of the project. The method allows both double and single layer samples to be grown with a high degree of order and both samples are much flatter than the one made from sedimentation.

Well-Ordered Films

The second sample under consideration, Fig. 4.1(b), was produced using capillary forces as outlined previously to produce a 700nm diameter sphere template (Fig. 4.7) . The appearance of the SEM images differ from the set in Fig. 4.5 due to the coarser resolution of the electron microscope used to take the images. As with the previous sample when thin, the film surface appeared slightly rough. The most apparent differences between the two samples are that the ordering in the second one is much better; it has distinctive long range order, and also the pore mouth shapes remain circular throughout the film except at the very thickest point (ix). The samples also show the presence of defects such as missing voids ((a) (Fig. 4.7(vii)) and line defects ((b) (Fig. 4.7(vii)). However, in both these cases the defects appear to have little impact on the overall order of the template. Multilayer samples can be made by either

changing the concentration of the solution or by repeating the deposition assembly process several times.

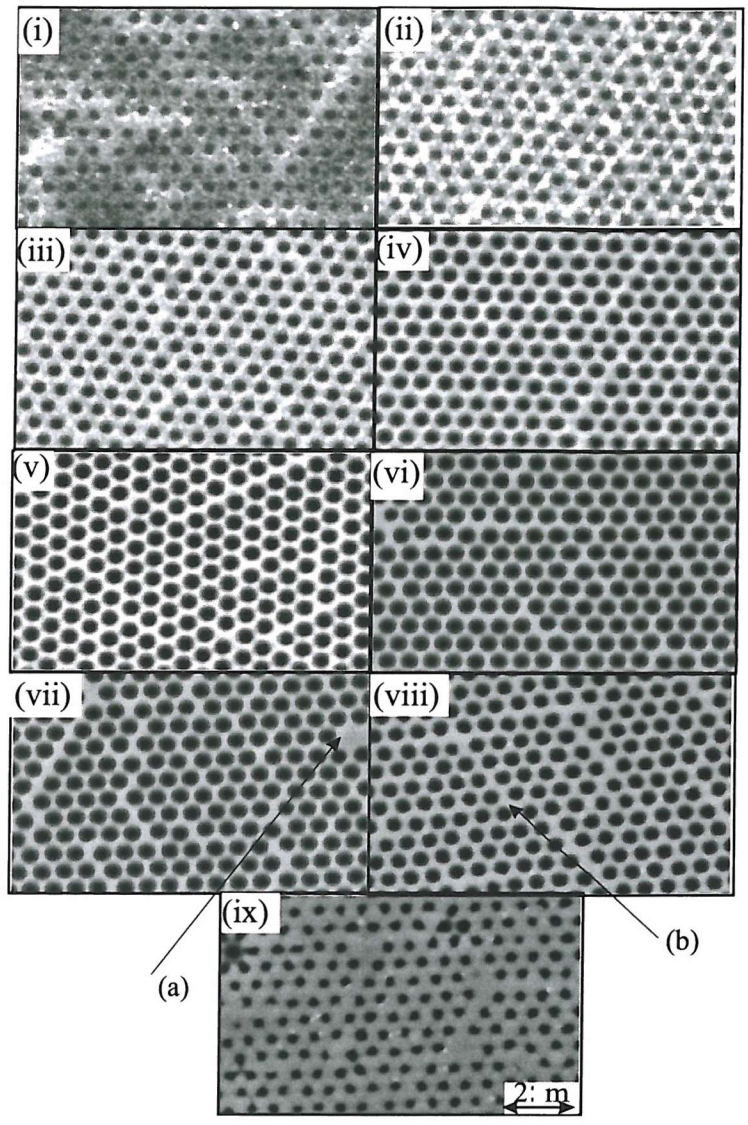

Figure 4.7: SEMs of a Au cast of a 700nm diameter monolayer sphere template and graded in four steps (i)-(iii), (iv)-(v), (vi)-(vii), (viii)-(ix). (a) A missing void (b) line defect.

4.2.3 Further Analysis of SEMs

One issue which has been of particular importance has been to understand the extent to which the voids are interconnected. The difficulty in finding out whether close packed arrays interconnect has been due to the pore mouth opening and the internal

void structure. The most compelling evidence comes from a new technique called "double templating" which allows the internal structure of the voids to be viewed (Fig. 4.8(a)). In this instance, polypyrole was first electrodeposited through a 900nm diameter sphere template and the template dissolved in THF. Gold was then electrodeposited in the voids and the polypyrrol removed through heating the structure to $2,500°C$. The resulting gold structure represents the air space inside the voids. SEM imaging clearly show the interconnects between the voids. Another method to reveal the internal structure of the voids was to take angled SEM images of a sample (Fig. 4.8(b); the interconnects are visible as dark circles where no metal has been deposited at the points where the voids touch.

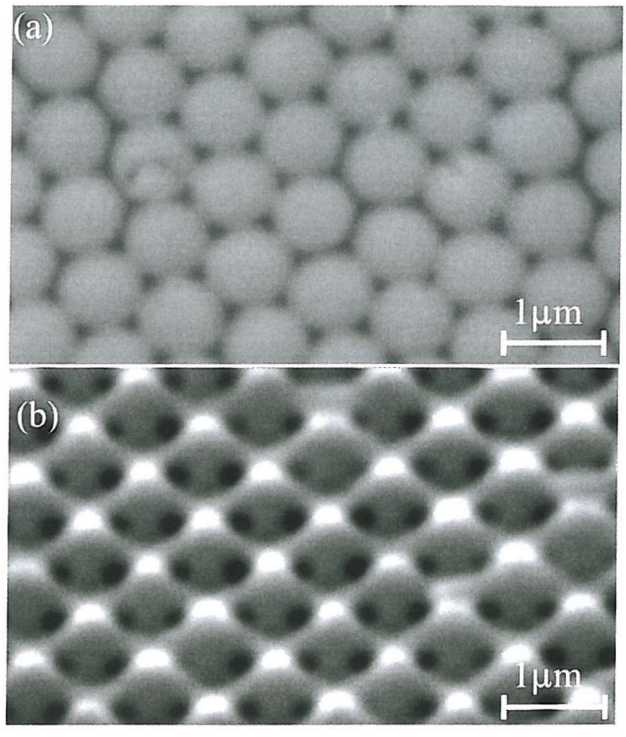

Figure 4.8: SEM images showing different views of the connections between voids (a) Mold of a close-packed interconnected void structure of a 900nm sphere template (b) Angled view of a gold sample, the interconnections between the holes are observed as dark circles.

One of the main difficulties in using SEM characterisation was in understanding how the surface morphology of the films relates to the film thickness. As mentioned above, film thickness is calculated from the pore mouth diameter which, by the nature of the calculation, becomes increasingly inaccurate as the film thickness approaches

half ball height. Furthermore, the variation in pore mouth diameter of voids in any SEM image complicates the process of determining the film thickness. Therefore, although much information can be understood merely from checking the visual appearance of the films we have recently developed a program to analyse film appearance in more detail. Through image analysis software it is possible to work out the eccentricity, pore mouth diameter, separation distance and angle between lines joining the centres of nearest neighbours. This software has yet to be used to its full potential, but initial usage has provided a useful analytic tool to study the film surface.

As an example of how the film surface morphology changes, two SEMs of the sample shown in Fig. 4.7 are used to illustrate the variation in pore mouth diameter, void separation, close packing and eccentricity change as the film grows up towards half sphere height. First, the pore mouth openings are observed as a distribution of values with the distribution becoming broader as half sphere height is reached (Fig. 4.9(a)). Also, the surface shown in SEM(ii) is more disordered with the nearest neighbour spacing and the eccentricity both showing a wider distribution than for the thinner film sample. From Fig. 4.9(c) it is noticeable that the crystal orientation is rotated between the two points on the sample although broadly both remain close packed. Although much of this information can be deduced from merely close observation of the images themselves, this method should, in the near future, be able to characterise an entire sample from its SEMs, in a far more efficient and quantative manner than by eye alone. This method will be especially useful in the future for checking whether how a film's template ordering varies across its structure and for working out the film thickness at one one point from all voids on a micrograph. However, it has proved less convenient to use SEMs to infer the size of individual crystals as template quality has increased, especially in respect with using optical techniques.

4.3 Characterisation using AFM

As mentioned at the beginning of this chapter, AFM measurements are hindered by the conical shape of the tip and the void topology, notably the pore mouth. Also, the tip is likely to slip down the sphere sides as it moves along the surface so creating

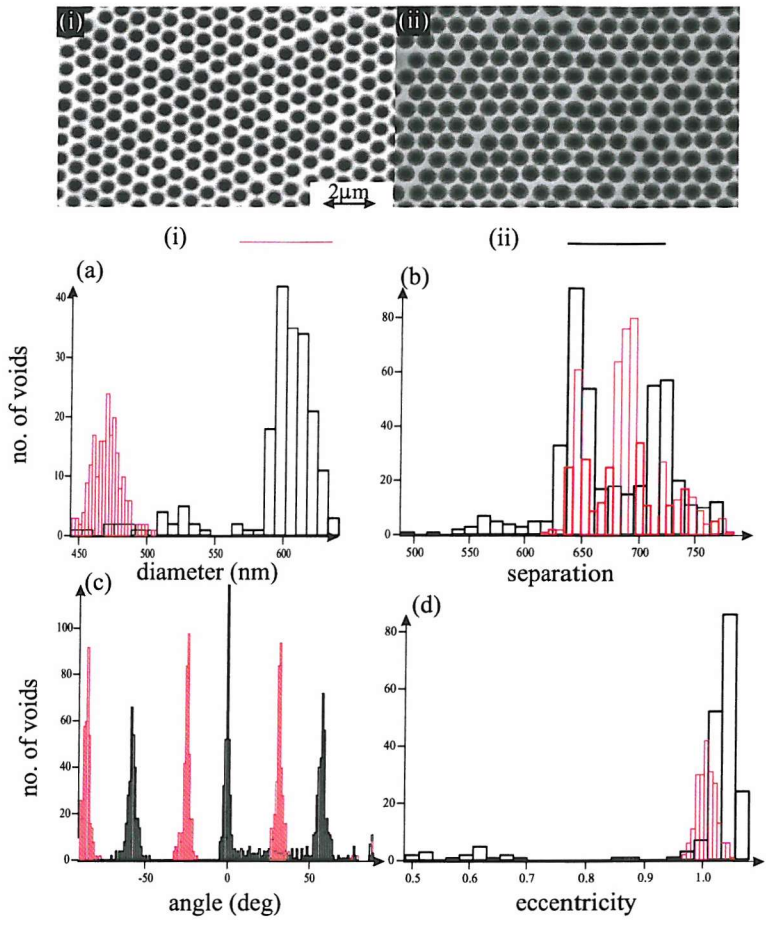

Figure 4.9: (i) and (ii) SEMS from sample in Fig. 4.7, (i) taken below half ball height and (ii) just after. The four graphs (a)-(d) reveal the differencs in film quality between the two (a) void diameter, (b) void separation (c) angle between lines joining centres of nearest neighbours (d) eccentricity of void openings.

artifical signals. Despite these problems, AFM measurements did provide a way of gaining some insight into surface quality and shape of the voids.

Three samples were subjected to AFM measurements; a Au sample 670nm thick from a 900nm diameter sphere template, a Au sample 2μm thick from 5μm spheres and a Pt sample 3μm thick from 10μm spheres, Fig. 4.10. The difficulty of producing reliable and meaningful results on samples with templates of sub-micron spheres, especially above radius height, is shown by Fig. 4.10(a)(ii). It seems likely that the explanation for one void being at a different height from the other will be an artifact of the experiment, such as the AFM tip being affected by the cavity sides, rather than having any physical relevance. The scans of the Au sample from 5μm spheres shows that the void surface is smooth and the rounding of the lip at the interface between the void and the surface, Fig. 4.10(b)(ii). From both Au samples it is clear that the top surfaces are not flat, but have undulations between the voids which were not observable with SEMs. This raises two issues; first, the measurement of the void's diameter is complicated by the rounding of the lip, and secondly the film surface is not flat so complicating modelling of reflections off the surface. The AFMs reveal the surface roughness of the films, especially prevalent in the Pt sample, Fig. 4.10(c)(ii), and which does not show up in the SEMs, Fig. 4.10(c)(i). The surface roughness of the Pt film shows the problems associated with electrochemical deposition, namely the need to control film growth so it does not become dendritic. The final part of Fig. 4.10 shows a series of AFM scans of different parts of a 5μm void. The surface of the void is generally smooth, with some evidence of roughness towards the void extremities but these could also be due to the scanning tip having difficulty following the spherical contours.

Other, more detailed, AFM studies on a 1μm template have also revealed that the bottom of the cavities is not spherical but is flat due to the templating spheres touching the substrate (Fig. 4.11). Careful measurements of this flat area have revealed that its diameter is approximately 10% the size of the diameter of the sphere template, which was also confirmed for template sizes of 5μm. This suggests that the hindrance to the growth is derived from the morphology of the template at the surface of the electrode and that a sphere of any size will always touch the surface with roughly

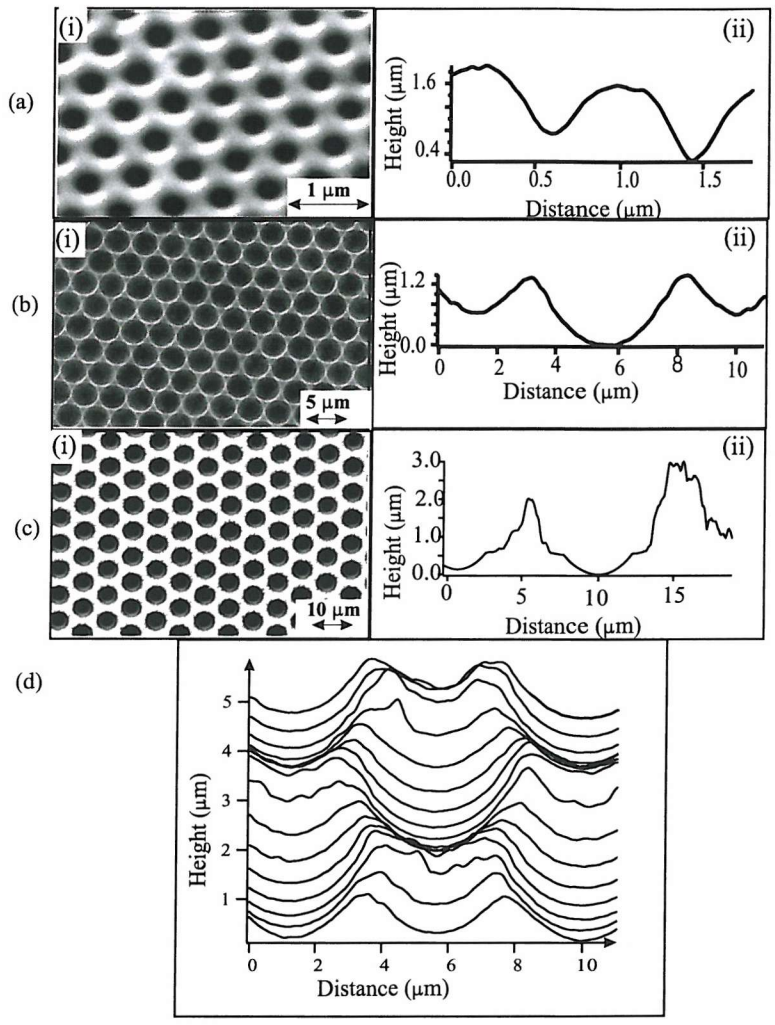

Figure 4.10: (i)SEMs and (ii) AFMs along the void diameter of (a) Au sample 670nm thick, 900nm diameter spheres; (b)Au sample 2μm thick, 5μ spheres; (c)3μm thick, 10μm spheres.(d) AFM height scans with translation in both directions of a void from Au sample in (b), scans are off-set for clarity.

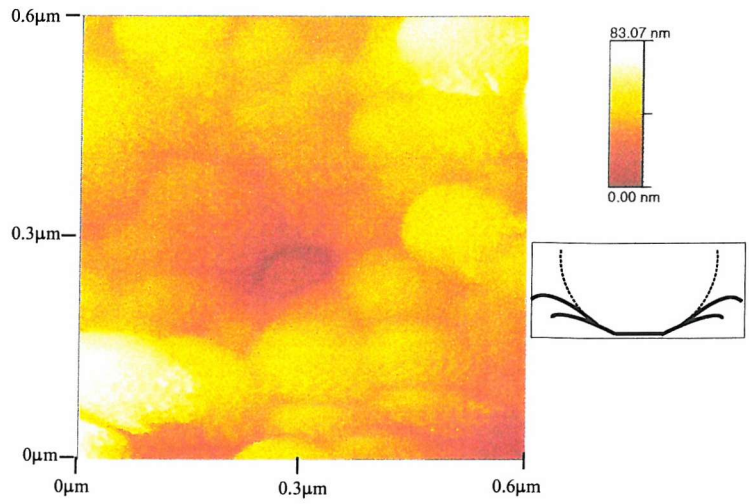

Figure 4.11: High resolution AFM scan of a void formed from 1μm sphere template grown to a thickness of 100nm plus a schematic showing how the gold has grown.

the same relative surface area. Further inspection of the AFM scan also shows that for thin films at least, the growth is not uniform but has an undulating topography. However, it is unlikely that these undulations will affect the optical properties as they are significantly sub-wavelength in comparison with visible radiation, and bigger than the coherence length of electrons within the metals. This AFM also indicates the surface quality of the films, which in general is controlled by the deposition conditions.

4.4 X-ray Analysis

In order to confirm the crystallinity and crystal structure of the walls within the voids, previous studies on these structures used powder X-ray diffraction [137, 138]. Figure 4.12 shows typical X-ray patterns for a Au film 5.8μm thick of a 500nm sphere template and a Pt film of 750nm sphere template. The diffraction patterns show that the characteristic reflections expected for polycrystalline metallic gold and platinum with face-centred cubic structures and a preferred (111) orientation [139]. Using the Scherrer equation [140], the widths of the peaks at half maximum give the grain sizes for gold and platinum as 68 and 8.2nm respectively. The grain sizes are significantly less than the diameters of the template spheres and can be accommodated in the interstitial spaces between the template's latex spheres. Furthermore, they are greater

than the coherence length of electrons within the metals which indicates that their response to electric fields will not be perturbed by the presence of grain boundaries.

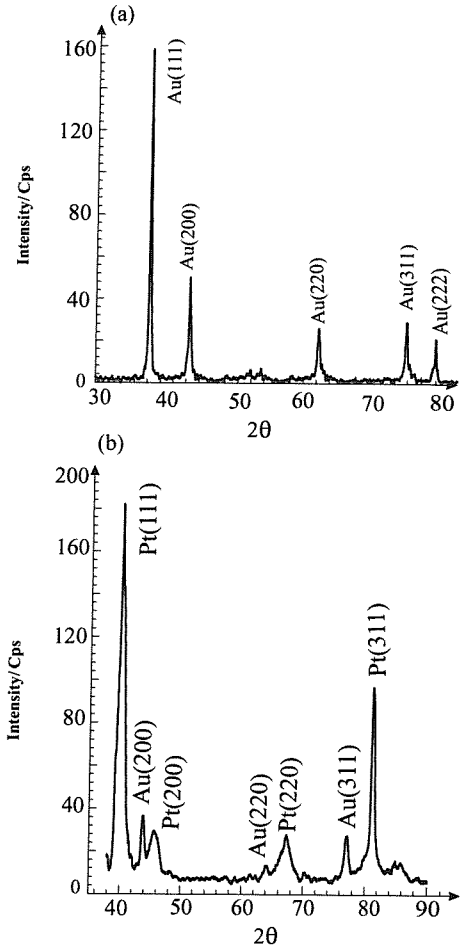

Figure 4.12: (a) Powder X-ray diffraction pattern for a macroporous gold film of 500nm diameter spheres grown 5.8μm thick; (b) typical X-ray powder diffraction pattern for a macroporous Pt film of 750nm sphere template from [137].

4.5 Recent Progress

4.5.1 Contact Angle

Although not directly related to optical properties, the change in contact angle of nanostructured materials is important not only in considering uses, but also in relation to further engineering of these films, such as filling the voids with liquid crystals, for example. The images shown in Fig. 4.13(a)-(b) show the different contact angles (θ) of a water droplet in a saturated atmosphere on different gold surfaces. On plain gold (Fig. 4.13(a)), the value of θ is about 70^o, but on structured gold (Fig. 4.13(b)) the contact angle varies considerably with film thickness and can increase beyond 90^o. The result is surprising; studies on changing the structure of a material show that it should still wet, i.e. the final contact angle is less than 90^o, if the original angle is less than 90^o [142]. A clue to why this happens can be found in Fig. 4.13(b) where the three droplets are placed at three different thickness, and therefore different surface morphologies. The three droplets have been place on a graded gold sample of 750nm diameter sphere template, with film thickness increasing left to right, from below radius height to radius height. Initially, for thin film thicknesses the contact angle is very similar to that of plain gold. As the film thickness approaches radius height, the contact angle changes dramatically and the droplet does not wet the surface, implying that water does not fill the voids.

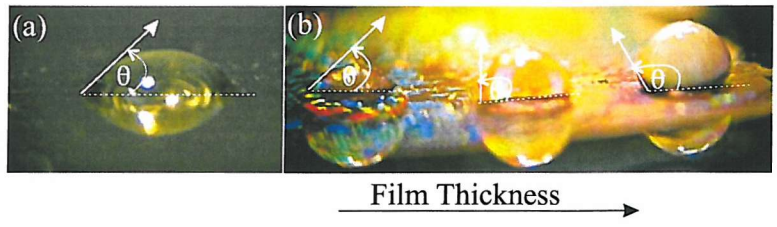

Figure 4.13: Water droplets on (a) a plain gold sample with original contact angle θ, (b) a structured gold sample of a 750nm diameter sphere placed at different film thicknesses (θ).

An explanation of the reason behind this phenomena can be found from considering the surface energy and surface tension of the water droplet (Fig. 4.14). The contact angle for a liquid on a surface is considered as the balance point between the horizontally resolved forces of the surface tension and surface energy of the solid/liquid

(γ_{SL}) and solid vapour (γ_{SV}) energies [143]. The balance of these forces gives Young's equation:

$$T\cos(\theta) = \gamma_{SV} - \gamma_{SL} \tag{4.2}$$

Through considering the energy needed to advance the liquid across the surface, and the fraction of the solid surface in contact with the liquid, the energy difference between the non-wetting and wetting scenario for a structured material is given by:

$$dF = -f(\gamma_{SV} - \gamma_{SL})dx + (1-f)Tdx + Tdx\cos(\theta^*) \tag{4.3}$$

where θ^* is the new contact angle. The first term is the energy gained from covering part of the surface, the second, the energy used in supporting the part of the bubble unsupported by the surface, and the third represents the energy needed to move the bubble front against the surface tension. Using eqn. 4.2 with the above yields;

$$dF = Tdx(1 - f - f\cos(\theta) + \cos(\theta^*)) \tag{4.4}$$

where dF is the energy change per unit length. Equating the change in force to zero gives:

$$\cos(\theta*) = f(1 + \cos(\theta) - 1) \tag{4.5}$$

For close-packed voids for a normalised thickness of 1 at 1 sphere thickness, the fractional coverage is given by

$$1 - f = \frac{\pi}{2\sqrt{3}}[1 - (1-2t)^2] \tag{4.6}$$

The fractional coverage of a non-wetting water droplet for a film grown through spherical voids for a film can be plotted against thickness, t, varying between 0 and 1 sphere height (Fig. 4.15(a)). Relating the fractional coverage to the contact angle through eqn. 4.5 yields the change in contact angle for different film thicknesses (Fig. 4.15(b)). This equation yields a maximum contact angle of 151^o, obtained when the film is grown to a thickness of 1/2 sphere diameter.

However, to understand the system better, the case of the droplet wetting the surface of the voids must also be considered. In this case the change in energy/unit

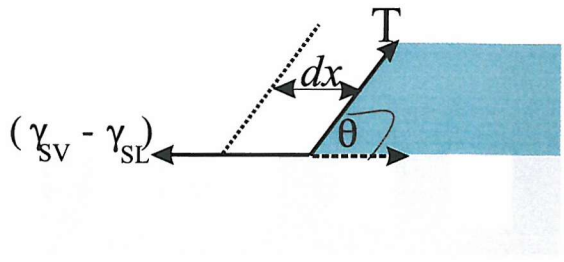

Figure 4.14: Schematic of a nanostructured surface supporting a non-wettting water droplet with the forces of the surface tension and the surface energies (γ_{SL}), (γ_{SV}) shown. The equilibrium position is evaluated if the droplet front expands by a small length dx.

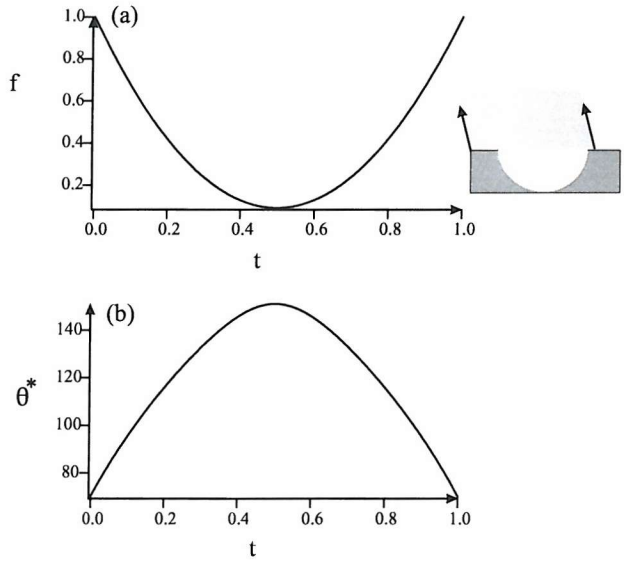

Figure 4.15: (a) Relationship of fractional coverage of a non-wetting water droplet on a surface patterned by voids, as shown by the schematic for a macroporous film grown from 0 thickness to one sphere height ($t = 1$). (b) Relationship between fractional coverage and contact angle for a macroporous structure with thickness increasing to 1 sphere height.

length is

$$dF = -r(\gamma_{SV} - \gamma_{SL})dx + Tdx\cos(\theta^*) = Tdx(-r\cos(\theta) + \cos(\theta^*)) \quad (4.7)$$

where r is a term that measures the greater increase in area of the curved surface compared with the area of the open aperture. It can be expressed as:

$$r = 2\frac{1-(1-2t)^3}{1-(1-2t)^2} \quad (4.8)$$

Through comparison of the energy terms from equations 4.4 and 4.7 the thermodynamic condition for wetting is given by:

$$r > f + (1-f)/\cos(\theta) \quad (4.9)$$

This is always true for a surface which was initially hydrophilic, implying that a nanostructured gold surface will never wet. Therefore, our task is to suggest why the voids do not wet and show behaviour similar to that implied by eqn. 4.5. One reason, perhaps, why the voids don't wet can be illustrated if we consider how water enters the voids. Locally, a water droplet should have a contact angle which matches the bulk surface, in order to keep equilibrium (Fig. 4.14). If the void lip is shallow it would be expected that the new contact angle would be given by $\theta^* \sim \theta - \phi$ (Fig. 4.16(a)). However, when ϕ increases beyond θ it is not possible for the droplet to move smoothly around the void edge, creating an energy barrier (Fig. 4.16(b)). This energy barrier comes from the strain energy of the bent bubble and is able to prevent the water from wetting the void, even though thermodynamically, it is feasible to do so.

This result is of fundamental importance to making macroporous metals because it shows that current models on contact angle for sub-micron structures are wrong. The very nature of manufacture of these films; using a liquid to dissolve the latex spheres after deposition of the metal, makes optical measurements very susceptible to surface makeup as the ability to remove all the latex material is of critical importance if understanding of their optical response is to be gained. As mentioned previously in this chapter, toluene was found to be ineffective at removing all the latex material, which in part was probably due to the transformation of the film from wetting to non-wetting with increase in film thickness.

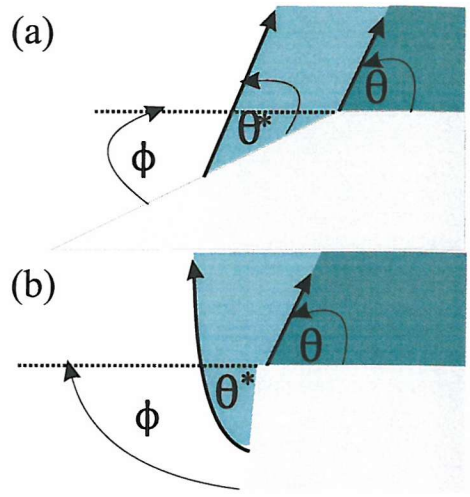

Figure 4.16: Schematics of how water can get into a void whose morphology changes with thickness. (a) Case for lip angle, ϕ, less than contact angle, and (b) lip angle greater than the contact angle.

4.5.2 Separated Cavities

Well-ordered metal casts have also been used as pre-patterned templates with which latex spheres were allowed to self-assemble onto. As with a planar sample, the metal surface is coated with cysteamine and clamped to a clean uncoated glass plate with a parafilm spacer. The space between the two substrates was filled with the aqueous suspension of polystyrene latex spheres. The filled cell was held tilted at 60°, with the patterned substrate on the lower side, in an incubator in order to control the rate of evaporation from the cell. The meniscus formed between the spheres and the substrate and the solution between the spheres produced substantial forces that directed the spheres to fill the pores of the patterned substrate. The structured arrangement of the assembled spheres on top of the patterned substrate was controlled by the ratio between the center-to-center distances for the pores and the size of the assembled spheres. Simply by varying these ratios it is possible to obtain different structures.

Spheres of the same diameter as the initial template assembled in a close packed hexagonal arrangement on top of the substrate pores (Fig. 4.17(a)). The spheres were in physical contact with each other because their periodicity matched that of the substrate. In contrast, spheres with diameters larger (Fig. 4.17(b)) or smaller (Fig. 4.17(c))than the substrate periodicity, have very different template arrangements.

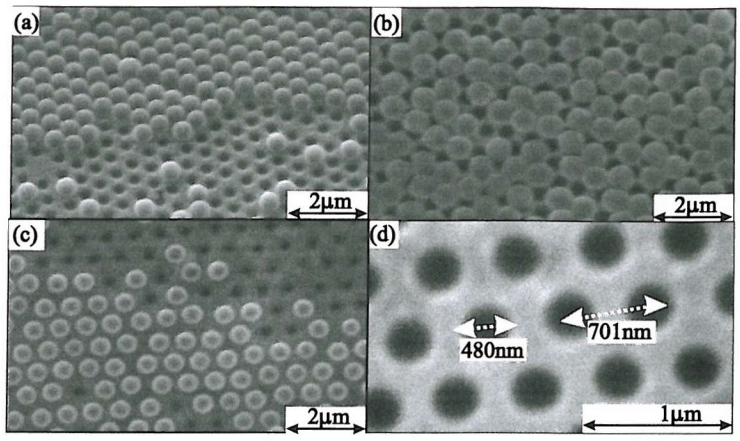

Figure 4.17: Assembly of polystyrene spheres on a patterned film of electrodeposited Au through a template of 700nm latex spheres. (a) Polystyrene spheres of 700nm diameter assembled on a substrate of 500nm pore diameter. (b) Polystyrene spheres of 900nm diameter assembled on a substrate of 690nm pore diameter (c) Polystyrene spheres of 500nm diameter assembled on a substrate of 400nm pore diameter. (d) Gold film prepared by electrodeposition through template shown in (c).

Spheres larger than the template do not show ordering, and instead aggregate in localised clusters. Spheres smaller than the periodicity of the substrate are well-ordered but do not touch each other, indicating a technique to produce cavities with independently controllable periodicity. Subsequent electrochemical deposition around the template in Fig. 4.17(c) produced isolated metallic voids of pore mouth 480nm and periodicity 701nm (Fig. 4.17(d)).

Chapter 5

Optical Measurements

This chapter describes the various experiments used to study the optical response of macroporous metals in the wavelength range $400 - 900$nm using coherent and incoherent broadband white light sources. Initial samples showed structural changes over very small length scales ($< 50\mu$m), which required a tightly focussed achromatic spot, implying the need to use a coherent light source. The setup used was developed from one used to study the properties of visible broadband photonic crystals [144]. Although useful, its inflexibility in changing the angle of incidence suggested a more convenient set-up was needed. Several designs based upon a femtosecond goniometer apparatus developed to study semiconductor microcavity dynamics evolved [145]. Investigations also centred on developing coherent broadband measurements using the nonlinear properties of holey fibres [159]. The purchase and development of a white light spectroscopy reflection microscope allowed samples to be simultaneously viewed and spectra taken of a small section of the image area. Thus, incoherent spectroscopy was then also available albeit at a small range of angles ($\sim 6^o$) around normal incidence. The subsequent improvement in the quality of the films, both in terms of template ordering and control over film thickness, allowed the use of an incoherent source at angles of incidence between $20^o - 60^o$.

This chapter is divided into two main sections, classifying experiments as to whether a coherent or incoherent light source was used. The main reason for using coherent light was due to the much smaller achievable focussed spot size with laser light, rather than any actual differences between the different light sources. The section on coherent sources first describes the initial experimental set-up which

provided data for our first two publications on macroporous metals. It then details the approach to find a more convenient way of studying the effect of angle of incidence. A third subsection describes white light generation in microstructured fibres and attempts to improve broadband spectroscopy. The use of these fibres in exploratory time-resolved pump-probe experiments is then discussed. The second section details the use of white light microscopy to understand the structures. Finally, an incoherent method to study angle dependent behaviour is described.

5.1 Coherent Broadband Spectroscopy

5.1.1 Optical Measurements using an Optical Parametric Amplifier

This section describes the experimental approach at the beginning of the collaboration and provided the data for the first two publications [146, 147].

Laser System

The phenomenon of spectral broadening of a strongly focused ultrashort high power pulse has been well-known and studied in many different materials since the 1970's [148] [149]. The Coherent laser (Fig. 5.1) system exploits the nonlinearity of a BBO crystal to generate ultra-broadband white light and consists of

· A 22 Watt Argon Ion Laser

· A titanium:sapphire modelocked laser (1)

· A titanium:sapphire regenerative amplifier laser (2)

· An optical parametric amplifier (OPA)

Each one of these lasers have been extensively studied and developed both commercially and academically and therefore each component is only discussed briefly.

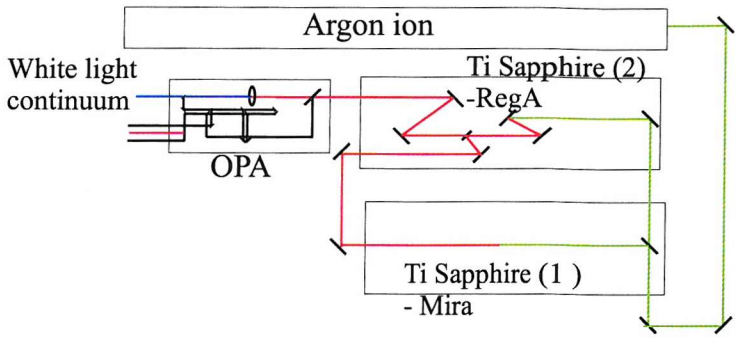

Figure 5.1: Setup of the four lasers

Ar Pumped Titanium:Sapphire (Ti:Al_2O_3) Mode Locked Laser The Titanium sapphire laser is an optically pumped laser source which has gained widespread usage due its wide tuning range (720nm to 990nm)and the ability to work in both continuous wave (cw) mode and in pulsed mode (modelocked). The instantaneous power of the pulse in the Ti:Sapphire is high enough to change the refractive index of the crystal, known as the Kerr Effect, creating a lensing effect. Since the cw component of the beam doesn't experience nonlinear effects, it can be separated from the pulsed component. The maximum output is 0.5Watt, the pulse length is typically 130fs, and a repetition rate of 76MHz which is steered to the regenerative amplifier.

Titanium:Sapphire Regenerative Amplifier The regenerative amplifier increases the peak power of individual pulses through reduction of the repetition rate from 76MHz to 250KHz. It has two input beams; the output from the first Ti:Sapphire laser and the remaining cw pump power from the Ar Ion which pumps another Ti:Sapphire. A TeO_2 acousto-optic cavity dumper injects a single pulse from the Mira into the regenerative cavity. The pulse is expanded in time to 30ps by a TeO_2 Q-switch and amplified over $20 - 30$ round trips of the cavity. The cavity dumper extracts a single pulse. The pulse is compressed through a system which passes it 4 times off a gold-coated holographic grating at near Littrow angle (the diffracted beam returns along the incident path). A 200fs pulse is extracted with an efficiency of about 50%. The output of the system is therefore a μJ pulse with a repetition rate

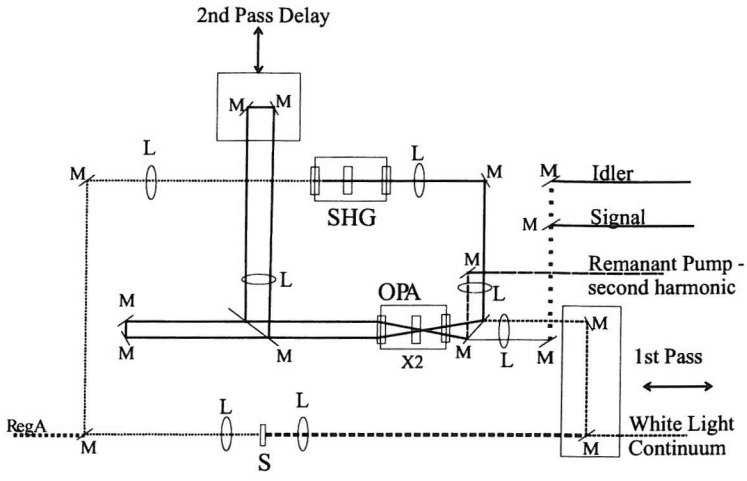

Figure 5.2: OPA schematic
SHG: Second Harmonic Crystal
OPA: OPA Crystal
S: Sapphire crystal

of 250kHz and is used as the input to the Optical Parametric Amplifier.

Optical Parametric Amplifier

The optical parametric amplifier (OPA) simultaneously produces four separate outputs:

· White light continuum

· Signal: femtosecond pulse tunable from 450 to 700nm

· Idler: tunable from 940nm to 2400nm

· Remanant pump at 400nm

The output beam from the Regenerative amplifier enters the OPA and is split with 25% going to the white light generation crystal and the rest going to the second harmonic generation optics (Fig. 5.2).

The pulse hitting the sapphire crystal experiences Kerr lensing and collapses in size to of the order its wavelength. This effect is balanced by strong diffractive behaviour associated with the collapse in beam size. The associated order of magnitude increase in power produces Self-Phase Modulation (SPM); this is the temporal analogue of the spatial collapse of the beam through a rapidly varying refractive index. This produces dramatic shifts in energy, generating wavelengths from the UV to the IR. The leading

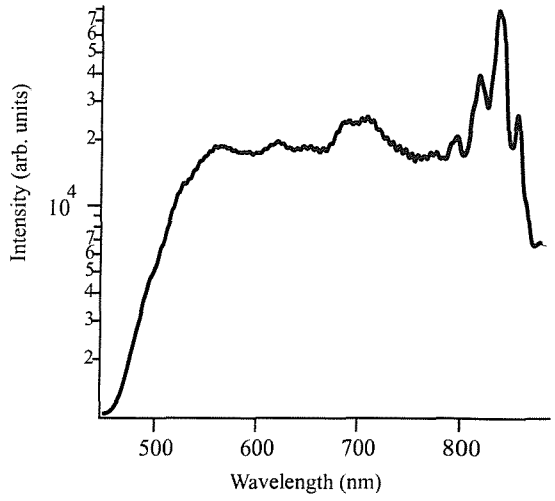

Figure 5.3: Output spectrum from OPA; the region 750 – 1000 was sampled with an integration time 20× shorter than for the rest of the spectrum.

edge of the pulse generates wavelengths in the IR whereas the trailing edge, which sees a higher refractive index, generates UV light. The process is not symmetric about the central pump wavelength; the time response of the Kerr effect means that the leading edge sees less of an effect than the trailing edge and so favours conversion to shorter wavelengths (Fig. 5.3). The pulse's spectrum has two main features, with most of the light converted to wavelengths within 50nm of the pump, as well as a broader continuum with a more gradual drop-off. The beam is observed to be uniformly white, indicating a constant divergence angle. The beam is collected by an achromat lens and then split into an output beam and an input into the second harmonic generation area of the OPA.

Most of the RegA's pump pulse is channelled to second harmonic generation using a Type I BBO crystal placed away from the beam's focus to produce frequency doubling. The pump is mixed with one of the wavelengths from the white light generation, the signal, to produce another beam, the idler. The optimum condition for this process depends on temporal and phase matching the pump and the signal by altering their path lengths and rotating the BBO crystal respectively. The pulses are reflected back along two arms to increase the efficiency of this process.

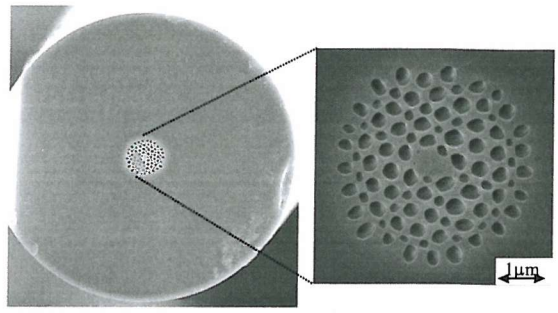

Figure 5.4: SEM of small core of holey fibre, courtesy of J. C. Baggett, ORC, Southampton

Reflectivity Measurements

The white light continuum from the OPA was focussed into a holey fibre constructed of a series of hollow tubes running down its length with a core size much smaller than standard fibres (Fig. 5.4). Fibres such as these have been shown to be single mode across a wide wavelength range [151]. The two main advantages of including the fibre in the set up was that the core produced a much smaller spot size and a more spatially stable beam. Spatial stability was important as the path length from OPA to the sample was around 10m, so small fluctuations in the laser beams at the source could produce significant deviations in the beam position. As the domain sizes of the samples were very small, beam stability was critical. Polarisation optics consisting of a polariser cube and a half wave plate were placed after the fibre to test the response to both TE and TM polarisations. A normal incidence beam splitter was used to split the beam into a reference and a signal beam.

The signal beam was tightly focussed onto the sample using a long working distance microscope objective, ($\times$16 magnification) with numerical aperture (N.A.) = 0.3, giving a spot size of 10μm. The objective was attached to a linear translation stage which allowed light to be accurately focussed on the sample. The sample was mounted on a series of stages to allow 2 dimensional linear translation (x and y), rotation of the angle of incidence (θ), and in the plane of incidence (ϕ)(Fig. 5.5(a)). The reflected beam was collected by a 5mm focal length, 25 mm diameter achromatic lens and then steered into the spectrometer parallel to, but off-set vertically from the reference beam. The two beams entered the spectrometer, resolution 0.1nm, and

were projected onto a 2 dimensional nitrogen cooled single photon resolution CCD array (Fig. 5.5(b)). This arrangement allowed spectra to be sampled rapidly at high resolution across a broad spectral range.

Measuring the spectral content of both beams simultaneously avoided the problem of temporal fluctuations in the spectral content of the white light continuum. In order to avoid problems associated with interference between the two beams an image of the two lines on the CCD was checked to see whether the two beams were spaced far enough apart on the detector (Fig. 5.5). Having found the vertical positions of the centres of each beam it was possible to define two areas on the chip where the spectra were to be found. Readings from the CCD array were only counted if they were found in these two areas, cutting down on the amount of information collected and avoiding interference at the edges of the two beams. Spectra were then analysed as a ratio between the reflected and the reference beam. To obtain as high a signal to noise ratio as possible across the desired wavelength range, the spectra were taken in two sections ($400 - 750$nm and $750 - 1000$nm) to account for the very high intensity of the wavelengths around the seed wavelength from the regenerative amplifier.

5.1.2 Initial Experiments on Angle of Incidence Dependence

Despite the sophistication of the above experiment, it had two drawbacks; the angle of incidence could not be changed easily and there was no convenient way to attempt angular time-resolved spectroscopy. Therefore, as part of a wider plan to develop broadband angular measurements, a goniometer, designed with a collaborator working on the Photonic BandGap materials project, Luca Plattner, was used as the basis for a femtosecond goniometer, modelled on the strategy pursued by research in semiconductor microcavities [145]. The goniometer (Fig. 5.6(a)), allowed two femtosecond pulses (the pump and white light continuum probe) to come in at varying angles of incidence without changing the time delay between them. The two beams were sent to mirrors mounted on different arms of the goniometer via mirrors mounted directly above the centre of rotation of the sample. The WLC beam is then split in two, one reference and one incident beam. The sample was mounted on a rotating stage,

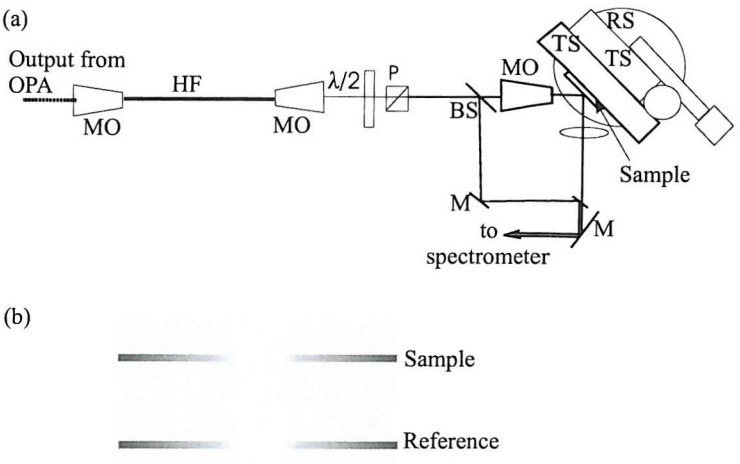

Figure 5.5: Initial experimental set-up using holey fibre to collimate beam, (b) Schematic of a typical image of the spectrometer's 2D CCD array with the sample and reference beams vertically displaced from one another.

P: Polariser Cube	$\lambda/2$: Half Waveplate
HF: Holey Fibre	TS: Translation Stage
RS: Rotating Stage	MO: Microscope Objective
BS: Beam Splitter	CR: Centre of Rotation

allowing the collection path to be fixed. Two translation stages mounted in the x-y plane position the sample in the centre of rotation of the goniometer and two more translation stages placed in the z-y plane scan the beam across the sample (Fig. 5.6(b)). The reference and reflected beam off the sample were then sent as vertically parallel beams into the spectrometer as described above.

Although some angular resolved measurements were made on this rig, there were several drawbacks to using the rig in this form. First, the WLC travelled many metres before hitting the sample, so spatial dispersion of the continuum became problematic. Also, ideally the angle of incidence of the WLC could be changed more conveniently if a fibre delivery design were to be implemented. Again, the spatial dispersion of the WLC provided a stumbling block and, coupled with competition for laser time, it became clear that another strategy was required to progress the research. Rather fortuitously, advances in fibre technology provided another method of supercontinuum generation.

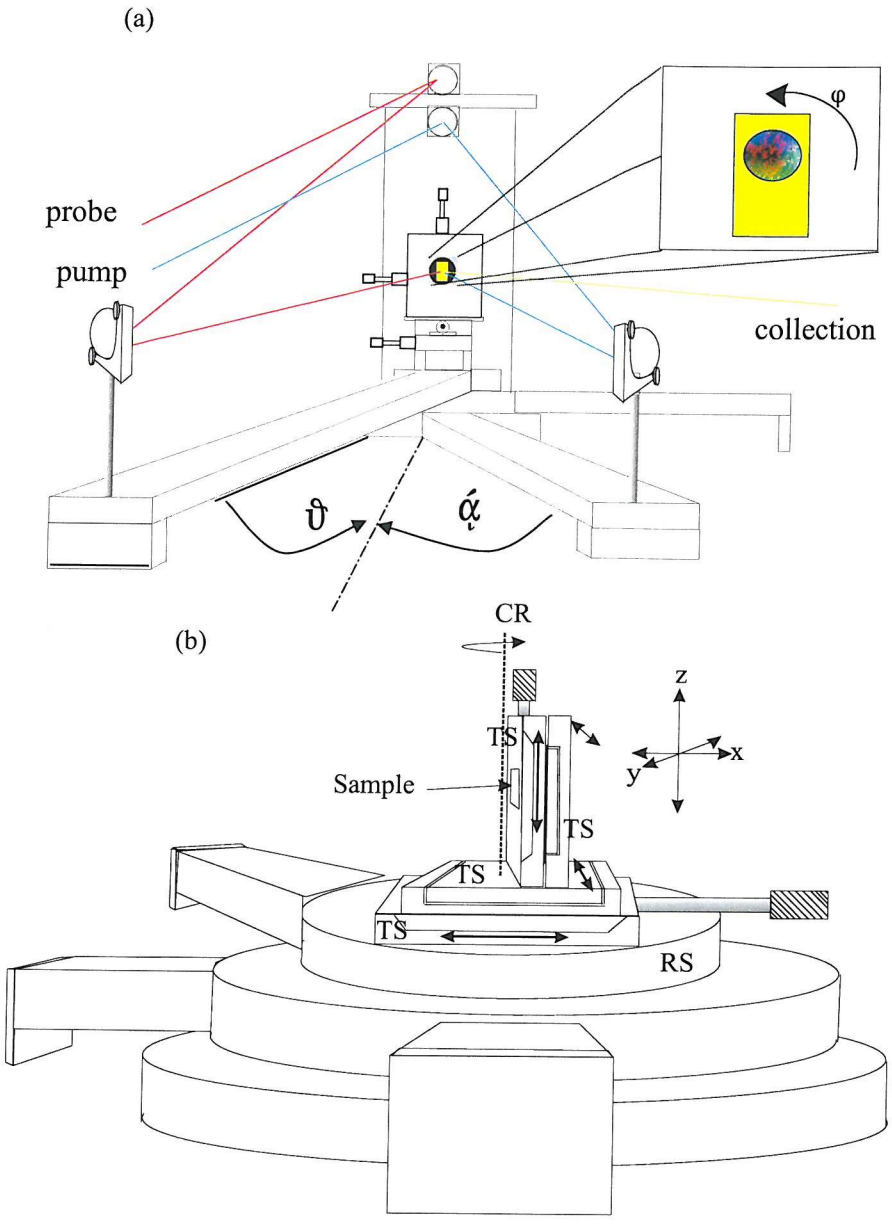

Figure 5.6: (a) Femtosecond Goniometer (b) Placing the sample in the centre of rotation (CR) using two translation stages (TS) mounted in the x-y plane which position the face of the sample (mounted on translation stages in the z-y plane).

5.1.3 White Light Generation through Holey Fibres

This thesis spans a period when there has been intense, worldwide interest in strategies to confine light in small dimensions. One avenue of research has been the development of photonic crystal fibres (PCF)[150, 151]; these strongly confine electric fields using an ordered array of holes running the length of the fibre to produce a photonic bandgap. Work at Southampton's Optoelectronics Research Centre (ORC) also showed that a roughly hexagonal array of holes in a fibre, known as a holey fibre (HF) (Fig. 5.4), produce many of the phenomena found in photonic crystal fibres [161, 162, 163]. One of the difficulties in describing a rapidly evolving area of research is the array of confusing and sometimes rather contradictory terms used to describe similar discoveries. The field of microstructured fibres is no exception, especially in the naming of fibres. Rather confusingly, photonic crystal fibre is applied to both light guidance using photonic band gaps, as well as guidance due to roughly periodic morphological microstructuring of the fibre cladding. In an attempt to avoid too much confusion, the second type of fibres will be referred to as Holey Fibres (HF), the term adapted by the ORC. Considerable effort has been made to make the fibres robust enough for use in experiments and the experiments described here were made possible by the expertise and generosity of the ORC.

Conventional fibres waveguide through total internal reflection inside a core with the necessary refractive index contrast between the core and the cladding. In contrast, HF waveguide because the presence of hollow cylinders running parallel to the core (Fig. 5.4) lower the effective refractive index of the surrounding silica in comparison with the defect free core. These fibres have many features which conventional fibres do not, and are controlled through the size of the core relative to the size of the air holes and the bridging silica between holes. Microstructured fibres with a small core and large air fraction cladding, as in the figure above, have a greatly reduced mode area in comparison with standard fibres (typically 30-50 times smaller). Decreasing the mode area produces many new interesting characteristics in the fibre by increasing its nonlinear response such as single mode operation over a wide wavelength range and unique group velocity dispersion properties (GVD) [152]. The GVD properties

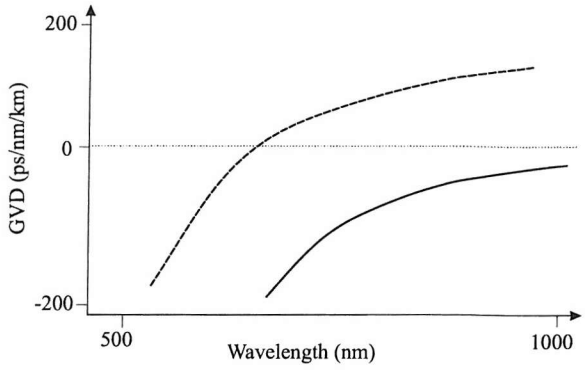

Figure 5.7: Dispersion of a holey fibre (dashed line) and a conventional silica fibre (full line).

are of particular interest because of their role in linear optics such as dispersion compensation [153] and, more importantly, nonlinear effects like continuum generation [154]. The GVD characteristics are derived from the very strong waveguide dispersion, producing anomalous dispersion at wavelengths where silica and conventional single mode fibres have normal dispersion. By engineering fibres in this way it is possible to shift the zero dispersion wavelength into the visible wavelength regime (Fig. 5.7). Single mode operation across a wide spectrum is made possible because shorter wavelengths are more tightly confined by the structure than longer ones, so keeping the conditions necessary for single mode operation.

Various research groups have shown that for ultrashort high peak power pulses at the zero dispersion wavelength produce ultra broadband white light supercontinuua. The WLC has been found to be coherent in both phase and space and of brightness at least five orders of magnitude greater than an ordinary light bulb [155]. The discovery of white light generation in microstructured fibres produced many competing theories of the mechanism behind this phenomenon and a definitive answer has yet to be reached . Competing theories have suggested Self Phase modulation (SPM) with evidence of an absence of Stimulated Raman Scattering (SRS)[154], whereas others claim SRS with Parametric Scattering is responsible [156], [158]. Yet another suggests a combination of SPM and SRS [157], with a final version suggesting soliton generation and soliton self frequency shifts[159]. Despite the differences of opinion

and in experimental methods, all agree that the important factor in generation of supercontinua is to pump the fibre at the wavelength at which there is zero dispersion.

As a technology, HF's therefore offer many advantages over free space alternatives in WLC generation for spectroscopic studies, notably a lower power threshold, a supposedly greater stability to variations in the input power and an inherently small output spot size. Fibres produced by the ORC had zero GVD positions in the near infra red (about 800nm), and were found to be convenient for spectroscopy. The lower threshold power meant that the high power of the OPA was not needed and the far lower power from the residual output from the Regenerative Amplfier, measured to be a maximum of 10mW, could be used to generate WLC. The use of an unused output greatly simplified laser usage in a very busy lab schedule. Whereas the HF used in previous experiments to guide light from the OPA was extremely brittle, later versions proved to be as flexible as conventional fibres and so useful for angular measurements. The efficiency of generation and throughput was found to be very dependent upon the lens used to couple light into the structure. The optimum was found to be a $\times 40, N.A. = 0.65$ microscope objective. An optimal coupling efficiency of $\sim 25\%$ of the incident power was measured using a bolometer, to account for all the wavelengths generated by the fibre. The fibre was integrated into the goniometer setup with a platform was made to accommodate the fibre, incorporating beam splitting with output coupling along the axis of one of the goniometer arms (Fig. 5.8).

Despite the benefits of the new system, the complexities of the continuum generation process in HF hindered experiments, not least because the spectral output was highly sensitive to small changes in the input coupling conditions [163]. The condition of the front facet was particularly important as the site of continuum generation. A related problem was the fibres' tendendency to degrade over time, as the high peak powers focussed onto it were capable of damaging it. Secondly, any sudden vibrations near the fibre input altered the alignment, immediately damaging it. The condition of the front facet is perhaps more important in a HF than in a standard fibre. Although, in both cases it is responsible for determining the coupling efficiency, in a HF the continuum generation process adds to its importance. Furthermore, HFs have many higher order propagation modes which are also capable of generating contiuua,

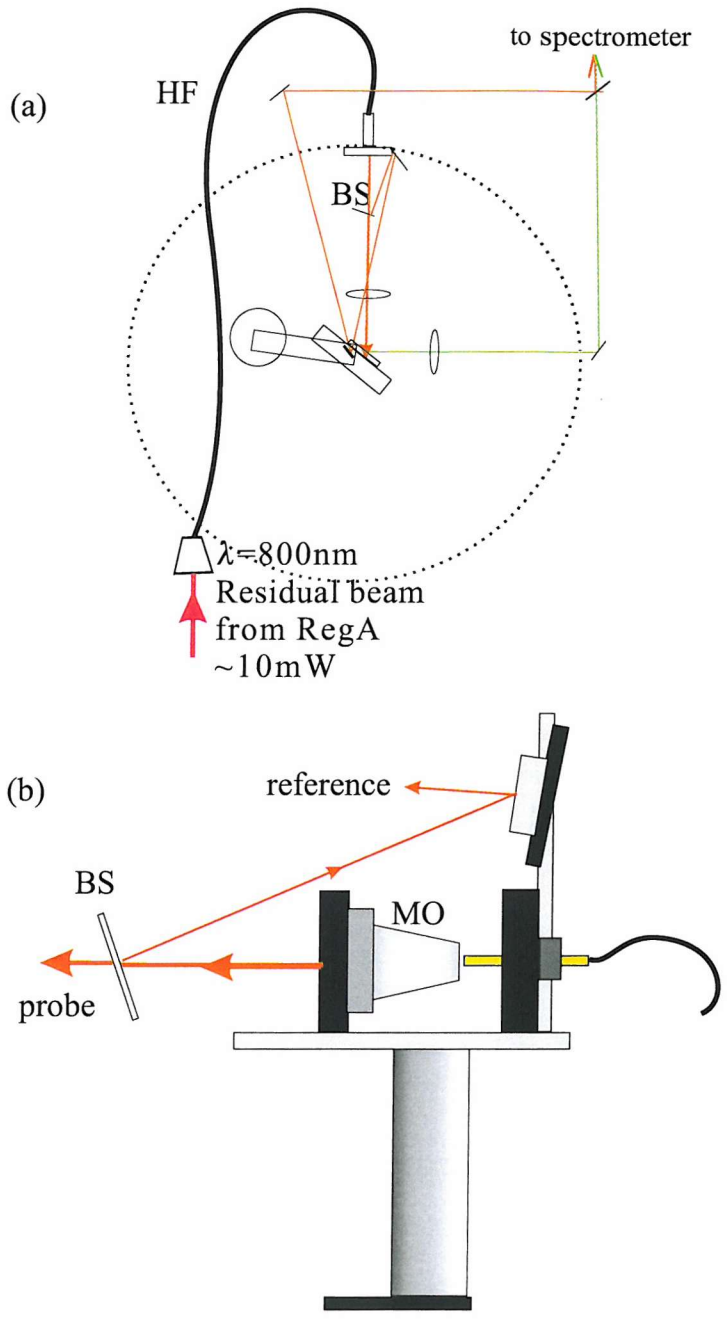

Figure 5.8: (a) Schematic of broadband spectroscopy experiment with varying angles of incidence using a holey fibre (HF)to generate WLC; a beam splitter (BS) divides the WLC into 90% probe and 10% reference beams. (b) A fibre output rig incorporating a microscope objective (MO) and beam splitter(BS)

but have radically different spectral contents. Damage in the front facet was found to prevent coupling to the primary mode, but increased the efficiency of UV generation. Recleaving the fibre recovered the primary mode. In attempting to understand the output of the fibres it was found that the fibre had many different output modes each with their own different spectral output and far-field spatial pattern. Some of these modes were also found to propagate through the cladding as well as the core and so dependent upon the length of the fibre, with modes in the fibre walls suffering the greatest leakage.

A further complication of HFs is their loss characteristics which are complicated by the electric field penetration into the cladding due to the absence of a refractive index contrast. Standard fibres are considered to have bend/loss characteristics primarily based on light leakage due to the increased phase velocity associated with a bend which is limited by the local speed of light (c/n); i.e. their bend/loss characteristic increases with wavelength [160]. Microstructured fibres, as well as having the above characteristic, also have a short wavelength component of loss, especially in large area core fibres [151, 161]. Shorter wavelengths experience a lower numerical aperture as the mode is more tightly confined to the core and therefore see less modulation in the effective refractive index, hence less bending is needed to allow leakage. In the case here, although the fibre inevitably suffers bending in laboratory conditions, the fibre used has a very small core, tightly confining the modes so that bending loss will not feature too much. The main source of loss therefore comes from confinement loss, which is a function of the number of rings of holes and the size of the holes themselves [164] [165]. In essence the mode is confined better with more rings and larger holes.

Despite these complications, HFs offer a valid route to make angular resolved measurements. Although the measured spectrum was extremely broad, being measured well into the infra-red, it was highly structured towards the blue end of the visible spectrum (Fig. 5.9); a change of a few orders of magnitude in intensity was observed over a relatively short wavelength range. The structuring of the fibre output was especially problematic in the study of gold structures which showed a sudden drop in reflectivity around 500nm. In order to avoid erroneous measurements it was necessary to take several sets of data across the wavelength range in question, which

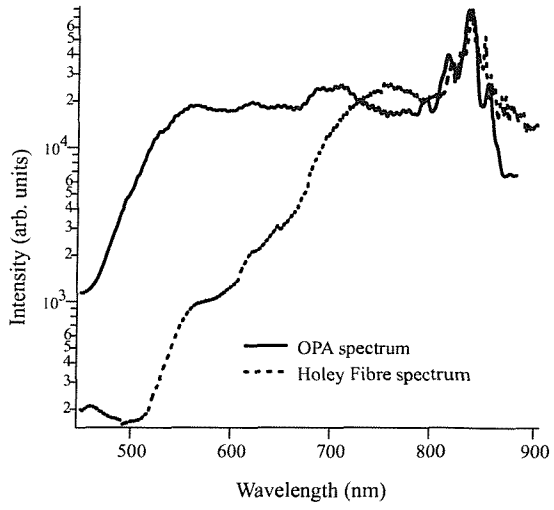

Figure 5.9: Comparison of continuum generated by commercial OPA system and by a Holey Fibre, as was the case with Fig. 5.3, the spectra are taken in sections to account for the many orders of magnitude greater intensity at wavelengths around the pump wavelength. The continuum generated by the HF is far more structured and had to be taken in four sections, hence the small discontinuities in the graph.

was time-consuming and, more importantly, appeared to add artificial features into the measured response of the fibre.

5.1.4 Time-Resolved Measurements with Holey Fibres

Although not the major focus of the thesis, (see appendix B for experimental results on gallium mirrors) the preliminary work into time-resolved measurements did reveal some more features of the continuum generated by HFs. The intention was to use broadband angle-resolved spectroscopy to probe the plasmons dynamics at different angles on the structured metal films. Briefly, the intention was to synchronise in time and space the white light probe and the tunable signal output from the OPA. Using a sample with more than one reflection minima at a point on its surface, the OPA's signal would be tuned to one of the reflection minima and then the second reflection minima's response would be observed with respect to the variance in time delay between the probe and the pulse. Therefore, before starting the experiment it was necessary to study the temporal qualities of the fibre. Although the group's photonic band gap programme [167],had performed experiments on the temporal properties of

the continuum through a HF, it used a short, straight piece of fibre in a transmission experiment using a Kerr gate. Here, the white light probe would be generated in a fibre approximately 1 metre in length and would also be used in testing the response with different angles of incidence. The temporal nature of the spectrum was likely to be very different from the WLC generated by the OPA. The proposed set-up, with the pump pulse being directed onto the sample via the method proposed above, and the WLC pumped by the residual pulse of the Regenerative Amplifier is shown in Fig. 5.10. The two pulses were focussed to the same point on the sample and the reflected pulse was analysed with respect to the reference beam using a monochromator and a two photodiode balance lock-in detection method. The photodiodes were fed to a lock-in amplifier and the pump pulse was mechanically chopped at 777Hz to avoid problems associated with harmonic frequencies.

To first understand the system, a gallium mirror took the place of the structured metal. Research into gallium's dynamic reflectivity changes has been pioneered at the University of Southampton by Professor Zheludev's group, who have shown that its reflectivity can be altered with a high peak power pulse which changes its structural phase. Although the change in reflectivity is stimulated over sub picosecond timescales, the relaxation occurs over microseconds, indicating that the heating process stimulates a change in electronic structure followed by a heating and structural change. The relaxation rate was slower than the repetition rate of the RegA (250kHz) so to see any time dependent change the laser's period between pulses was decreased to 10kHz. The reduction in repetition rate reduced the average power by a factor of 25, although WLC was still possible because the peak intensity also increased. The impact of this change on the HF output was that it was less stable. Recent ,work has shown that noise in HF extends well beyond the frequency range of laser technical noise and in some cases has been found to lead to noise approaching 50% amplitude fluctuations [155]. The origin of this noise has been found to be the nonlinear amplification of quantum fluctuations in the input laser and in the Raman scattering process within the fibre. The noise consists of two components, a low frequency part due to experimental conditions (laser power fluctuation and beam pointing stability) which can be reduced by controlling the parameters more closely and the part due

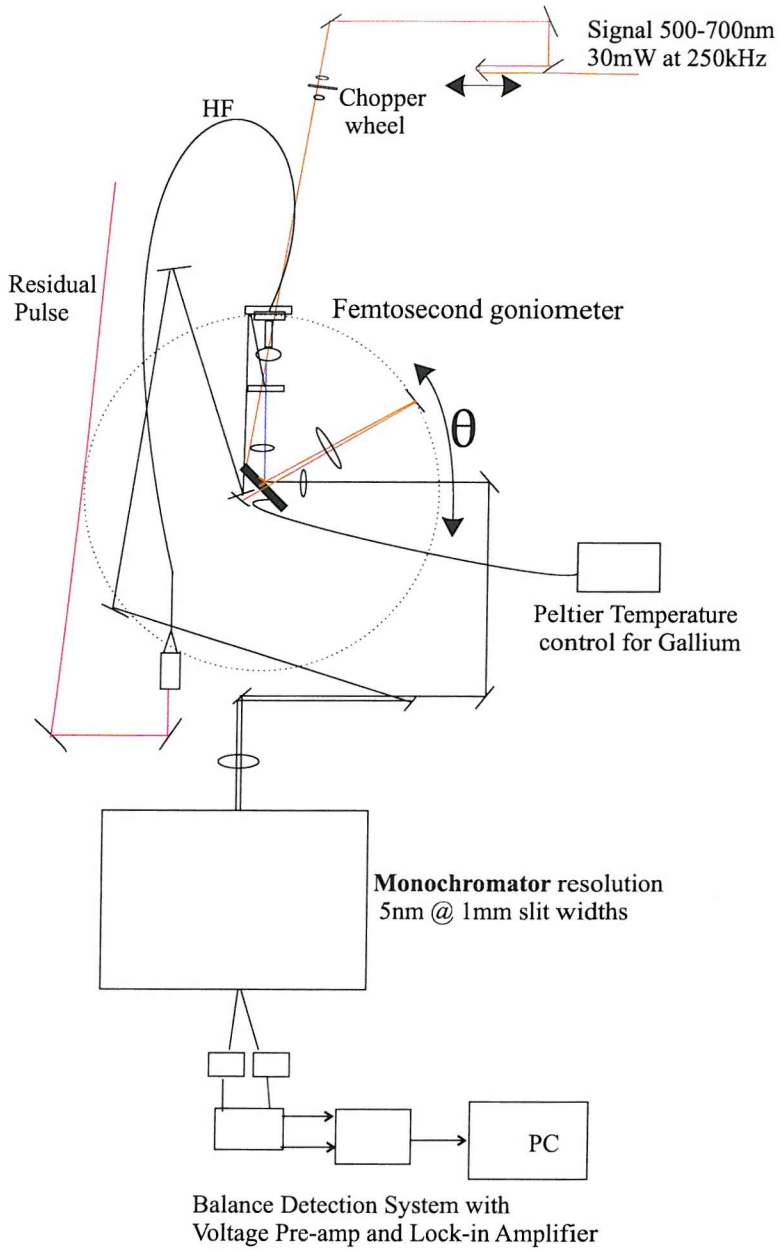

Figure 5.10: Femtosecond Goniometer Setup; θ is tha variable angle of incidence. The pump pulse is focussed tightly on the chopper wheel to ensure a clean on/off pulse.

from the broadband generation. This second component is inherent to the supercontinuum generation process because the origins are quantum noise sources with the only experimental parameter being the input pulse duration which shows a reduction for shorter pulses [155]. Studies have also revealed that the fine spectral structure is extremely sensitive to input beam conditions, which are usually not observed due to averaging over many pulses [166]. However, in time resolved spectroscopy concerning wavelength ranges of 1nm, as was the case here, this effect is very important. Although promising as a future spectroscopic tool, clearly much research needs to be conducted into producing greater stability.

The noise described above was observed in this experiment which, coupled with the low light level, made detection of individual wavelengths extremely difficult, especially at shorter wavelengths.

5.2 Incoherent Broadband Spectroscopy

Incoherent reflectivity methods were first tried in an attempt to see whether there was any difference in a film's response in comparison with coherent radiation. The films appeared to show little dependence on the type of light source allowing incoherent light to be used. Three different set-ups were used for incoherent reflectivity measurements, exploiting the strengths and weaknesses of each to allow different features of the samples to be studied. These included the ability to observe the samples under different magnifications, spectroscopy of small areas, polarisation experiments and angle of incidence dependent measurements.

5.2.1 Optical Microscopy

The purchase of a research standard Olympus BX51 microscope and the subsequent development of a spectroscopy apparatus to probe the illuminated image allowed samples to be tested more quickly and provided a greater insight into the films' responses than had been possible with previous experiments. These experiments were

the most important so far as improving the film quality and developing a theoretical understanding of the structures were concerned. With the ability to image the samples under high magnification, their structure, ordering and surface quality could be observed directly, rather than inferred from their overall diffractive properties. By changing the magnification and range of incident and collected angles the reflective properties were more apparent allowing development of a new theory of their response based on ray optics. The microscope set-up (Fig. 5.11) allowed both reflection and transmission observations. The anatomy of the microscope is discussed followed by the experimental methods.

Anatomy of The Microscope

The continual development of the microscope over many years has produced a device so well designed that, in contrast to other experimental equipment, the user has to know comparatively little about its inner workings to produce good results. In an attempt to limit the amount of material presented here, only the features most pertinent to the experiment will be discussed. The diagram in Fig. 5.11 shows the most important features as far as imaging and spectroscopy are concerned. Most modern microscopes use the Köhler illumination method to produce a uniform intensity distribution across the sample, achieved through the use of conjugate planes, or planes of common focus [168]. There are two sets of planes, one with the tungsten halogen lamp (THL) in focus and the other where the object is in focus. The conjugate planes of the THL (filament path, FP) are:

· The condenser aperture diaphragm (CAD)

· The back focal plane of the objective

· The eyepoint of the eyepiece, the point of the front of the eye during observation.

· At L1

The lens L1 is a 10cm focal length lens used to conjugate the plane for the fibre coupled spectrometer.

The conjugate planes of the image forming path are (image path, IP):

· The Field Diaphragm (FD)

· The focussed sample

· The fixed plane of the fixed diaphragm of the eyepiece

· The retina

· The CCD chip

· The front facet of the fibre optic cable to the spectrometer

Placing two diaphragms in opposite planes allows control over two different properties of the light. The CAD controls the range of angles that illuminate the sample while the numerical aperture of the objective determines the range of collection angles (Fig. 5.12(a)). The field diaphragm determines the size of the area under illumination. In terms of spectroscopic measurements, the CAD is the more important to control because it has the greater effect on the absolute intensity of the illumination and it controls the available illumination angles, critical in the study of angle dependent phenomena such as grating plasmons.

Transmission illumination use the same idea as described for reflection but with the position of the two diaphragms reversed. The condenser mounted just below the sample is used to to determine the range of angles illuminating the sample in transmission.

In reflection mode two different types of illumination were used to look at the sample, Bright field (BF) and Dark Field (DF). BF illumination is simply the reflection off the sample with the range of incident angles set by the condenser aperture. It tests the normal reflective characteristics of the sample, but gives no indication of the degree to which the surface scatters light. To indicate the level of scattering, DF optics are used, which as shown in Fig. 5.12(b), allows only the peripheral light paths through. Both the FD and the CAD are opened fully to allow the large angle rays through. The light then hits a mirror with its centre removed which directs the light onto the sample. The sample is therefore illuminated at oblique angles and the only light collected is that which fits through the central hole in the mirror. In other words only features which scatter light at large angles are observed. This technique is extremely useful for testing the surface quality of a film; smooth films appear dark, whereas rough ones appear bright.

Polarisation properties are analysed using a linear polariser ($1 : 10^3$) placed before,

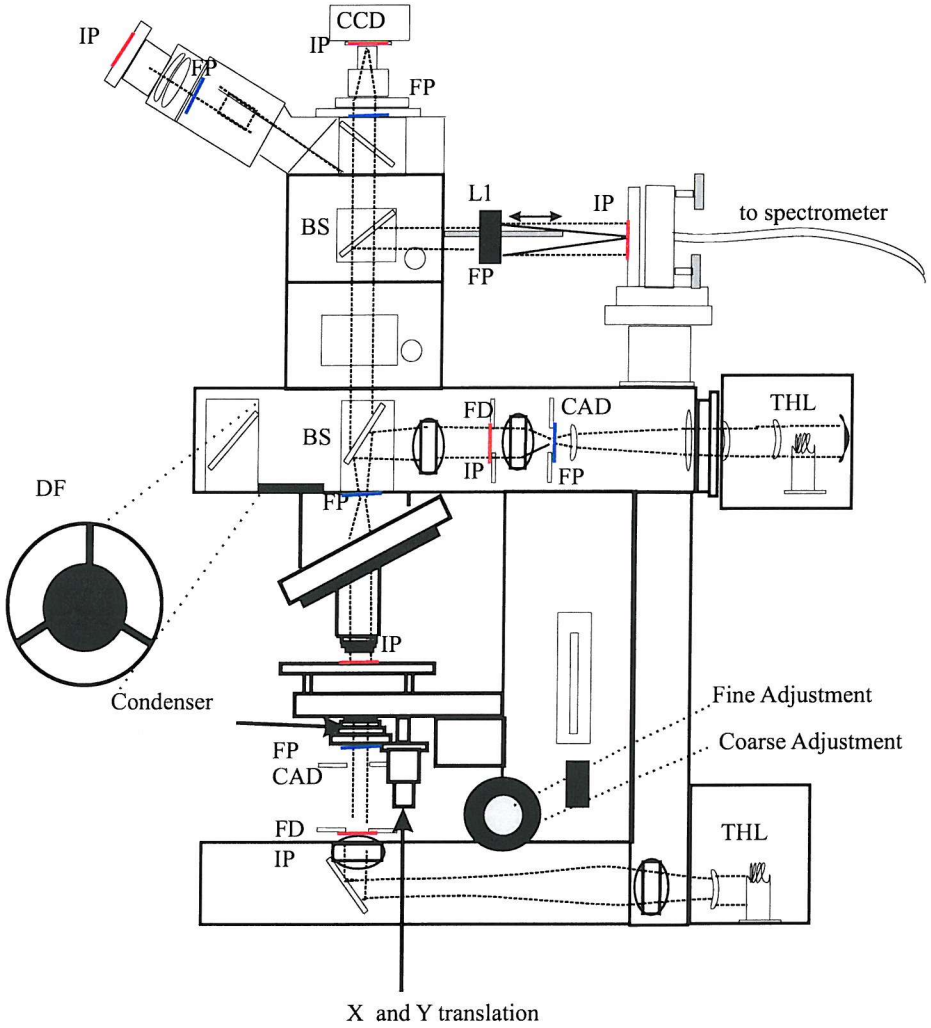

Figure 5.11: Diagram of Microscope
CAD: Condenser Aperture Diaphragm
FD: Field Diaphragm
BS: Beam Spitter
CCD: CCD Camera
THL: Tungsten Halogen Lamp
FP: Filament Path
IP: Image Path
inset - DF: Image of Dark Field Apparatus

and a rotating analyser placed after the sample. To avoid complications associated with stereo imaging of polarised light the analyser is a de Senarmont Compensator, consisting of a linear polariser and quarter wave retardation plate so that the observed light is circularly polarised. Changing the polarisation after the second linear polariser is important in order to avoid complications in observation associated with polarisation dependent reflections.

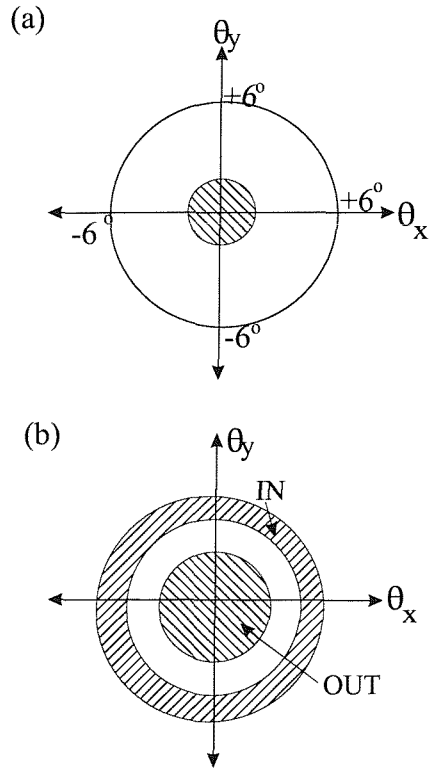

Figure 5.12: (a) The "angular plane" over which the condenser aperture diaphragm (shaded area) can be adjusted, with the calculated range of angles of incidence that are accessible using a ×10 microscope objective. (b) Dark field (DF) illumination set-up showing the large input angles and the collection of only light scattered up the centre of the objective.

The microscope objectives used were

- ×10 N.A. = 0.30, Angle collected: 17.5°
- ×20 N.A. = 0.46, Angle collected: 27.4°
- ×50 N.A. = 0.80, Angle collected: 53.1°
- ×100 N.A. = 0.90, Angle collected: 64.2°

The numerical aperture is defined as the sine of the angle subtended by the most

oblique angle of incidence focussed by the lens and the line through the centre of the lens. Also, another optionally inserted lens after the objective was used to increase the magnification by a factor of two.

Optical Measurements using the Microscope

The sample was placed on a X-Y vernier scale translation stage. The front facet of a fibre was placed at the focal point of the lens, L1, and could be moved accurately into place using XYZ translation stages. The spectrometer, Ocean Optics USB 2000, had a spectral range of $300-1000$ nm and resolution 1 nm, probed the spectral response of a small area of the sample, approximately 50μm in diameter at $\times 10$ magnification. The setup allowed simultaneous observation and spectral analysis of a small area of the sample ($1\mu m^2$ - $100\mu m^2$), with images recorded using a high resolution 3MPixel CCD camera. Spectra from illumination using an incoherent white light were normalised with respect to the reflection off a silver mirror. The position of the point on the image where spectra was taken was found using reverse illumination through the fibre onto the CCD camera and was confirmed using defects on the film's surface. The films' robustness meant that their response did not change over time and a point could easily be revisited to test its spectral response.

The domain size of the crystallites in a template are measured through observation of diffracted wavelengths from wide angle white light illumination (Fig. 5.13). Scanned images taken of the samples allowed their spectral response to be measured at representative points using $\times 10$ magnification. Images of a "stripe" of the film are used as a map to pin-point where these points can be found on the sample (see Figs 8.1, 8.3). Through comparison of each optical image with an SEM image, especially the presence of defects or irregularities in the film, it was possible to correlate changes observed in the reflectivity spectra with change in film thickness.

5.2.2 Angle Measurement

With the improvement in sample quality and the production of step-changes in film thickness, samples were characterised more quickly and accurately. The ability to

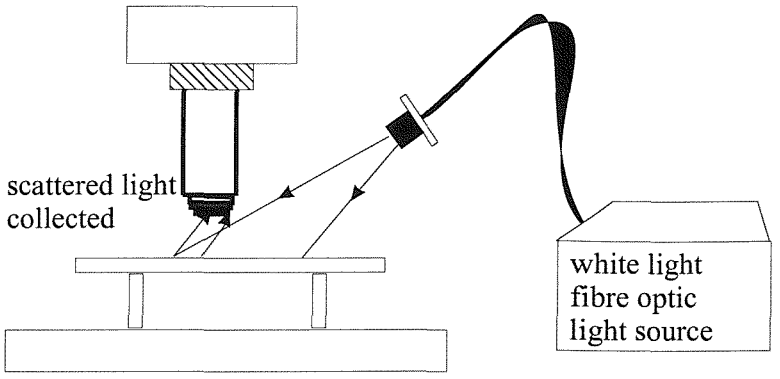

Figure 5.13: Wide angle white light illumination using a fibre optic illuminator.

make a monolayer template also helped to simplify analysis with the absence of a second layer and the associated complications of pore mouth distortion. The ability to make large domains also lessened the need for very small spot sizes and so it was more convenient to use measurements with incoherent white light. The white light source was collimated using a condenser from a microscope and was then focussed onto the sample using a 0.5cm focal length achromatic lens (Fig. 5.14). The sample was placed in a goniometer rig with the incident path fixed. The reflected beam was collected and focussed onto the front face of a fibre-coupled spectrometer (resolution 1nm) mounted on one of the goniometer arms, greatly simplifying the procedure for collecting angular reflection data. The positions of the points on the samples where reflectance measurements taken with the microscopy set-up were measured with respect to the top of the sample allowing the same position to be found using the goniometer setup. An aperture was used to limit the range of angles incident on the sample to $\sim 4^o$.

There were two differences in the illumination between this set up and the microscopy set up. First, as can be seen in Fig. 5.14(b), the light level around 800nm falls rapidly due to the presence of a cold reflector in the fibre illuminator. Secondly, rather than Köhler illumination, the light is focussed into a small spot onto the sample, and also onto the surface of the fibre. As well as complicating the coupling in of light to the fibre, the area of illuminated sample which is analysed is much greater than with the microscope ($\sim 100\mu m^2$ as compared to $1\mu m^2$). Although the samples tested did have large well-ordered areas with minimal change in sample thickness, the results

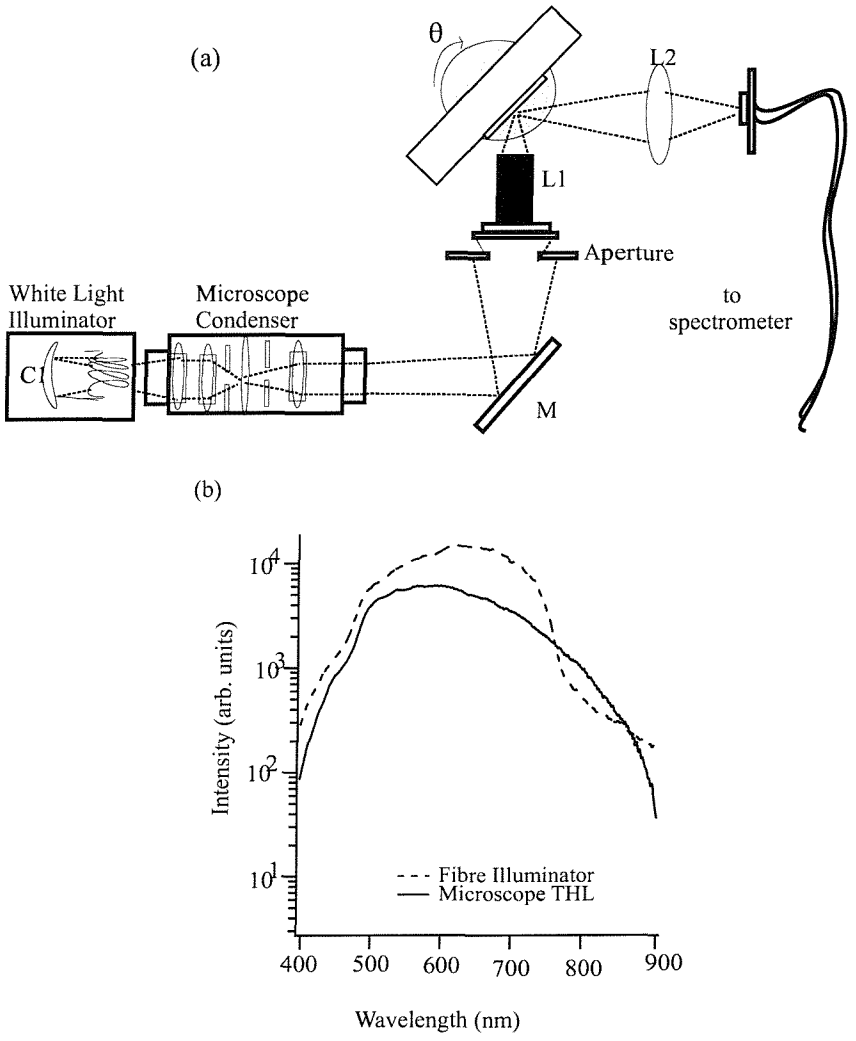

Figure 5.14: (a)Fibre illuminator setup
L1: ×16 long working distance microscope objective
L2: 50mm focal length lens
C1: Cold Mirror
M: Mirror
(b) Spectrum of light sources used in microscopy and in the angle measurements (un-normalised).

found could be different. To check that this was not the case, the mirror M, was replaced with a beam splitter and reflected light at normal incidence was collected for normalisation. Also, the long working distance objective was placed in the microscopy set-up to ensure the obtained spectra corroborated previous findings. In general, the various data sets appeared to agree well.

5.2.3 Angle and Polarisation Dependent Microscopy

The addition of a rotation stage to the microscope allowed a new set of experiments to study the azimuthal dependence of the samples. The rotation stage was first adjusted in order to ensure that the area of interest viewed by the CCD camera did not suffer lateral displacement with rotation. To ensure the fibre was placed in the appropriate position to sample the centre of rotation, a 25μm pinhole was used and the transmission spectrum viewed online to adjust the fibre's position.

Further modification of the microscope allowed the angle and polarisation dependence to be studied. The incident polarisation was set using the fixed polariser. The angle of incidence was altered by translating the CAD either vertically or horizontally as viewed with the eyepiece removed (Fig. 5.12). As well as changing the angle of incidence, this also changed the polarisation properties of the incident light, set afterwards by the polariser. Therefore, translating the CAD vertically produced TE incident light and translating it horizontally produced TM incidence. The angle of incidence was estimated from direct observation of the lamp through removal of the BF/DF carousel. The CAD was measured when fully open and fully closed. The relative position was then multiplied by the half angle deduced from the numerical aperture of the objective. The angle was estimated to be 6^o. Placing a second linear polariser before the front facet of the fibre-coupled spectrometer which could be rotated allowed the co and crossed polarised reflectivity of the sample to be observed as a function of crystal orientation. The sample properties were measured at the same points as in other experiments, with spectra taken every 5^o rotation in the azimuthal plane between 0 and 60^o (covering all symmetry directions). To work out the azimuthal angle relative to the lattice vectors of the sample, the sample was viewed

under very high magnification where individual cavities could be resolved.

Chapter 6

Modelling Structures

Modelling the electric field response of arrays of wavelength scale metallic void arrays presents some challenging problems. Neither the long or short wavelength approaches are strictly valid; the use of Mie scattering is complex and unsatisfactory as it cannot be conveniently adapted easily to model open cavity structures. Furthermore, these models also ignore the interaction of surface states with each other and with the more conventional surface plasmons which can be coupled to the film through the void periodicity. As mentioned in section 3.2.2, surface plasmons can be perturbed by the grating if the grooves are particularly deep or, as in the case of lamellar or bottle shaped gratings, the grooves have their own modes which can also interact with surface fields. However, the theoretical studies of these structures were simplistic, restricting themselves with 2D structures which, yet again, are not directly applicable to understanding spherical voids. Likewise, the effect of thickness and template-ordering dependent sizes and morphologies of the pore mouths is difficult to model. Presently, modelling using Finite Difference Time Domain (FDTD) methods have yet to be successful. Although this technique has been found to extremely useful in modelling two dimensional photonic crystals, as yet solutions to three dimensional problems have proved extremely difficult to solve due to the large number of calculations and high memory required in a 3D mesh. Therefore, currently no complete theoretical approach to understanding the response of macroporous metals to light exists. Instead, different features in the reflectivity of these films require a combination of models. The approach here is to show the essential physics that plays a role, from ray optics - 3D mirrors, interference, surface plasmons, confined plasmons and

finite difference calculations.

6.1 Interference Model

6.1.1 Two Dimensions

Geometrical Reflections

The first model considers interference between reflections off the top surface of the film and geometric reflections from within the cavity as constituting the optical response. Geometrical reflections refer to those reflections which return parallel to flat surface reflection paths In the interests of simplicity, only four reflection paths are considered for light reflecting from the void; one reflection off the bottom of the film, two double reflection paths and a three reflection path (Fig. 6.1). Reflection paths lengths from the cavity increase only relative to the reflection from the top surface and not each other. Our model assumes that light can travel along any of these paths and will interfere with reflections off the flat surface. The paths interfere for all intents and purposes at infinity because of the microscope geometry. Furthermore, increasing the magnification/resolution weakens the strength of the interference effects as the ray paths are separated further on the imaging detector.The effect of the four ray paths inside the cavity are dependent on film thickness, and reflect light with differing angles. Interference effects are modelled as a path difference effect as a function of film thickness for a specific sphere size from 0 to 1 sphere height.

The assumption of only considering the interference of geometric reflections for wavelength scale structures does of course veer towards contradiction. Also, using two dimensions is also restrictive and difficult to justify for a three dimensional object. However, the intention of starting with this simple model is as an initial attempt to consider what spectral response this result generates. Although, the two dimensional model does not preclude the presence of ray reflection paths other than geometric reflections, for simplicity these will not be included. Generating interference effects requires the interaction between two coherent light rays with a relative phase difference which is calculated as the extra distance travelled by one ray compared to the other.

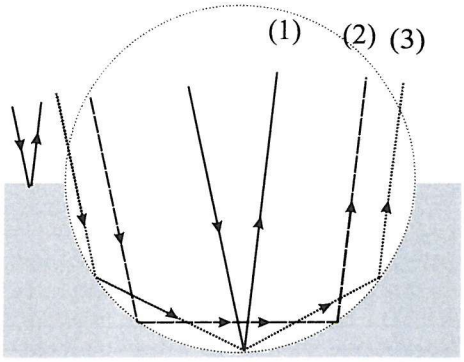

Figure 6.1: Geometric ray reflection paths of an incident plane wave in a 2D model of a an open void.

Focussing: The Gouy Effect

One feature of reflections from a spherical cavity is the effect of focussing light. In the case of a single reflection off the bottom of the cavity, light focussed by the cavity produces a beam that diverges rapidly from the cavity (Fig. 6.2(a)). For the two reflection case the light is focussed and recollimated by the structure(Fig. 6.2(b)). Before moving on to describe the calculations used to model the response of a void, the effect of focussing on the phase shift associated with passing through a focus, known as the Gouy shift is discussed [173]. Gouy was the first to experimentally observe an phase shift due to focussing by overlapping two beams from a pinhole; one beam was reflected off a planar mirror and the other off a curved mirror. At transverse planes near the image of the pinhole circular interference rings were observed. Furthermore, the central fringe changed from dark to light if the fringes were observed just before and just after the focal point, implying a relative phase change between the beams. Following [173] and assuming a gaussian beam; the wave's axially-varying phase shift is contributed to by a component ψ(z) given by

$$\psi(z) = \arctan\left(\frac{z}{z_R}\right) \tag{6.1}$$

where z_R is Rayleigh range determined by

$$z_R = \frac{\pi w_0^2}{\lambda} \tag{6.2}$$

w_0 is the width of the beam at focus.

The Rayleigh range is the distance between the beam waist to the point where the spot size is $\sqrt{2}w_0$ and z is taken to equal zero at the beam focus. The effect of eqn. 6.1 is a π phase shift through the focus, with most of the shift occurring within two Rayleigh ranges either side of the waist (Fig. 6.2(c)).

A further intricacy of this effect is to examine this effect inside the voids. In the case of a single reflection off the base of the void, the phase shift will be πradians as the beam is just focussed and diverges. However, in the case of the double reflection model the light is focussed to a point at radius/2, but travels a distance of $\sqrt{2}$radius before reflecting off the opposite side of the cavity. Therefore, the beam is not perfectly recollimated, but slightly refocussed away from the surface indicating that the phase shift will be slightly more than π.

Phase Change on Reflection

In calculating the final detected electric field from a void we have to take into account the actual optical response of the metal and to this end we calculate the phase change on reflection [9] using data based on the calculated response of metals [78]. The phase change ϕ is calculated using the equations given in 3.2.2 which are reproduced here:

$$\tan(\phi_{TE}) = \frac{2v_2 n_1 \cos(\theta_1)}{u_2^2 + v_2^2 - n_1^2 cos^2(\theta_1)} \tag{6.3}$$

$$\tan(\phi_{TM}) = 2n_1 n_2 \cos(\theta_1) \frac{2\kappa_2 u_2 - (1 - \frac{\kappa^2}{n_2^2})v_2}{n_2^4(1 + \kappa_2^2)cos^2(\theta_1) - n_1^2(u_2^2 + v_2^2)} \tag{6.4}$$

The actual reflectivity of the three metals studied were shown in Fig. 3.8. The wavelength dependence of their response is therefore also accounted for in the model.

Calculating Path Difference

The extra distance travelled by light reflecting from inside the void rather than reflecting off the surface are denoted by L_1, L_2 and L_3 and are individually calculated from trigonometry (Fig. 6.3). As well as taking into account the path taken, the effect of the pore mouth size must also be considered as it will obscure different numbers

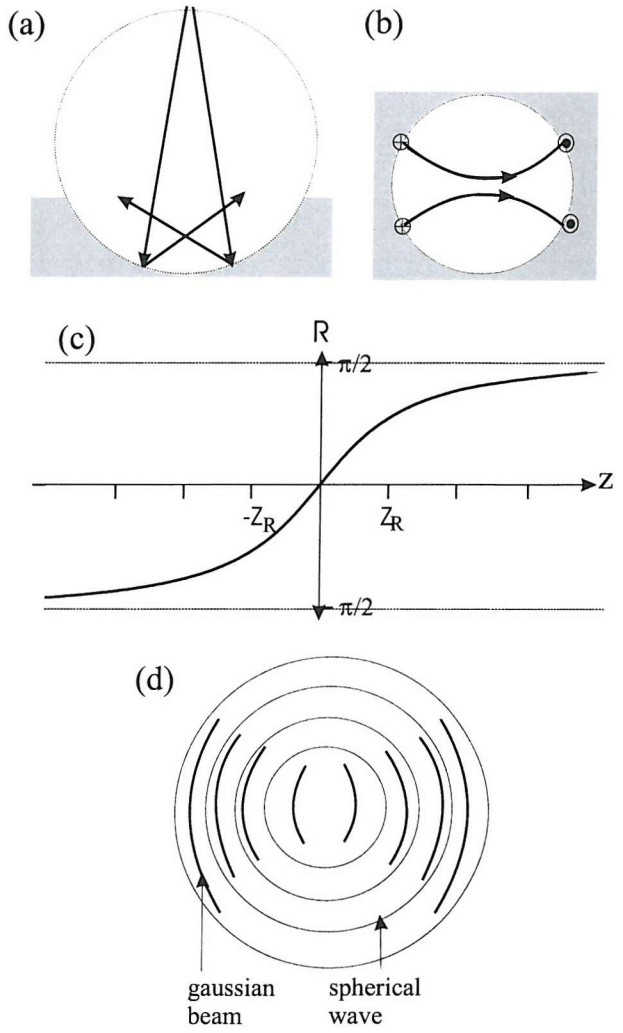

Figure 6.2: (a) Off-axis reflections off the bottom of the cavity are focussed and diverge rapidly. (b) (Top view) Double bounce reflection; the geometry of the void focusses light with the first reflection and then re-collimates the beam with the second. (c) Gouy phase shift through the waist region of a gaussian beam (d) Gouy phase shift through the waist region compared to an ideal spherical wave.

of bounces at different thicknesses. The pore mouth opening, a, is given by:

$$a = \sqrt{r^2 - (t - r)^2} \tag{6.5}$$

The paths lengths are given by:

$$L_1 = 2(q - w) \tag{6.6}$$

$$w = v\sin(\theta), v = t\tan(\theta), q = t/\cos(\theta) \tag{6.7}$$

This path is obscured if $a < v$ (Fig. 6.3(a)).

$$L_2 = 2(p + q) - 2w \tag{6.8}$$

$$\psi = \frac{180 - 2\theta}{4}, p = r\sin(\theta), u = r(1 - \cos(\psi)), v = p + (t - u)\tan(\theta), w = v\sin(\theta) \tag{6.9}$$

This path is obscured if $a < v$ or $u > t$ (Fig. 6.3(b)).

The double reflection path also has a second route which can return incident rays parallel to their incident paths and is calculated by:

$$L_{-2} = 2(p + q) + 2w \tag{6.10}$$

$$\psi = \frac{180 - 2\theta}{4}, p = r\sin(\theta), u = r(1 - \cos(\psi)), v = p - (t - u)\tan(\theta), w = v\sin(\theta) \tag{6.11}$$

Again, this path is obscured if $a < v$ or $u > t$ (Fig. 6.3(c)).

The three reflection path is given by:

$$L_3 = 2(2p + q) - 2w \tag{6.12}$$

$$\psi = \frac{180 - 2\theta}{6}, p = r\sin(2\theta), u = r(1 - \cos(2\psi)), v = p + (t - u)\tan(\theta), w = v\sin(\theta) \tag{6.13}$$

path obscuration is given by the same relations as for the two bounce model (Fig. 6.3(d)).

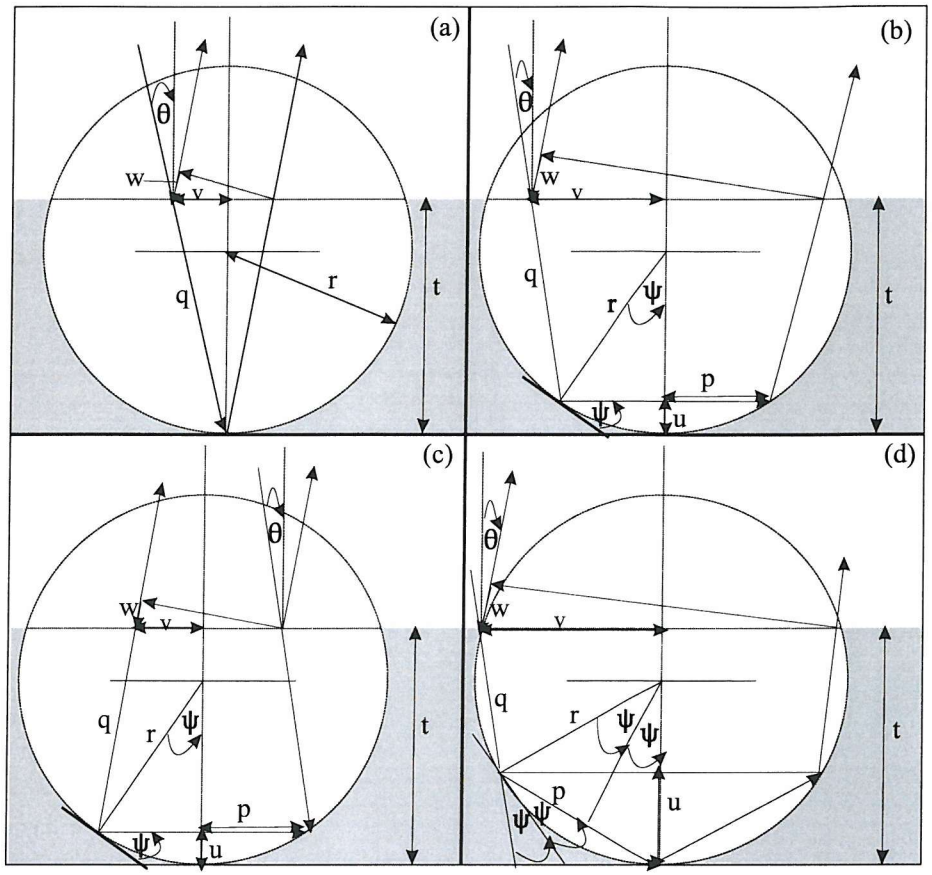

Figure 6.3: Geometrical ray paths for rays entering and leaving along parallel paths to interfere with reflections off the flat surface. (a)Single reflection, (b) double reflection, (c) reverse double reflection and (d) triple reflection off the void surface.

In general, for n bounces the extra path length, $L_n$is given by;

$$L_n = 2((n-1)p + q) \tag{6.14}$$

$$\psi = \frac{180 - 2\theta}{2n}, p = r\sin((n-1)\theta), u = r(1 - \cos((n-1)\psi)), w = (p + (t-u)\tan(\theta))\sin(\theta) \tag{6.15}$$

Limitations of the 2D Model

Before discussing the results generated by this theory, its limitations due to geometrical considerations should be mentioned. If the effect of changing the angle of incidence is studied for both the single and double bounce paths it is found that increasing the angle of incidence increases the range of angles which are blocked by

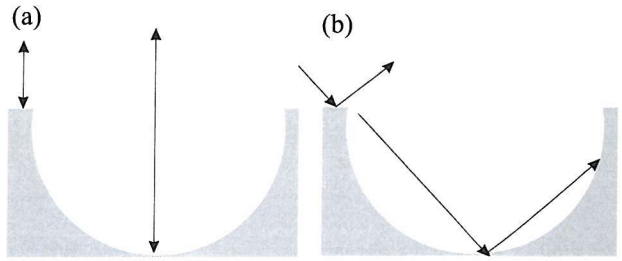

Figure 6.4: (a) Geometrical normal incidence rays reflect off the structure (b) Angles away from normal incidence obscure the geometrical reflections off the void.

the void aperture (Fig 6.4). In the case of three bounces the range of angles will be less than the other configurations. In Fig. 6.5 the values of angle of incidence and dimensionless film thickness (film thickness divided by template sphere diameter) are plotted for all possible geometrical reflections (white); conditions where only single reflections from the void occur are represented by dark grey areas and light grey areas indicate conditions for single and reverse double reflections. The black areas in Fig. 6.5 indicate ranges of film thickness and incident angle for which no geometrical ray reflection can occur. This graph shows the limitations of the model used, with angles away from normal incidence not explained by such a simple model. Despite this shortcoming, and the exclusion of ray paths other than geometric reflections incident on the void which are not reflected in the same direction as a flat surface, the model is still useful as a first step to understanding the experimental data.

Calculating the Electric Field Response

The reflectivity response of a void is calculated separately for one, two or three reflections so as to get an understanding of the potential solutions. Furthermore, it is assumed that the separate paths inside the void do not interfere with one another as their relative path differences are independent of film thickness and therefore provide little insight. Furthermore, at this point we want to get as simple an idea of the sorts of behaviour that could be observed experimentally. The field response for a void is calculated for a reflection off the top surface of the film and reflection/s of the inside of the void. The resulting reflectivity is composed of the response due to the reflectivity profile of the bulk metal which were presented for gold, silver and platinum (Fig. 3.8(a)). The relative phase between the alternative paths is produced

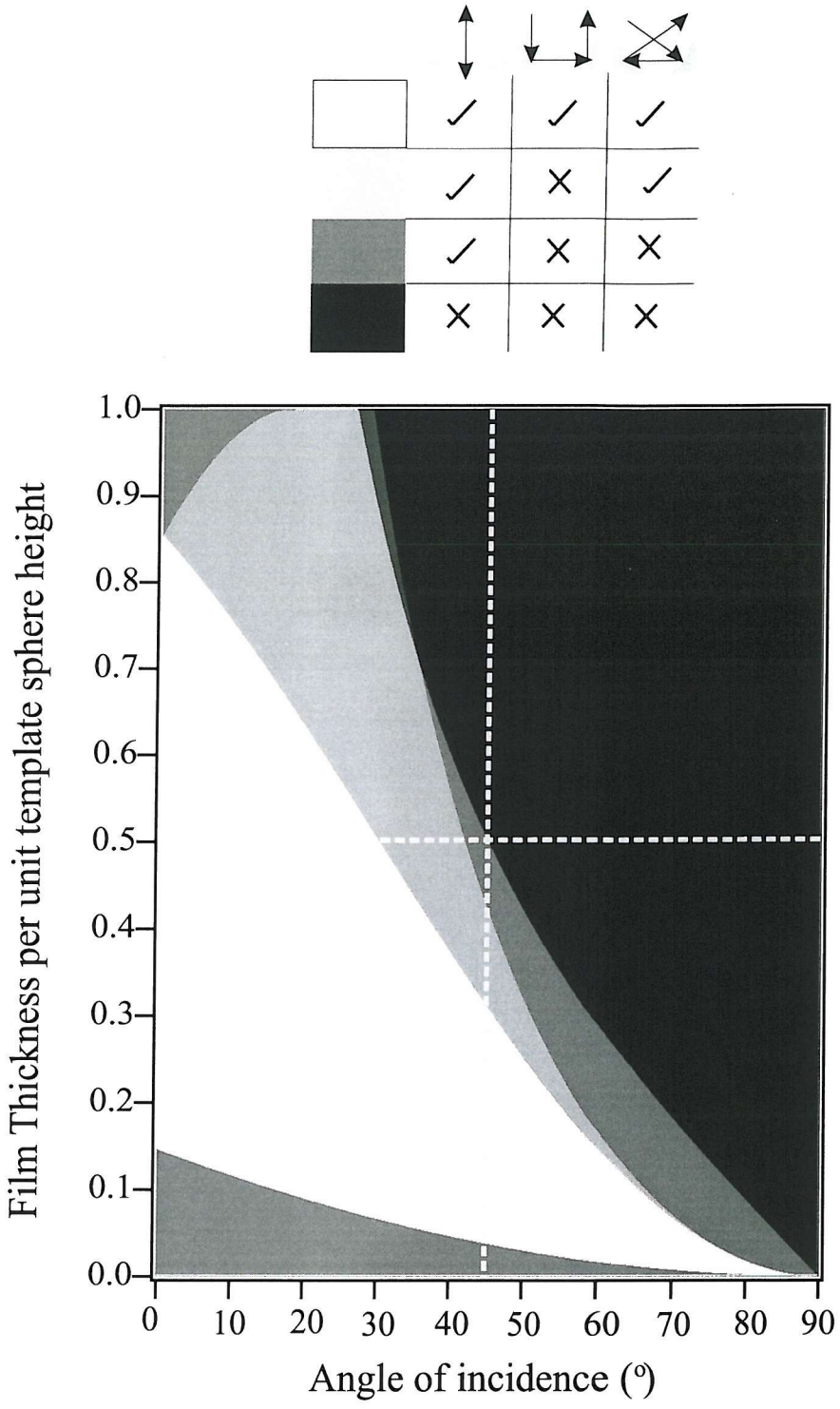

Figure 6.5: Plot of the different ranges of values of normalised film thickness and angle of incidence for which different geometrical reflection modes are possible. White: all reflections possible; dark grey: only single bounce possible; light grey: single and double bounce possible; black no reflections possible. The different reflection modes are shown by the inset diagrams.

by three phase-altering behaviours; reflection from the metal, the extra path travelled by one ray in comparison with the other and the Gouy effect. Using the values for the wavelength dependent complex refractive index with the angle of incidence allows the phase change on reflection to be calculated. The phase change due to the extra path length is calculated through working out the number of wavelength cycles (for a particular wavelength) the extra path length represents. The equations for each of the four scenarios described above are additions of the field response of both ray paths. The equations constructed for this model are as follows.

One reflection with top surface

$$R_1 = R_m(\theta,\lambda)\exp\left(i\phi(\theta,\lambda)\right) + R_m(\theta,\lambda)\exp\left(i2(\pi)L_1/\lambda + i\pi + i\phi(\theta,\lambda)\right) \quad (6.16)$$

Two reflections with top surface

$$R_2 = R_m(\theta,\lambda)\exp\left(i\phi(\theta,\lambda)\right) + R_m(\theta,\lambda)^2\exp\left((i2\pi)L_2/\lambda + i\pi + 2i\phi(\theta,\lambda)\right) \quad (6.17)$$

Three reflections with top surface

$$R_3 = R_m(\theta,\lambda)\exp\left(i\phi(\theta,\lambda)\right) + R_m(\theta,\lambda)^3\exp\left((i2(\pi)L_3/\lambda + i\pi + 3i\phi(\theta,\lambda)\right)) \quad (6.18)$$

Where R_m =reflectivity of bulk metal ϕ =phase change on reflection λ =incident wavelength θ =angle of incidence L = path length difference.

Rather than attempt to merge results for one, two and three bounces, as a first step in understanding the response of this system the spectra for different film thicknesses for each case will be considered separately (Fig. 6.6(a), (b), (c)). All graphs show dips in reflectivity moving linearly with thickness to longer wavelengths. Plots of double and triple reflection paths have regions which exhibit the reflective characteristics of a flat surface when the reflections from the void are not allowed either because the void surface is too small, or are obscured by the pore mouth opening. Single bounces are allowed for all thicknesses at normal incidence. The most noticeable differences between all three graphs are in the spectral position and their extent of the dips in reflectivity with film thickness.

The effect of adding the Gouy effect in the model can be seen by considering the reflectivity of a Pt void, 700nm in diameter, with and without the extra phase shift

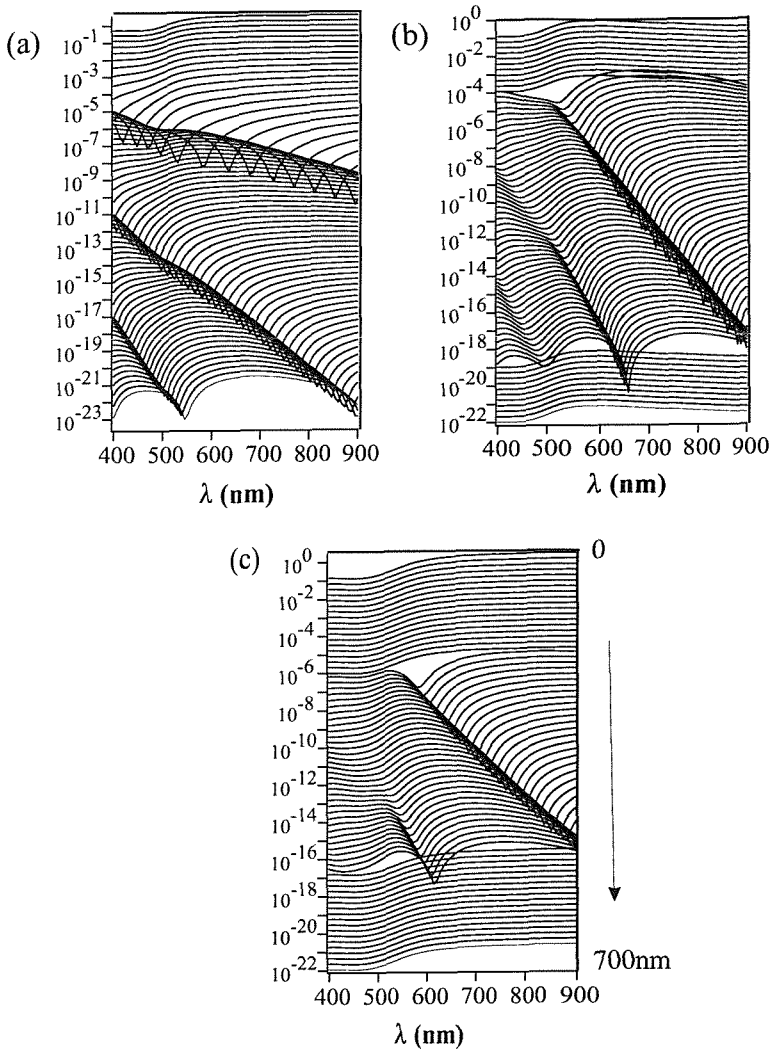

Figure 6.6: Theoretical plots of interference between reflections of the top surface and (a)one, (b)two and (c)three reflections from a cavity. The plots are off-set on a log-scale for clarity with thickness increasing from 0 to 700nm in steps of 10nm down each graph.

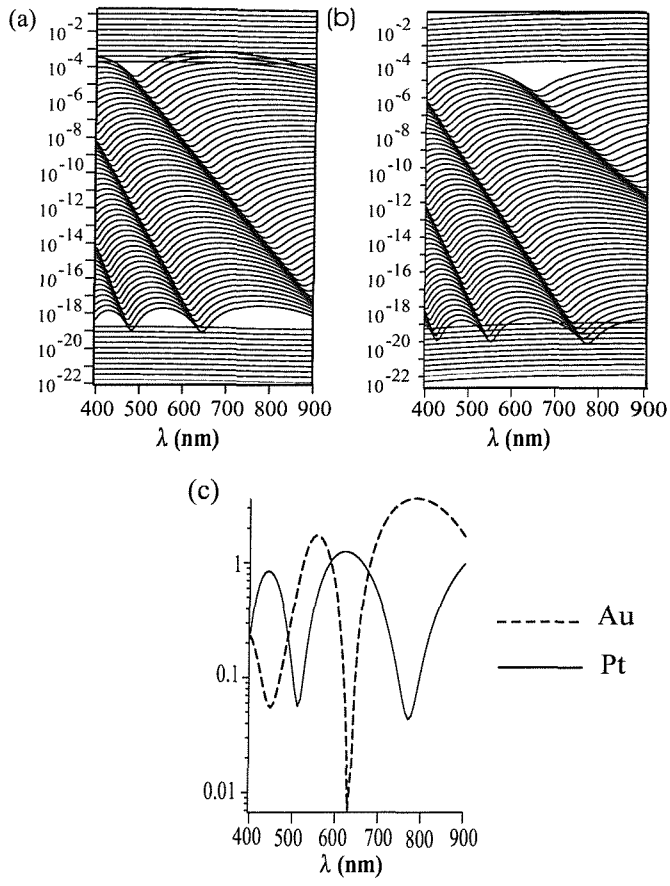

Figure 6.7: Effect of Guoy shift for a Pt sample with thickness ranging from 0 to one sphere height for a latex sphere of size 700nm (a) No Guoy shift(b) Extra shift of π due to beam passing through a focus (c) Comparison of a the reflectivity of a Au and a Pt void grown to a thickness of 610nm.

for the two reflection model (Fig. 6.7). The effect of adding in the value of π is shown only to shift the position of all the dips a fixed value, with the distance between dips remaining constant. Also, the effect of using different metals becomes apparent with comparison with the previous results for gold (Fig. 6.6). As well as controlling the overall shape of each reflectivity spectra, the metals also show different dip positions and dip widths (Fig. 6.7).

6.1.2 Three Dimensions

Vector Notation

To solve the problem of ray tracing in three dimensions, light rays are represented as 3D vectors of unit length. As well as describing how the rays reflect and exit the

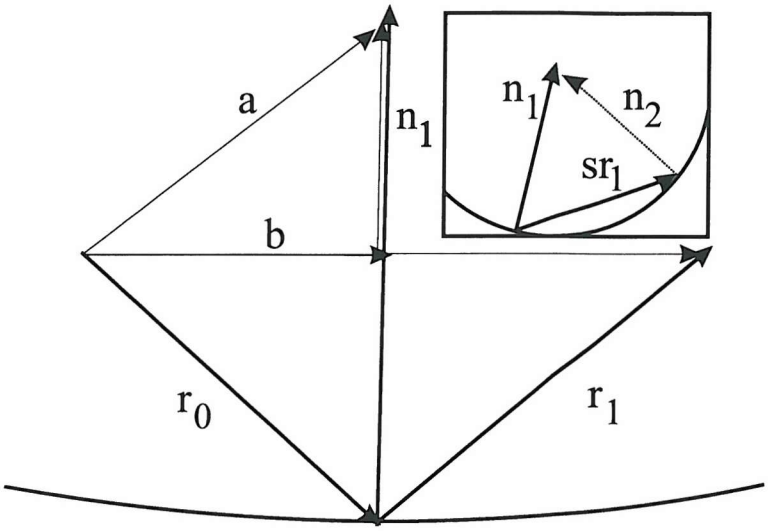

Figure 6.8: Vector solution for ray tracing inside a sphere. Relationship between incident($\vec{r}_0$, reflected($\vec{r}_1$) and surface normal vectors ($\vec{n}_1$), Inset; finding where the reflected ray hits the void with $\vec{n}_2$ the surface normal at the point where the reflected ray is incident on the void and s is a scalar.)

sphere, the collection angle of the collection microscope objective or lens has to be accounted for. The vector relationship between the incident light, denoted by $\vec{r}_0$, the reflected ray, $\vec{r}_1$, and the normal to the surface, $\vec{n}_1$, is shown in Fig. 6.8. The relationship between $\vec{r}_0$ and $\vec{n}_1$ can be expressed using three additional vectors; $\vec{a}$, $\vec{b}$ and $\vec{c}$.

$$\vec{a} = \vec{r}_0 + \vec{n}_1 \tag{6.19}$$

$$\vec{c} = (\vec{a} \cdot \vec{n}_1)\vec{n}_1 = (\vec{r}_0 \cdot \vec{n}_1)\vec{n}_1 + \vec{n}_1 \tag{6.20}$$

$$\vec{b} = \vec{a} - \vec{c} = \vec{r}_0 - (\vec{r}_0 \cdot \vec{n}_1)\vec{n}_1 \tag{6.21}$$

$$\vec{r}_1 = -\vec{r}_0 + 2\vec{b} = \vec{r}_0 - 2(\vec{r}_0 \cdot \vec{n}_1)\vec{n}_1 \tag{6.22}$$

The second part of this process is to derive a relationship between the reflected ray vector, $\vec{r}_1$, and the inside of the void, also taken to have a radius of unit length (Fig. 6.8). Writing the equation of the line (eqn. 6.23) and then taking the modulus of both sides (eqn. 6.24):

$$-\vec{n}_2 = -\vec{n}_1 + s\vec{r}_1 \tag{6.23}$$

$$1 = |(\vec{n}_1 + s\vec{r}_1)|^2 = 1 + s^2 - 2s\vec{n}_1 \cdot \vec{r}_1 \tag{6.24}$$

Ignoring the second (zero) solution for s the scalar is derived to be

$$s = 2\vec{n}_1 \cdot \vec{r}_1 \tag{6.25}$$

The second surface normal can therefore be expressed in terms of the ray incident at that point and the surface normal from its source.

$$\vec{n}_2 = \vec{n}_1 - 2(\vec{n}_1 \cdot \vec{r}_1)\vec{r}_1 \tag{6.26}$$

As well as considering the different phase changes on reflection for different polarisations, the geometrical differences also have to be considered. TM polarisation undergoes a π phase flip on reflection (Fig. 6.9). The electric field vector, $\vec{e}_0$, can be written in terms of electric field vectors for TE ($\vec{e}_{TE}$), and TM polarisation ($\vec{e}_{TM}$).

$$\vec{e}_0 \cdot \vec{r}_0 = 0 \tag{6.27}$$

$$\vec{e}_0 \cdot \vec{n}_1 = \vec{e}_{TM} \cos(\alpha) \tag{6.28}$$

Using $\sin^2(\alpha) = \sqrt{1 - \sin^2(\alpha)}$, and $\sin(\alpha) = \cos(90 - \alpha) = \vec{r}_0 \cdot \vec{n}_1$, TM polarisation can be written in terms of the original electric field vector and the surface normal.

$$\vec{e}_{TM} = \frac{\vec{e}_0 \cdot \vec{n}_1}{\sqrt{1 - (\vec{r}_0 \cdot \vec{n}_1)^2}} \tag{6.29}$$

The two polarisation vectors after reflection can then be expressed in terms of the surface normal and the new ray path.

$$\vec{e}_{TE} = \vec{n}_1 \times \vec{r}_1 \tag{6.30}$$

$$\vec{e}_{TM} = \vec{e}_{TE} \times \vec{r}_1 \tag{6.31}$$

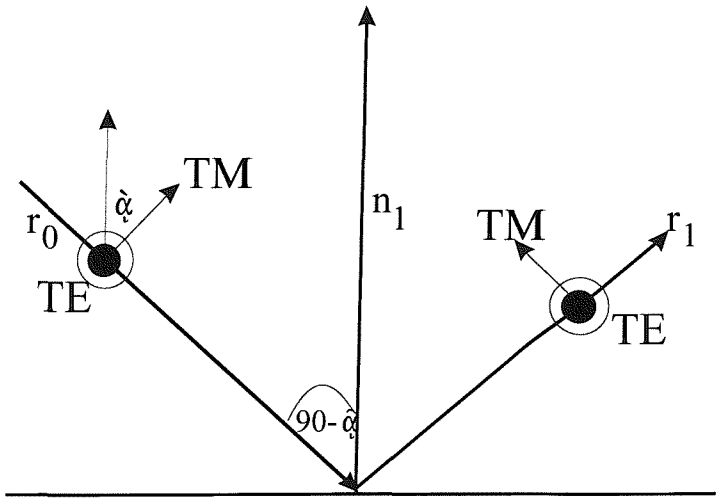

Figure 6.9: Polarisation rotation on reflection of TM due to phase change of π.

Reflections from a Void

The geometry of the system is shown in Fig. 6.10, with the incident ray, $\vec{r_0}$, defined by the angle of incidence, θ as;

$$\vec{r_0} = \sin(\theta)\vec{x} + 0\vec{y} + \cos(\theta)\vec{z} \tag{6.32}$$

where $\vec{x}, \vec{y}, \vec{z}$ are unit vectors in the x, y and z planes respectively. The rays arriving at each point are tracked in 3 dimensional matrices of vectors for each polar angle, θ, and azimuthal angle, ψ. The film thickness is denoted by t and is scaled to be unity when equal to the radius of the sphere. Light reflecting off the flat surface is represented by reversing the polarity of the $\vec{z}$ coordinate. The polarisation vectors are defined by the cross product relationships in eqns. 6.30, 6.31 between the vectors $\vec{r_0}$ and the y axis $(0\vec{x} + \vec{y} + 0\vec{z})$. The input polarisation $(\vec{E_0})$ is defined in terms of the incident vectors $\vec{e}^0_{TE}, \vec{e}^0_{TM}$ and a polarisation angle $(\psi)$where 0 represents TM polarisation.

$$\vec{E_0} = \cos(\psi)\vec{e}^0_{TM} + \sin(\psi)\vec{e}^0_{TE} \tag{6.33}$$

Output detection is represented by another electric field vector, $\vec{E}_{out}$, the polarisation angle of an analyser (ψ_{an}) placed before the detector and the polarisation vectors

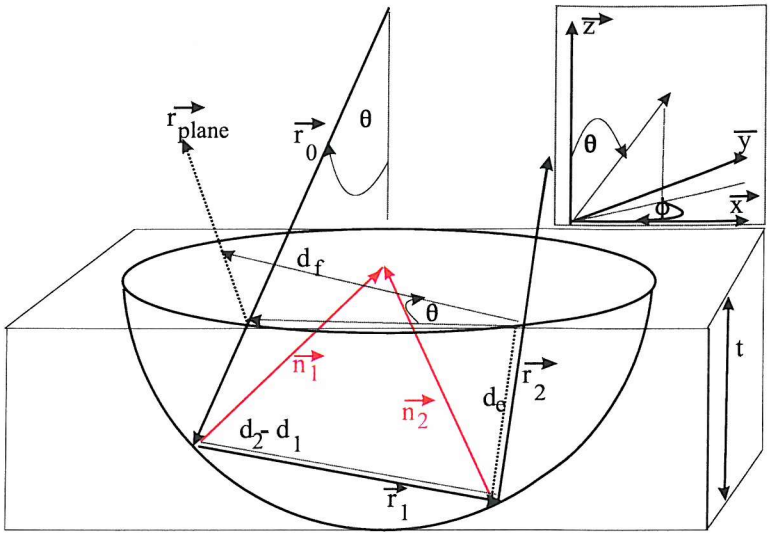

Figure 6.10: Three dimensional co-ordinate system to model reflections from the voids with ray paths $\vec{r}_0, \vec{r}_2, \vec{r}_2$ shown by full black arrows, surface normals $\vec{n}_1, \vec{n}_2$ shown by red arrows and dotted lines showing some of the distances relevant to the text. Inset: Coordinate system used with definitions of θ, ϕ.

after reflection off the surface.

$$\vec{E}_{out} = \cos(\psi_{an})\vec{e}^1_{TM} + \sin(\psi_{an})\vec{e}^1_{TE} \tag{6.34}$$

The surface normal, $\vec{n}_1$, is defined in spherical coordinates with polar angle θ (0 to 2π rads) and azimuthal angle ϕ (0 to π rads):

$$\vec{n}_1 = -\cos(\theta)\sin(\phi)\vec{x} + \sin(\theta)\cos(\phi)\vec{y} + \cos(\phi)\vec{z} \tag{6.35}$$

The distance travelled by a reflection off the flat surface, d_0, is calculated from the z component of the incident light and the surface normal:

$$d_0 = |\frac{t - 1 + (\vec{n}\vec{z})}{\vec{r}_0\vec{z}}| \tag{6.36}$$

where $(\vec{n}_1\vec{z})$ represents the z component of $\vec{n}_1$

Considering reflections off the void, the reflected ray path is calculated using eqn. 6.22. In deciding whether the ray path enters the void or is inhibited by the (assumed to be) circular pore mouth opening, the z-components of the surface normal, the film thickness and the z-component of the incident ray in the direction of $\vec{r}_0 \cdot \vec{n}_1$ (the path of the beam into the void) are combined to find whether the vector is inside or outside

of the void. The use of -1 because the vectors for the sphere are defined from its centre.

$$\vec{n}_1\vec{z} - 2(\vec{r}_0 \cdot \vec{n}_1)\vec{r}_0\vec{z} - 1 + t \tag{6.37}$$

If this condition is < 0 the ray hits the sphere, and if > 0, the ray reflects off the top surface. As with the approach above, the polarisations can be calculated along with the new direction of the ray using equations 6.27, 6.28 and 6.30, 6.31. This approach can be repeated to obtain expressions for three bounce models as well.

The distance travelled inside the sphere, d_{final}, for 1 (d_1), 2 (d_2), and 3 (d_3) reflections is given by:

$$d_1 = d_0 \tag{6.38}$$

$$d_2 = d_1 + |2\vec{r}_1 \cdot \vec{n}_1| \tag{6.39}$$

$$d_3 = d_2 + |2\vec{r}_2 \cdot \vec{n}_2| \tag{6.40}$$

Each of the distances above have to also take into account the extra path taken to leave the void, d_e.

$$d_e = |\frac{t - 1 + (\vec{n}_{1,2,3}\vec{z})}{\vec{r}_{1,2,3}}| \tag{6.41}$$

where the numbers 1, 2 and 3 denote the number of reflections inside the void being considered.

Finally, as with the two dimensional case, the distance between the reflection from inside the void and off the top of the void needs to be calculated (Fig. 6.11). The vector ($\vec{d_f}$) is the extra path length distance between the two possible resultant reflections from the top of the void and is given by:

$$\vec{d_f} = d_0\vec{r}_0 + \vec{n}_1 - \vec{n}_{final} + d_{final}\vec{r}_{out} \tag{6.42}$$

where d_{final} is the distance determined by the number of reflections inside the cavity as given above, $\vec{n}_{final}$ is the final surface normal also determined by the number of

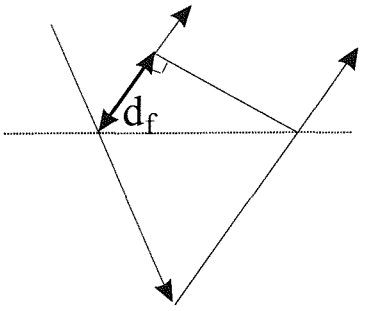

Figure 6.11: $\vec{d_f}$ The extra path length distance between the two possible resultant reflections from the top of the void.

reflections in the void. The distance between the two vectors is then calculated and taken away from the distance d_{final} to give the path length d_L.

$$d_L = d_{final} - \sin(\theta)|\sqrt{\vec{d_f} \cdot \vec{d_f}}| \tag{6.43}$$

Only rays exiting the void in nearly the same direction as the reflection of the plane surface are used. This is expressed as a collection matrix m_c and a polarisation matrix m_{pol} at each point.

$$m_c = \vec{r}_{final} \cdot \vec{r}_{out} \tag{6.44}$$

$$m_{pol} = \vec{e}_{final} \cdot \vec{e}_{out} \tag{6.45}$$

where e_{final} is the polarisation of the final ray to leave the void. m_c is further modified to take account of the collection angle (θ_c) of the lens/microscope objective (m_{ca}).

$$m_{ca} = \exp\left\{ -\left(\frac{\Delta\theta}{\theta_c}\right)^2 \right\} \tag{6.46}$$

where $\Delta\theta = \arccos(m_c)$, the angle between the plane reflected ray and the ray emerging from the void at at that point. The collection matrix and polarisation matrix are then expressed in cartesian coordinates to give a representation of the rays reflecting off the sphere for different angles of incidence. The collection rays are denoted as m_{rays}, the collection polarisation as m_{pol} and the resulting intensity is expressed as m_I.

$$m_I = (m_{rays} \times m_{pol})^2 \tag{6.47}$$

Some results of note generated by this ray tracing model are shown in Figs. 6.12, 6.13 for co- and cross-polarised behaviour at normal incidence for 1 and 2 reflections and the behaviour of co-polarised light as the angle of incidence is varied inside a hemispherical void respectively. Fig. 6.12(a) looks down into the void and shows how it reflects light using the ray paths, polarisation and intensity properties for co-polarised light. In the case of the ray paths (m_{rays}), the two images (Fig. 6.12(a)(i) and (ii)) show the rays which return back to the microscope at normal incidence and retain their polarisation. The polarisation picture shows the regions which retain their original polarisation (white) and the areas which rotate the polarisation of incoming light (black). The intensity, m_I, shows the void as it would be imaged. The polarisation properties of the voids shows that double reflections can rotate polarisation due to the geometrical nature of the reflection. Also, the single reflection shows polarisation rotation which is unlikely to be observed experimentally as it is comparatively weak as it comes from angles away from normal incidence.

The results for co-polarised light at angles away from normal incidence show how the pore geometry distorts the ray profile with increasing angle away from the normal. These simulations show that single reflections become increasingly elliptical (Fig. 6.13(i)), whereas double reflection paths are even more sensitive to incident angle (Fig. 6.13(ii)). Most importantly in the double reflection case is the different sensitivity to angles for reflections along the y axis, in comparison to those along the x-axis. Hence, tilting the angle of incidence away from the normal breaks the four fold symmetry.

Spectral Response of a 3D Cavity

The ray paths and path lengths generated above can be used to show the reflective response of a metallic void using ray optics. In the interests of brevity only one size template size will be used, 700nm and the effect of changing both the thickness and the angle of incidence will be modelled. The reflectivity will be only considered between 300 and 1000nm and diffractive effects are not considered.

In calculating the response, the amount of light initially hitting each part of the

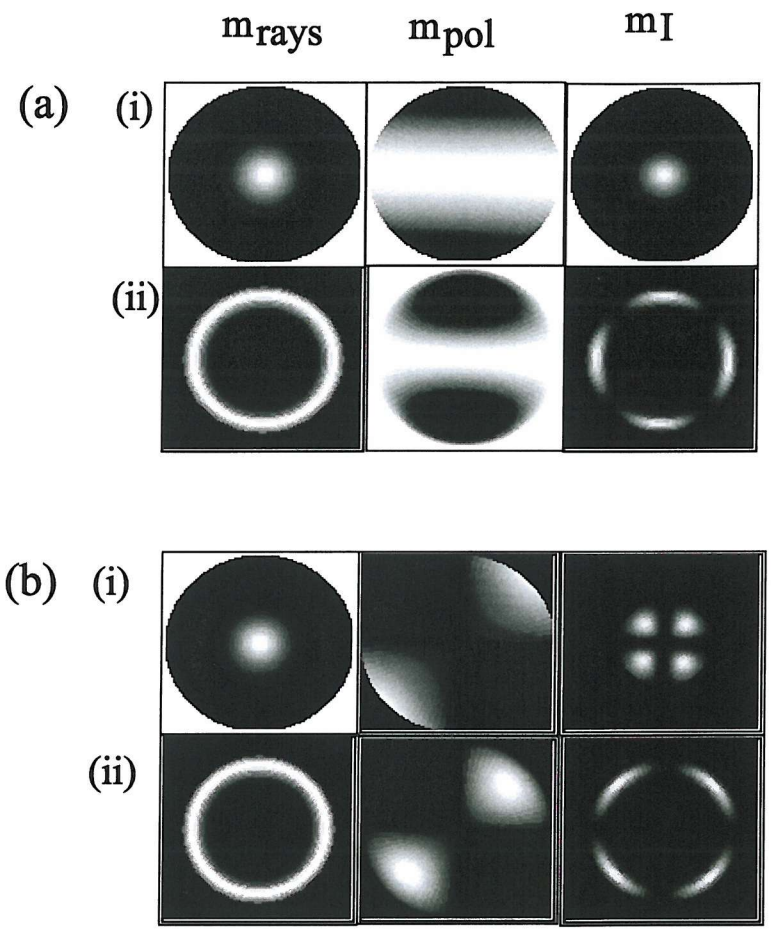

Figure 6.12: Vector ray tracing results for 1 (i) and 2 (ii) reflections from a hemispherical void at normal incidence for (a) co-polarised observations and (b) cross-polarised observations.

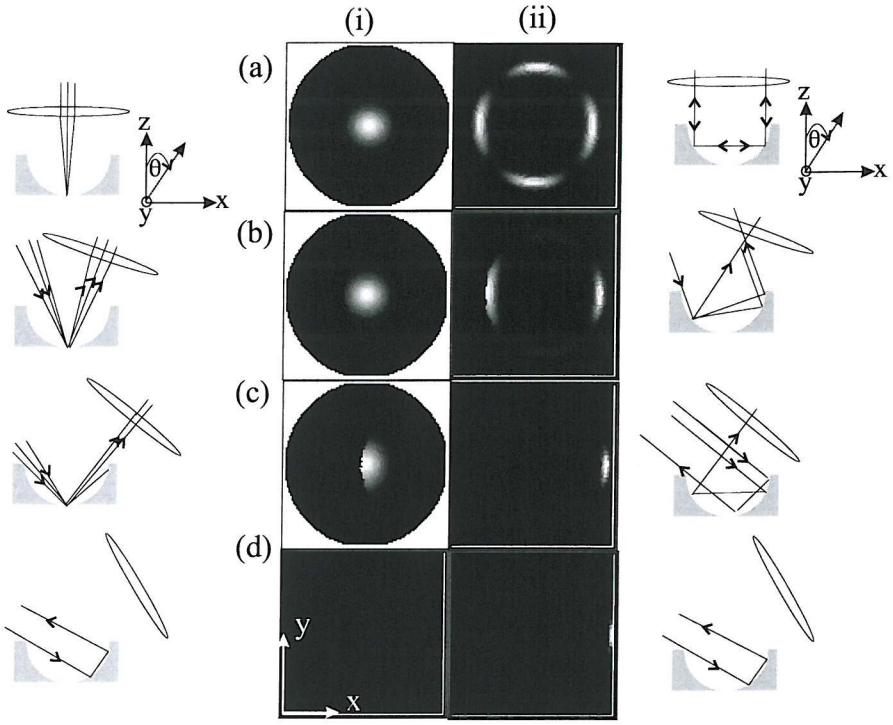

Figure 6.13: Vector ray tracing results for co-polarised observations for a hemispherical void for (i) one and (ii) two reflections in the void at (a) normal incidence, (b)$\theta = 20^o$, (c)$\theta = 40^o$, (d) $\theta = 60^o$. The grey scale indicates the reflection intensity from each point from high intensity (white) to no reflections (black). The diagrams either side of the images indicate the ray paths, showing how the image becomes distorted as the angle of incidence moves away from normal incidence.

void must be considered using a matrix m_{pixel}.

$$m_{pixel} = \vec{r}_0 \cdot \vec{n}_1 \tag{6.48}$$

Also, the ray divergence, m_{div} must be calculated:

$$m_{div} = \vec{r}_{final} \cdot \vec{r}_{out} \tag{6.49}$$

The angle between the reflection from inside the void and the reflected beam from the top surface, m_θ, must be compared with the acceptance angle of the collection lens. The spectral response is calculated in very much the same way as in the two dimensional case except a 3D matrix m_{spec} is used.

$$m_{spec} = R_m^a m_{pixel} m_{div} m_{pol} \exp(i\pi(a-1) + \frac{D}{2} d_L N 2\pi/\lambda) \tag{6.50}$$

where a =the number of reflections, D is the sphere diameter, N is the refractive index inside the void and R_m is the reflectivity of the metal of the void as used for the two dimensional case.

To get a spectrum for each cavity and individual orientation the response is summed for all values of ϕ and the available θ's. The flat surface area will also vary according to the film thickness, and the rescaled reflectivity, R_{flat}, is then needed.

$$R_{flat} = 2\sqrt{3} - \pi r_{pore}^2 \tag{6.51}$$

where r_{pore} is the pore radius and the area of the hexagonal unit cell is $2\sqrt{3}r^2$, and r is defined as equal to unity.

Results

The results generated by this 3D model for normal incidence reflectivity of a Au film through a 700nm sphere template with co-polarised detection and azimuthal angle, 0^o light are shown (Fig. 6.14). All three theoretical plots are off-set on log scales with film thickness increasing down the graph with a thickness increase of 35nm between consecutive spectra. The reflectivity for the single reflection condition (Fig. 6.14(a)) and two reflections (Fig. 6.14(b)) not only differ in spectral content but

also in magnitude, hence the need for different scaling factors for the graphs. All graphs are re-scaled to account for the significant drop in overall reflectivity as the film approaches half templating sphere height due to the decrease in flat surface area with increasing pore mouth diameter. Although an important consideration, as a first step this is ignored in the interests of observing the change with film thickness.

Both conditions show a series of reflectivity minima which move towards longer wavelengths with increasing film thickness. However, with the two dimensional method reflectivity minima appeared across the spectrum, which was not reproduced experimentally. The results from the 3D model show a much more complex relationship because of the greater range of ray paths from the void taken into account and also the relative intensity on each part of the void being accounted for. The 3D model can also account for the variation in the width and depth of the dips. These simulations also show that the reflective behaviour of the films is influenced by both one and two reflection paths, in contrast to a clear preference for the two-reflection path in the 2D model.

Having briefly mentioned that small angles show only small changes in spectral content, it should also be stated that over there are significant changes in the reflectivity simulations for angles from $0^o - 60^o$ (Fig. 6.15). As above, the results shown here are for co-polarised light at an azimuthal angle of 0^o. The film thickness was kept constant and the angle of incidence altered for 1 (6.15(a)) and 2 (6.15(b)) reflections for angles of incidence 5^o apart. Three pairs of graphs are shown for films 175, 350 and 525nm thick. The simulations show that features present in the graphs shift to shorter wavelengths with increasing angle. Generally, the features also flatten out towards larger angles, as the relative contribution from the void and the flat top become very unequal, although some features do appear very sharply between 20^o and 30^o. As with simulations for varying film thickness, the single reflection behaviour overall shows sharper, stronger features than the two reflection model.

The observation of increasing frequency with angle of incidence in a Fabry-Prot etalon is well-known [175]. Briefly, the field inside a Fabry-Prot etalon has to add constructively; if the in-plane wavevector increases the mode frequency also increases (Fig. 6.16). Using simple trigonometry and Fig. 6.16(b), the relationship between

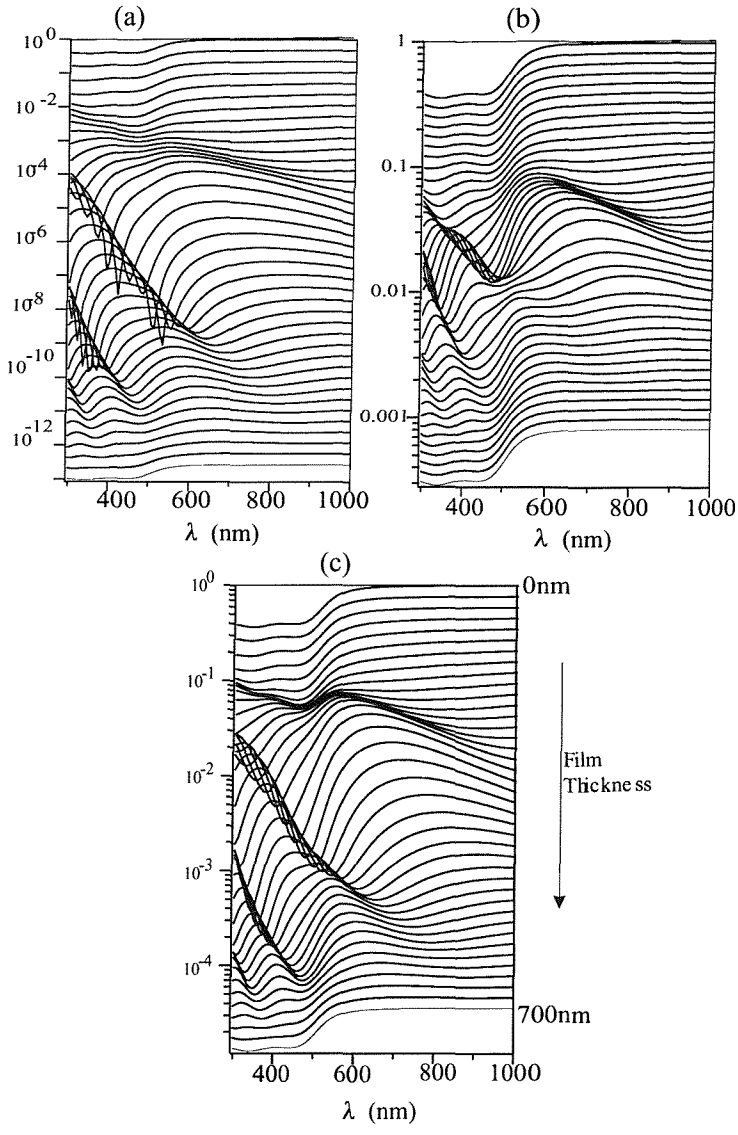

Figure 6.14: Theoretical reflectivity plots on log scales for a Au film through a 700nm sphere template at normal incidence due to interference between reflections off the top surface and (a)one and (b) two 3D reflections of form the void for film thicknesses which increase by 17.5nm down the graph and are off-set for clarity. (c) Addition of both spectra from (a) and (b) at each thickness. These results can be compared with the experimentally derived results for a Au film with 700nm sphere template at normal incidence (see Fig. 8.1).

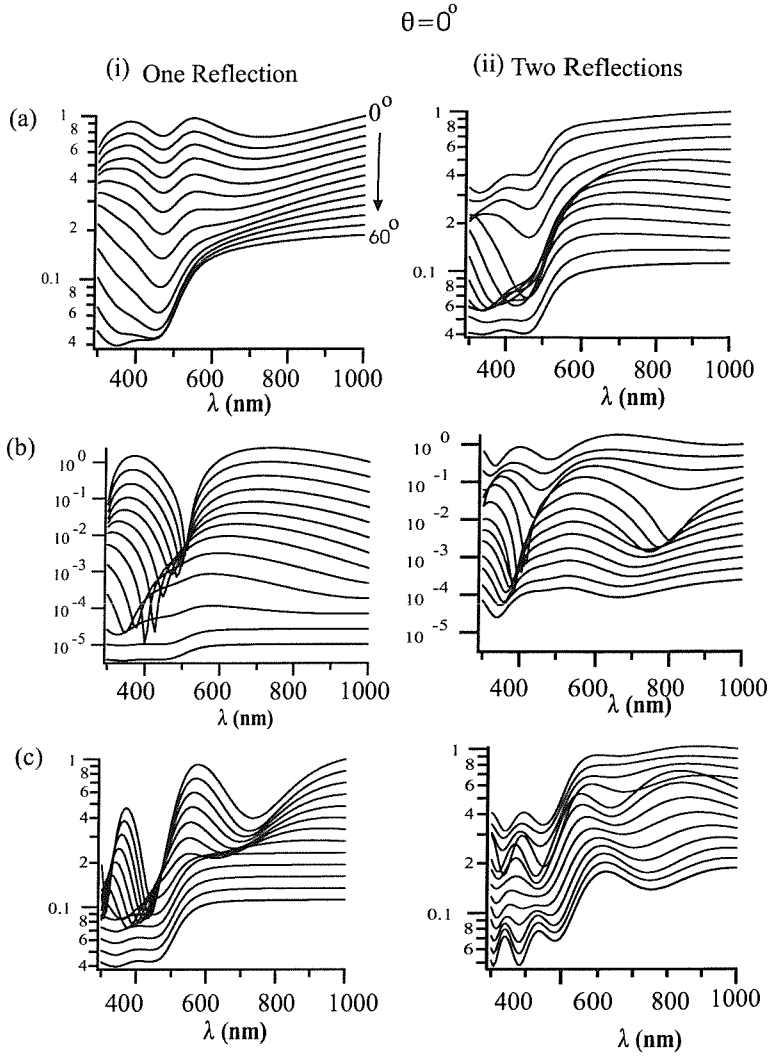

Figure 6.15: Angle of incidence response between 0^o and 60^o for (i) one and (ii) two reflections from a void 700nm in diameter at film thicknesses of (a) 175nm (b) 350nm and (c) 525nm. Graphs off-set on log scale for clarity with angle of incidence increasing down the page

the mode frequency, ω, in-plane wavevector, $k_{||}$, distance between the mirrors, L, and the mode frequency, N, is given by;

$$\left(\frac{\omega^2}{c^2} - k_{||}^2\right)^{1/2} = N\pi \tag{6.52}$$

The frequency therefore increases as the square of the in-plane wavevector. This approach can also be applied to the case of interference from a spherical void and can explain why the reflectivity dips move towards blue wavelengths.

In considering the effect of polarisation rotation of incident light by the voids, the angle of incidence is kept constant at 0^o (Fig. 6.17) and 45^o (Fig. 6.18) for a void

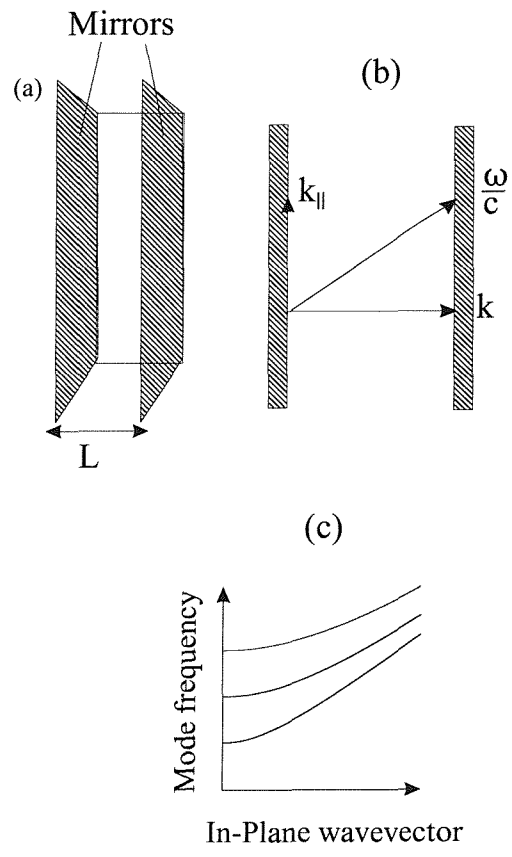

Figure 6.16: (a) A schematic of a Fabry-Prot etalon, (b) top view of etalon with light incident at an angle θ, (c) Graph of frequency versus parallel wavevector of incident light.

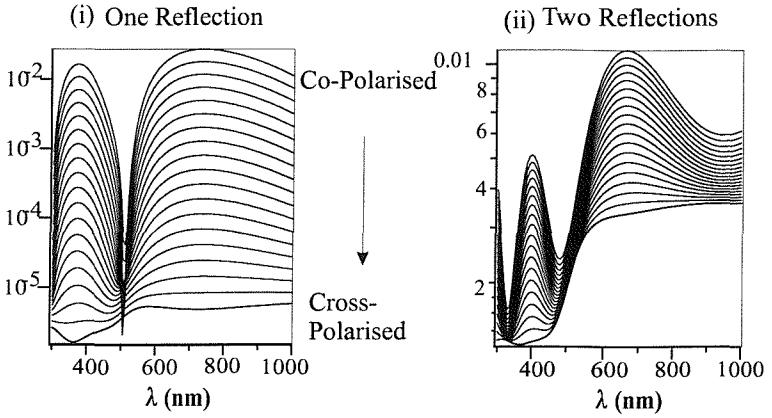

Figure 6.17: Polarisation sensitive features for (i) one an (ii) two reflections for normal incidence from a void 700nm diameter and thickness 350nm. Graphs show a fixed input polarisation angle (ψ) with the angle of the analyser rotated from co-polarised to cross-polarised with respect to the input polarisation in 5^o steps with the graphs off-set on a log scale down each graph.

identical to the one modelled above. The input polarisation angle is varied between 0^o and 90^o in 5^o steps with the analyser rotated between 0^o and 90^o for each of the chosen input polarisation angles. Starting with the less complex simulation first; normal incidence and input polarisation angles 0^o, 45^o and 90^o. The single reflection model shows that for all input polarisation angles Fig. 6.17 the strongest dips in reflectivity occurs when the analyser is co-polarised with respect to the incident rays. In all cases the features remain at the same wavelength; only their relative strength changes. In this first instance of normal incidence reflections, the independence of the response to input azimuthal angle is a convincing argument of the model's accuracy.

In the case of an angle of incidence of 45^o (Fig. 6.18) the reflectivity minima are less pronounced than those observed at normal incidence. Also for cross-polarised analysis, the bulk reflectivity of gold is recovered. Simulations also show that the response is insensitive to the azimuthal angle for co-polarised analysis.

6.1.3 Conclusion

Using a geometric model for ray paths of light incident on a spherical void we have built a model which shows spectral features due to interference. We have shown that these interference dips shift as a function of film thickness, incident polarisation and angle of incidence. We will later show how the model can account for some features

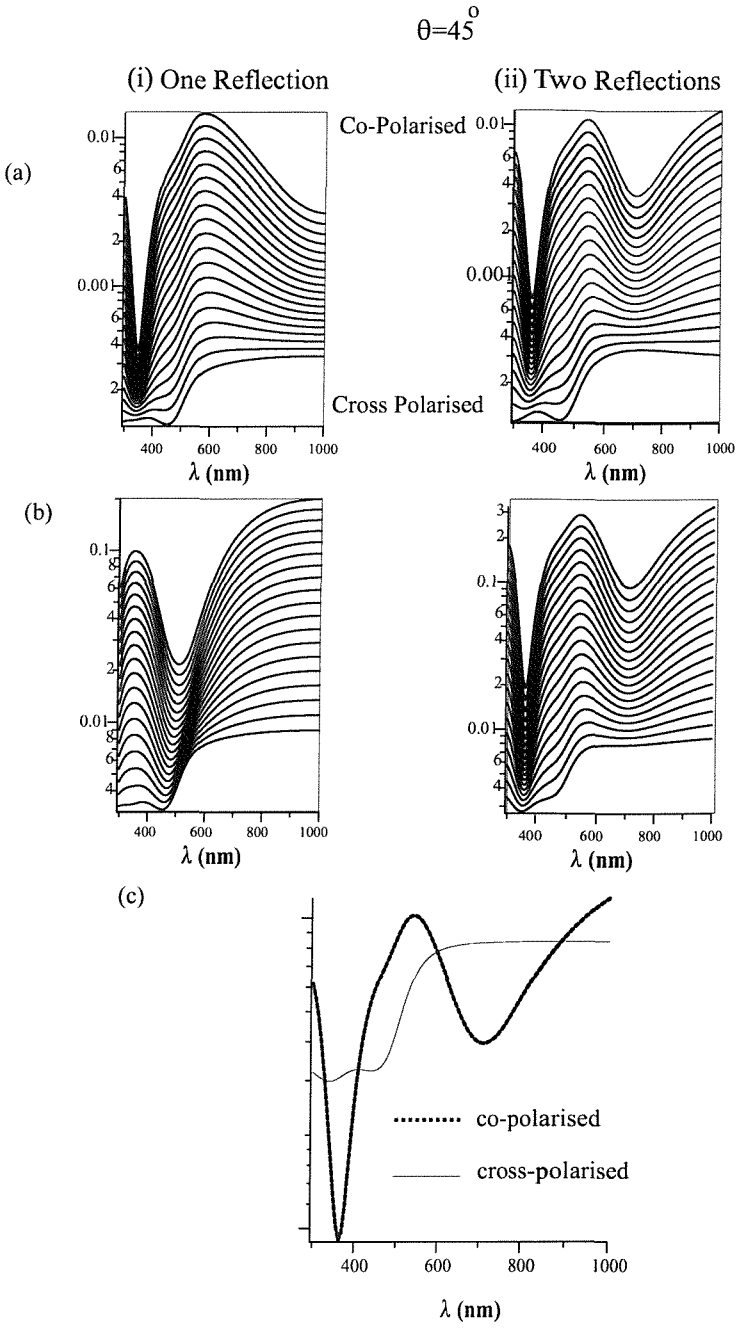

Figure 6.18: Polarisation sensitive features for (i) one and (ii) two reflections for 45^o incidence from a void 700nm diameter and thickness 350nm. Graphs show a fixed input polarisation angle (ϕ) with the angle of the analyser rotated from co-polarised to cross-polarised in 5^o steps with the graphs off-set on a log scale descending towards to cross-polarisation. Input polarisation angle (a) 0^o, (b)90^o, (c)Co-and crossed polarised response for input polarisation angles 0^o and 90^o for two reflection model.

in our experimental data. Such interference phenomena have not been previously observed in sub-micron structured mirrors.

6.2 Confined Plasmon Model

The approach of using ray optics is a first basis for describing the response of mono-layered macroporous films to light. However, as discussed earlier in chapter 4, many of the first samples to be made had more than one sphere layer, causing the pore mouths to exhibit increasing eccentricity with increasing film thickness. Some of these samples showed strong dips in reflectivity (section 7.2), which cannot be adequately explained using ray optics. Before discussing the more recent approach of using FDTD methods (section 6.5), the approach of solving the problem of a complete spherical void in a metal for a sphere of size comparable with the scattering wavelengths is described (section 3.2.1). Such a description is difficult and unsatisfactory as light cannot couple to these modes. However, in the case of samples produced through a many layered template with highly eccentric pore mouths (section 4.2.2), some agreement between this approach and experimental data was found.

Before discussing the exact model, a qualitative idea of the problem can be obtained from considering the plasmon energies of very small voids by analogy to the energies of a small sphere [172]. Voids posses a surface plasmon mode in which the free electron gas executes radial oscillations around the cavity. The dispersion relation for a void is given by [172]:

$$\omega_\ell = \omega_p \left(\frac{l+1}{2l+1} \right)^{1/2}, \ell = 0, 1, 2, 3 \tag{6.53}$$

where ω_p is the plasmon energy of the metal

Similarly, the relation for a metallic sphere is given by the expression.

$$\omega_\ell = \omega_p \left(\frac{l}{2l+1} \right)^{1/2}, \ell = 1, 2, 3 \tag{6.54}$$

In both cases ℓ is an angular quantum number denoting a spherical harmonic charge oscillation (Fig. 6.19(b)). The slight mathematical difference between these two equations has a significant difference in the energy levels of the two "particles".

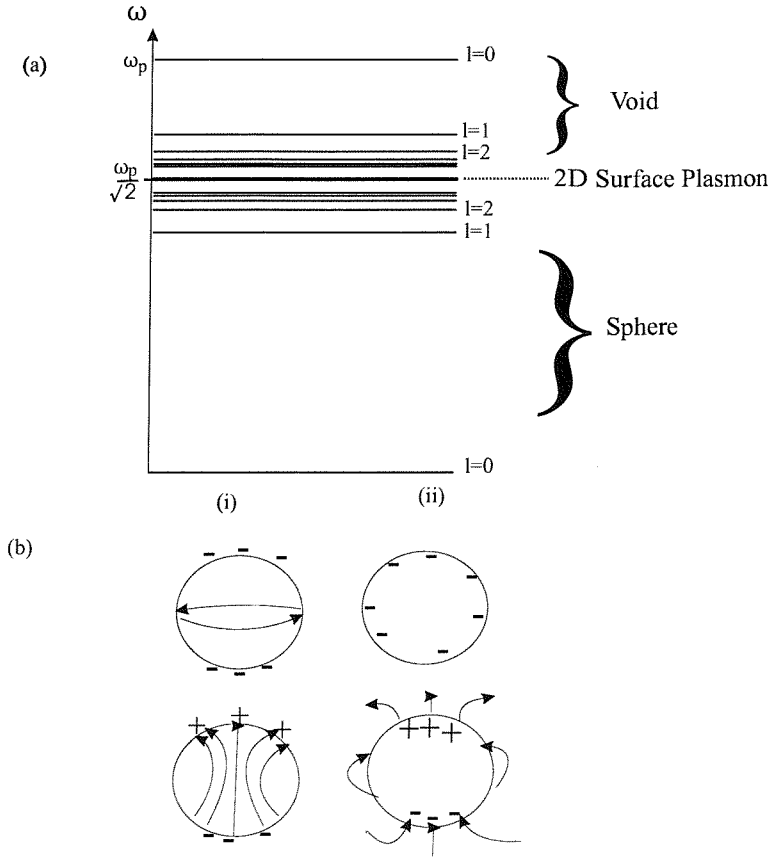

Figure 6.19: (a) Energies of possible surface plasmon quanta of a spherical metallic particle (bottom half) and a spherical void (top half). For large ℓ both converge to the limit $\omega_p/\sqrt{2}$. (b) Mode patterns of around (i) a void and (ii) a sphere for values of $\ell = 0$ and 1.

Both equations show that for increasing values of ℓ, the energy of both tends towards that of a flat surface plasmon of $\omega_p/\sqrt{2}$. However, the frequencies of the voids are shifted above this value, whereas for a sphere they are shifted below (Fig. 6.19(a)). Metallic voids and spheres have very different surface plasmon spectral responses, especially evident in the absence of an $\ell = 0$ mode in the case of spheres. The $\ell = 0$ mode around a void is referred to as a "breathing mode", corresponding to a radially symmetric oscillation with zero field inside the void. In the surrounding metal the field is equal to that of a central point charge oscillating at the plasma frequency. This modes is a surface oscillation with fields and currents that decay away from the centre. The $\ell = 0$ mode for a sphere would correspond to a static ($\omega = 0$) accumulation of charge, which would have to be provided from an external source and would also require a sink of electrons at the sphere centre, which is unphysical.

The above model shows that voids could have as interesting a response to light as nanoparticles. Their behaviour has not been well studied because of the difficulty in making samples. The approach of making hemispherical voids electrochemically offers a way of producing such voids. In the instance of large voids (> 50nm) the electrostatic solutions outlined above are not valid and instead attention is focussed on equation 3.48, which satisfies the continuity of the tangential field components for a spherical particle. In the case of a void, the order of the dielectric functions are reversed. The solution for a void of radius, a, in an infinite metallic medium is given by.

$$\epsilon(\omega)H_\ell(k_m a)[k_i a J_\ell(k_i a)]' - \epsilon_i J_\ell(k_i a)[k_m a H_\ell(k_m a)]' = 0 \qquad (6.55)$$

J_ℓ and H_ℓ are spherical Bessel and Hankel functions and the prime denotes differentiation with respect to (ka), ϵ_i and ϵ_m are the dielectric constants inside and outside the void with $k_i = \sqrt{\epsilon_i}\omega/c$ and $k_m = \sqrt{\epsilon_i}\omega/c$ the corresponding wave numbers. It is assumed that $\epsilon_i = 1$ and that $\epsilon(\omega) = 1 - \omega_p^2/\omega^2$, i.e. an ideal metal, although we have used the full dielectric response in recent calculations. To simplify the calculations all frequencies are expressed in units of ω_p, so that solutions to equation 6.55 depend only on the angular momentum quantum number, ℓ, and the void radius, expressed as $R = a\omega_p/c = 2\pi a/\lambda_p$. From symmetry requirements all solutions have to be degenerate with respect to the azimuthal quantum number, m.

Applying eqn. 6.55 to the case of gold voids and spheres with different submicron radii shows that voids are indeed shifted above the surface plasmon dispersion in energy, while the modes in spheres are shifted below this dispersion(Fig. 6.2). Although at first sight this would seem to suggest that voids have modes which can couple to light, in practice plasmon modesin a void are non radiative because their electromagnetic field cannot radiate into the metal because of its negative dielectric function [174]. However, these calculations are confirmed by [174], which models metallic nanoshells and finds eigenmodes of the system with the characteristics similar to those shown in Fig. 6.2.

The experimental data which will be presented in the proceeding chapters concerns voids with the added complexity of an aperture. Initial investigations suggest that

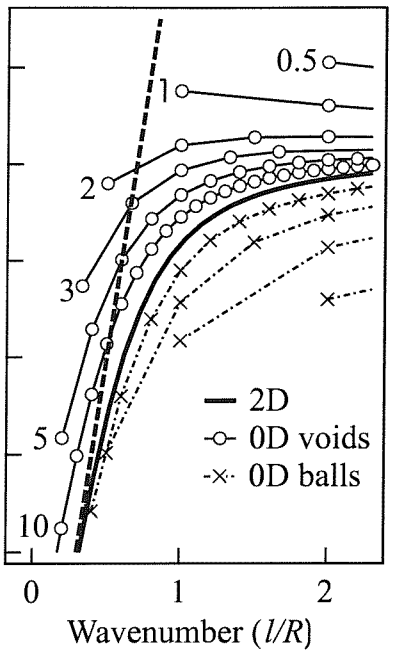

Figure 6.20: Calculated surface plasmon modes of voids and spheres made of gold for different radii and angular momentum. The thick line denotes the 2D flat surface plasmon dispersion and the dashed line denotes the photon dispersion in air.

the spherical harmonic solutions are concentrated around the equator of the void and so perturbed relatively little by the top aperture. These modes have maximum quantum number $|m| = \ell$ as shown by Fig. 6.21, and the presence of the aperture is hypothesized to break the m degeneracy, complicating the mode structure. Of great interest is the degree to which such modes become localised inside cavities which progress from an open cavity geometry to a closed spherical cavity.

6.3 Two dimensional Grating

An array of three dimensional voids exhibits two dimensional grating effects. In the case of close packed spheres, two planes spacing distances are of importance (Fig. 6.22(a)). The figure shows that the planes are spaced more closely together than the diameter of the spheres. The plane spacing distances, $\Lambda_{1,2}$, for a close packed array of spheres of diameter, d, are given by:

$$\Lambda_1 = d/2, \quad \Lambda_2 = \sqrt{3}d/2 \tag{6.56}$$

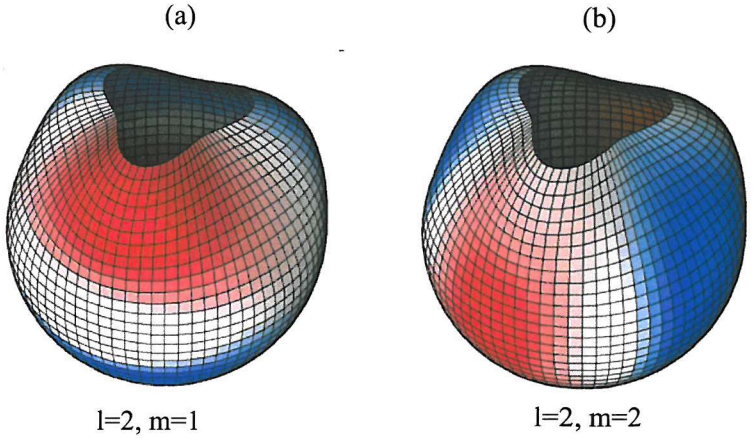

Figure 6.21: Calculated radial electric fields on the void surface for $\ell, m = (2, 1)$ $(2, 2)$ with the red areas indicating strong concentrations of positive charge and blue negative charge.

The effect of this is to shift the energy at which diffraction occurs above that of what would be expected from a one dimensional grating of period, d (Fig. 6.22(b)). Considering the case of voids of 700nm in comparison with a grating of period 700nm it is found that diffraction occurs above both 606nm and 350nm for the spherical void array and 700nm for the grating. The second issue to consider about arrays of spheres is how strongly they should diffract. The high degree of symmetry in the planes themselves would suggest that diffraction would be of considerable importance. However, this effect will be highly sensitive to the degree of order across the sample. Through the use of scanning electron microscopy shown in chapter 4 the degree of irregularity in the surface is exposed as being quite high, even in the most ordered samples. It is also unclear how, if at all, the morphology of the voids contributes to the suppression or enhancement of any diffractive effects.

6.4 Plasmonic Band Gap Model

In general, three approaches exist to explain how surface morphology perturbs propagating surface plasmons; green function volume integral approach of surface defects [176], shallow gratings with a second modulation on the surface [113], or the use of high-aspect ratio structures [119]. In the case of well-ordered macroporous metals, surface plasmon states will experience perturbing effects due to the 2D

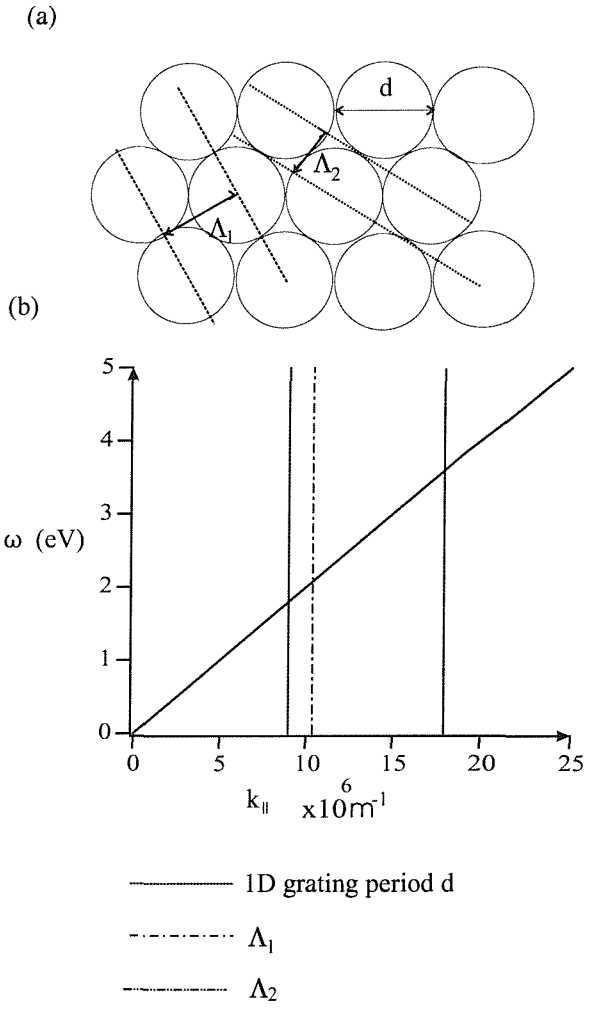

Figure 6.22: (a) Distances between adjacent planes of spheres of diameter, d, represented by Λ_1 and Λ_2 (b) Dispersion relation of light line plotted with grating momenta for a period of 700nm and an array of voids 700nm in diameter .

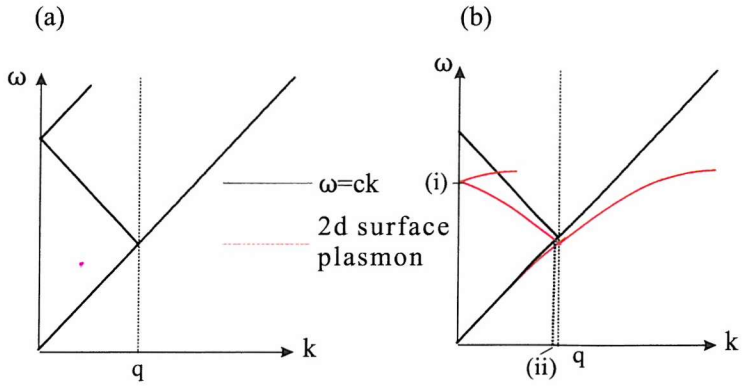

Figure 6.23: Zone folding of the dispersion relation due to a periodic surface; the 2D surface plasmon mode is assumed to be unperturbed (a) Light cone only (b) light cone and surface plasmon.

surface modulation and can, as discussed above, confine plasmons in the voids. In common with most other surface plasmon phenomena, these states are only accessible with TM polarisation. Therefore, the approach used here will quantitively follow the approach of [113] in considering the effect of surface plasmon dispersion due to band folding effects.

The macroporous surface can be considered to act as a two dimensional grating, dispersing incident energy in the six symmetry directions. Representing the structure using the reduced zone method the diffracted light cone is shown to be folded back on itself (Fig. 6.23(a)). A structure with a periodicity of 700nm produces first order diffraction will be seen out in the infra-red, whereas the second order (where the light cone crosses the $q = 0$ line) will be seen in the visible. The surface plasmon dispersion relation will also be folded back on itself by the structure's periodicity but in this case the physics becomes more involved as it lies beneath the light cone (Fig. 6.23(b)). The plasmon will therefore be seen at longer wavelengths due to the $q = 0$ point being lower in energy for the surface plasmon (Fig. 6.23(b)(i)). However, the plasmon dispersion also crosses the light cone at a much lower energy (Fig. 6.23(b)(ii)) suggesting some plasmonic features in the infra-red. Calculations by Hooper et al [116] have shown that in the case of sinusodial gratings with groove depth comparable to the periodicity, the plasmon dispersion is perturbed very strongly, flattening it into a series of bands. However, for the purposes of simplicity the model used here will

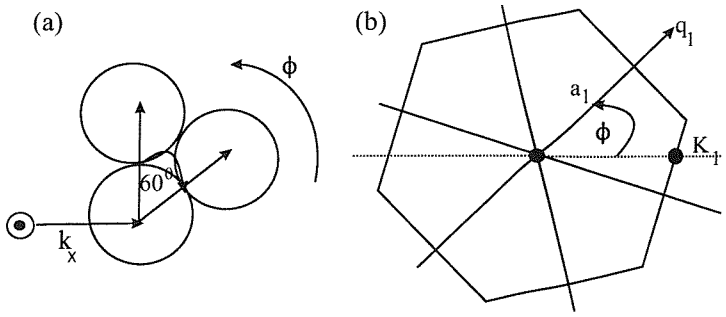

Figure 6.24: (a)Top view of incident TM light on a close-packed template. (b) Top view of k-space representation of the system.

not attempt to take into account this extra effect except to note that experimental results are likely to deviate from our first order approach.

Considering the general conditions for diffraction to occur for a close packed lattice of voids, a beam incident at an angle θ and wavelength λ will have an in-plane wave vector K.

$$K = (2\pi/\lambda)\sin(\theta) = k_o sin(\theta) \tag{6.57}$$

K is oriented at an azimuthal angle, ϕ, with respect to the lattice vectors. For diffraction to occur the energy contour centred at $k = q$ must cut the point K_1, Fig. 6.24(b). The lattice momentum is denoted by q and is given by $q = 2\pi/d$, with d the spacing between the voids. The radius of the energy contour is:

$$a_1 = K_1 \cos(\phi) \tag{6.58}$$

This relationship will also be valid for the other lattice directions q_{2-6}, which can be written collectively as:

$$a_{1-6} = \pm K_1 \cos(\phi), \pm K_1 \cos(60 - \phi), \pm K_1 \cos(60 + \phi) \tag{6.59}$$

The energy of the wavevector $(q - a)$ has to match that of the incoming photons;

$$\omega(q - a) = ck_o \tag{6.60}$$

Assuming that the photon scatters in the plane, i.e. $\omega(k) = ck$ the momenta can be equated.

$$q \pm K_1 \cos(\phi) = k_o \tag{6.61}$$

This is then re-arranged to:

$$\lambda = d(1 \pm \sin(\theta)\cos(\phi)), d(1 \pm \sin(\theta)\cos(60 - \phi)), d(1 \pm \sin(\theta)\cos(60 + \phi)) \quad (6.62)$$

The plasmon energy modes are dependent on the launch direction relative to the lines of the voids as well as the angle of incidence. At normal incidence all the modes are equivalent, but at angles away from the normal the system's symmetry is broken. The symmetry breaking considerably complicates the dispersion relation shown in Fig. 6.23(b); instead of one line there are now six, all converging at point (i), which splits the degeneracy of the system creating 6 anti-crossing modes. The resulting modes calculated using the formula above for an angle of incidence 6^o are shown (Fig. 6.25), with the angle of incidence chosen judiciously for use later on. The strength of the reflectivity due to the presence of modes is indicated by the the line widths (Fig. 6.25(a)). Of course this does not reveal the true response as the surface plasmons do not have a bosonic nature, and so will exhibit anti-crossing, as shown by 2D photonic bandgap calculations (Fig. 6.25(b)). The surface plasmons are therefore scattered across the metal surface by the voids, with equivalent direction at different energies (Fig. 6.25(c)(i-ii)).

6.5 Finite Element Calculations

The first three sections of this chapter have attempted to explain the various possible features which could influence the spectral response of macroporous metals. Each approach can explain some, but not all of the features. One of the problems of obtaining a definitive model is the intricacy of the method used to calculate the exact electromagnetic response of complex materials such as photonic crystals and gratings. In the case of metallic gratings, section 3.2.2, results using FDTD calculations were carried out on 2D rather than 3D structures, vastly simplifying and reducing the computation. Recently, work has begun on attempting to produce three dimensional models using FDTD methods of the response of metallic cavities to light of approximately the same wavelength to diameter ratio as in experiments. As explained in previous chapters, the one bonus of solving Maxwell's equations is that they are scalable so results generated across one part of the spectrum apply equally to other scales.

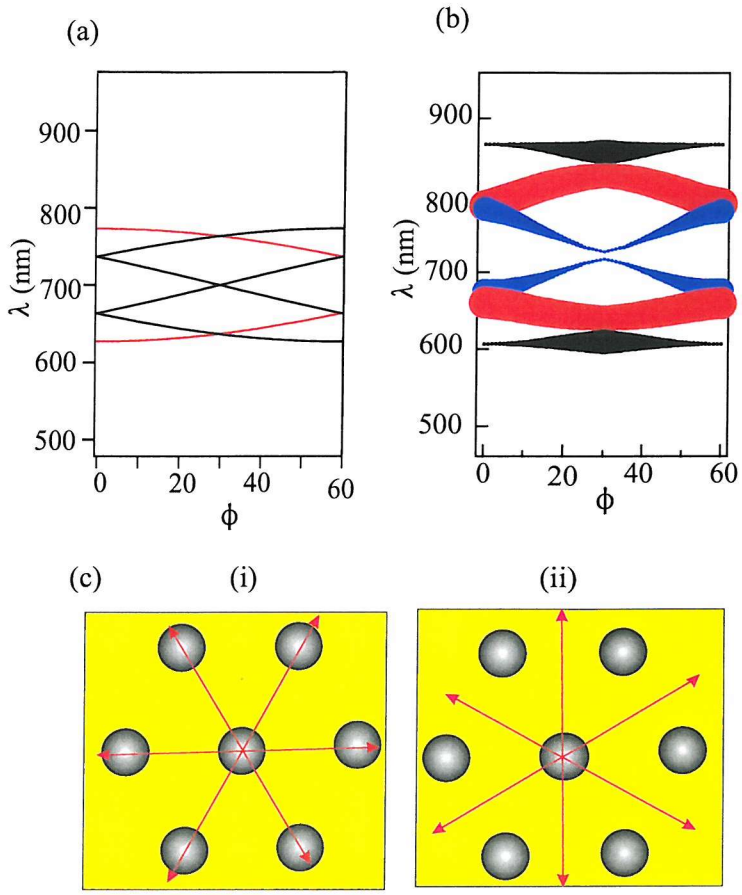

Figure 6.25: (a) Reflection modes for a two dimensional grating with a lattice constant of 700nm and angle of incidence $\theta = 6^o$, size of lines reflects the strength of each mode. (b) Calculations of a 2D dielectric photonic bandgap material with a period of 70nm. (c) Schematic of surface plasmons moving on a macroporous metallic film at (i) $\phi = 0^o, 60^o$ and (ii) $\phi = 30^o$.

Attempting to study macroporous metals using FDTD methods should answer some of the remaining questions about their response to light.

(a) How valid is the ray path model on the wavelength scale?

(b) How valid is the confined plasmon model for nearly closed voids?

(c) What interaction, if any, is there between modes inside voids and surface plasmons generated by the periodicity of the film?

(d) What effect does the aperture size and shape have on the response to light?

(e) Are there any interesting effects which can occur between multilayer voids?

(f) How good are macroporous films at concentrating electric fields in small volumes? This last point is very important for applications using Surface Enhanced Raman Spectroscopy (SERS).

Presently, these questions remain unanswered, although some progress has been made towards understanding how isolated hemispherical voids reflect light.

Chapter 7

Chameleon Response to Visible Light

The optical properties of many samples have been tested during the course of this research. In some cases samples with the same template size, metal and similar thicknesses gave distinctly dissimilar results due to differences in packing and in the number of layers of spheres in the template. This is an extremely challenging problem, producing anomalies in the film reflectivity due to random defects in the film's structure. Therefore, understanding the properties of these structures is not just a matter of comparing theory with experimental result, but choosing which samples to study. The samples will be discussed starting with the largest structures tested ($> 1\mu$m) as these are in the ray optic regime and have the most easily explained reflections. The sub-micron structures will then be discussed, first in comparison with the larger structures and then in comparison with the models developed in the last chapter.

7.1 Response of Films Patterned with Spheres Larger than a Micron - The Ray Optic Regime

Structures greater than a micron in size are large enough to be studied in detail in a reflection microscope without diffraction artefacts. The micrograph shown in Fig. 7.1(a) shows Au cavities of $\phi = 5\mu$ m and $t = 2\mu$m, in a close packed arrangement. The geometric reflection paths of incident light on a curved reflector are shown in Fig. 7.1(b). For normal incidence the rays collected in the focal plane are those that

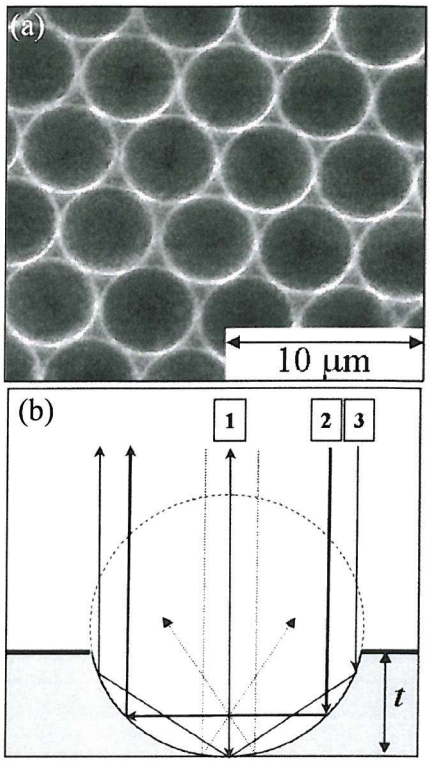

Figure 7.1: (a)SEM of a Au micro-reflector with diameter =5 m, thickness t=2 m. (b) Ray paths of reflections of an incident plane wave off the micromirror, full lines show collimated beams which are collected and dashed lines show near-axis paraxial rays which are focused inside the structure and defocused in collection.

leave the film near normaly. Rays incident on other points of the surface either leave the film at large oblique angles such that they are not collected, or are collected but focused in a different focal plane.

Contact-mode AFM measurements of two films, the Au film ($\phi = 5\mu$m, $t = 2\mu$m) shown in Fig. 7.1(b) and a Pt film ($\phi = 10\mu$m, $t = 3\mu$m) revealed significant differences in their topography (Fig. 7.2) compared to the latex template (shown dashed). Cavities in the Au film (Fig. 7.2(a)) had a smooth, spherical surface around their base, and although the upper surface undulates, the surface around the latex sphere was smooth. In contrast, the surface of the Pt sample was much rougher (Fig. 7.2(b)) for the particular deposition conditions; only the first 0.5μm thickness of the film had a smooth spherical shape. Above this the growth slowed down except for points directly between the latex spheres, producing uneven surfaces. These observations were typical of the differences between micro-reflectors of Au and Pt across samples

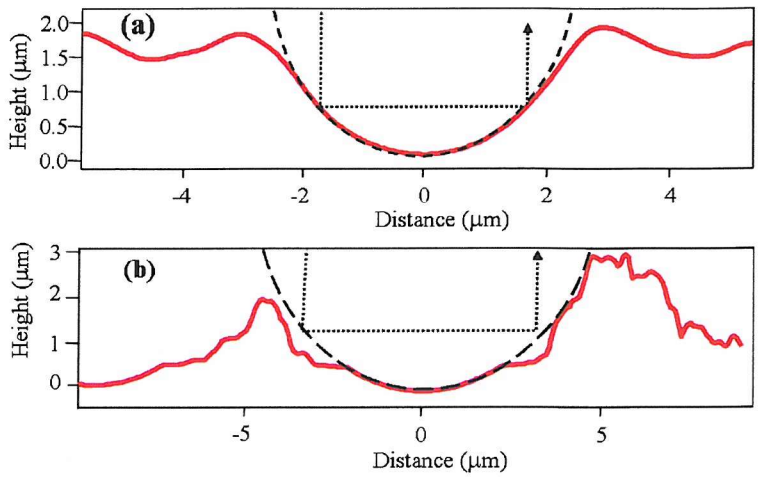

Figure 7.2: Contact-mode AFM cross-sections of (a) Au and (b) Pt films, across the centre of a cavity. The outline of the latex sphere (dashed line) and the ray path of the two-bounce reflection (dotted line) are marked.

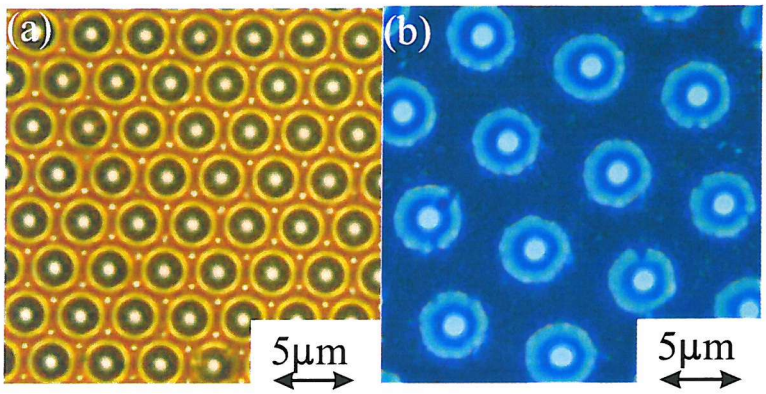

Figure 7.3: High magnification Optical micrographs of (a) Au template and (b) Pt samples

of many thousands of cavities. We found little effect in either the structure or the optical properties due to changes in the proximity between cavities, thus enabling a large variety of microcavity device designs. While the Au film could support double (and triple) bounces (Fig. 7.2(a), dotted line), the Pt mirrors showed only single bounce reflections (Fig. 7.2(b)).

Optical images of the two samples were taken with x200 magnification, (N.A. = 0.9). Bright field images of the Au cavities showed that each cavity had a bright central spot seen in the centre of a dark circle, which in turn was surrounded by a bright ring (Fig. 7.3(a)). Further out, each cavity had six hexagonally arranged bright spots around it, which are Au pillars growing up through the triangular interstices between

the latex spheres. The top surface of the film was reflective, despite the mild irregularity seen in the AFM images (and common in thick electrodeposited metal films). In contrast, bright field images of the Pt sample (Fig. 7.3(b)) showed the surrounding surface of the film was non-reflective, as suggested by the AFM scans. Dark field images showed background reflections of $< 1\%$ on the mirror surfaces confirming that their granular morphology acts to absorb the incident light. Thus, by adjusting the parameters for electrodeposition of different metals, it is possible to control whether the spherical micro-reflectors are embedded in reflecting or absorbing films, which is of considerable advantage for their application in microcavity devices since background reflection outside the microcavities can be suppressed. The surrounding rings of high reflectivity observed arise from multiple bounces that are not normally seen from spherical reflectors due to their typically small curvature, $t/\phi \ll 1$. However, for the structures here $t \sim \phi/2$, and these multiple bounce reflections were clearly present. By growing different thicknesses, the multiple bounces can be removed leaving only the central spot.

Sections of the intensity profiles for each sample, normalised with respect to a planar silver mirror, are shown in Fig. 7.4(a, b). Both showed a reflectivity greater than 100% at the centre spot, demonstrating that light was indeed focused by the curved surfaces. Dashed lines indicate the predicted position of the double bounce from a cavity with a perfect spherical structure. Good agreement between theory and experiment was found for the Au sample, whereas the Pt sample showed a separate single-bounce reflection ring off the plateau region, which was confirmed by the AFM measurements. Thus the optical quality of the metal surfaces can be directly confirmed, and used to optimise the electrochemical growth around the latex micro-molds.

The validity of the ray model was further tested by analysing the polarisation state of the reflection from the micro-mirrors. Bright-field images of the Au sample were taken through collinear polarisers (Fig. 7.5(a)) and through crossed polarisers (Fig. 7.5(b)), with the incident polarisation set to be vertical with respect to the images. Collinear polariser alignment only imaged cavity reflections which preserve the polarisation state, such as from the single reflection off the bottom of the cavity.

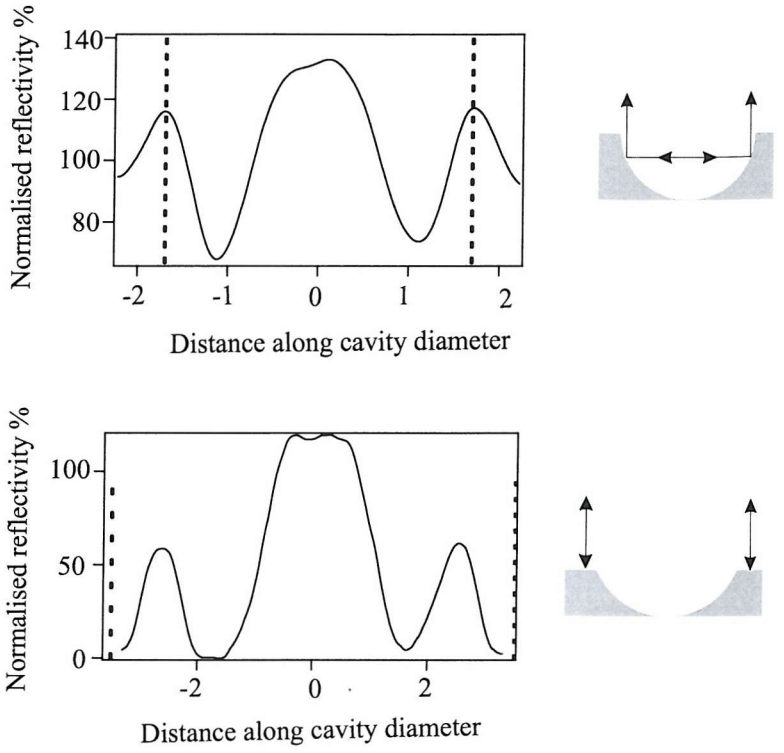

Figure 7.4: Cross-section of optical micrographs normalised with respect to an image of a silver mirror, dashed lines indicate the theoretical positions of the double bounce.

Light experiencing a multiple reflection off the sides of the cavity acquired a more complicated polarisation state depending on where on the sphere the light hit with respect to its polarisation. In the figure, the polarisation state was preserved for light hitting the top, bottom, left and right sides of the micro-reflector. At other positions on the sides of the reflector (i.e. along the diagonal orientation) the polarisation was rotated as seen in Fig. 7.5(b). In order to model this system we denote the angle, θ, as that between the incident polarisation and the point on the ring at which an incident ray hit. The origin of the polarisation rotation is geometric - at each interface the light picks up a twist in linear polarisation of due to the out-of-plane reflection geometry. Hence for the double bounce this polarisation rotation is 2θ. The intensity distribution through collinear polarisers is therefore given by $I = cos^2(2\theta)$ (Fig. 7.5(c, d)). Using the full ray model in the previous chapter (Fig. 7.5(e, f)) the predicted intensity distribution of the microcavity modelled for a co- or cross-polarised analyser (Fig. 7.5(c, d)) matched the results extremely well for both the single and double bounce reflections. The triple reflection paths have yet to be modelled using the 3

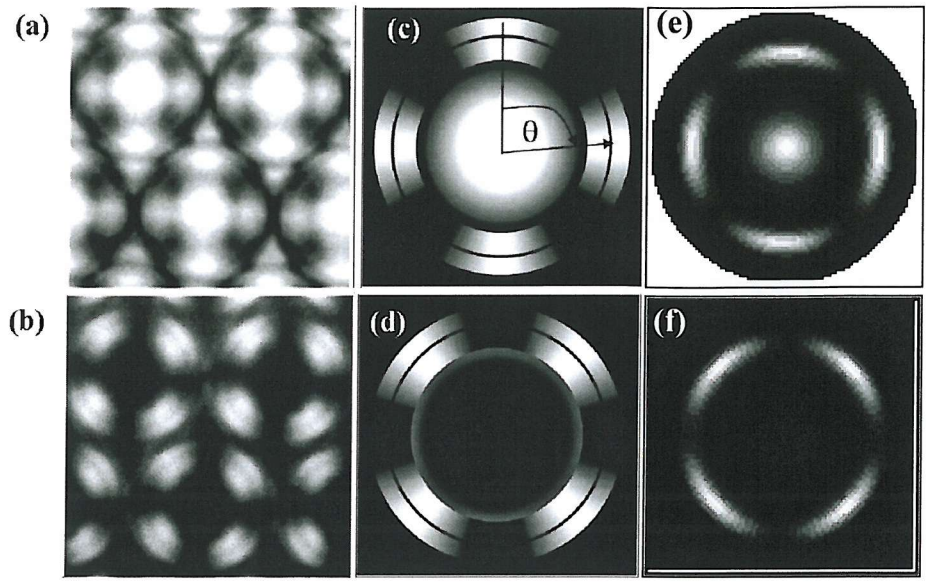

Figure 7.5: Bright field reflection images at x200 magnification of Au microcavities for (a) collinear polarisation and (b) cross-linear polarisation. (c, d) Predicted images of a cavity illuminated by plane waves, from geometric polarization rotation. (e,f) Predicted images of a cavity illuminated by plane wave from full 3D ray model.

dimensional vector model, hence the obvious discrepancies between Fig. 7.5(e, f) and the other images. As predicted, these polarisation effects observed for Au were not present for the Pt samples which had no double bounce when grown in this way. These polarisation anisotropies are thus a useful optical signature for large curvature micron-scale reflectors.

The ability to make arrays of well-ordered arrays of small reflectors has had tremendous technological potential as shown by the success of the Texas Instruments designed Digital Micromirror Device [169]. The mirrors described above are now being investigated by other members of the Ultrafast group as a possible route to make 3 dimensional mirror cavities by capping them with planar reflectors. In addition they can be filled with a wide variety of optically active materials, including liquid crystals, semiconductors, chemical dyes, fluorescently tagged biomolecules or semiconductor quantum dots. The double-bounce reflection also offers the opportunity to make Raman oscillators by exciting whispering gallery modes in embedded dielectric microspheres [170]. The model described here can also be applied to much smaller cavities (ϕ = 100nm to 950 nm) which cannot be so easily imaged optically, and

do not give such a simple ray picture due to the comparable influence of diffraction. However, the observations discussed above indicate that the ray optic model is a route to understanding the optical responses discussed below.

7.2 Disordered Samples

The local reflectivity of a macroporous Au film in Fig. 4.5 was measured using the white light laser described in section 5.1.1. The white light laser was focused to a 10μm diameter spot and the reflectivity was measured for an angle of incidence of 45^o. The amorphous microstructure suppressed diffraction, which was confirmed through the insensitivity to azimuthal rotation of the reflectivity spectra at one point (Fig. 7.6(a)), suggesting the ordering range was much less than 10μm. However, at the very edges of the sample, some well ordered regions were found, which were confirmed with the observation of a sharp six-spot diffraction pattern (Fig. 7.6(b)). The image was obtained through focusing the white light laser through a small hole in a piece of tracing paper placed just in front of the sample, so imaging the diffracted reflected beams. Subsequent measurements concentrated on the amorphous region of the sample to avoid complications arising from diffractive effects and because the edges of the sample were not graded in thickness.

Reflection spectra were taken for both TE and TM polarisation at 50μm steps along the gradient change in film thickness. The film displayed strong dips in reflectivity, up to three in number in the wavelength range $400-900$nm, with extinction ratios of up to 20dB observed for the strongest dips (Fig. 7.7(a, b)). The sharpest set of resonances, which were also coincident for the two polarisations, were observed at above radius sphere thickness to nearly a diameter thickness (r<t< 2r). Scanning electron micrographs of the sample (Fig. 4.5), along the growth gradient allowed film thickness calculation through measurement of the size and shape of the pore openings at the sample surface (Fig. 7.8). The extracted energies of the dips are shown in (Fig. 7.7(c,d)) for the two polarisations. When the voids in the film were small, the change in energy with film thickness is small. Near half-sphere height the energies shifted rapidly to lower energies (region I), suggesting that surface plasmons orbiting

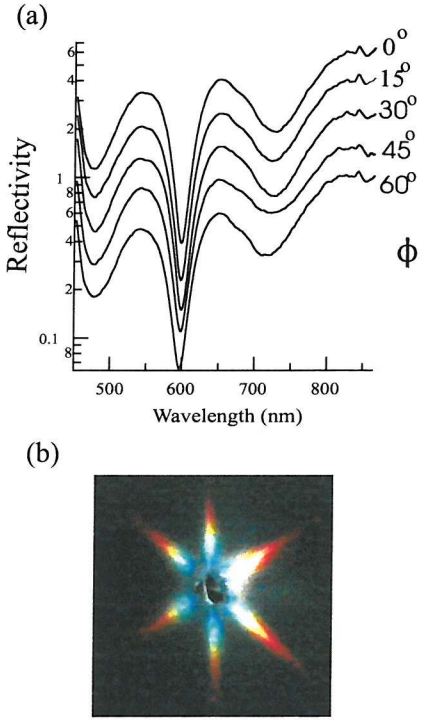

Figure 7.6: (a) Au sample reflectivity at increasing azimuthal angles (ϕ); the graphs are vertically off-set on a log scale to aid clarity. (b) Optical image of six spot diffraction pattern off an ordered part of the Au sample projected onto paper.

the rims of the voids are not responsible for the reflectivity changes because the pore circumference changes least around half-sphere height. After half sphere thickness, the energies shifted little until almost one sphere thickness (region II), again suggesting that the cavity aperture does not control the response. At the interface between the two layers of spheres the optical extinction became strong. At greater thicknesses the nanoarchitecture repeats and similar modes were observed once passed the highly eccentric region (region III).

The results presented here were shown to be in good agreement with the confined plasmon model (section 6.2). In simplifying the mathematics, the explanation of the solutions becomes somewhat more complex than is ideal. In order to test the theory, the results are plotted on the same graphs as the theoretical results. The first graph (Fig. 7.9(a)) shows a plot of energy normalised with respect to the plasmon energy of gold, taken to be $3.5eV$, with respect to the normalised radius of the voids for integer values of ℓ. The experimental results are derived for voids of radii of 200nm, 500nm, 750nm and 1000nm from samples made from many layered, weakly ordered templates.

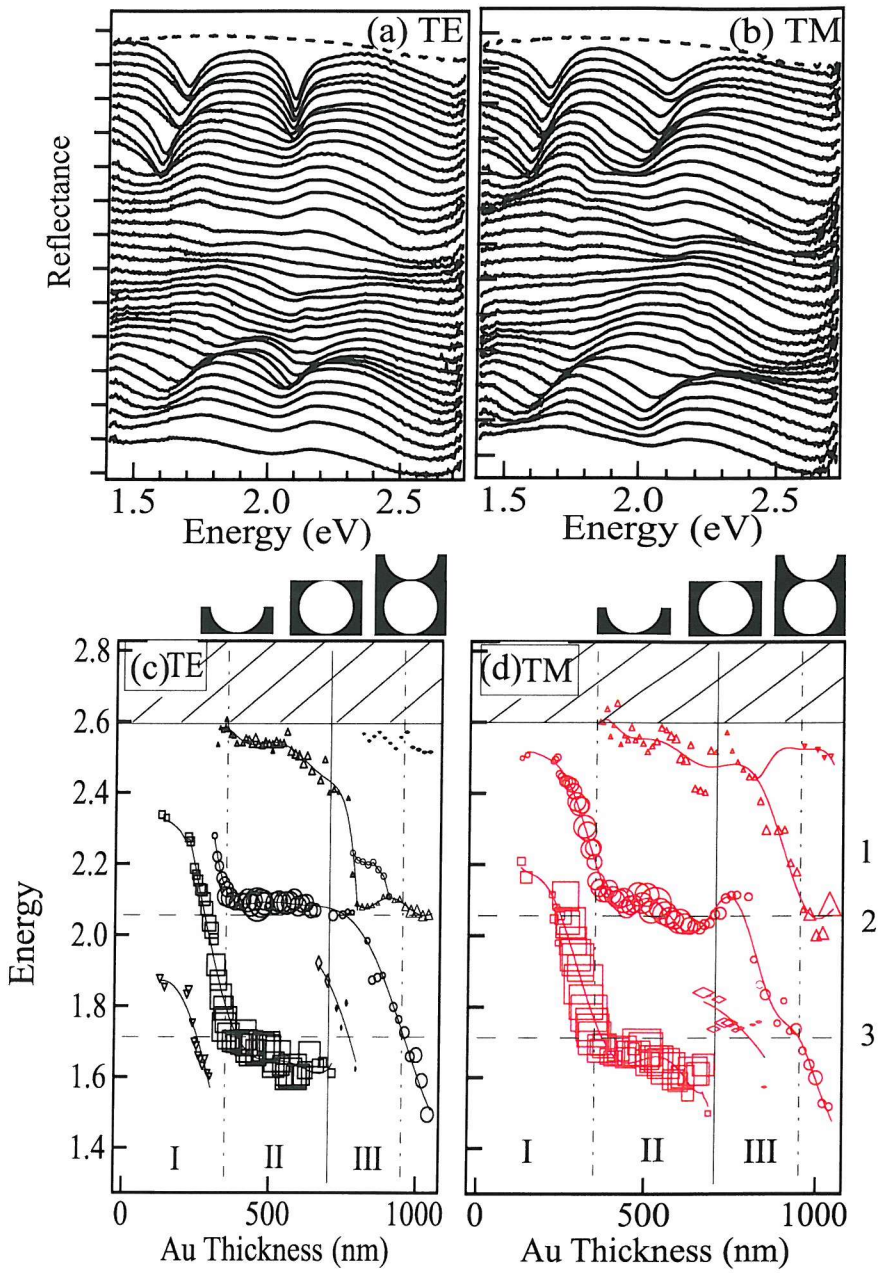

Figure 7.7: (a), (b) Reflectivity spectra on the Au sample at different locations for a a film thickness range $500 - 1100$nm for both TE and TM polarisation at 45^o with graphs off-set vertically on a logarithmic scale for clarity with film thickness increasing down the graph. The dotted line at the top of the graphs is the reflectivity signal off the un-patterned flat gold substrate. (c),(d) Extracted mode energies for TE and TM polarisation at an angle 45^o as deduced from the position of reflectivity minima above. The symbol size indicates the mode sharpness (depth/linewidth). The vertical lines mark the heights of $\frac{1}{2}$, 1, $\frac{3}{2}$, and above. Horizontal lines are solutions of the spherical void model for $\ell = 2, 3$.

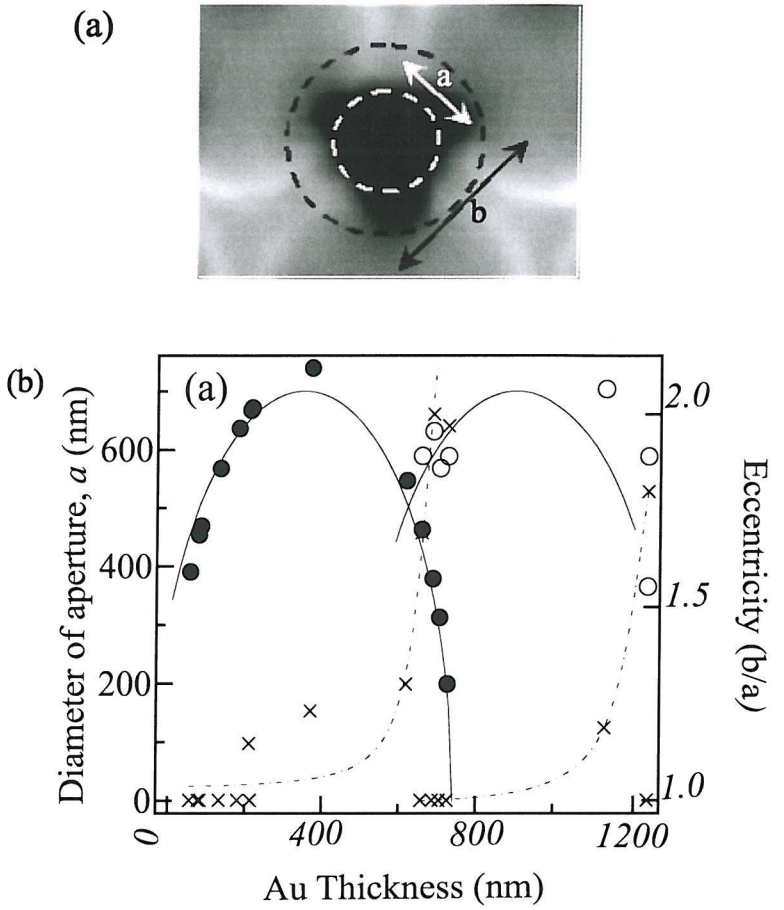

Figure 7.8: (a)Void aperture parameterised by circumscribed and inscribed diameters. (b) Aperture characteristics for different Au thicknesses defined by the minimum aperture defined by the minimum aperture diameter for the lowest (•) and second (○) layers and their eccentricity (×). The lines are a guide to the eye.

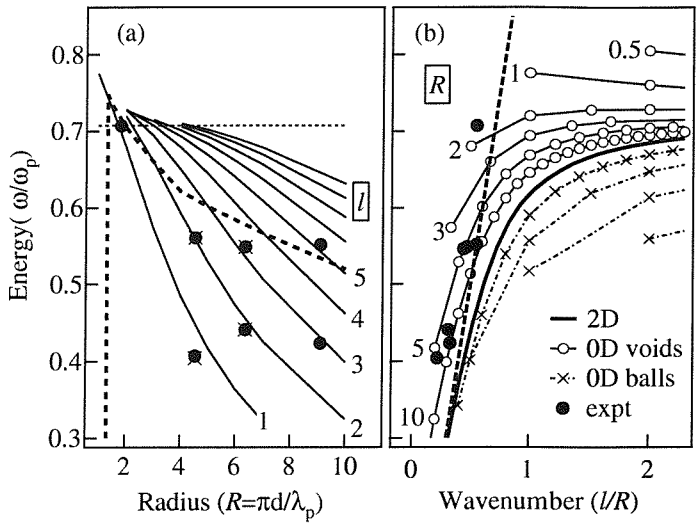

Figure 7.9: (a) Calculated energy, normalised to 3D plasmon energy for different radius, labeled by angular momentum ℓ. The region below the dashed line indicates states which interact with incoming photons. The experimental points are plotted first on this graph and their corresponding angular momentum number found, and then plotted on graph (b) (b) Localised plasmon energy for Gold spheres and voids for different radii and angular momentum. The thick line denotes 2D SPP dispersion curve and the dashed line denotes photon dispersion in air. Interactions to the left of the light line strongly interact with incoming photons. All our experimental points lie to the left of the line, confirming strong absorption resonances.

The thin dotted line indicates the limiting value of the flat surface plasmon which increasing values of ℓ tend to. The two thick dashed lines indicate the parts of the curves which are accessible to light. Of particular interest are the results for $R = 6.5$ (corresponding to a void diameter of 750nm) which map onto the $\ell = 2, 3$ lines.

The calculated plasmon dispersions for values of normalised radius R from experiment, are plotted as a function of ℓ/R which is dimensionally equivalent to wave number (Fig. 7.9(b)). In the limit of large radii voids ($R \gg 1$) the surface is effectively flat on the scale of the plasmon wavelength (λ_p) and the dispersions lie on top of the 2D planar surface plasmon curve (thick black line). For finite values of R, the dispersion curves are shifted above the planar values, as was shown above for very small voids. This is in contrast to the dispersion behaviour of spheres, whose values are shifted below the planar values (shown by dot-dashed lines). The dashed line in Fig. 7.9(b) indicates the dispersion of light in air, which in a 2D geometry separates

modes which can decay radiatively on the left to those to the right of it which only have an evanescent component. Although, this is not strictly the case in 3D, as any angular momentum state can couple to external plane waves, the light line should separate states which couple strongly and those which couple weakly. The angular momentum derived from Fig. 7.9(a) assigns the angular momentum ℓ of the observed dips in reflectivity which allows them to be plotted on the dispersion curve. The expectation that preferential coupling to states to the left of the light line is borne out through plotting these results on the dispersion curve, where they all lie to the left of the line.

The experimental results show that the reflectivity dips did not shift much for film thicknesses above radius height, suggesting that the spherical harmonic solutions are concentrated around the equator of the void and so perturbed relatively little by the top aperture. These modes have maximum quantum number $|m| = \ell$ as shown previously (Fig. 6.21). The presence of the aperture is hypothesized to break the m degeneracy, complicating the mode structure. Of great interest is the degree to which such modes become localised inside cavities which progress from an open cavity geometry to a closed spherical cavity. Furthermore, as is discussed later, the samples which showed these results did not exhibit azimuthal dependence, suggesting that the ordering of the initial template was not sufficient to induce grating surface plasmons.

This model is further supported by experimental results which show that for Au films grown above half-sphere height have modes which are independent of film thickness but for metals with large complex dielectric functions, such as Pt and Co, no dips in reflectivity are observed. A macroporous sample of polyaniline was also shown to lack the features described above. Initially, the reason for the differences were ascribed to the dielectric properties of Au being able to support surface plasmon modes and the more lossy characteristics of Pt and Co (or the absence of charge carriers in the case of polyaniline) rendering them unable to do so. Although this claim remains correct, in the light of subsequent findings, notably the discovery of unsmooth metallic surfaces of Ag and Pt and the presence of residual latex in the voids, it does not explain fully the optical properties of any of these samples in their entirety.

7.3 Transmission Through Thin Films

The ability to electrodeposit gold films onto Indium Tin Oxide (ITO) raised the possibility of testing the transmission properties of macroporous gold films in a similar fashion to the discoveries mentioned in section 3.2.3. However, the transmission properties of the films proved to be less eye-catching than expected, with reflection/transmission measurements on the same point on gold samples showing that very little light is transmitted by the metal (Fig. 7.10) for a 240nm thick film grown through a latex sphere template of 750nm diameters. One issue to contend with in this experiment was how to quantify exactly how much light is reflected and how much is transmitted, especially as the two light levels differ markedly from one another. A reasonably good estimate of the relative intensities can be achieved from measuring the reference beam relative to each signal and taking into account the amount of attenuation required before the spectrometer, which assumes the light level of the reference was stable throughout the course of the experiment.

The results show that the transmission is extremely small in relation to the reflected signal and that it cannot be used to explain the dips observed in reflectivity (Fig. 7.10). The sample was also reversed and the reflectivity and transmission measured from the backside. The transmission spectra stayed very much similar and the reflectivity was that of bulk gold. Therefore, the dips in reflectivity are due entirely to the front face of the sample and the surface plasmon coupling responsible for the discovery of enhanced transmission [4] is not present in this case. Also shown, is the theoretical fit for white light transmission through a 200nm thick flat uniform gold film . The result shows that the theoretical fit is reasonably accurate which suggests that the transmission is not helped by the presence of small holes at the bottom of the film (see Chapter 4). However, as this experiment has yet to be tested on a well-ordered template it is premature to dismiss the idea of surface plasmon interaction in enhancing transmission.

As an attempt to understand how light penetrates a void structure a simulation of the expected intensity distribution through a void of 750nm diameter latex sphere assumed to be grown to a thickness of half the diameter for simplicity. For each point

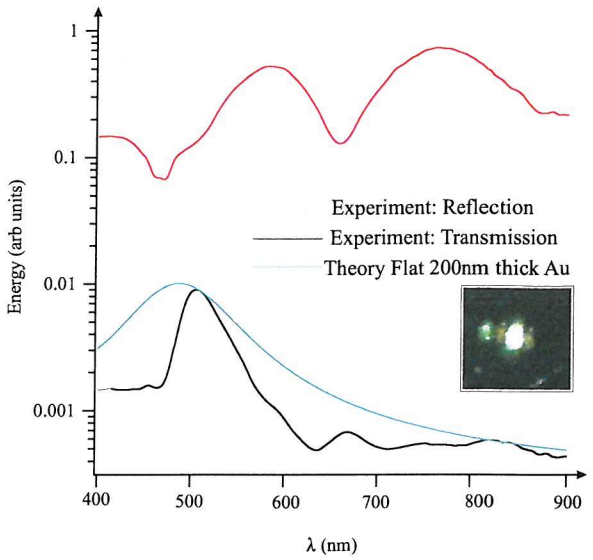

Figure 7.10: Reflection/Transmission experiments from the same point on a gold sample, grown through a 750nm diameter latex sphere template to a pore mouth diameter of 575nm, corresponding to a thickness of 240nm. Also so shown expected intensity for a uniform gold sample 200nm thick using the exact dielectric constants. Inset: picture showing transmission of white light continuum.

along the void the intensity is calculated using

$$Intensity = \exp(-2t/\delta(\lambda)) \tag{7.1}$$

where t is the film thickness, δ is the penetration depth and λ the incident wavelength. First, the intensity distribution from each part of the void is calculated for a wavelength of 500nm (Fig. 7.11(a)). The intensity distribution is highly concentrated in the region around the base of the void where the metal at its thinnest. Confirmation of this is found in the FWHM of the distribution, which is found at a void thickness of only 64nm. This suggests that this method will exaggerate the transmission intensity and is confirmed through comparison of the two theoretical wavelength dependent intensities (Fig. 7.11(b)). Assuming a plane wavefront incident on the back of the void, the intensity predicted for a void of thickness 375nm is almost an order of magnitude greater than that predicted by a 200nm thick film and also that found experimentally. This result suggests incident light experiences an average penetration depth when incident on wavelength scale voids. In light of the

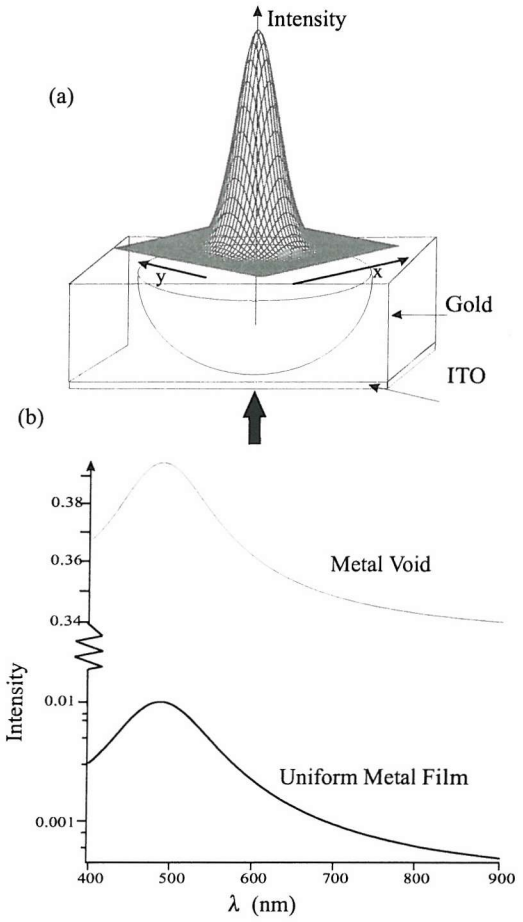

Figure 7.11: (a) Simulation of transmission through a void shows that the intensity distribution is concentrated at the centre of a void of pore mouth diameter 750nm. (b) Wavelength dependent intensity for a metal hemsipherical void and a uniform slab of gold 200nm thick.

result from periodic hole structures this also suggests that surface plasmon coupling between the two sides of Au films on ITO is not present.

7.4 Samples Viewed Under High Magnification

7.4.1 Reflection

Viewing patterned films under high magnification (×100) has already been shown to provide much insight into the properties and surface quality quality in the case of voids greater than a micron in diameter. However observations at high magnification have on occasion produced results which so far have not been explained. One of the key challenges in analysing data from self-assembled materials is to separate results

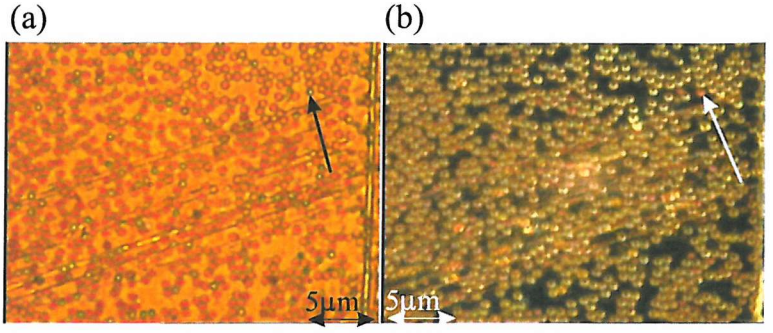

Figure 7.12: Images of the same position taken at high magnification (×100, ×2) of (a) bright field illumination and (b) dark field illumination. The two arrows indicate the same void in both images.

into those inherent to the structure in general and those arising from anomalies in the film's structure. An example to illustrate this is given here with regard to high magnification (Fig. 7.12). The same position on a Au film grown through a disordered 750nm diameter sphere template is viewed through bright field (Fig. 7.12(a)) and dark field (Fig. 7.12(b)) illumination. The sample was made when production methods had not been perfected and it was yet to be realised that latex could be left inside the voids. Coloured voids are randomly dispersed and their colour does not seem to be due to local environment. The dark field image is equally intriguing; whereas dark field images of samples are either bright, indicating a roughened surface or are dark, indicating a smooth surface, the cavities here all appear to be coloured. The arrow highlight the colour change of one void in the different illuminations. This effect was not observed in many samples, and in none of the high-quality, well-ordered monolayer samples which were treated with THF to remove the latex. Therefore, although these effects are probably linked to residual latex inside the cavities and so not immediately important in deciphering the behaviour of macroporous films, it does suggest a possible avenue for future research.

7.4.2 Transmission

High magnification images of Au films in transmission have also proved to be both revealing and intriguing. As would be expected from the transmission data presented above, Au films generally appear green and become less transmissive with increasing film thickness. Generally, when viewed in transmission the Au films appear as an

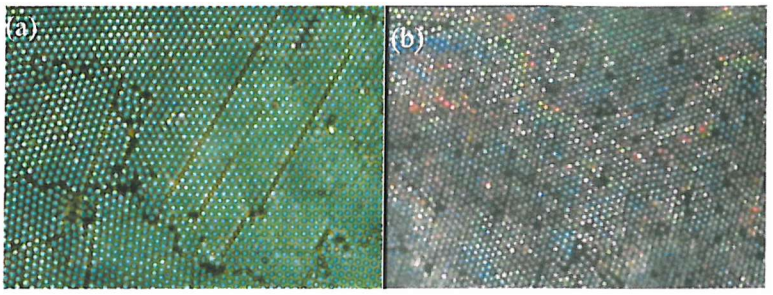

Figure 7.13: (a) High magnification through a graded gold sample with a 700nm sphere template (b)High magnification (×100) image of transmission through the disordered gold sample grown though a 750nm diameter sphere template on ITO whose spectrum was shown in Fig. 7.10.

array of green circles patterning the surface (Fig. 7.13(a)). However, as in the case of the sample discussed above there are areas which have revealed anomalies that have, as yet, not been explained (Fig. 7.13(b)). The film appears to be blue rather than the expected green with many of the voids observed to be red or orange. Again, the chief suspect in producing this rather anomalous result is the presence of residual latex as these results were only observed in earlier samples. However, although these observations were only made for a number of samples, they are intriguing enough for further study.

7.5 Conclusions

The ability to visualise the reflections off large-scale cavity structures gives some indication of the response to light of sub-wavelength cavities excluding the effect of surface modes. The inclusion of the reflectivity of highly disordered samples at an angles of incidence away from the normal suggests that as well as simple reflectivity a more complicated response of surface mode coupling can occur inside individual cavities. However, the presence of residual latex, evidenced by the high magnification images of sub-wavelength cavities, and the complicated pore mouth morphology suggests that to understand theses films more fully more control over the template formation is needed.

Chapter 8

Ordered Samples

8.1 Introduction

The steady increase in control over film quality and template ordering allowed more detailed spectroscopy and investigation into the properties of macroporous films to be conducted. In order to gain a better understanding of the samples' response to light, it was decided to concentrate on producing well-ordered monolayer templates, which would avoid the complications associated with understanding the interaction with a second layer and the pore mouth deformation seen in earlier samples. Furthermore, whereas earlier samples were tested at angles of incidence far away from the surface normal it was decided to concentrate on normal incidence reflectivity. The benefits of imaging microscopy, namely the ability to simultaneously observe and take spectra of the same point to understand how the structure's appearance changed, far outweighed the potential downsides of not accessing all the potential interactions with the sample. This chapter is split into three sections; the first presents normal incident reflectivity for gold, platinum and silver films of different thicknesses, the second describes observations of the polarisation preserving and rotating behaviour of gold and platinum films and the third gives a detailed analysis and discussion of the phenomena present. The number of samples considered is limited to only five as the complexity and range of samples is large enough to cause much confusion. The samples have been selected on the basis of film quality, ordering and their representation of the results gained in general.

8.2 Reflectivity at Normal Incidence

The reflection spectra from 700nm sphere monolayer templates of Au and Pt samples graded in thickness to 625nm for wavelengths 400nm to 900nm are shown plotted on log scales, and off-set for clarity with film thickness increasing down the page (Fig. 8.1). The Au film here was deposited onto an ITO covered glass slide and the Pt film was deposited onto a gold covered glass slide. Reflectivity data taken for a variety of Au films on both ITO and Au slides have revealed little difference in their spectral response, except at very thin film thicknesses when the backing substrate's reflectivity is noticeable. The films' reflectivity were observed through a $\times 10$ microscope objective (N.A.= 0.30). Spectra were monitored continuously along the growth gradient, spectra were taken at each point of noticeable change, hence the appearance of a linear progression along step-graded samples.

The visual appearance of both films changed dramatically with thickness, which could be followed visually by taking a series of images as a cross-section of each sample along their direction of growth (Fig. 8.1). Both films were of high quality with the cavities of both confirmed to be smooth through visual checking using the microscope's Dark Field (DF) optics. Both sets of data of spectra having two distinct regimes of response. When the films are thin (< 100nm), region I , features reminiscent of grating phenomena are observed (Fig. 8.1). The Au sample shows a sharp dip in reflectivity observed at 675nm which moves to 660nm, corresponding to the surface plasmon energy. The plasmon is observed at slightly lower energies than the calculated ones, suggesting that the grating morphology is still relevant even with shallow cavities. With Pt however, no surface plasmon effect is seen, instead a broader dip is observed with a proceeding increase in reflective efficiency, consistent with Wood's predictions. As the films become thicker (region II) dips appear in the reflectivity at short wavelengths and shift to longer wavelengths as seen in the interference model. The spectra of the Au film appears to show that the separate modes interact, with the minima in region II, suppressing the effect of the surface plasmon. As the film thickness increases further the surface plasmon disappears totally leaving only the interference dips. In the case of Pt, no interaction appears to take place between the

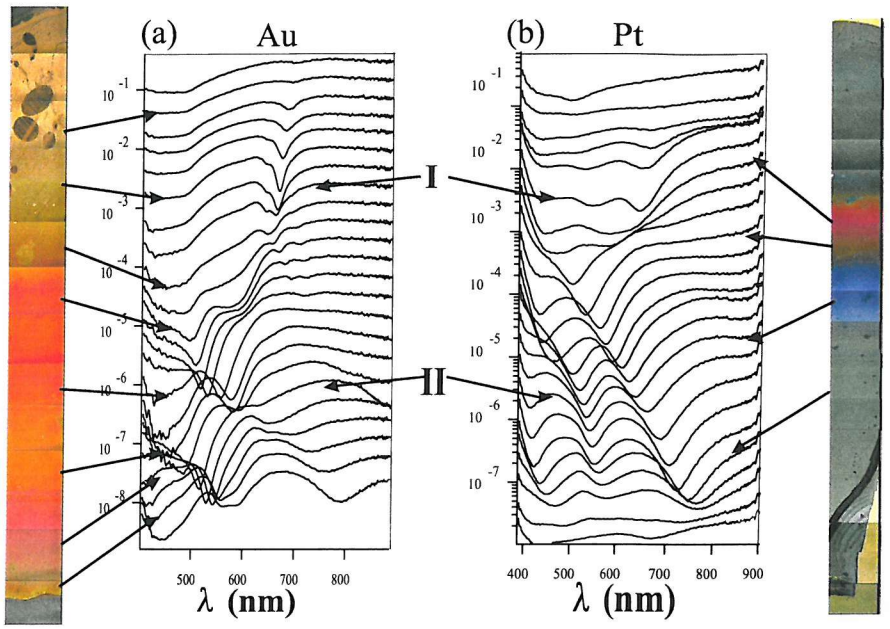

Figure 8.1: Visual appearance under ×10 magnification and reflectivity response of two digitally graded samples of Au and Pt both grown on templates composed of 700nm diameter spheres to a thickness of 620nm.The spectra are displayed on a log scale and off-set for clarity, with film thickness increasing down the page.

two effects; suggesting that Pt cannot support surface modes and that the dips in region II are indeed produced by interference effects. These results also indicate that although both sets of data are similar there are subtle differences produced by the response of the metals' surfaces.

A well-ordered sphere monolayer plated with Ag was also tested. Complications with electro-plating caused the surface quality of the film to be rougher than the samples studied above. When viewed at high magnification under DF illumination, the cavities appeared bright, suggesting surface roughening. This was confirmed through SEM measurements (Fig. 8.2) and were markedly different from those seen in (Fig. 8.1). The optical responses are once again off-set for clarity (Fig. 8.2). The main feature of interest is the dip in reflectivity very much like the behaviour shown by the Au sample above in region I above. The shape of this resonance changes little across the sample, suggesting that the resonances observed in region I of the Au sample occurred in the absence of reflectivity modes inside the cavities.

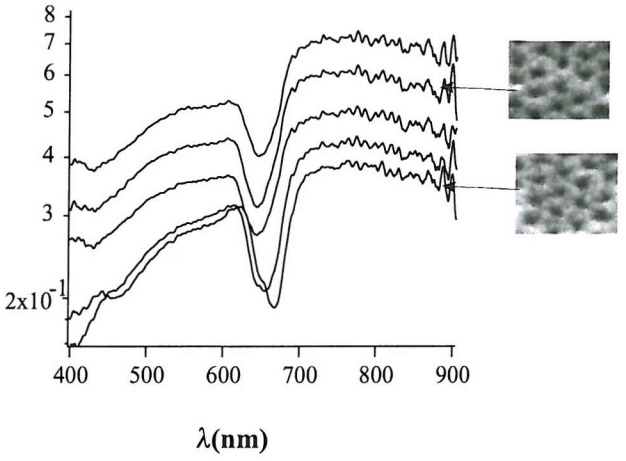

Figure 8.2: Reflection of Ag plated on a 700nm template, no interference peaks are seen, only the appearance of a reflectivity dip at around $700nm$ due to the periodicity of the cavities is observed.

Two more reflectivity spectra of step-graded samples of Au and Pt, but on templates of 500nm diameter spheres are shown (8.3) and differ markedly from one another. In the case of the Au sample, many of the same features as for the 700nm template but with two modifications. The grating periodicity is smaller and consequently the surface plasmon is found at shorter wavelengths where the reflectivity of Au begins to drop off due to absorption, diminishing the effect of the surface plasmon. Secondly, although the dips do still progress to longer wavelengths with film thickness they also appear to move together, suggesting the interference model is less valid on this size scale. The Pt sample's reflective response is very different from the other film's responses. Variation in the spectra is observed but has fewer features compared with the other films although the observed colour change is still dramatic. The reflectivity drops markedly in overall intensity as the film becomes thicker, which could suggest the film quality was not as high as for the other samples.

8.2.1 Observation Under Different Magnifications

Support for an interference explanation for some features comes from changing the numerical aperture of the objective lens. Imaging the Pt sample grown through a 700nm diameter sphere template, whose reflectivity was shown in Fig. 8.1, at different magnifications at the same point revealed that the structured reflectivity was lost at high magnification (Fig. 8.4(a)). In the case of a Au film grown through

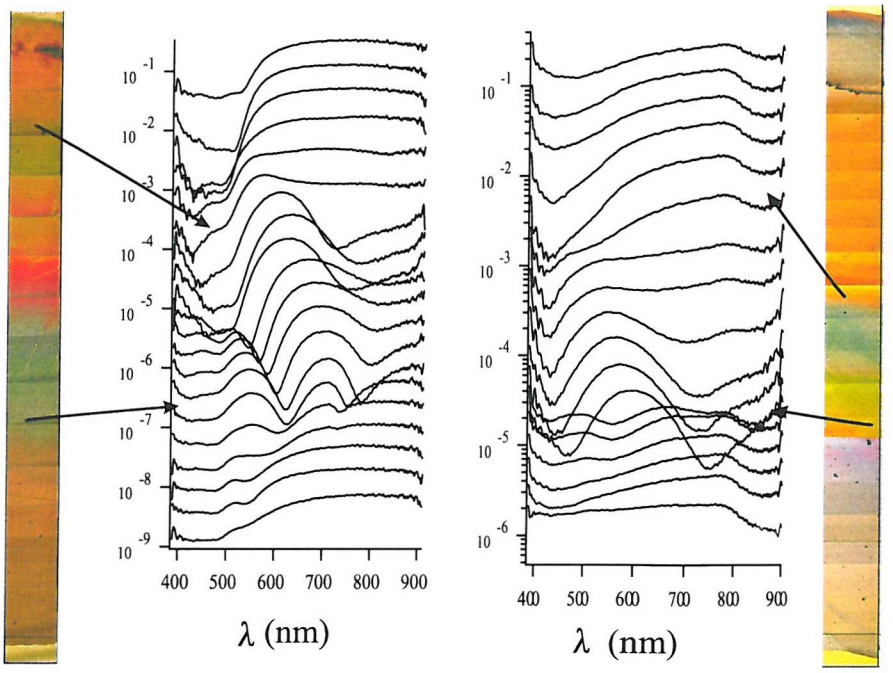

Figure 8.3: Reflectivity response of two digitally graded samples of Au and Pt both grown on templates composed of 500nm diameter spheres .The spectra are displayed on a log scale and are off-set for clarity. Film thickness increases down the page.

a disordered template of 750nm diameter spheres, the same behaviour was observed, with the highest magnification regaining the spectra of plain gold (Fig. 8.4(b)). Optical CCD images of the Au film at the same point for different magnification reveals how the film's appearance changes (Fig. 8.4(c)). There was little difference in the obtained images of (i)$\times$10 and (ii) $\times$20, at $\times$50 (iii) the individual voids begin to become recognisable, although the resolution of the CCD camera is insufficient to show this. At $\times$100 ($\times$2)(iv) individual cavities are clearly visible and appear gold in colour. The extra $\times$2 magnification is an additional magnification stage placed after collection which does not change the collection geometry but was used to obtain a higher resolution picture.

Increasing the magnification has two consequences as far as the measured reflectivity of the films are concerned. First, increasing the magnification separates individual ray paths, which increases the resolution and decreases the strength of interference effects. Secondly, the collection angle increases and so the more highly scattered rays will be observed and the sample will also experience excitation from a greater range

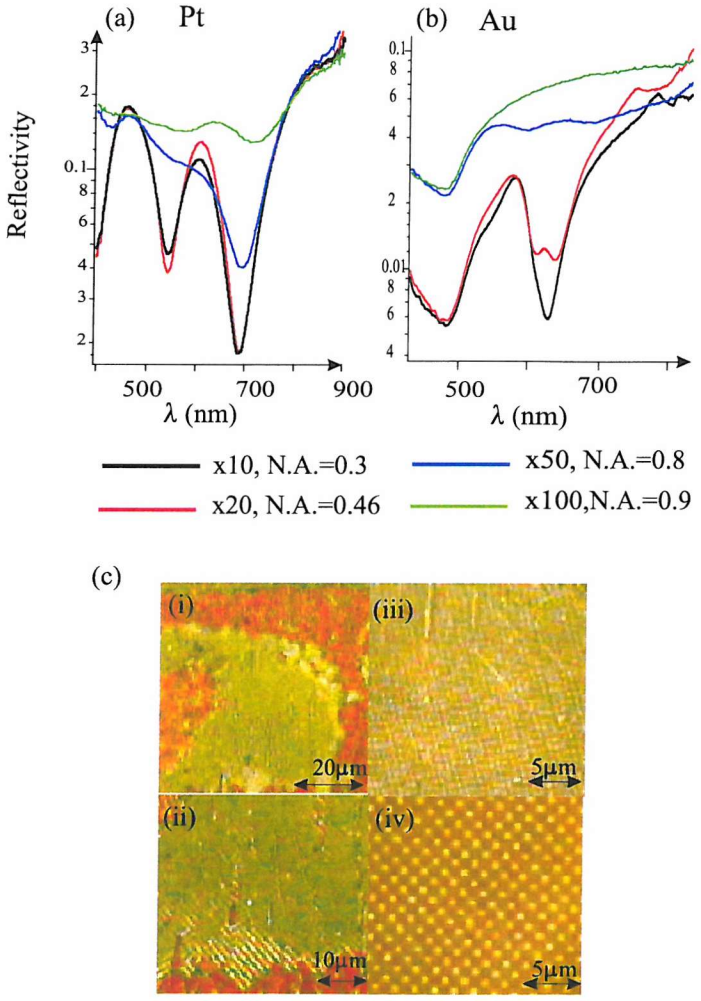

Figure 8.4: (a)A set of normal incidence reflection spectra recorded at 4 different magnifications for a 555nm thick nanostructured platinum film grown through a 700nm diameter sphere monolayer template.(b)Normal incidence reflection spectra of a disordered Au film grown through a 750nm sphere template and (c) images of the Au sample taken at the same point as the reflection spectra: (i) $\times$10, (ii)$\times$20, (iii)$\times$50, (iv)$\times$100 $\times$ 2.

of angles, which would diminish angle dependent excitation effects. Therefore any experiment which varies the magnification as well as the collection angle is incapable of establishing whether the loss of effect is due to scattering or interference effects. However, from the very high magnification image, individual cavities can be resolved, suggesting that light does still see a separate void and surface. Furthermore, the appearance of the voids as the same colour as the bulk, and the inability to resolve individual ray paths, in contrast to films with voids larger than a micron, leads us to speculate on the confirmation of the prediction of the ray model that the one reflection and two reflection paths contribute to the reflection spectra observed at lower magnifications.

8.2.2 Changing the Refractive Index Inside the film voids

The reflectivity spectra above share many of the same features as models based on interference between reflections of the top surface and from inside the cavity. To further test this hypothesis, the refractive index inside the voids was altered using index matching fluids of $n = 1.3(\pm 0.0002)$ and $n = 1.508(\pm 0.0002)$. A small drop of one of the fluids was placed on each sample followed by a cover slip to ensure an even spread of fluid. In light of experiments showing that the sub-micron macroporous films exhibit hydrophobicity, the samples were heated to ensure that the fluid filled the cavities. Visual inspection revealed that the films' colours had changed. Using imperfections in the film it was possible to find the same points to take spectra from as had been used for measurements in air. The spectra were analysed and dips from each graph were extracted and their wavelengths divided by the refractive index inside the cavity.

Both films appear as if their colours have been shifted systematically indicating that the cavities had been filled. This was confirmed through checking the contact angle of the fluids on plain gold which were found to be significantly smaller than that of water on gold. Water droplets placed on the samples were observed not to change the sample reflectivity, indicating that the cavities didn't fill. To show this, the results for a Au and Pt sample from 700nm templates are shown in Fig. 8.5. Both samples used here were deposited on Au substrates as these produced the more

robust films. After extracting the dip position and dividing by the refractive index, the data for the Pt film correlate well with the 3 sets of data showing a high degree of overlap. However, in the case of Au the refractive index of the two fluids is not used, instead a figure slightly less than n is used as these provide a better correlation between the different conditions than using the actual values. In the case of $n = 1.3$ the figure used is 1.27 and for $n = 1.5$,1.45 is used. This is not an experimental artifact, the results here are mirrored exactly with Au and Pt cavities of different sizes, again suggesting that subtle difference between voids of these metals in their response to visible light when structured on comparable length scales.

Of further interest, the grating behaviour, observed when the films are thin, shows a clear linear relationship in both the Au and Pt case. This observation has three consequences. First, it reveals the linear dependence of the surface plasmon, in the case of Au, and Wood's anomaly, in the case of Pt, on the dielectric next to the metallic surface. Secondly, it must therefore also follow that this experiment does not necessarily confirm the existence of interference behaviour for the appearance of dips in the reflectivity because the other identified phenomena have also been shown to have a linear relationship with dielectric material. Thirdly, in relation to the remarks made with respect to the "anomalous" high magnification images of Fig. 7.12 and the effect of residual latex in the voids, which has refractive index 1.59, indicates that interference could be responsible for the observed behaviour because of the difference in refractive index inside and outside of the void.

8.3 Comparison of Theory and Experiment for Normal Incidence Reflectivity

The two samples concentrated on are the two graded samples shown in Fig. 8.1. As with the experiments changing the refractive index above, extracting the position of the reflectivity dips provides the most convenient method of analysis. The film thickness was determined from pore mouth measurements from SEMs of the films at its thickest and thinnest, where the error in the calculated film thickness will be the smallest. The method of only taking spectra when there was a noticeable change

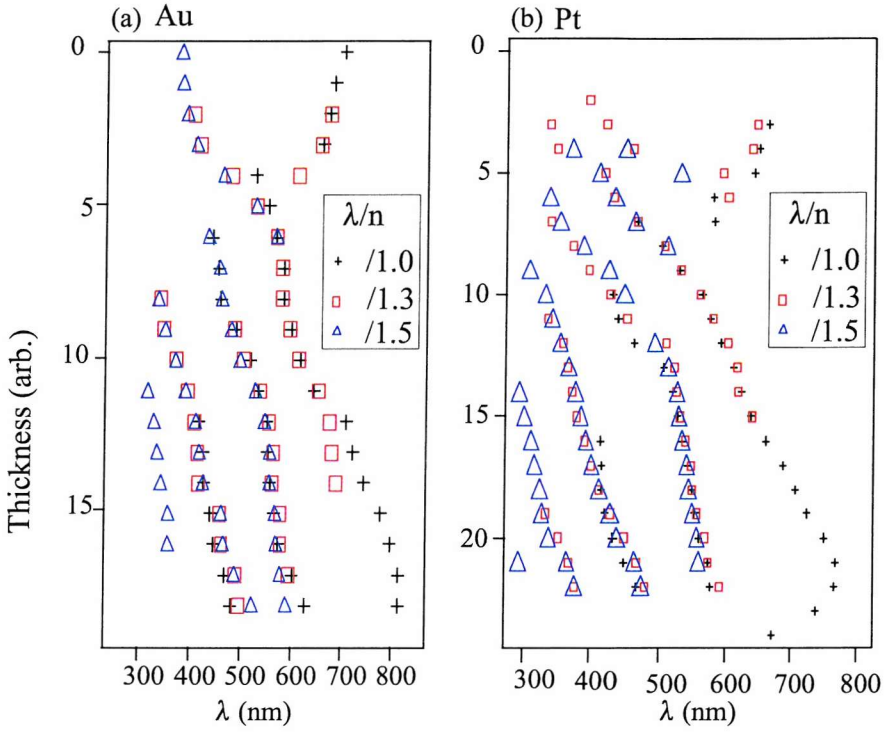

Figure 8.5: Position of dips in reflectivity spectra (in nm) as a function of position on the film, with film thickness increasing down the page for (a) Au sample and (b) Pt sample both on $700nm$ templates. In both case three sets of data are overlaid, results from refractive index $n = 1, 1.3, 1.5$ with peak position divided by the refractive index for Pt sample and by slightly less than the refractive index for Au sample.

in the spectra produced a linear progression of roughly equal spacing in thickness between each reflectivity minima. Although at first this may appear a less satisfactory method than merely measuring the film thickness at each point, the intricacies of these structures shown by the AFM measurements indicate that the relationship between pore mouth opening and film thickness are not strictly related because the metal preferentially deposits away from the latex spheres. This is therefore, the best available method to characterise these films.

8.3.1 Platinum

We shall discuss the case of platinum first as it does not show surface modes due to the presence of strong interband transitions. In contrast, gold surfaces do show surface modes, which complicates the analysis of the gold sample somewhat. Therefore, in discussing the response of a Pt film first it should be possible to separate the more complicated response on Au films into those due to responses due to the structure and those due to the metal. Returning to the theoretical discussion in chapter 6, several possible mechanisms were discussed as to the origin of the reflectivity minima; interference between different path lengths, the presence or otherwise of the Gouy phase shift and the effect of having a two dimensional grating. In order to analyse the data, reflectivity minima found in the experiments are plotted on the same film thickness vs wavelength axis as the theoretical results obtained from the two dimensional interference model for single reflections, and two reflections (Fig. 8.6). Also shown on the graph is the thickness at which two reflection interference would occur (the same for both forward $(+2)$ and backward (-2) reflections), and the wavelength below which diffraction due to the void array would be expected.

Several comments arise from Fig. 8.6, not least the difficulty in deciding which, if any, of the possible reflection paths for the interference model are closest to experimental reality. On close inspection it is clear that all three possibilities could exist. In this case it was decided from examination that the phase shift due to the Gouy anomaly (Fig. 8.6(b)) does not fit the data as well as without it (Fig. 8.6(b)). Furthermore, the discrepancy between theoretical positions of reflectivity minima due to interference and the experimental data. There are two distinct positions which show

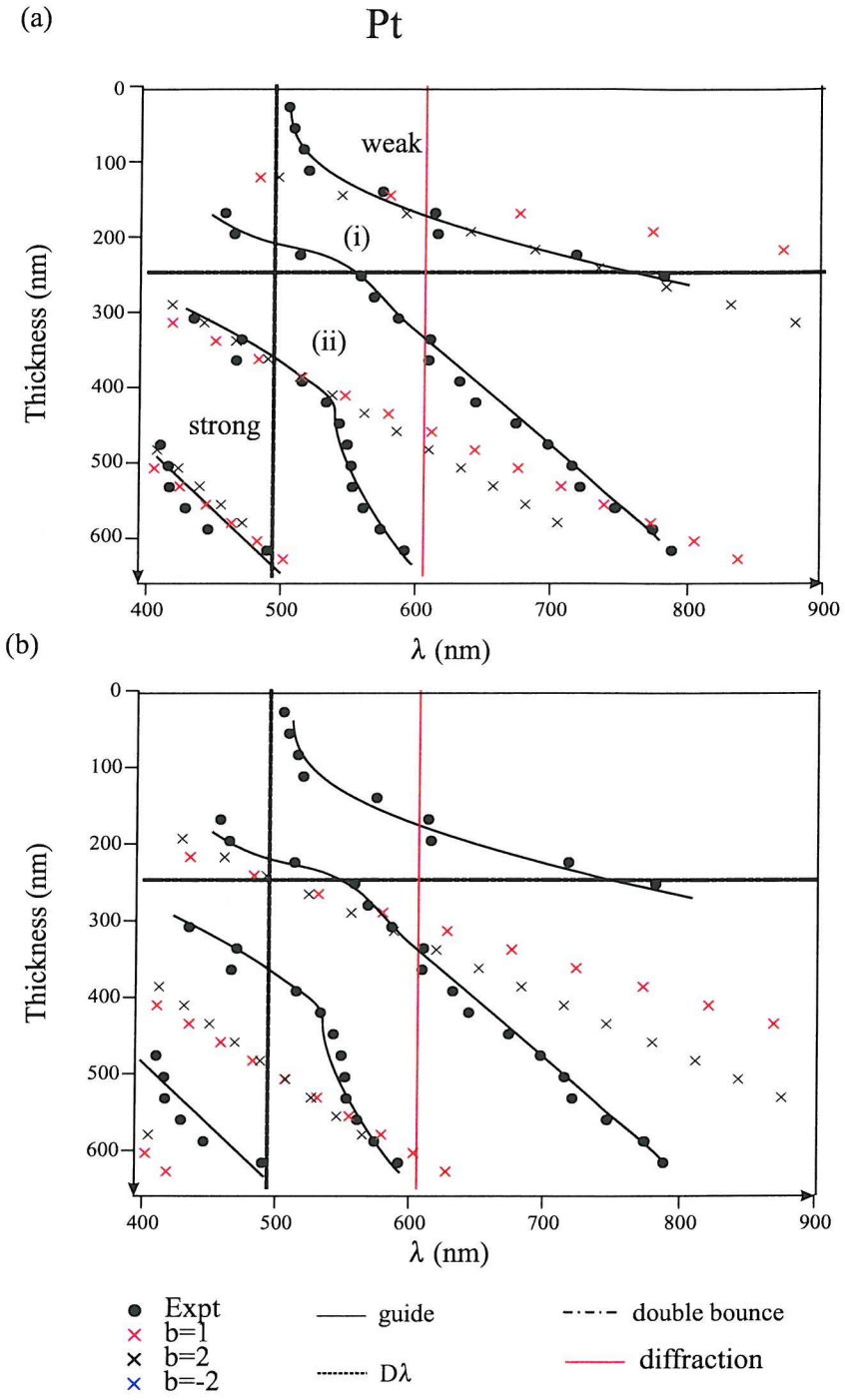

Figure 8.6: Extracted experimental reflectivity minima positions for normal incidence and theoretical reflectivity minima for 1 reflection, 2 reflections, forwards (+2) and "backwards" (−2)against extrapolated film thickness for Pt sample (Note: b= 2, −2 are the same for normal incidence). Weak and Strong refer to the relative strength of the reflectivity dips for (a) no Gouy shift and (b) with Gouy shifts. The solid lines are used as a guide to the eye only, (i) and (ii) represent "anti-crossing"points. The term "Dλ" refers to the distance between the two reflection points for two reflection interference.

significant deviation ("anti-crossing points") from the theoretical results ((i)and (ii)). This feature occurs at $\lambda \sim 500$nm, smaller than the void diameter and just larger than the distance which light travels across the sphere in the double reflection case, and is indicated on the graphs as Dλ . It is also debatable whether the point at which diffraction can occur plays a role in the anomalous regions.

It is clear that the theory of interference is qualitatively correct for metallic voids but is not quantitatively correct. There is no clear reason why experimental results deviate away from the theoretical values in the way that they do. Through comparison of the two graphs in Fig. 8.6 there is some suggestion that one of the reasons for the deviation is that wavelengths near to the value Dλ do suffer a phase shift due to focussing, whereas longer wavelengths do not appear to be focussed. The apparent agreement with theory and experiment in Fig. 8.6(a) for thin films, below the thickness at which double reflections can occur suggests the single reflection dominates here and doesn't focus reflected light. The presence of anti-crossing points strongly suggests that the interference effects are modulated by either the diffraction effects due to the surface periodicity, or more likely, the influence of the wavelength of incident light and the size of the void.

8.3.2 Gold

We now use the above observations to understand the experimental results for the Au sample graded in thickness from a 700nm diameter sphere template, with the position of reflectivity minima extracted from Fig. 8.1. Once again, considering experimental data with theoretical interference minima with Fig. 8.7(a)) and without (Fig. 8.7(b)) the effect of the Gouy phase shift are shown.

As with the Pt sample, reflectivity minima that progress towards longer wavelengths with increasing film thickness are observed in fairly good agreement with theory. However, the sample also exhibits a series of minima which appear to have little or no correlation to the film thickness (marked as (i) and (ii) on the figures). Unlike the case above, where the anomalous region was near the diffraction and length scale of the inside of the void, the anomalous region occurs around the diameter of the sphere (distance between the centres). However it should also be noted that in

the case of Au its reflectivity drops significantly around the region $\lambda \sim 500$nm and this may also explain some of the differences between Au and Pt in this part of the visible spectrum.

The two anomalous regions are likely to be surface plasmons, especially at very thin thicknesses where they cannot be accounted for by the interference model. The three modes, indicated by (i), appear just below 700nm and show complex anti-crossing behaviour with each other and also appear to begin to move towards longer wavelengths with thicker films. These modes are below the energy at which diffraction occurs, which could suggest that they are in fact due to coupling between neighbouring spheres, rather than the influence of diffracting planes. Other surface modes are also observed (indicated by (iii))which show anti-crossing behaviour with interference effects. In comparison with the Pt film, the reflectivity minima due to interference seem more strongly perturbed by other effects.

8.4 Polarisation Dependent Reflectivity

To further confirm the observation of interference or plasmon effects, polarisation white light spectroscopy was introduced as a way of distinguishing between phenomena due to individual voids and those due to the periodicity of the surface. Using polarisation optics and off-setting, then closing the condenser aperture, enabled non-normal incident light on the microscope to be used to probe the surface plasmon effects of macroporous films. On flat films, only TM light couples to surface plasmons and requires that the angle of incidence deviates away from the normal. The results presented here are for the same Au and Pt samples and the same positions as shown in Fig. 8.1. Spectra were recorded for co and crossed polarisation responses for both TE and TM incident light for azimuthal angles between 0^o and 60^o in steps of 5^o, where 0^o is defined along one of the lattice vectors. The two samples show very different changes in their reflectivity for TM co-polarised response in comparison with their normal incident behaviour (Fig. 8.8). Platinum shows virtually no difference between the two sets of spectra, suggesting that the observed features are due to reflections from individual cavities. In contrast, the response of the Au sample under

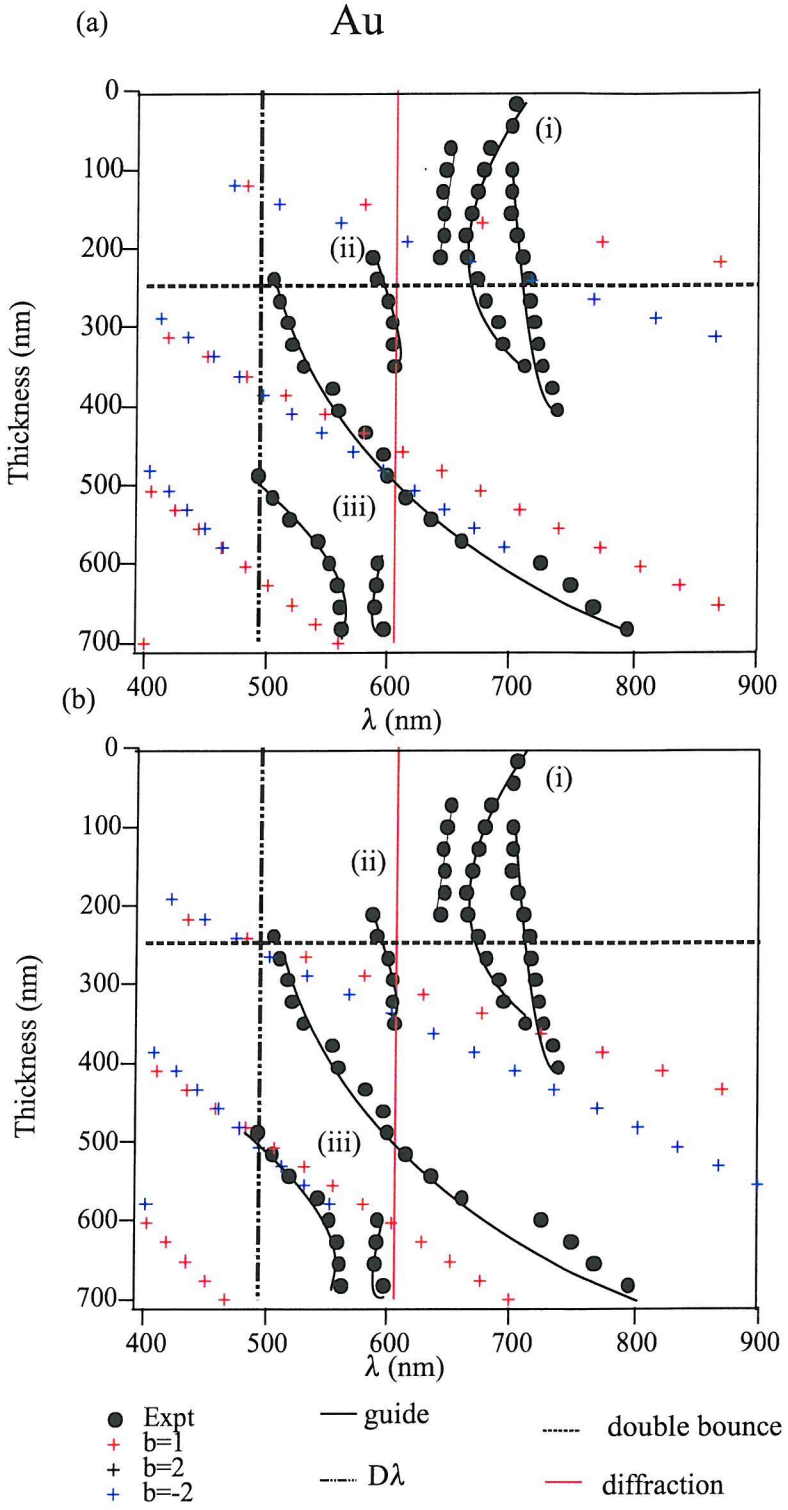

Figure 8.7: Extracted experimental reflectivity minima positions for normal incidence and theoretical reflectivity minima for 1 reflection, 2 reflections, forwards (+2) and "backwards" (−2)against extrapolated film thickness for Au sample (Note: b= 2, −2 are the same for normal incidence) (a) no Gouy shift and (b) with Gouy shifts. The solid lines are used as a guide to the eye only, (i) and (ii) represent modes which appear to be independent of thickness, (iii) indicates anti-crossing behaviour. The term "Dλ refers to the distance between the two points of two reflection interference.

the same conditions is noticeably different. At thin film thickness TM polarised light has two grating anomalies rather than one, which do not disappear with increasing film thickness. As film thickness increases, these two dips are observed to move to lower energies, in contrast to the surface plasmon with unpolarised light. The second set of dips, so far attributed to interference phenomena appear at the same point on the sample as in the previous experiment, with the only difference in nature due to their increased strength. Interestingly, this increase in strength of these minima suggests an element of surface coupling of the electric fields.

Further analysis of the Pt sample revealed that its optical response was polarisation and ordering independent. The intricacy of the response of Au is consistent with previous observations and suggests a more in depth study of the sample to be important. Experimental data for three sets of measurements is presented, TM co- and cross polarised response and TE co-polarised results from each position on the Au sample for azimuthal angles between 0^o and 60^o. The table below summarises the data taken at each point on the sampleas shown in Fig. 8.1 in terms of its assigned name, the angle of incidence, the range of angles over which the sample is rotated, the input polarisation and the associated polarisation analysis of the output.

Poln	θ	ϕ	ψ_{in}	ψ_{out}
TM_{co}	6	0-60	0	0
TM_{cross}	6	0-60	0	90
TE_{co}	6	0-60	90	90

Before discussing the results in their entirety, the results from just one point for both polarisations and co-and cross-polarised analysis for orientations from $\phi = 0^o$ to $\phi = 60^o$ are presented (Fig. 8.9). The direction of ϕ is defined to be 0^o and 60^o when the momentum component of the light parallel to the surface is along the line of void centres.

For TM_{co}, dips in reflectivity that are independent of the void orientation, ϕ, are observed at the periodicity of the diffraction planes at 606nm. At longer wavelengths the reflectivity is more complex, with minima exhibiting ϕ dependence. At $\phi = 0^o$, there is just one minimum at 740nm which is then split into two minima at $\sim$ 700nm

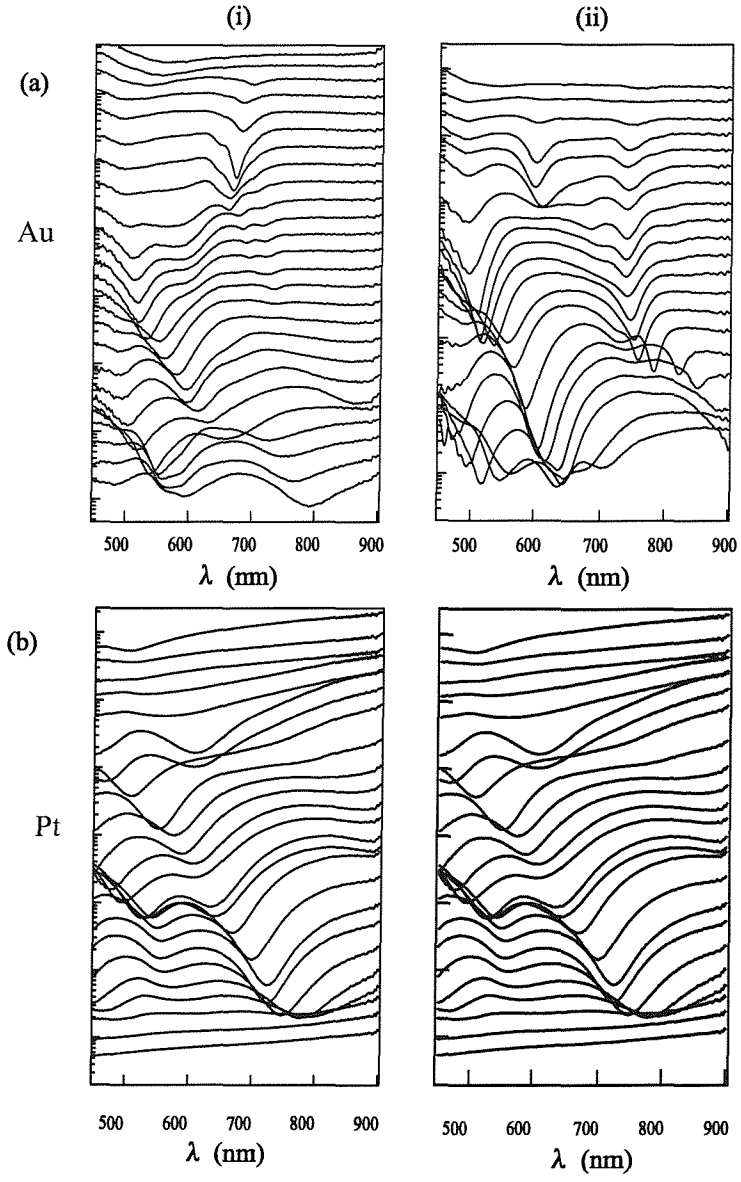

Figure 8.8: Reflectivity spectra of unpolarised light at (i) normal incidence and (ii)TM polarised light at $\theta = 6^o, \phi = 0^o$ for films of (a) Au and (b) Pt deposited through a 700nm sphere monolayer. The graphs are off-set on a log scale for clarity with thickness increasing down the graph.

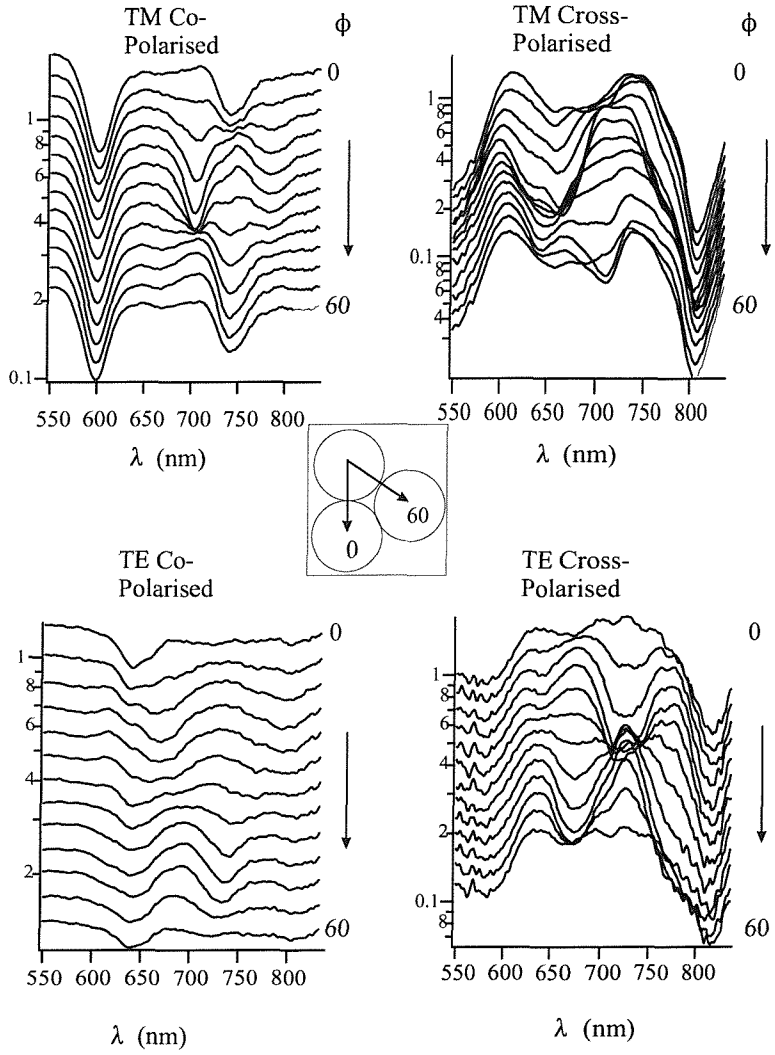

Figure 8.9: Spectra taken at one point on a graded gold sample, below half sphere height, for both TM and TE polarisations with co- and cross-polarised analysis for $0^o \leq \phi \leq 60^o$, Inset: the direction of ϕ defined in the schematic at the bottom of the figure.

and $\sim$ 780nm as the light now travels exactly between nearest neighbour void centres. This appears to suggest that the surface of the gold has two surface modes; one is independent of the void orientation and so likely to be localised in the voids, and the second which is dependent on the void orientation and is therefore likely to act as a more conventional surface plasmon.

The behaviour of the other three possible permutations are more complex than for the case of TM_{co}. The two sets of data for cross-polarised analysis show evidence for polarisation rotation similar to that uncovered by Watts et al [120]. Again, the

modes appear to be dependent on sample orientation suggesting the polarisation is rotated by the void array rather than individual voids themselves. Furthermore, TE_{co} incident radiation also shows evidence of coupling energy to surface modes.

As an an attempt to gain a better understanding of the response of the surface to incident light, the data for each position and at each sample orientation is overlaid as a 2D image (Fig. 8.10). TM co-polarised response is represented by red colouring, TE co-polarised by blue and TM cross-polarised light by green; TE cross-polarised light was sufficiently weak to be found unimportant. When the film is relatively thin, the two sets of dips observed in the spectra towards the top of the graph Fig. 8.8(a)(ii) are shown. One dip is invariant to rotation and is described as a localised plasmon (LP), because it is unaffected by the direction of the nearest voids. The other dip is shown to be angle dependent, with a repeat periodicity of 60^o and is described as a surface plasmon (SP). While this attribution is still preliminary, it is advanced as a way to make sense of the data.

The modes of the film when thin, compare favourably with the calculated modes for a 2D dielectric photonic crystal described in section 6.4, with the response at point 6 (from Fig. 8.10) compared with the calculated modes is shown in Fig. 8.11. This suggests that the 2D plasmons propagate and scatter off the voids. The LP progresses towards lower energies with increasing film thickness, while the SP remains constant. As the energy of the LP and the SP become increasingly similar they appear to show anti-crossing behaviour (point 12 , Fig. 8.10), at around half sphere thickness. The behaviour of these two modes has yet to be further investigated, although their dispersion with film thickness and azimuthal orientation would suggest that the LP mode is pinned to the curvature of the voids, effectively confining it to each individual cavity. In contrast, the SPs behaviour is consistent with traveling on the surface of the film. With analogy to the anti-crossing point of propagating plasmons, the anti-crossing point suggests that the confined modes and the travelling modes become ever more equivalent; the surface of the film becomes less flat as the void edges begin to touch, forcing the travelling surface modes to spend ever more time inside the voids rather than on the flat surface. At a certain point it is likely that the SP modes "fall" into the voids and mix with the LP modes (Fig. 8.12(b)).

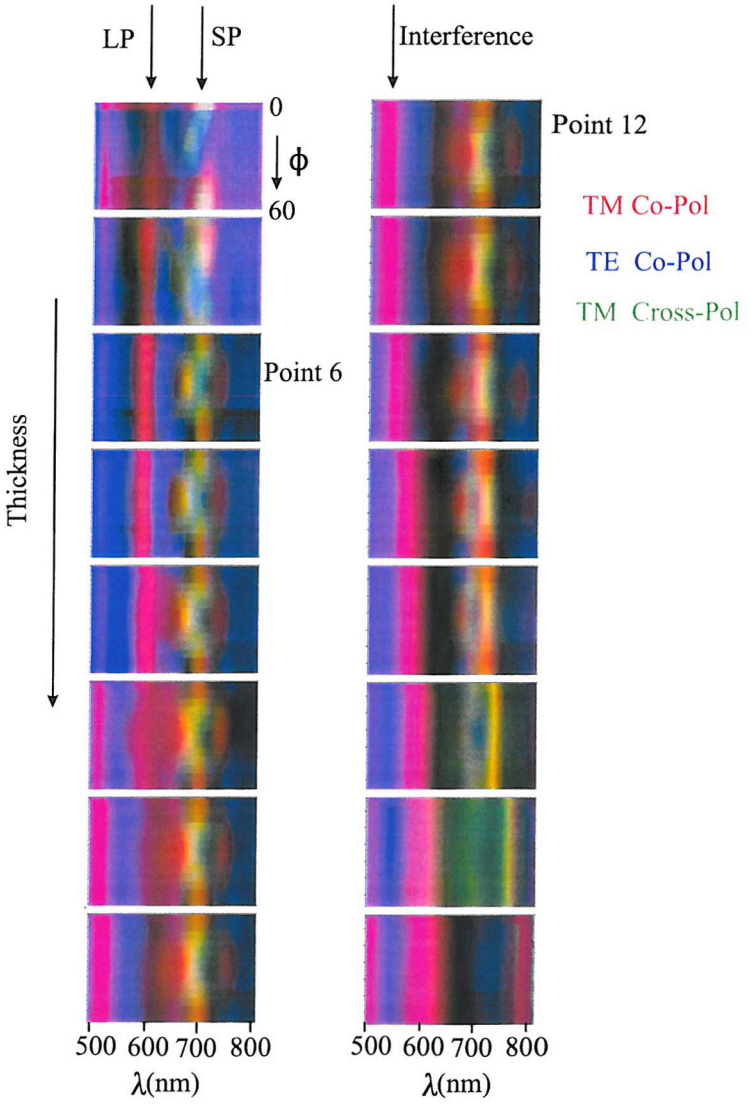

Figure 8.10: Plasmonic Behaviour of a graded Au film deposited through a 700nm diameter sphere template. The numbers on the extreme left and right of the images refer to the point where the spectra were taken with respect to the graphs shown in Fig. 8.8(a). Each image shows the response of the film to increasing azimuthal angle (ϕ) which increases down each image. LP refers to the localised plasmon, and SP the surface plasmon.

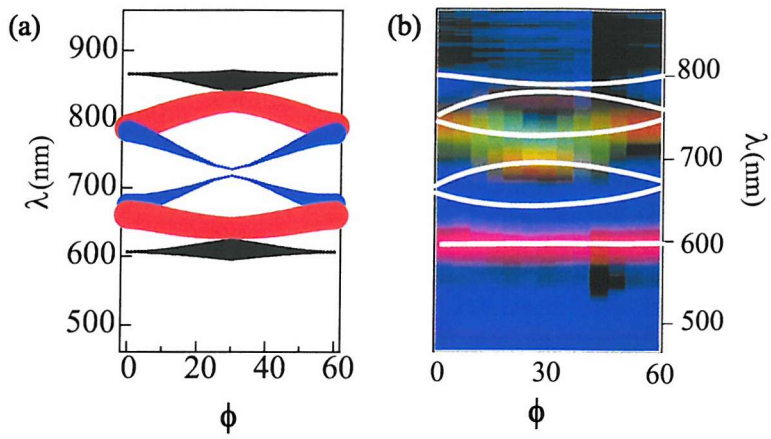

Figure 8.11: Comparison of 2D Photonic Bandgap calculations with results for 2D plasmonic behaviour of the Au sample at point 6. The white lines are a guide to the eye.

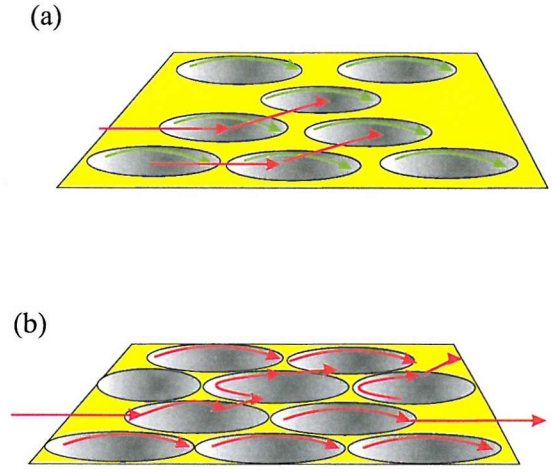

Figure 8.12: (a) Surface plasmon propagation across the film surface for small voids, with localised plasmons confined to the voids. (b) Surface propagation at half template sphere height, the surface plasmons and localised plasmons have equivalent energies; surface modes can both be trapped inside and escape from the voids.

Dips attributed to the interference effect are also visible in the data, which, like the LP mode, are orientation invariant and present in both TE and TM modes. With increasing film thickness the reflectivity minimum moves to longer wavelengths and appears not to interfere with the two plasmon modes. However, the last three images appear to show that the SP mode begins to move towards lower wavelengths, and the appearance of a relatively large signal from rotated TM polarisation which could suggest the interaction between the two sets of modes.

8.5 Analysis - Reflectivity at Normal and Near Normal Incidence

The results from the Pt and Au sample for normal and near normal incidence are once again compared with the results obtained from the 3D ray model developed in section 6.1.2.

8.5.1 Platinum

The Pt sample's reflectivity minima for both normal and near normal are very nearly identical to each other. Also of note, the splitting of the degeneracy of the (+2) and (−2) ray paths due to the deviation away from normal incidence.

8.5.2 Gold

The extracted minima for the Au sample for normal incidence, and TM co-polarised light at $\phi = 0^o, 30^o$ is shown with minima calculated from the 2D ray path model for interference spectra expected for one reflection and two reflections against film thickness without the inclusion of the Gouy shift (Fig. 8.14). The two double reflection interference paths are used to account for the rays to travel around the void in the opposite direction to which they enter. The graph shows that the "forward" double reflection (+2) is the closest match to the experimental reality, although all the models are clearly deficient. The minima around 600nm and 700nm are observed as stationary modes which then appear to follow the theoretical dips at the appropriate thickness. The two horizontal lines which represent these modes indicate the

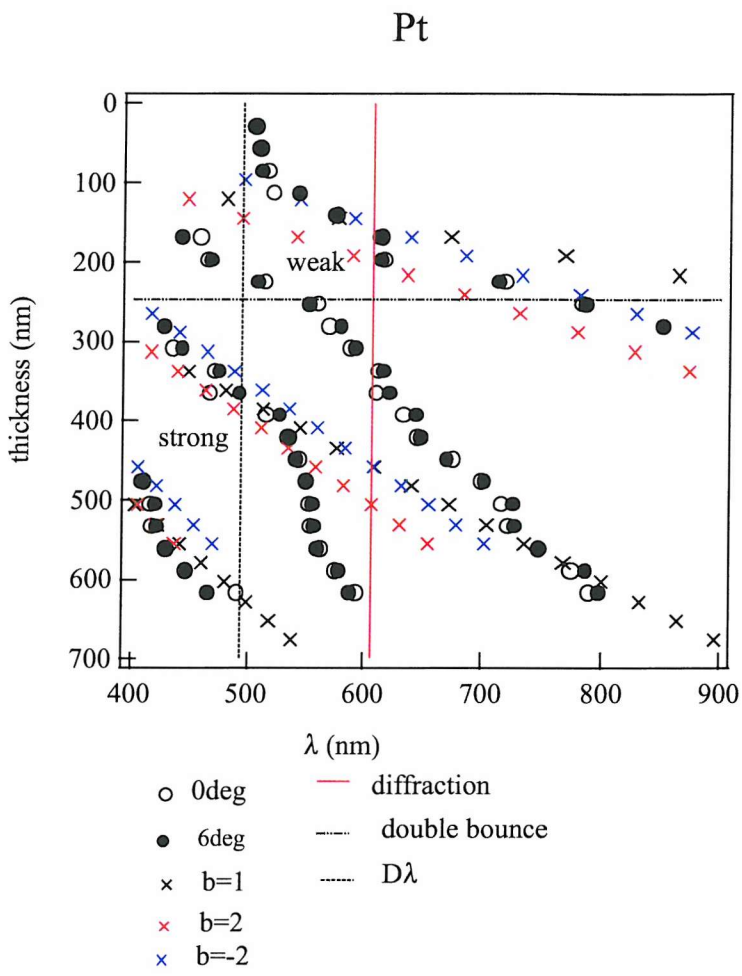

Figure 8.13: Extracted experimental reflectivity minima positions for normal incidence and TM co-polarised light and theoretical reflectivity minima for 1 reflection, 2 reflections, forwards (+2) and "backwards" (−2)against extrapolated film thickness for Pt sample. Weak and Strong refer to the relative strength of the reflectivity dips.

points where the reflectivity minima deviate most strongly from the ray model, indicating the presence of plasmon coupling. The gradient change of minima position with film thickness also appears to increase with film thickness, perhaps suggesting that the rays only experience a Guoy shift in phase when they can travel further than one wavelength. The modes detected at $\sim$ 600nm appear at thinner films for the 6^o incident path than the normal incident case, perhaps suggesting an angle of incidence requirement for the mode which is supplied by individual void surfaces. The area indicated by the ellipse is the interaction points of the LP and SP modes as well as their crossing with the interference modes.

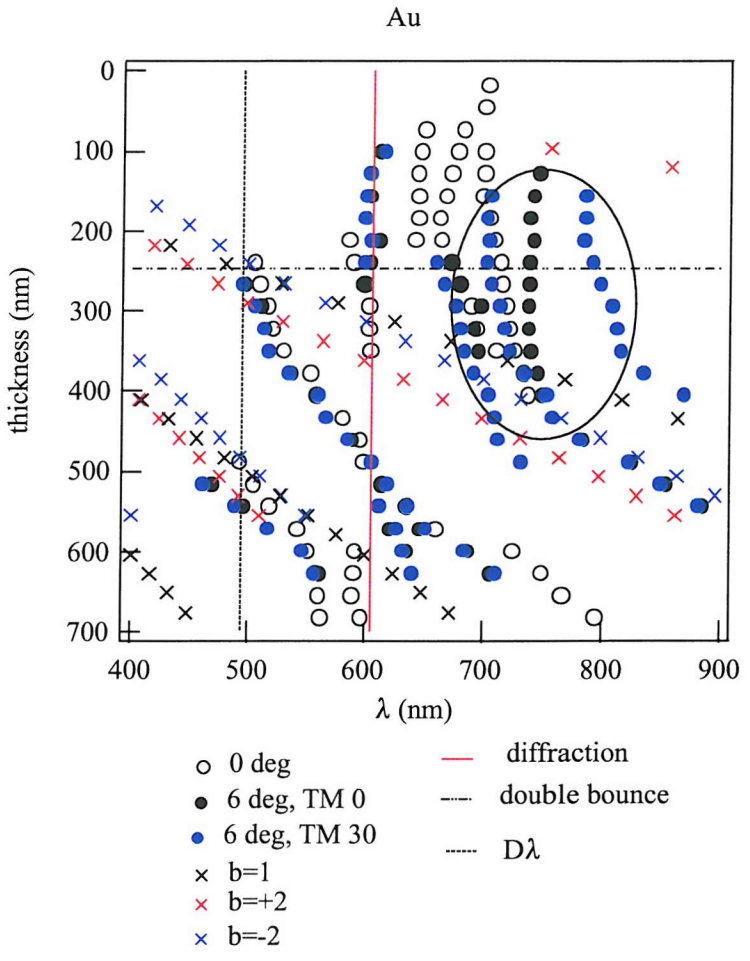

Figure 8.14: Extracted experimental reflectivity minima positions for normal incidence and TM co-polarised light at azimuthal orientation $\phi = 0^o, 30^o$ and theoretical reflectivity minima for 1 reflection, 2 reflections, forwards (+2) and "backwards" (−2) against extrapolated film thickness for Au sample. The two horizontal lines indicate possible modes. The ellipse highlights the region of anti-crossing surface plasmon interaction.

8.6 Conclusions

8.6.1 Platinum

Platinum films with surface patterned through electrochemical deposition through self-assembled sub-micron sphere templates show a series of reflectivity minima which shift towards longer wavelengths with increasing film thickness towards one template sphere height. There is clear experimental evidence that the ray model set out in chapter 6 of interference is qualitatively correct, although it is quantitatively incorrect as it cannot predict the correct positions of minima or their change in energy with respect to film thickness. This last point is especially valid for voids of size close to the wavelength of incident light, suggesting that diffraction effects, including Gouy shifts play a complex role in reflections off the surface.

Currently it is envisaged that only finite element solutions of Maxwell's equations at high resolution are capable of progressing these issues theoretically. Early results have shown the need for large computing power because of the requirement to solve the solutions in three dimensions. Work is continuing to overcome these difficulties.

8.6.2 Gold

Macroporous gold films show similar discrepancies in comparison with models based on the 2D reflectivity from voids. However, in addition to these there is clear evidence of the presence of interactions between incident light and surface plasmons. Polarisation sensitive experiments have shown that the surface plasmon propagation is sensitive to the direction and proximity of nearest-neighbour voids. Evidence also emerges that there are two different sorts of surface plasmons which we can plausibly attribute to being localised within voids and propagating along the top surface. When the film is grown to half sphere height the two types of surface plasmons show evidence of exhibiting complex anti-crossing behaviour. Further experimental work continues to gain a better understanding of this phenomenon.

Chapter 9

Conclusions and Outlook

This thesis has presented investigations into the physical and optical properties of novel macroporous metallic films structured through electrochemical deposition through self-assembled nanoscale latex spheres. The resulting open pore structures can be grown to well-controlled thicknesses through accurate control of the charge passed in deposition and have been proven to have smooth curved surfaces.

Films grown from micron sized spheres show reflections from within the cavity and off the top flat surface. The geometrical nature of reflections off the sides of the voids, have been shown to undergo polarisation rotation. Films of gold and platinum grown through sub-micron sphere templates have been shown to exhibit dramatic colour changes in reflectivity with film thickness. Initial white light reflectivity measurements at an angle of incidence of 45^o on samples from close packed, but irregularly ordered 750nm spheres, indicated that minima in the spectrum moved to longer wavelengths with increasing film thickness and remained at reasonably constant energies above radius height. These results were attributed to confined plasmon modes which are invariant to rotation of the sample in the the plane of incidence and to pore mouth morphology.

A better understanding of the response of the sub-micron structured films was gained with greater control over the sphere packing and number of layers of spheres. Reflectivity measurements at normal incidence using white light microscopy on well-ordered graded samples indicated that reflectivity minima moved continuously towards lower energies with increasing thickness. At high magnifications, the films are observed to recover their flat film reflectivity, hinting that the origin of the colour

change was due to interference between reflections from the top surface of the film and the voids. Further investigations into the response of these films to polarised light at normal incidence, and at a small deviation away from the normal, revealed that platinum films did not show any new features, whereas gold films showed significant differences, suggesting the presence of directly accessible surface plasmon modes.

Modelling the intricate responses of these films remains a challenging task. Several competing theories have been advanced during the course of this thesis to explain different facets of the films' responses. Two interference models based on 2D and 3D geometric reflections from inside the voids and off the top surface show qualitative agreement with experimental data taken at normal incidence. However, they also show significant differences, suggesting reflections from inside the voids do not follow exactly the ray optic paths. Away from normal incidence, the interference models are unable to explain the experimental data. Instead, models based on grating phenomena such as surface plasmons travelling on a patterned 2D surface show some agreement with data collected from a gold sample. Rotating the gold sample in the plane of incidence showed a set of modes similar to those observed for a 2D photonic crystal. However, the data also shows that one surface plasmon is rotationally invariant, suggesting it is localised within the voids (localised plasmon, LP), whereas the other surface plasmon features appear to move across the surface (surface plasmon, SP). Investigations will continue to explain the highly complex region where these two spectral features appear and co-exist.

The model of confined plasmons within voids was only shown to be satisfactory for disordered films away from normal incidence. The divergence in the behaviour between the reflectivity at near normal incidence at large angles cannot, as yet, be explained by any of the the models. The main reasons for this lie in the inherent problems associated with comparing results from different experiments and different samples with a complex response to light. Clearly this area is need of further research before any real conclusions can be drawn.

The outlook for research on macroporous metals is promising not least because understanding of their response is as yet incomplete. There are now two avenues to pursue in developing this avenue; studying the time dynamics of different spectral

features should allow a better understanding of the behaviour of surface modes and developing finite element calculations should indicate the extent to which the proposed models are correct. As well as studying the original samples further, advances in the templating of metals should allow more sophisticated metal structures. For example, not only is there the possibility of independently controlling the periodicity and void size, samples with different layers of metals could also be made. For example, a platinum film with a thin layer of gold on the top surface should show surface plasmons but not localised plasmons. Furthermore, a gold sample plated with a layer of platinum will not support surface plasmons, and may also prove whether or not localsied plasmons do really exist in the voids. Experiments on larger samples are now underway to use the 3D structures to make 0D (non-travelling) cavity states.

Appendix A

Reflectivity at Large Angles

A.1 Reflectivity at Large Angles

Testing the reflectivity of the Au and the Pt sample at angles greater than 6^o required the set-up described in section 5.2.2, with the drawback of having a narrower measurable spectrum. Again, the main guide to the sample's response was to extract the position of reflectivity minima. As was the case for the experiments in chapter 8, the reflectivity of Pt did not show many features of interest, and the number of minima reduced with increasing angle of incidence. Once again, macroporous samples made of Au exhibited more interesting features and the samples used were the same as used in chapter 8. Again, the spectra were analysed with the spectral position of the dips extracted from reflectivity data. The behaviour of the Au sample is analysed first. The data is presented in two different ways; at a fixed angle with variation in thickness (Fig. A.1) and at fixed thickness with angular rotation (Fig. A.2).

Considering fixed angle data first; the variation with film thickness at different angles is both rich and varied but with the same general trend, of modes progressing to longer wavelengths with increasing thickness. The apparent presence of anti-crossing modes (indicated by circles) and mode splitting /merging (indicated by squares) are shown in in Figures A.1 and A.3. The width of the modes are indicated by the the size of their square markers. The two calculated surface plasmon energies calculated are also indicated by horizontal lines (SP1 and SP2). A vertical line marks the point where the film is at half ball thickness. The data extracted for zero incidence from the microscope is used rather than the data collected using the angle measurements

because the surface plasmon data is easier to observe with the better signal to noise ratio. At zero degrees, the thinnest part of the film has two distinct minima (a1 and a3). The first, a1, represents the drop in reflectivity of gold at 500nm and the second shows the grating surface plasmon. Although in chapter 3 two surface plasmon energies were calculated only one is seen experimentally, which moves between these two calculated values as the film thickness increases. It appears to suffer anti-crossing with a third set of dips (a3), although both could be repelled by the first surface plasmon energy (SP1). At half sphere thickness the modes a1 and a2 appear to merge. The strongest modes in the spectrum appear to be found as around half ball height.

At 25 degrees, the modes appear to flatten out, especially the mode between SP1 and SP2 (b4). No modes are seen for the first few data points where the features present are very weak and therefore difficult to extract. This was in part caused by the white light source used in the angle measurements which was of lower intensity than that used in the normal incidence experiments. Again, the mode between SP1 and SP2 interacts strongly with other modes; b3 and b4 merge just before half ball thickness is reached. Also another mode, b2, appears to show flattening towards the energy level SP1 and splits into two other modes. One of these modes merges with b1 while the other continues to move towards longer wavelengths. At 35^o mode interactions are not observed, but the mode between SP1 and SP2 appears to flatten out at before half sphere height suggesting some form of resonance localisation. In contrast, the modes between these two theoretical values at 45^o appears to localise at the higher energy level of the two with the modes showing a more flat energy change with thickness. The mode interaction at 60 degrees appears to show a stationary energy level halfway between SP1 and SP2.

Despite the large variation in angle and the presence of modes interactions at some of the angles the graphs in general show a remarkable degree of similarity - something which cannot be explained using either the interference model or standard grating theories. Further confirmation of this can be seen when the data is plotted as a function of angle at a fixed film thickness (Fig. B.2). Several graphs are chosen to represent the general trends across the sample for a fixed point at different angles

of incidence. Deficiencies within the data collection process prevented data points being taken between 2-20 degrees. The first four points on the sample where data was taken did not show any clear minima at angles away from 0 degrees. The angular dispersion for these five points shows that in general as the film becomes thicker the variation in mode energy with angle flattens out suggesting that as the spherical cavity becomes more complete it localises the electric field. Again the marker size represents the width of an individual peak, and in general the modes tend to stay the same strength.

The Pt sample (Figs. A.3, A.4) shows a number of differences from the gold sample. First, the dips in reflectivity with change in thickness at different angles are shown with the positions of half ball height and the two calculated surface plasmon energies (SP1 and SP2). At angles away from normal incidence, no reflectivity minima are seen inside the region between SP1 and SP2; at normal incidence the modes become noticeably weaker in this region. Very few modes are observed at wavelengths longer than 620nm. Again, as with the gold sample, when thin the reflectivity minima (a Wood's anomaly) moves towards higher energies. Also, the modes at normal incidence appear to have split, this time at around 400nm. Once again as the angle of incidence, is increased the modes of the system vary less with change in thickness. As the angle of incidence was increased the reflectivity of the film decreased noticeably, unlike the Au sample whose reflectivity by comparison remained reasonably constant. Extracting the data with respect to constant film thickness (Fig A.4) confirms the stability of the modes to change in angle, particularly around half ball height (Fig. A.4(c),(d)).

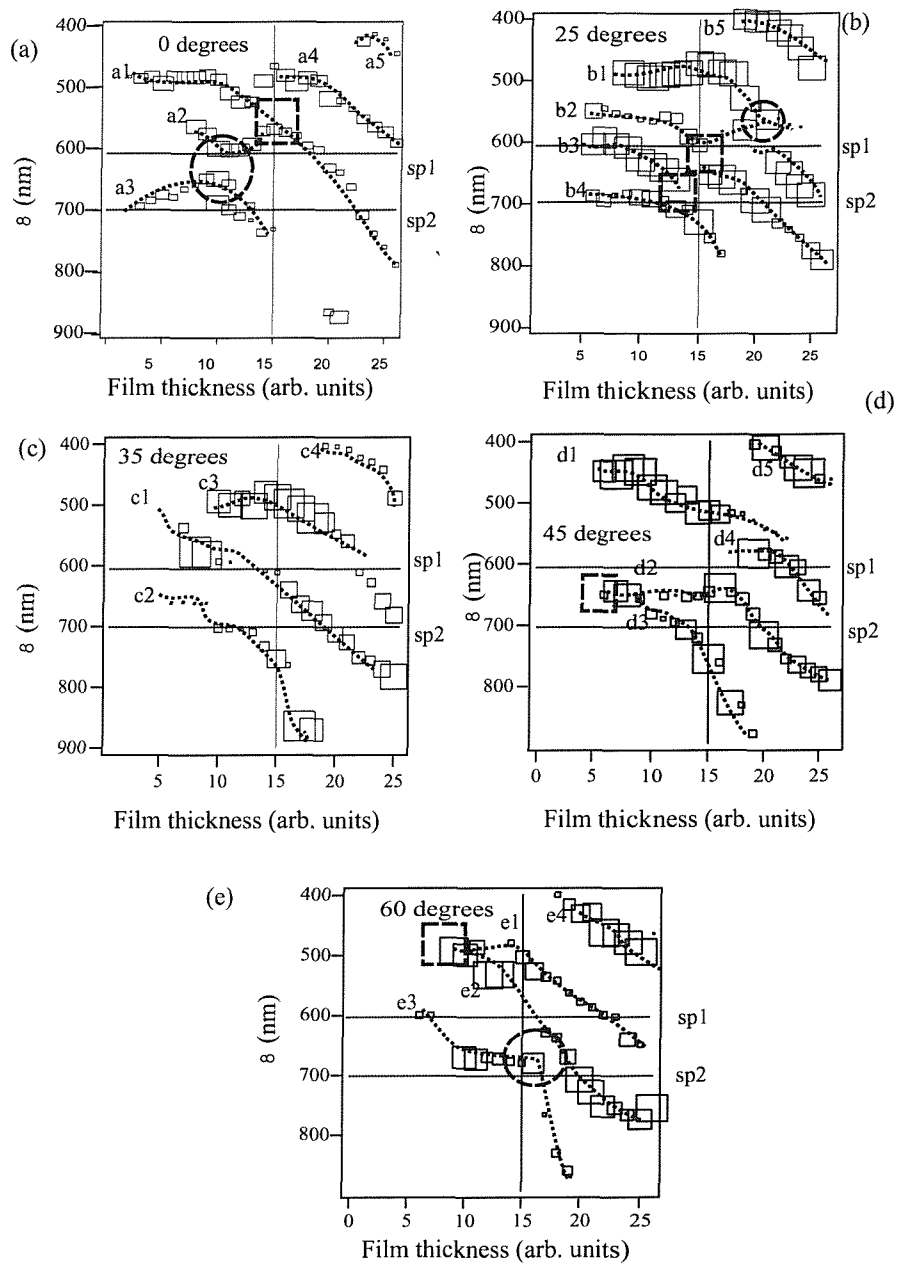

Figure A.1: Position of reflectivity minima at fixed angles as the film thickness changes for Au sample (700nm template)(a) 0 (b) 25 (c)35 (d) 45 (e) 60 degrees. The vertical line on each graph indicates where the film is half sphere height

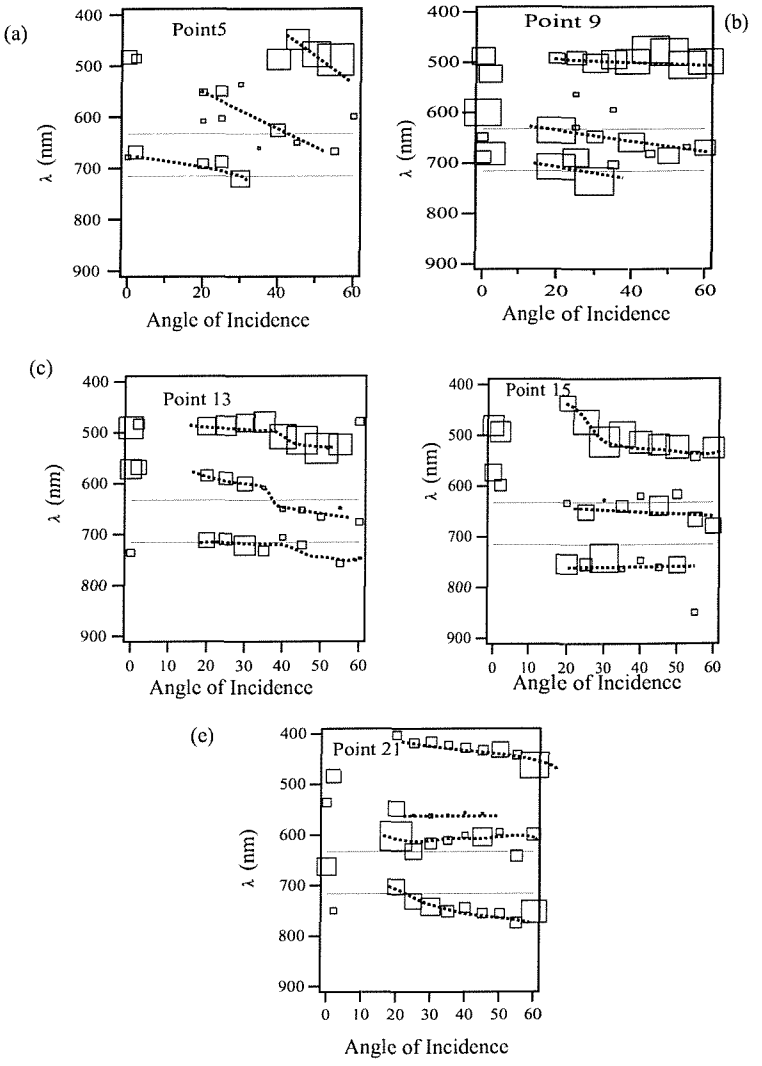

Figure A.2: Position of reflectivity minima at fixed film thickness as the angle of incidence varies for Au sample (700nm template) (a) Position 5, 80nm, (b) Position 9, 100nm, (c) Position 13, 220nm, (d) Position 15, 500nm, (e) Position 21, 570nm

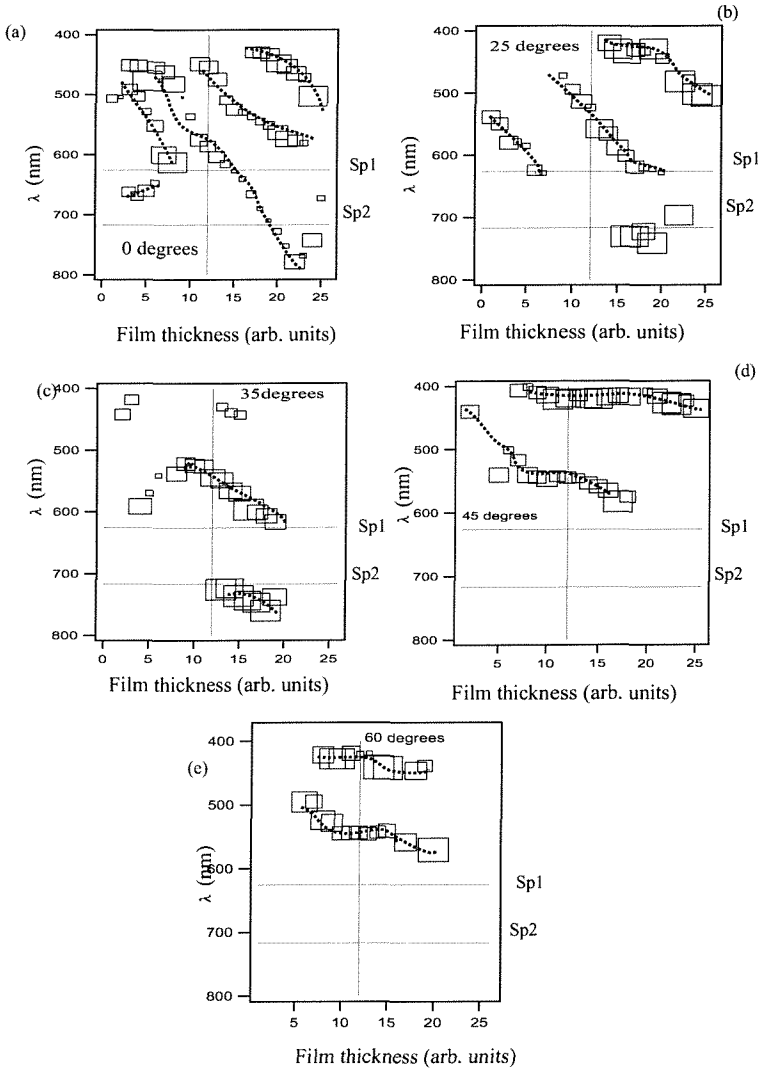

Figure A.3: Position of reflectivity minima at fixed angles as the film thickness changes for Pt sample (700nm template)(a) 0 (b) 25 (c)35 (d) 45 (e) 60 degrees. The vertical line on each graph indicates where the film is half sphere height.

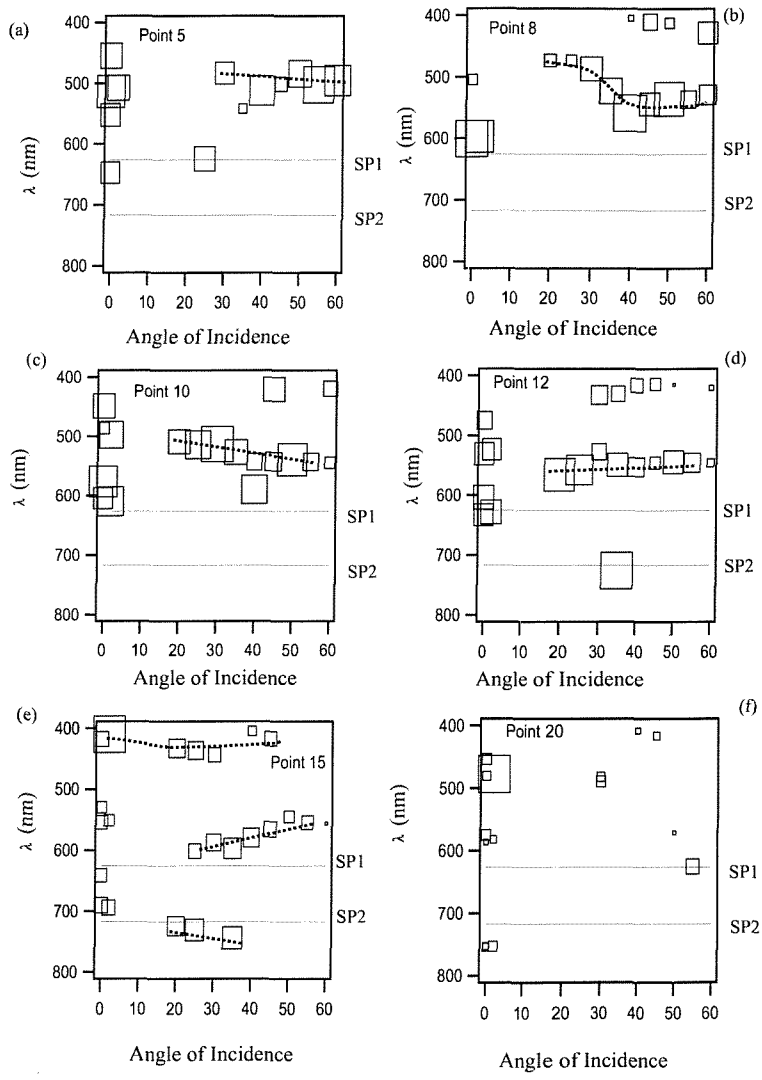

Figure A.4: Reflectivity minima at fixed angles as the film thickness changes for Pt sample (700nm template)(a) Position 5, 105nm, (b) Position 8, 175nm, (c) Position 10, 245nm, (d) Position 12, 240nm, (e) Position 15, 520nm, (f) Position 20, 625nm

Appendix B

Time Resolved Experiments with Gallium

B.1 Introduction

As an attempt to understand the temporal properties of a white light continuum generated in a holey fibre, the experiment described in section 5.1.4 was attempted. This chapter describes the salient features of gallium mirrors and presents some of the broadband time-resolved results using a pump-probe set-up.

The response of gallium on silica to light is complex; it has a number of phases with different reflectivities at energies close to room temperature. The basis for this research is the increase in reflectivity from R$\sim$ 0.5 to R$\sim$ 0.8 for gallium above and below it transition point between α-gallium and a more free electron-like phase [177]. The response is generated for a wide wavelength range of at least $(480-1800\text{nm})$ and have been shown to be capable of being used as a Q-switch in fibre lasers [178].

The root cause of the reflectivity change can be found in the nature of the gallium/silica interface onto which the gallium is grown, which supports a phenomenon known as "surface melting". Here a very thin layer ($\sim$ few nm) of liquid Ga forms between the rest of the Ga and the silica. The liquid gallium layer has a much higher reflectivity than the rest of the material; heating the sample increases the amount of Ga in its liquid phase which accounts for the increase in reflectivity of the sample [179]. Therefore, although the gallium sample has to be held at below its transition temperature, the actual process of changing the reflectivity does not have to be thermal. Observations of the effect of just using light show that it is possible to

increase the reflectivity for both cw and pulsed beams (picosecond or shorter). In the case of pulsed beams, the change in reflectivity occurs over time scales which preclude a thermal mechanism from involvement in the phase change. Instead, it occurs due to the unique coexistence of both covalent and metallic bonds in α-Ga. Some of the bonds consist of Ga_2 dimers with a binding energy of 1.435eV [180]. Light incident on the sample can break these bonds leading to a transition to a more reflective state.

B.2 Experimental Details

Of great importance in deciding whether to use a Ga mirror to attempt to characterise the holey fibre was the pulse energy required to induce the change, the recovery time of the mirror to its original reflectivity and the best temperature to hold the mirror at. From previous experiments, a clear threshold of power density was obtained of $0.5mJ/cm^2$, well below the power density produced from the OPA's signal. Of more concern were the recovery dynamics of gallium; although the reflectivity change occurred on picosecond timescales, the recovery to the initial state occurred over much longer period of around 1×10^{-4}s [180]. This meant that the repetition rate of the pulses had to be cut, which, as mentioned in section 5.2.2 complicated the experiment as the power falling on the diodes was also reduced to nearer the noise of the detection system. The dependence of the reflectivity change on the temperature of a gallium mirror was possible as it had been prepared on a Peltier stage for accurate temperature control.

B.3 Results

After the zero delay point had been found the reflectivity change for the Gallium was observed at two different temperatures of 24°C and 26°C for incremental step changes in the time delay of 100fs (Fig. B.1). Several observations about the properties of the system could be made. First, a lower temperature did show a greater change in reflectivity, as well as a more rapid increase, than at higher temperatures. Secondly, the reflectivity change occurred in two distinct phases; initially a rapid increase in reflectivity on the order of only a few ps, followed by a much slower increase. This

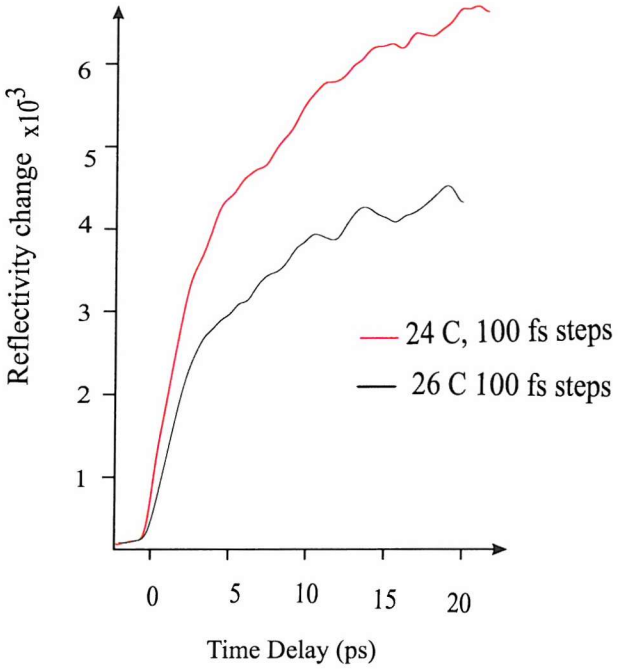

Figure B.1: Reflectivity change as a function of time delay between pump pulse and white light continuum

suggests that the change in reflectivity is due to two different processes occurring at the same time, with one occurring much more quickly than the other. The fast response time of this system suggests that the initial increase is dominated by the breaking of the Ga_2 dimer, followed by a phase change across in the sample.

The second experiment was conducted to see the extent to which the change in reflectivity was affected by temperature, and also how well the sample recovered to its initial phase. Changing the length of each step in the increasing the time delay to 5ps allowed the full increase in reflectivity to be noted. The experiment was conducted at one point on the sample for temperatures of 12^{o}C, 14^{o}C, 16^{o}C and 18^{o}C. The experiment was then repeated for 18^{o}C, followed by repeating the process for 12^{o}C. The results show that the first run of the experiment at 12^{o}C exhibited the largest change on reflectivity, although it also appears that it was not the most rapid; this occurred at 14^{o}C (Fig. B.2). The increase in reflectivity decreased considerably with increasing temperature, although it is difficult to tell whether this was not partly due to the sample being damaged by the intense pump beam. This process was not helped by the gallium mirror having a non-uniform response and reflectivity

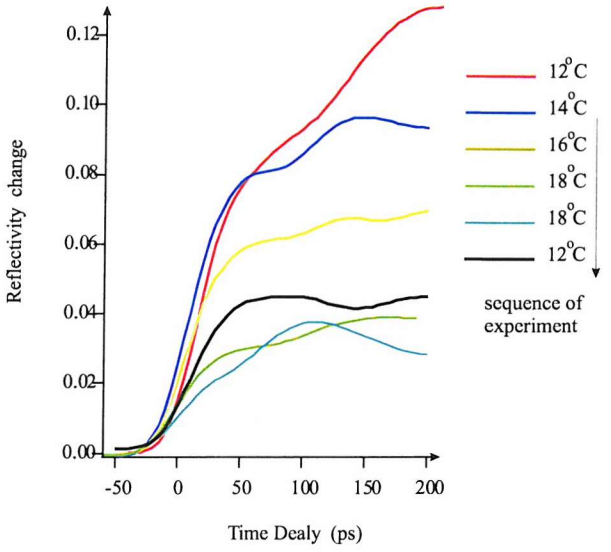

Figure B.2: Reflectivity change as a function of time delay between pump pulse and white light continuum for steps of 5ps, the key lists the results in the order in which they were taken and the temperature of the gallium sample.

change, which meant that the experiment had to be conducted at the same point. Certainly the last experiment in the set, carried out at 12^{o}C showed a slightly larger increase in reflectivity than the previous one at 18^{o}C. However, this difference is small, and the large discrepancy between the two tests at 12^{o}C suggest a degree of sample degradation had occurred.

The final set of experiments which were tried attempted the same experiment carried out above at 21^{o}C, but now concentrating on the time response of 2nm segments of the white light continuum spectrum. The first experiment was carried out for the seed wavelength of the continuum generation (819nm). Other wavelengths were also tested 900nm, 750nm, 630nm, 500nm (Fig. B.3). The results showed that it was extremely difficult to find out where the time difference between different wavelengths due to the inaccuracy of the experiment, in particular the large increase in noise for wavelengths away from the seed wavelength and the rate of change in gallium's reflectivity. Furthermore, the strength of the signal at some wavelengths was so poor that the time delay between it and the pump pulse was indeterminate.

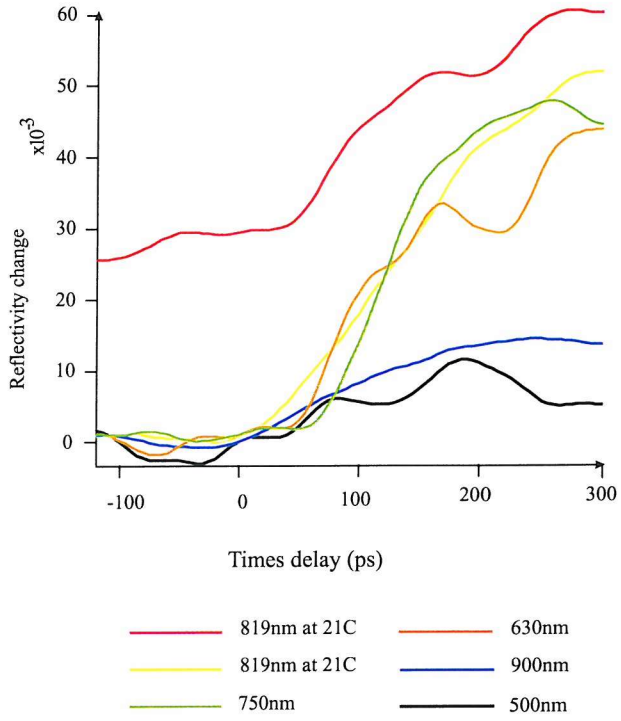

Figure B.3: Pump probe results for different parts of the holey fibre white light continuum.

Bibliography

[1] R. P. Feynman, http://www.zyvex.com/nanotech/feynman.html

[2] E. Yablonovitch Phys. Rev. Lett. **58**, 2059 (1987)

[3] S. John Phys. Rev. Lett. **58**, 2486 (1987)

[4] T. W. Ebbesesn, H. J. Lezec, H. F. Ghaemi, T. Thio, P. A. Wolff Nature **391**, 667 (1998)

[5] P. Vukusic, J. R. Sambles, C. R. Lawrence, R. J. Wooton Nature **410**, 36 (2001)

[6] M. Srinivasarao Chem. Rev. **99**, 1935 (1999)

[7] A. R. Parker, R. C. McPhedran, D. R. Mckenzie, L. C. Botten, N-A. P. Nicorovici Nature **409**, 36 (2001)

[8] A. Sweeney, C. Jiggins, S. Johnsen Nature **423**, 31 (2003)

[9] M. Born, E. Wolf Principles of Optics *Electromagnetic Theory of Propagation, Interference and Diffraction of Light*, Pergamon Press (1970)

[10] H. J. Lezec, A. Degiron, E. Devaux, R. A. Linke, L. Martin-Monroe, F. J. Garcia-Vidal, T. W. Ebbesen Science, **297**, 820 (2002)

[11] http://newton.ex.ac.uk/research/thinfilms/butterflies/

[12] http://www.physics.usyd.edu.au/ nicolae/seamouse.html

[13] T. F. Krauss, R. M. De. La Rue Prog. Quant. Electron. **23**, 51 (1999)

[14] C. Kittel (Chapter 7) *Introduction to Solid State Physics*, John Wiley and Sons, (1996)

[15] http://www.mesophotonics.com

[16] J. D. Joannopoulos, R. D. Meade, J. N. Winn *Photonic Crystals - Moulding the Flow of Light*, Princeton University Press, (1995)

[17] J. B. Pendry Current Science **76**, 1311 (1999)

[18] T. Baba IEEE Journal Select. Topics Quant. Electon. **3**, 808, (1997)

[19] E. Yablonovitch, T. J. Gmitter, K. M. Leung Phys. Rev. Lett. **67**, 2295 (1991)

[20] Y. Ohtera, T. Sato, T. Kawashima, T. Tamamura, S. Kawakami Electron. Lett. **35**, 1271 (1999)

[21] S.-Y. Lin, E. Chow, V. Hietala, P. R. Villeneuve, J. D. Joannopolous Science **282**, 274 (2002)

[22] H. Kosaka, T. Kawashima, A. Tomita, M. Notomi, T. Tamamura, T. Sato, S. Kawakami Phys. Rev. B. **58**, R10096 (1998)

[23] M. Plihal, A. A. Maradudin Phys. Rev. B. **44**, 8565 (1991)

[24] A. Barra, D. Cassagne, C. Joanin Appl. Phys. Lett. **72**, 627 (1998)

[25] S. S. M. Cheng, L.-M. Li, C. T. Chan, Z. Q. Zhang Phys. Rev. B. **59**, 4091 (1999)

[26] Y. S. Chan, C. T. Chan, Z. Y. Liu Phys. Rev. Lett. **80**, 956 (1998)

[27] M. E. Zoorob, M. D. B. Charlton, G. J. Parker, J. J. Baumberg, M. C. Netti Nature **404**, 740 (2000)

[28] E. Ozbay, E. Michel, G. Tuttle, R. Biswas, M. Sigalas, K.-M. Ho Appl. Phys. Lett.**64**, 2059 (1994)

[29] N. Yamamoto, S. Noda, A. Sasaki Jpn. J. Appl. Phys. **36**, 1907 (1997)

[30] O. Toader, M. Berciu, S. John Phys. Rev. Lett. **90**, 233901 (2003)

[31] S. G. Johnson, J. D. Joannopoulos Appl. Phys. Lett.**77**, 3490 (2000)

[32] H. W. Deckman, J. H. Dunsmuir Appl. Phys. Lett.**41**, 377 (1981)

[33] K. Busch, S. John Phys. Rev. E **58**, 3896 (1998)

[34] R. Biswas, M. M. Sigalas, G. Subramania, K. -M. Ho Ohys. Rev. B. **57**, 3701 (1998)

[35] P. Jiang, J. F. Bertone, V. L. Colvin Science **291**, 453 (2001)

[36] M. Bardosva, R. H. Tregold J. Mater. Chem. **12**, 2835 (2002)

[37] D. G. Grier Nature **393**, 621 (1998)

[38] W. R. Bowen, A. O. Sharif Nature **393**, 663 (1998)

[39] S. Auer, D. Frenkel Nature **413**, 711 (2001)

[40] S-C. Mau, D. A. Huse Phys. Rev. E. **59**, (4396)

[41] Y. A. Vlasov, V. N. Astratov, A. V. Baryshev, A. A. Kaplyanskii, O. Z. Karimov, M. F. Limonov Phys. Rev. E. **61**, 5784 (2000)

[42] J. Zhu, M. Li, r. Rogers, W. Meyer, R. H. Ottewell, STS-73 Space Shuttle Crew, W. B. Russel, P. M. Chaikin **387**, 883 (1997)

[43] P. A. Rundquist, P. Photinos, S. Jagannathan, S. A. Asher J. Chem. Phys. **91**, 4932 (1989)

[44] N. D. Denkov, O. D. Velev, P. A. kralchevsky, I. B. Ivanov, H. Yoshimura, K. Nagayama Langmuir **8**, 3183 (1992)

[45] K. P. Velikov, F. Durst, O. D. Velev Langmuir **14**, 1148 (1998)

[46] P. A. Kralchevsky, V. N. Paunov, N. D. Denkov, I. B. Ivanov, K. Nagayama J. Colloid. Inter. Sci. **155**, 420 (1993)

[47] P. A. Kkralchevsky, K. Nagayama Langmuir **10**, 23 (1994)

[48] A. S. Dimitov, K. Nagayama Langmuir **12**, 1303 (1996)

[49] P. Jiang, J. F. Bertone, K. S. Hwang, V. L. Colvin Chem. Mater. **11**, 2132 (1999)

[50] Z.-Z. Gu, Q.-B. Meng, S. Hayami, A. Fujishima, O. Sato J. Appl. Phys. **90**, 2042 (2001)

[51] J. D. Joannopoulos Nature**414**, 257 (2001)

[52] Y. A. Vlasov, X.-Z. Bo, J. C. Sturm, D. J. Norris Nature **414**, 289 (2001)

[53] R. M. Amos, J. G. Rarity, P. R. Tapster, T. J. Shepherd, S. C. Kitson Phys. Rev. E. **61**, 2929 (2000)

[54] M. Trau, D. A. Saville, I. A. Aksay Langmuir **13**, 6375 (1997)

[55] S. H. Park, D. Qin, Y. Xia Adv. Mater. **10**, 1028 (1998)

[56] S. H. Park, Y. Xia Adv. Mater. **10**, 1045 (1998)

[57] B. Gates, Y. Xia Adv. Mater. **12**, 1329 (2000)

[58] H. A. Biebuyck, N. B. Larsen, E. Delamarche, and B. Michel IBM Journal of Research & Development **41**, 159 (1997)

[59] J. Aizenberg, P. V. Braun, P. Wiltzius Phys. Rev. Lett. **84**, 2997 (2000)

[60] A. Blanco, E. Chomski, S. Grabtchak, M. Ibisate, S. John, S. W. Leonard, C. Lopez, F. Meseguer, H. Miguez, J. P. Mondia, G. A. Ozin, O. Toader, H. M. van Driel Nature **405**, 437 (2000)

[61] A. A. Zakhidocv, R. H. Baughman, Z. Iqbal, C. Cui, I. Khhayrullin, S. O. Dantas, J. Marti, V. G. Ralchenko **282**, 897 (1998)

[62] P. N. Bartlett, P. R. Birkin, M. A. Ghanem Chem. Commun. 1671 (2000)

[63] J. E. G. Wijnhoven, W. L. Vos Science **281**, 802 (1998)

[64] Z.-Z. Gu, S. Hayami, S. Kubo, Q-B. Meng, Y. Einaga, D. A. Tryk, A. Fujishima, O. Sato J. Am. Chem. Soc. **123**, 175 (2001)

[65] D. J. Norris, y. A. Vlasov Adv. Mater. **13**, 371 (2001)

[66] O. D. Velev, P. M. Tessier, A. M. Lenhoff, E. W, Kaler Nature **401**, 548 (1999)

[67] P. V. Braun, P. Wilzius Nature **402**, 603 (1999)

[68] S. Y. Lin, J. G. Fleming, I. El-Kady Opt. Lett. **28**, 1909 (2003)

[69] P. N. Bartlett, P. R. Birkin, M. A. Ghanem, C.-S. Toh J. Mater. Chem. **11**, 849 (2001)

[70] L. Xu, W. L. Zhou, C. Frommen, R. H. Baughman, A. A. Zakhidov, L. Malkinski, J.-Q. Wang, J. B. Wiley Chem. Commun. 997 (2000)

[71] L. K. van Vugt, A. F. van Tjekstra, L. Bechger, W. L. Vost, D. Vanmaekelbergh, J. J. Kelly Chem. Commun. 2054 (2002)

[72] D. F. Sievenpiper, M. E. Sickmiller, E. Yablonovitch Phys. Rev. Lett. **76**, 2480 (1996)

[73] J. G. Fleming, S. Y. Lin, El-Kady, R. Biswas, K. M. Ho Nature **417**, 52 (2002)

[74] S. Y. Lin, J. G. Fleming, D. L. Hetherington, B. K. Smith, R. Biswas, K. M. Ho, M. M. Sigalas, W. Zubrzycki, S. R. Kutz, J. Bur Nature **394**, 251 (1998)

[75] M. Suffcznski Phys. Rev. **117**, 663 (1960)

[76] P. B. Johnson, R. W. Christy Phys. Rev. B **6**, 4370 (1972)

[77] E. A. Taft, H. R. Philipp Phys. Rev. **121**, 1100 (1961)

[78] A. D. Rakić, A. B. Djurišić, J. M. Elazar, M. L. Majewski Appl. Optics **37**, 5271 (1998)

[79] C. Sönnichsen, T. Franzl, T. Wilk, G. von Plessen, J. Feldman, O. Wilson, P. Mulvaney Phys. Rev. Lett. **88**, 077402 (2002)

[80] C. F. Bohren, D. R. Huffman *Absorption and Scattering of Light by Small Particles*, John Wiley & Sons (1983)

[81] M. R. Beversluis, A. Bouhelier, L. Novotny Phys. Rev. B. **68**, 115433-1 (2003)

[82] M. Guerrisi, R. Rosei Phys. Rev. B **12**, 557 (1975)

[83] H. P. Meyers (p.212) *Introductory Solid State Physics*, Taylor & Francis (1990)

[84] O. K. Andersen Phys. Rev. B. **2**, 883 (1970)

[85] C. B. Sommers, H. Amar Phys. Rev. **188**, 1117 (1969)

[86] M. A. Faraday Phil. Trans. **147**, 145 (1835)

[87] J. A. Creighton, D. G. Eadon J. Chem. Soc. Faraday Trans. **87**, 3881 (1991)

[88] H. A. Atwater SPIE OE, July, 42 (2002)

[89] N. J. Halas Optics & Photonics News, August, 26 (2002)

[90] Ch.9 R. Rupin, etd. A. D. Boardman *Electromagnetic Surface Modes*, John Wiley & Sons (1982)

[91] M. Perner, S. Gresillon, J. März, G. von Plessen, J. Feldmann, J. Porstendorfer, K. -J. Berg, G. Berg Phys. Rev. Lett. **85**, 792 (2000)

[92] R. H. Ritchie, J. C. Ashley, T. L. Ferrell, etd. A. D. Boardman *Electromagnetic Surface Modes*, John Wiley & Sons (1982)

[93] M. Perner, P. Bost, U. Lemmer, G. von Plessen, J. Feldmann, U. Becker, M. Mennig, M. Schmitt, H. Schmidt Phys. Rev. Lett. **78**, 2192 (1997)

[94] E. J. Zeman, G. C. Schatz J. Phys. Chem. **91**, 634 (1987)

[95] S. A. Maier, P. G. Kik, M. L. Brongersma, H. A. Atwater Proc. SPIE **4456** 22 (2001)

[96] S. Linden, J. Kuhl, H. Giessen Phys. Rev. Lett. **86**, 4688 (2001)

[97] J. R. Krenn, A. Dereux, J. C. Weeber, Y. Lacroute, J. P. Goudonnet, G. Schider, W. Grotschy, A. Leitner, F. R. Aussenegg Phys. Rev. Lett. **82**, 2590 (1999)

[98] R. D. Averitt, D. Sarkar, N. J. Halas Phys. Rev. Lett. **78**, 4217 (1997)

[99] R. D. Averitt, S. L. Westcott, N. J. Halas J. Opt. Soc. Am. B. **16**, 1824 (1999)

[100] S. J. Oldenburg, R. D. Averitt, S. L. Westcott, N. J. Halas Chem. Phys. Lett. **288**, 243 (1998)

[101] R. W. Wood Proc. Phys. Soc. **18**, 296 (1902)

[102] R. W. Wood Phys. Rev. **48**, 928 (1935)

[103] M. C. Hutley Diffraction Gratings , Academic Press (1982)

[104] Lord Rayleigh Philos. Mag. **14**, 70 (1907)

[105] U. Fano J. Opt. Soc. Amer. **31**, 213 (1941)

[106] D. Maystre, Chapter 17, *Electromagnetic Surface Modes*, etd. A. D. Boardman, John Wiley&Sons

[107] R. H. Ritchie Phys. Rev. **106**, 874 (1957)

[108] H. Raether *Surface Plasmons on Smooth and Rough Surfaces and on Gratings*, Springer-Verlag (1988)

[109] W. L. Barnes, A. Dereux, T. W. Ebbesen Nature **424**, 824 (2003)

[110] J. E. Stewart, W. S. Galloway Appl. Opt. **1**, 421 (1962)

[111] W. L. Barnes, T. W. Preist, S. C. Kitson, J. R. Sambles Phys. Rev. B **54**, 6227 (1996)

[112] R. A. Watts, J. R. Sambles J. of Mod. Optics **44**, 1231 (1997)

[113] W.-C. Tan, J. R. Sambles, T. W. Preist Phys. Rev. B **61**, 13177 (2000)

[114] S. J. Elston, G. P. Bryan-Brown, J. R. Sambles Phys. Rev. B **44**, (1991)

[115] M. B. Sobnack, W.-C. Tan, N. P. Wanstall, T. W. Preist, J. R. Sambles Phys. Rev. Lett. **80**, 5667 (1996)

[116] I. R. Hooper, J. R. Sambles Phys. Rev. B **65**, 165432-1 (2002)

[117] F. J. García-Vidal, J. B. Pendry Phys. Rev. Lett. **77**, 1163 (1996)

[118] , W.-C. Tan, T. W. Preist, J. R. Sambles, N. P. Wanstall Phys. Rev. B **59**, 12661 (1999)

[119] M. Kreiter, S. Mittler, W. Knoll, J. R. Sambles Phys. Rev. B. **65**, 125415-1 (2002)

[120] R. A. Watts, A. P. Hibbins, R. A. Watts, J. of Mod. Optics **46**, 2157 (1999)

[121] R. A. Watts, T. W. Priest, J. R. Sambles Phys. Rev. Lett. **79**, 3978 (1997)

[122] A. Wirgin, A. A. Maradudin Phys. Rev. B. **31**, 5573 (1985)

[123] T. López-Rios, D. Mendoza, F. J. García-Vidal, J. Sanchez-Dehesa, B. Pannetier Phys. Rev. Lett. **81**, 665 (1998)

[124] D. C. Skigin, R. A. Depine Phys. Rev. E. **63**, 46608-1 (2001)

[125] R. A. Depine, D. C. Skigin Phys. Rev. E. **61**, 4479 (2000)

[126] S. C. Kitson, W. L. Barnes, J. R. Sambles Phys. Rev. Lett. **77**, 2670 (1996)

[127] M. Kretschmann Phys. Rev. B **68**, 125419 (2003)

[128] H. F. Ghaemi, T. Thio, D. E. Grupp, T. W. Ebbesen, H. J. Lezec Phys. Rev. B **58**, 6779 (1998)

[129] H. A. Bethe Phys. Rev. **66**, 163 (1944)

[130] A. Krishan, T. Thio, T. J. Kim, H. J. Lezec, T. W. Ebbesen, P. A. Wolff, J. C. Pendry, L. Martin-Moreno, F. J. Garcia-Vidal Opt. Commun. **200**, 1, (2001)

[131] D. E. Grupp, H. J. Lezec, T. W. Ebbesen, K. M. Pellerin, T. Thio Appl. Phys. Lett. **77**, 1569 (2000)

[132] J. A. Porto, F. J. Garcia-Vidal, J. B. Pendry Phys. Rev. Lett. **83**, 2845 (1999)

[133] Q. Cao, P. Lalanne Phys. Rev. Lett. **88**, 057403 (2002)

[134] A. P. Hibbins, J. R. Sambles, C. R. Lawrence Appl. Phys. Lett. **81**, 4661 (2002)

[135] L. Martin-Moreno, F. J. Garcia-Vidal, H. J. Lezec, K. M. Pellerin, T. Thio, J. B. Pendry, T. W. Ebbesen Phys. Rev. Lett. **86**, 1114 (2001)

[136] A. Degiron, H. J. Lezec, W. L. Barnes, T. W. Ebbesen Appl. Phys. Lett. **81**, 4327 (2002)

[137] M. A. Ghanem, PhD Thesis, *Electrochemical Synthesis of Nanostructured Porous Materials using Liquid Crystal and Colloidal Templates and their Magnetic and Optical properties*, University of Southampton (2002)

[138] P. N. Bartett, J. J. Baumberg, P. R. Birkin, M. A. Ghanem, M.C. Netti Chem. Mater. **14**, 2199 (2002)

[139] International Centre for Diffraction Data PCPDF win V 20.1 card no. (01-1172) 1998

[140] Hammond. C *The Basics of Crystallography and Diffraction*, Oxford University Press (1997)

[141] N. Bonod, S. Enoch, L. Li, E. popov, M. Nevire Opt. Express **11**, 482 (2003)

[142] A. B. D. Cassie, S. Baxter

[143] J. Bico, U. Thiele, D. Quéré Colloids&Surfaces **206**, 41 (2002)

[144] M. C. Netti, J. J. Baumberg, M. D. Chalton, G. J. Parker Appl. Phys. Lett. **76**, 991 (2000)

[145] P.G. Savvidis, J. J. Baumberg, R. M. Stevenson, M. S. Skolnick, D. M. Whittaker, J. S. Roberts Phys. Rev. Lett. **84**, 1547 (2000)

[146] M. C. Netti, S. Coyle, J. J. Baumberg, M. A. Ghanem, P.R. Birkin, P. N. Bartlett, D. M. Whittaker Adv. Mater. **13**, 1368 (2001)

[147] S. Coyle, M. C. Netti, J. J. Baumberg, M. A. Ghanem, P. R. Birkin P. N. Bartlett, D. M. Whittaker Phys. Rev. Lett. **87**, 176801, (2001)

[148] R. R. Alfano, S. L. Shapiro Phys. Rev. Lett. **24**, 584, (1970)

[149] W.Lee. Smith, P. Liu and N.Bloembergen Phys. Rev. A **15**, 2396 (1977)

[150] J. C. Knight, T. A. Birks, P. St. J. Russell, D. M. Atkin Opt. Lett **21**, 1547 (1996).

[151] T. A. Birks, J. C. Knight, P. St. J. Russell Opt. Lett **22**, 961 (1997).

[152] J. C. Knight, J. Arriaga, T. A. Birks,A. Ortigosa_Blanch, W. J. Wadsworth, P. St. J. Russell IEEE Photon. Tech. Lett. **12**, 807 (2000).

[153] T. A. Birks, D. Mogilevstev, J. C. Knight, P. St.J. Russell IEEE Photon. Tech. Lett. **11**, 674 (1999)

[154] J. K. Ranka, R. S. Windeler, A. J. Stentz Opt. Lett. **25**, 25 (2000)

[155] K. L. Corwin, N. R. Newbury, J. M. Dudley, S. Coen, S.A. Diddams, K. Weber, R. S. Windeler Phys. Rev. Lett. **90**, 113904-1 (2003)

[156] S. Cohen, A. H. L. Chau, R. Leonhardt, J. D. Harvey, J. C. Knight, W. J. Wadsworth, P. St. J. Russell Opt. Lett. **26**, 1356 (2001)

[157] P. A. Champert, S. V. Popov, J. R. Taylor Opt. Lett. **27**, 122 (2002)

[158] A. Efimov, A. J. Taylor, F. G. Omenetto, J. C. Knight, W. J. Wadsworth, P. St. J. Russell Opt. Express. **11**, 910 (2003)

[159] J. H. V. Price, W. Belardi, T. M. Monro, A. Malinowkski, A. Piper, D. J. Richardson Opt. Express. **10**, 382 (2002)

[160] A. W. Snyder, John. D. Love, Optical Waveguide Theory, Chapman & Hall (1983)

[161] J. C. Baggett, T. M. Monro, K. Furusawa, D. J. Richardson Opt. Lett **26**, 1045 (2001)

[162] T. M. Monro,V. Pruneri, N. G. R. Broederick, D. Faccio, P. G. Kazansky, D. J. Richardson IEEE Photn. Tech. Lett. **13**, 981 (2001)

[163] J. H. V. Price, T. M. Monro, K. Furusawa, W. Belardi, J. C. Baggett, S. Coyle, J. J. Baumberg, R. Paschotta, D. J. Richardson, Appl. Phys. B, (2003)

[164] D. Ferrarini, L. Vincetti, M. Zoboli, A. Cucinotta, S. Selleri Opt. Express. **10**, 1314 (2002)

[165] T. P. White, R. C. Mchphedran, C. McPhedran, C. M. de Sterke, L. C. Botten, M. J. Steel Opt. Lett. **26**, 1660 (2001)

[166] A. L. Gaeta, Opt. Lett. **27**, 924 (2002)

[167] M. C. Netti, C. E. Finlayson, J. J. Baumberg, M. D. Charlton, M. E. Zoorob, J. S. Wilkinson, G. J. Parker Appl. Phys. Lett. **81**, 3927 (2002)

[168] http://www.olympusmicro.com/

[169] http://www.dlp.com/

[170] S. M. Spillane, T. J. Kippenberg, K. J. Vahala Nature **415**, 621 (2002)

[171] T. Lopez-Rios, D. Mendoza, F. J. Garcia-Vidal, J. Sanchez-Dehesa, B. Pannetier Phys. Rev. Lett., vol. **81**, 665 (1998)

[172] A. A. Lucas Phys. Rev. B. **7**, 3527 (1973)

[173] A. E. Siegman, *Lasers*, University Science Books (1986)

[174] T. V. Teperik, V. V. Popov, F. J. García de Abajo Phys. Rev. B. **69**, 155402 (2004)

[175] P. Lagoudakis, PhD Thesis University of Southampton, UK

[176] F. Pincemein, A. A. Maradudin, A. D. Boardman, J. -J. Greffet Phys. Rev. B. **50**, 15261 (1994)

[177] K. F. MacDonald, V. A. Fedotov, R. W. Eason, N. I. Zheludev, A. V. Rode, B. L-Davies, V. I. Emel'yanov J. Opt. Soc. Am. B. **18**, 331 (2001)

[178] P. Petropolous, H. L. Offerhaus, D. J. Richardson, S. Dhanjal, N. I. Zheludev Appl. Phys. Lett. **74**, 1 (1999)

[179] K. F. MacDonald, V. A. Fedotov, N. I. Zheludev, B. V. Zhdanov, R. J. Knize Appl. Phys. Lett. **79**, 2375 (2001)

[180] A. V. Rode, M. Samoc, B. L-Davies, E. G. Gamaly, K. F. Macdonald, N. I. Zheludev Opt. Lett. **26**, 441 (2001)